Mathematical Problems in Engineering

Seismic Mitigation and Isolation of Engineering Structures: Analysis, Monitoring and Assessment

Lead Guest Editor: Hao Wang
Guest Editors: Kaiming Bi and Jian Li

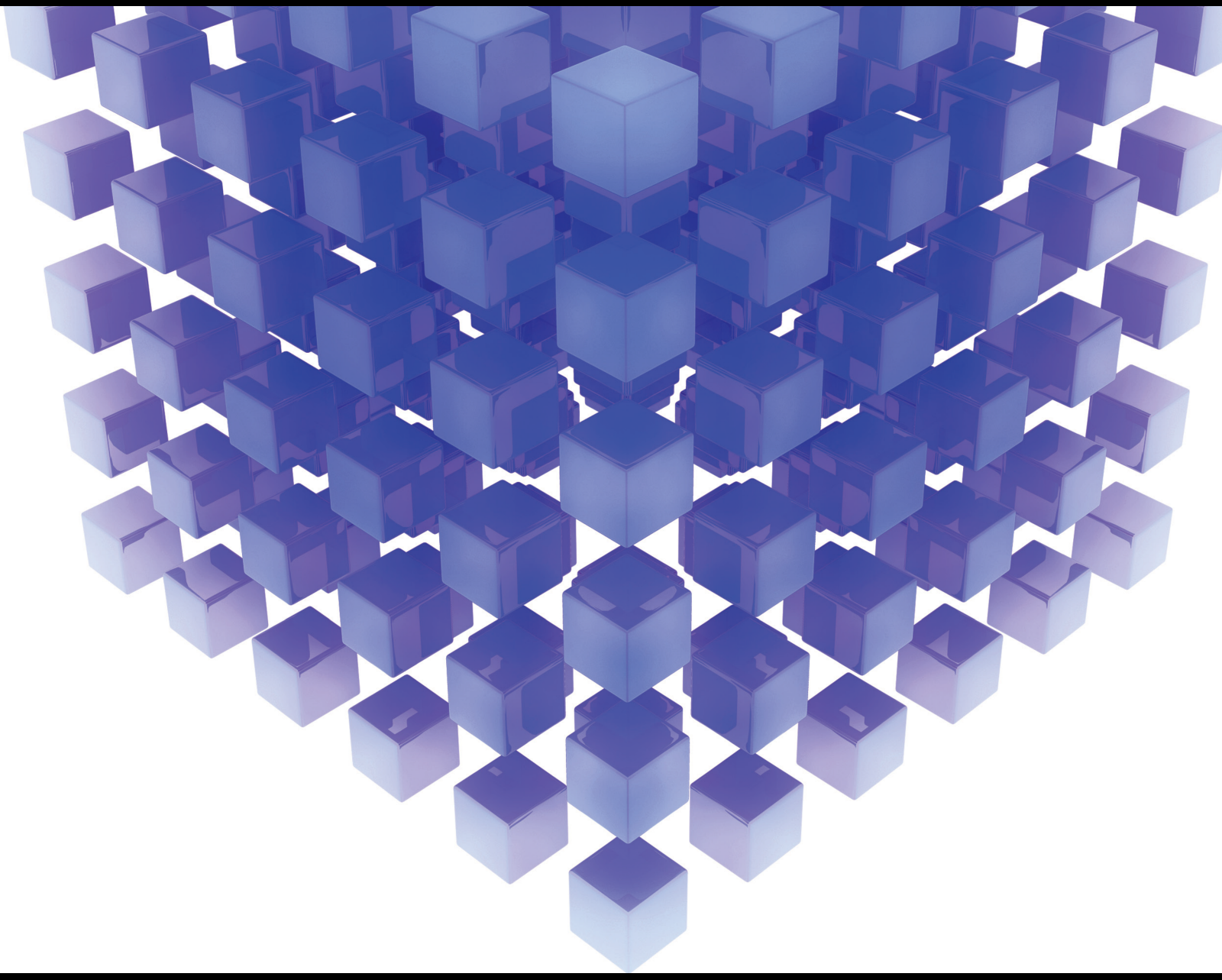

Seismic Mitigation and Isolation of Engineering Structures: Analysis, Monitoring and Assessment

Mathematical Problems in Engineering

Seismic Mitigation and Isolation of Engineering Structures: Analysis, Monitoring and Assessment

Lead Guest Editor: Hao Wang
Guest Editors: Kaiming Bi and Jian Li

Contents

Hindawi
Mathematical Problems in Engineering
Volume 2021, Article ID 6667446, 17 pages
https://doi.org/10.1155/2021/6667446

Research Article

Study on the Semiactive Control and Optimal Layout of a Hydropower House Based on Magnetorheological Dampers

Shaopei Hu,[1] **Chao Su**,[1] **Mingjiao Yan**,[1] **Yang Yang**,[2] **Jiawei Bai**,[1] **and Enhua Cao**[1]

[1]*College of Water Conservancy and Hydropower Engineering, Hohai University, Nanjing 210098, China*
[2]*PowerChina KunMing Engineering Corporation Limited, KunMing 650051, China*

Correspondence should be addressed to Chao Su; csu_hhu@126.com, Mingjiao Yan; ymjwing@qq.com, and Yang Yang; yangyhhu@foxmail.com

Received 11 December 2020; Revised 21 January 2021; Accepted 3 November 2021; Published 3 December 2021

Academic Editor: Hao Wang

With the continuous development of hydropower stations, the capacities and the heads of hydro generator units are increasing, and the plant vibration problem is becoming more and more serious. A numerical simulation method for the vibration reduction control of magnetorheological (MR) dampers suitable for large-scale complex structures was proposed. The method is simple and easy to implement, and the semiactive control of the MR damper could be achieved by adjusting the current switch and size. On the basis of a numerical simulation, a mathematical model for the optimal layout of an MR damper device was established. The objective function was the vertical velocity and the vertical acceleration response of the generator floor. The results showed that the proposed semiactive control numerical simulation method could be applied to the vibration control of the hydropower plant structure, and the vertical velocity and vertical acceleration were reduced by 10.96% and 12.90%, respectively, compared with those without structural vibration control. At the same time, the proposed optimized layout method was effective and feasible, and the damping effect of the MR damper could be effectively improved through the optimized layout.

1. Introduction

The vibration of hydropower generating units is a major issue related to the safe and stable operation of hydropower generating units. The vibration will not only consume part of the power, reduce the efficiency of the unit, and shorten the maintenance cycle and service life but also cause the entire plant structure and the water pipes to be forced to stop [1–3].

As a new type of intelligent vibration damping device, magnetorheological (MR) damper has the advantages of simple structure, a wide range of damping force, fast response (millisecond level), low energy consumption, and large output damping [4]. In recent years, scholars around the world have carried out a lot of research on the vibration damping control of MR dampers. Mohajer Rahbari et al. [5] used MR dampers to study the semiactive control of three- and eleven-layer shear wall structures, and they evaluated the performance of the conversion controllers. Zahrai and Salehi [6] selected nine- and twenty-story buildings and used MR dampers to conduct semiactive control studies on the buildings. The results showed that the maximum acceleration of the structure was reduced by more than 21%, so the use of semiactive control could greatly reduce the structural response. Ok et al. [7] used MR dampers to conduct semiactive control studies on cable-stayed bridges. The simulation results showed that the use of MR dampers significantly reduced the structural response of cable-stayed bridges. Bhaiya et al. [8] used a limited number of MR dampers to optimally control a ten-story building frame structure, and they studied the influence of the position of the MR dampers on the response. The semiactive control of the damper could effectively reduce the response of the frame structure. Abdeddaim et al. [9] used MR dampers to link two adjacent buildings on the top layers of two adjacent buildings, and this coupling strategy effectively reduced the vibration response of the structure. At present, MR dampers have achieved good vibration reduction effects in bridges, buildings, offshore platforms, and other constructions.

However, they have not been used in the vibration reduction of the hydropower plant.

The process of reducing the dynamic response of the structure is called structural vibration control by applying a control system to the structure to make the structure resist the action of dynamic load [10]. In 1972, Yao [11] gave the notion of structural control, and since then, this field has emerged by leaps and bounds. To date, it is commendable to have adopted some control strategies. The displacement response of the bridge in earthquakes can be effectively reduced by employing the shape memory alloy (SMA) in the sliding-lead rubber bearing (LRB) system [12, 13]. During an earthquake, the temperature adjustment of the SMA in the pendulum friction bearing (FPB) system effectively alters its hysteresis energy dissipation capacity, thereby changing the control efficiency of the isolation system [14]. The new basic vibration isolator using sliding implant-magnetic bearing and sliding hydromagnetic isolators achieves better performance in earthquake/vibration isolation and mitigation [15, 16]. The use of a hybrid controller can improve the comfort of the vehicle and the stability of the movement [17–19]. The application of damper control strategies to reduce the displacement response of buildings in earthquakes has been proven [20, 21]. These strategies offer the prospect of developing applications, improving efficacy, and providing better acceptability. Among them, the semiactive control strategy combines the excellent control effect of active control and the advantages of simple and easy passive control, while overcoming the shortcomings of active control requires a large amount of energy supply and narrow tuning range of passive control. Therefore, semiactive control has a greater prospect for research and application development [22], and it has attracted more and more attention from scholars. Bathaei et al. [23] used two different fuzzy controllers to study the seismic vibration of an adaptive MR damper. This method could further reduce the maximum displacement, acceleration, and foundation shear force of a structure. Lee et al. [24] proposed a semiactive damping control strategy based on a neural network controller and an MR damper. Compared with passive control, the numerical simulation results showed that the proposed controller could significantly reduce floor acceleration, base shear, and angular displacement. Hazaveh et al. [25] used discrete wavelet transform (DWT), a linear quadratic regulator (LQR), and a limiting optimal control algorithm to determine the optimal control force. The semiactive control performance was evaluated by comparing the maximum displacement, the total shear force of the substrate, and the control energy. The damping effect of the MR damper depended on the size of the input current, the control method, and the arrangement of the MR damper. Kim and Lee [26] proposed a sensitivity evaluation algorithm to make the neurocontrol system compact and reduce the total training time without an emulator. At present, the theoretical researches on the damping control of MR damper require a certain simplification of the structure in the calculation. The analysis of structural control by instantaneous dynamics was used in ABAQUS simulation analysis, and the characteristics of material nonlinearity and geometric large deformation could also be considered.

Installing energy damping devices at optimal locations helps designers achieve the desired reduction of vibrations with minimum costs. At present, the commonly used methods for this problem are the "trial and error method" and the "exhaustive method." The former method generally obtains a local optimal solution, while the latter method is only suitable for systems with small spaces [27]. A more precise inspection of all feasible arrangements to find out which one would produce the expected structural reduction dynamic response turned out to be very time-consuming. Dealing with this problem, researchers have suggested different approaches. Singh and Moreschi [28] used a genetic algorithm to find the optimal position of an MR damper. Amini and Ghaderi [29] proposed an improved ant colony optimization algorithm to optimize the installation position of an MR damper. Agranovich and Ribakov [30] proposed a heuristic solution for the efficient placement of active dampers in seismically excited structures. Main and Krenk [31] presented the studies concerning the allocation and sizing of viscous dampers. Lewandowski [32] investigated the optimal distribution of viscous dampers by an objective function in the form of a sum of weighted, nondimensional modal damping ratios. Singh and Moreschi [33] obtained the optimal arrangement of dampers based on the gradient method. A genetic algorithm is a randomized search method derived from the evolution of biological evolution law, and it can automatically and gradually seek the optimal solution or approximate the optimal solution of the problem space [34].

In this paper, we realize the passive control and semiactive control of the magnetorheological damper by using two subroutines, URDFIL and DLOAD, based on the Bouc–Wen model. Then, a mathematical model for the optimization design of the plant layout of the MR damper was established, and the optimization objective function was selected to minimize the vertical velocity and acceleration response of the generator floor. Using a multiobjective genetic algorithm, the encoding methods, population initialization, crossover, and mutation adaption to the spatially optimized layout of the MR dampers were proposed to optimize the layout of the MR dampers. Finally, the different vibration damping control methods were used to evaluate the damping effect of the MR damper after the optimized arrangement.

2. Magnetorheological Damper

MR damper is currently the fastest research and development field for MR fluids. It is a new type of intelligent damping device that uses MR effects. MR damper is a damper made of MR fluid, and its structure is shown in Figure 1. It is composed of electrical control lines, piston rod, piston, orifice, and buffer accumulators. MR damper has a simple device, low energy consumption, fast response, large damping, and wide dynamic range. The damping force can be controlled by adjusting the current or voltage, so it can be well integrated with the control system. Even when the

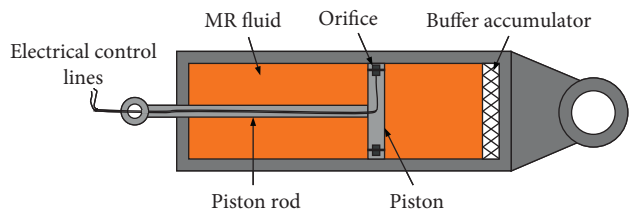

Figure 1: Schematic diagram of the magneto-rheological damper.

control system fails, it can also be used as a passive controller with strong reliability.

3. Bouc–Wen Model

Wen [35] proposed a simple mathematical hysteresis model, called the Bouc–Wen model in 1976. The model consisted of a hysteretic system, a spring and a damper in parallel, as shown in Figure 2. The Bouc–Wen model was universal and easy to be digital modeling. It could accurately reflect the nonlinear performance of the MR damper at a low speed and simulate the hysteretic characteristics of the MR damper.

The damping force of the model can be expressed as follows:

$$F = c_0\dot{x} + k_0(x - x_0) + \alpha z, \tag{1}$$

$$\dot{z} = -\gamma|\dot{x}|z|z|^{n-1} - \beta\dot{x}|z|^n + A\dot{x}, \tag{2}$$

where F is the damping force of an MR shock absorber; α represents the model parameters related to the MR yield stress; k_0 is the spring stiffness; c_0 is the viscosity coefficient of the MR material after yielding; x and $\dot{x}$ are the relative displacement and the relative velocity of the MR damper piston and cylinder, respectively; z is the hysteresis displacement; x_0 is the initial deformation of the spring; and $A, \beta, \gamma,$ and n are constants that were determined by the structural characteristics of the MR damper.

The solution flow chart of the Bouc–Wen model is shown in Figure 3. This model contains eight unknown parameters. As shown in Figure 3, x is a sinusoidal displacement excitation signal $x = A\sin(2\pi f t)$, where A is the amplitude, f is the frequency, and Partialz is a Simulink subsystem that was used to evaluate the hysteresis $\dot{z}$ in the model.

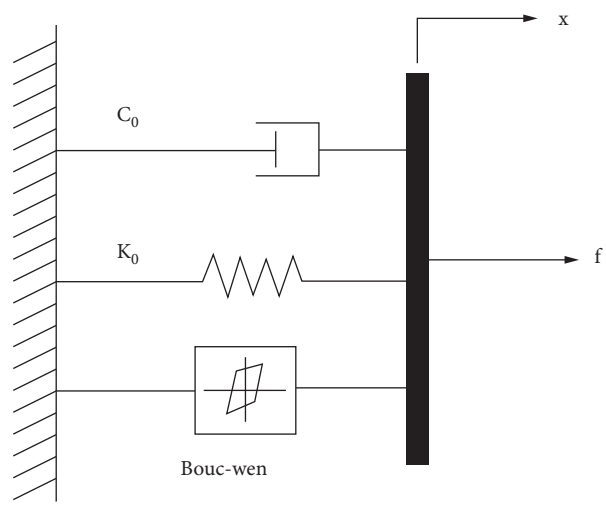

Figure 2: Schematic diagram of the Bouc–Wen model.

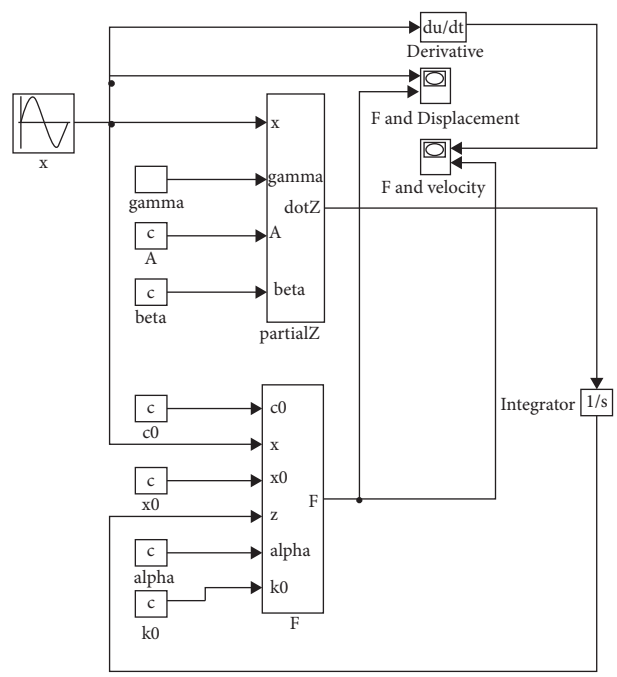

Figure 3: The solving chart of the Simulink simulation for the Bouc–Wen model.

4. Numerical Simulation Method

The damping control of the MR damper involved changing the dynamic characteristics of the structure by applying a control force to the structure through the MR damper, thereby achieving a damping effect. For the MR damper control system, its motion differential equation could generally be expressed as follows:

$$[M]\ddot{x}(t) + [C]\dot{x}(t) + [K]x(t) = -[M]\Gamma\ddot{x}_g + [\Lambda]F, \tag{3}$$

where M is the structural mass matrix; C is the structural damping matrix; K is the structural stiffness matrix; $\ddot{x}_g$ represents the external incentives; F is the control force provided by the MR damper; $\ddot{x}(t)$, $\dot{x}(t)$, and $x(t)$ are the acceleration, velocity, and displacement vectors of the structure, respectively; Γ represents the external incentives; and Λ is the MR damping force indicator matrix.

The state vector was introduced as follows:

$$Z(t) = \begin{bmatrix} x(t) \\ \dot{x}(t) \end{bmatrix}. \tag{4}$$

Then the equation of motion could be transformed into an equation of state as follows:

$$\dot{Z}(t) = [A]Z(t) + [B]u + [E]\ddot{x}_g, \quad (5)$$

$$Y(t) = [C]Z(t) + [D]F, \quad (6)$$

where A and C are the characteristic matrices describing structural systems, B and D are the performance parameter matrices of the MR damper, and E is the external stimulus position matrix. In the simulation analysis of the MR damper vibration reduction, the optimal control force F was determined by solving the state equation.

4.1. Realization of the Passive Control Method for the MR Damper. In this investigation, the Bouc–Wen MR damper mechanical model was selected for vibration reduction research. The model used the reciprocating displacement x and the velocity $\dot{x}$ of the structural vibration to change the control force of the MR damper. An RD-8041-1 MR damper [36] produced by the United States LORD company was selected to study the vibration damping control of the structure. This type of MR damper controls a damper by controlling the input current. Therefore, the passive control of this MR damper included two modes: passive-off (the current was zero) and passive-on (the current was not zero). Through the secondary development of Abaqus, the passive control of the MR damper was achieved. The overall idea was that for the constant current state, the control force of the MR damper calculated by the Bouc–Wen model was equivalent to an equivalent uniform load that was applied to the corresponding damping control area to achieve the MR damping passive control of the device. The flow of the passive control algorithm of the MR damper is shown in Figure 4, which specifically includes the following steps:

(1) The displacement x and the velocity $\dot{x}$ of each incremental step of the control point were obtained with the URDFIL subroutine, and the data was stored in the global variable COMMON block. The displacement keyword in the .fil file was 101, and the speed was 102.

(2) In the constant current state, according to the displacement x and the velocity $\dot{x}$, the Bouc–Wen MR damper mechanical model was used to calculate the control force F of each incremental step, and the data was stored in the global variable COMMON block.

(3) The control force F was transferred to the subroutine DLOAD through the global variable COMMON block, thereby applying the control force F to the corresponding control area.

(4) The above process was repeated for each incremental step until the end of the program.

4.1.1. URDFIL Subroutine. The URDFIL subroutine is used to read the data in the result file (.fil) at the end of the increment. In this research, the URDFIL subroutine is used to read the displacement and speed of each incremental step of the control point.

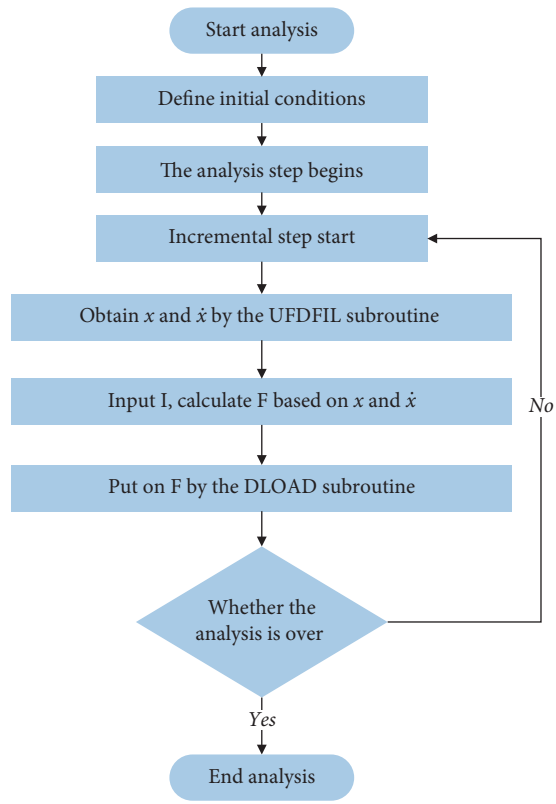

Figure 4: The flow chart of the passive control algorithm for the MR damper.

The flow chart of the URDFIL subroutine is provided in Figure 5.

In Figure 5, N represents the number of monitoring points; M represents the number of finite element model nodes; and Key is also the keyword defined in the subroutine. The diagram above shows the flow chart of the URDFIL subroutine.

(1) All parameters are entered into the subroutine

(2) Determine whether N and M are equal

(3) If N is equal to M, get the value of the keyword and read the corresponding data of the keyword

(4) Output the read data

4.1.2. DLOAD Subroutine. The DLOAD subroutine could be called at each integration point to customize the non-uniformly distributed pressure load that changes with position, time, element, and node number. In this research, the DLOAD subroutine is used to apply damping force to the control area of the MR damper in each incremental step

The flow chart of the DLOAD subroutine is provided in Figure 6.

In Figure 6, I represents the input current; X and V represent the displacement and velocity obtained through the URDFIL subroutine respectively; SNAME represents the name of the loading surface; FNAME represents the name of the surface in the finite element model; and 11 is the parameter of the

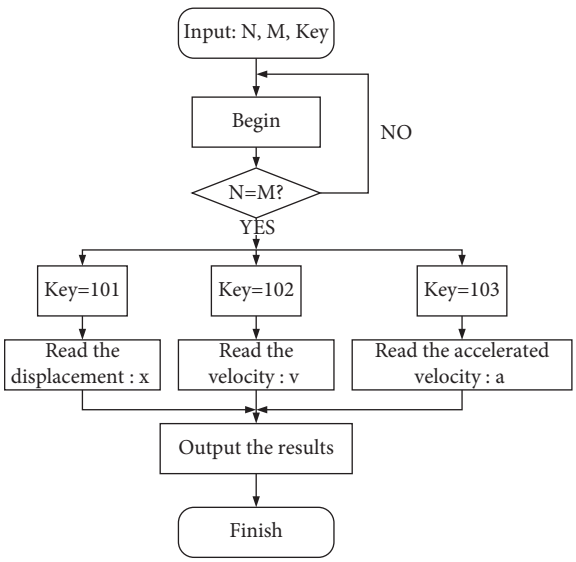

Figure 5: The flow chart of the URDFIL subroutine.

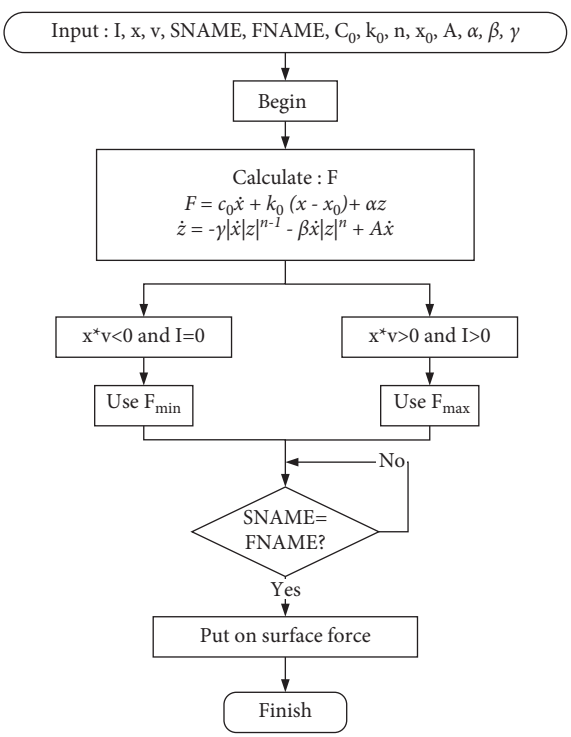

Figure 6: The flow chart of the DLOAD subroutine.

magnetorheological damper. The diagram above shows the DLOAD subroutine flow chart.

(1) All parameters are entered into the subroutine

(2) Calculate damping force F

(3) If $x * v$ is less than zero and I is equal to zero, output $F_{\min}$; if $x * v$ is greater than zero and I is greater than zero, output $F_{\max}$

(4) Determine whether SNAME and FNAME are equal

(5) If SNAME is equal to FNAME, apply surface force to the corresponding SNAME; otherwise, rejudge

4.2. Realization of the Semiactive Control Method of the MR Damper. The semiactive control belongs to the parametric control and depended on the structural response and the external excitation information [37]. The control process was to reduce the response of the structure by changing the stiffness or the damping parameters of the structure in real time with a small amount of energy. The semiactive control did not require a large amount of external energy input to provide the control force. The actuators that exert control forces require a small amount of energy in order to actively take advantage of the reciprocating relative deformation or the velocity of structural vibration. The semiactive control strived to achieve the optimal control force, so a semiactive control algorithm was needed to control the MR damper to apply the optimal control force F. The specific semiactive control algorithm flow of the MR damper is shown in Figure 7. The specific steps included:

(1) The displacement x and the velocity $\dot{x}$ of each incremental step of the control point were obtained through the URDFIL subroutine, and the data was stored in the global variable COMMON block at the same time.

(2) According to the displacement x and the velocity $\dot{x}$, the semiactive control algorithm was used to calculate the optimal control force F' of the MR damper based on the Bouc–Wen model, and the data was stored in the global variable COMMON block.

(3) The optimal control force F' was transferred to the subroutine DLOAD through the global variable COMMON block so that the control force was applied to the corresponding control area.

(4) The above process was repeated for each incremental step until the end of the program.

The current semiactive control algorithms mainly included the simple bang-bang control algorithm [38, 39], the optimal bang-bang control algorithm [40, 41], and the limited Hrovat optimal control algorithm [42, 43]. To solve the shortcoming of the simple bang-bang control algorithm, in that the acceleration would change suddenly, we proposed an improved simple bang-bang control algorithm to achieve the semiactive control of the MR damper. Figure 7 shows the response state of the structure when there was a sudden change in acceleration. As shown in Figure 8(c), there was a sudden change in acceleration in section AB. As shown in Figures 8(a) and 8(b), when the speed at point A was zero, the structure moved from one end of the direction to the center equilibrium position. Therefore, according to the simple bang-bang algorithm, when the current of the MR damper was zero at that time, the AB segment applied the minimum damping coefficient. In the Bouc–Wen model, the calculated damping force is smaller when the velocity at point A was zero. When the speed increased to point B, the damping force could reduce the structure acceleration. In

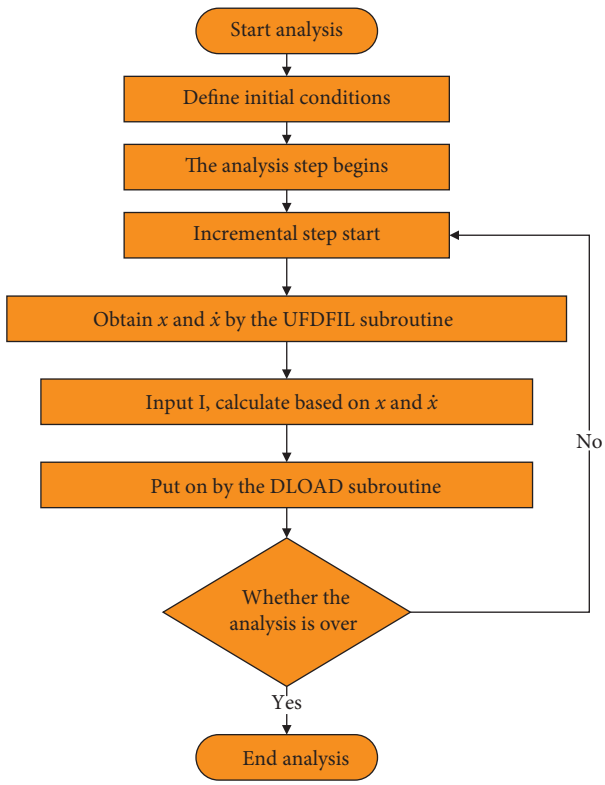

Figure 7: The flow chart of the semiactive control algorithm for the MR damper.

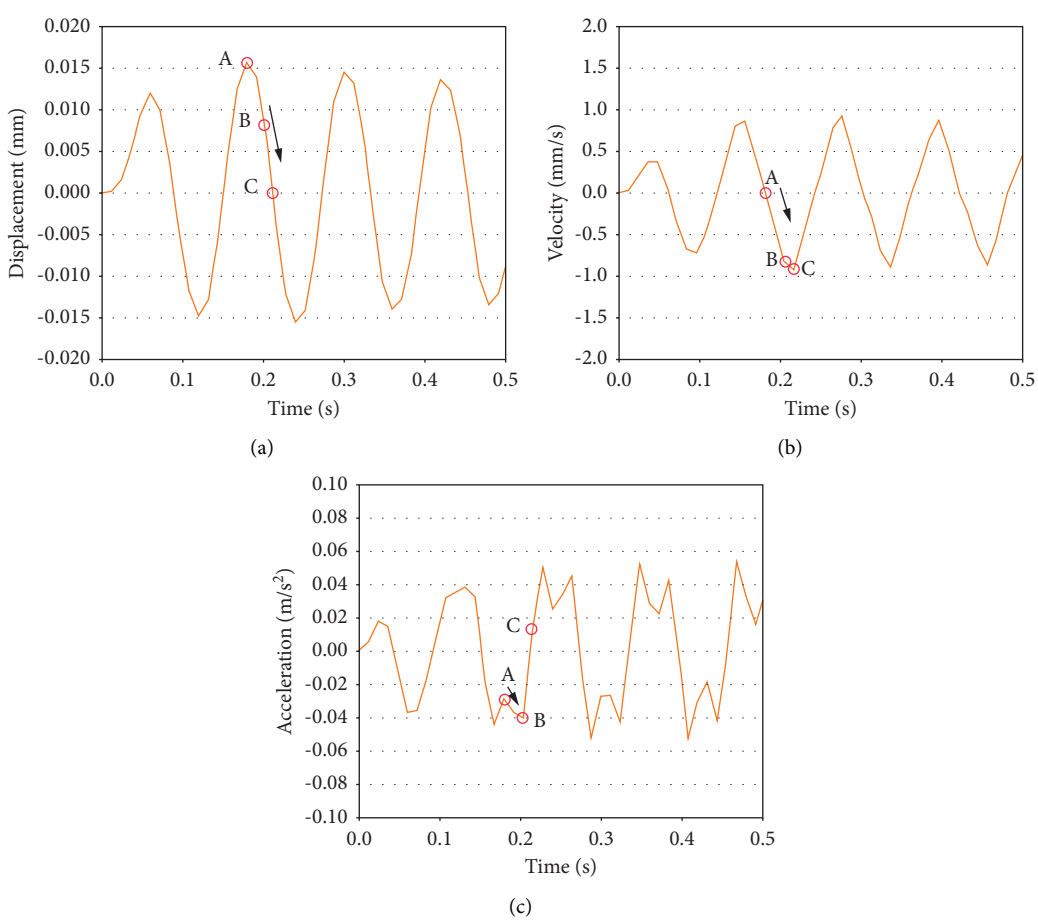

Figure 8: The response state of the structure with the sudden change of acceleration: (a) displacement, (b) velocity, and (c) acceleration.

order to eliminate the sudden change of acceleration in the AB segment, the damping force in this segment needed to be increased. In other words, the input current value of the AB segment MR damper needed to be increased.

5. Optimal Layout Method for MR Dampers

Research has shown that increasing the number of MR dampers can improve the effect of vibration reduction control [44]. However, too many MR dampers will increase the cost, the weight of a system, and the difficulty of construction. At the same time, the time required for data collection, analysis, calculation, and control signal input and output will become longer, and the probability of failure of the control device, the maintenance cost, and the probability of system failure will also increase. Under the premise of not affecting the function of a plant [45], the vibration reduction effect and the requirements for the use of plant space are comprehensively considered to maximize the vibration reduction effect of a plant. When arranging MR dampers, the arrangement and spatial distribution of MR dampers should be selected reasonably to maximize the effect of vibration reduction.

The previous research results have shown that the vertical velocity and acceleration of a generator floor are relatively large [46]. Under no-load conditions, two-phase short-circuit conditions, and half-pole short-circuit conditions, the vertical speed and acceleration exceeded the vibration control standard values. Therefore, in this research, the control of the vertical speed and the vertical acceleration of the generator floor were mainly considered. With the premise of a certain number of MR dampers, the objective function was to minimize the vertical velocity and acceleration of the generator floor. The optimal arrangement of MR dampers could be expressed as the following multiobjective function optimization problem:

$$\min f(x) = \begin{cases} \min f_A(x), \\ \min f_V(x), \end{cases} \tag{7}$$

where $f_A(x)$ is the objective function of the vertical acceleration response, $f_V(x)$ is the vertical velocity response objective function, and x is the MR damper layout scheme.

In most engineering optimization problems, multiple objectives need to be optimized at the same time, and the optimization process needs to maximize or minimize multiple objective functions at the same time. The multiobjective optimization problem can be expressed as follows:

$$\begin{aligned} &\min f(x) = \min\left[f_1(x), f_2(x), \cdots f_n(x)\right], \\ &\mathbf{X} = \left[x_1, x_2, \cdots x_n\right]^T \in E^n, \\ &\text{s.t. } g_i(x) \le 0, \quad i = 1, 2, \cdots, m, \end{aligned} \tag{8}$$

where $f_i(x)$ is the optimized subobjective function, $\mathbf{X} = [x_1, x_2, \cdots, x_n]^T$ is the decision vector, and $g_i(x)$ represents the restrictions.

In the multiobjective optimization problem shown in Figure 8, the two objective functions $f_1(x)$ and $f_2(x)$ were contradictory. As shown in Figure 9, $A_1 < B_1$ and

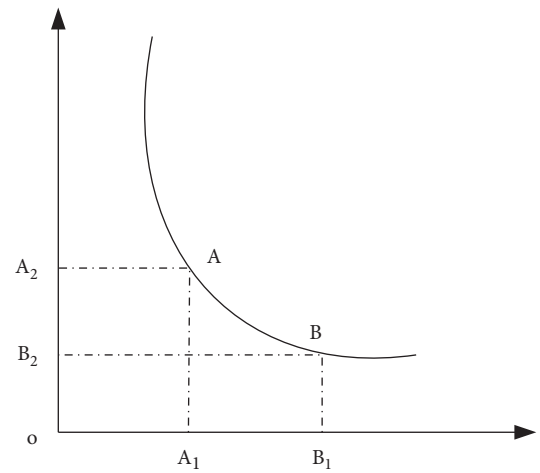

Figure 9: The problem of multiobjective optimization.

$A_2 > B_2$, that is, if one objective function was improved, another objective function reduction is required as the cost; hence, solutions A and B of the multiobjective optimization problem were called noninferior solutions or Pareto optimal solutions. The Pareto optimal solution was a set in which each Pareto optimal solution was only a noninferior solution, and the multiobjective optimization problem searched for these Pareto optimal solutions [47].

The current method for solving multiobjective optimization problems is generally to convert multiobjective problems into single-objective function optimization problems. The methods of using genetic algorithms to solve multiobjective optimization problems Pareto solutions mainly include [48, 49] the weight coefficient method, the vector evaluation method, the maximum and minimum value method, the parallel selection method, and the shared function method. In this research, the weight coefficient method was used to solve the multiobjective function. For a multiobjective optimization problem, each subobjective function $f_i(x)$ $(i = 1, 2, \cdots, n)$ was assigned a corresponding weight w_i $(i = 1, 2, \cdots, n)$. Therefore, a multiobjective optimization problem could be transformed into a single-objective optimization problem, and its mathematical expression could be expressed as follows:

$$f(x) = \sum_i^n \omega_i \cdot f_i(x). \tag{9}$$

Then through the weight coefficient method, the multiobjective optimization problem of formula (7) was transformed into the following single-objective optimization problem:

$$f(x) = \omega_A f_A(x) + \omega_V f_V(x), \tag{10}$$

where $f_A(x)$ is the objective function of the vertical acceleration response, $f_V(x)$ is the vertical velocity response objective function, ω_A is the objective function weight coefficient of the vertical acceleration response, ω_V is the objective function weight coefficient of the vertical velocity response, and x is the MR damper layout scheme.

With the premise of considering the principle of symmetry as far as possible between the center of mass and the center of rigidity, an optional position where the dampers could be arranged was selected according to the structural characteristics of the hydropower plant and the requirements of space use. After determining the optional installation position of the MR damper, a suitable coding method was proposed to encode the damper, and the spatial position information of the damper was converted into a code that could be recognized by the genetic algorithm.

When optimizing the layout, the number of dampers needed to be fixed, and the population needed to ensure the same number of dampers during initialization, mutation, and crossover. Finally, through the genetic algorithm, the optimal layout of the MR damper could be obtained to meet the space requirements of the hydropower plant.

5.1. Programming of the Optimal Arrangement of MR Dampers. At present, there are two methods for the secondary development of Abaqus, using Fortran for the solution level and Python for the pre- and postprocessing levels. Based on the multiobjective genetic algorithm, in this research, Python scripts and Fortran were used to perform the secondary development of Abaqus to achieve the optimization program of the MR damper of the hydropower plant structure. The flowchart is illustrated in Figure 10. The pre- and postprocessing module adopted Python scripting language for secondary development, and the solving module adopted Fortran for the secondary development of subroutines. The specific steps were as follows:

(1) In the Abaqus preprocessing module, the optional installation position of the MR damper was binary coded, and the position matrix of the MR damper was initialized.

(2) The position matrix was decoded, and the installation position of the MR damper was active with the Python script, that is, the surface applied by the load at that position was active.

(3) The vibration reduction was calculated with Abaqus.

(4) The objective function value was extracted from the result file ODB through a Python script, and the function fitness value was calculated. Subsequently, the operator was operated through the selection, crossover, and mutation of the genetic algorithm to obtain a better offspring population. This progeny population was a new MR damper position matrix.

(5) Steps 2, 3, and 4 were repeated until the end of the calculation.

(6) The optimal position matrix of the MR damper was decoded and output.

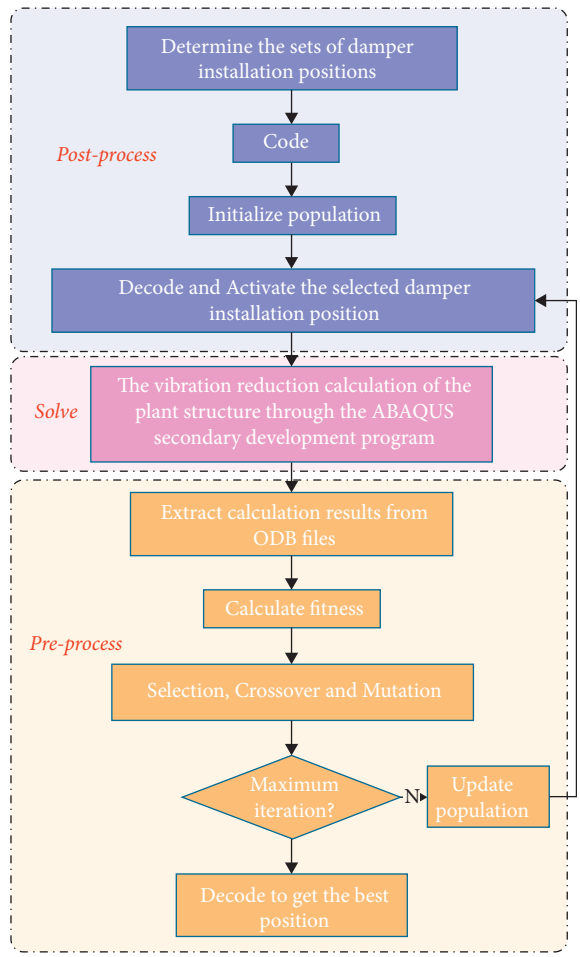

Figure 10: Flow chart of MR damper optimal layout program.

5.2. MR Damper Position Coding. When using genetic algorithms to solve optimization problems in engineering, we first used a reasonable coding method to properly represent the solution space of the optimization problem. Before optimizing the arrangement of the MR damper, we first selected all of the positions N where the damper could be installed according to the structural characteristics, and we numbered the selected installation positions. The arrangement information of the MR damper could be represented by a tuple $S(n, i)$, where $n(n \in 1, 2, \cdots, N)$ is the installation position number of the MR damper and i indicates whether the damper was installed here (1 means installation and 0 means no installation). Therefore, the optional installation positions of the MR dampers in the plant structure were binary coded in sequence. The length of the chromosome was equal to the total number N of possible positions in the structure. Assuming that the number of optional arrangements of MR dampers was 12 and the number of dampers selected was 6, the chromosome could be expressed as follows:

Location / Chromosome	1	2	3	4	5	6	7	8	9	10	11	12
P1	0	0	1	1	0	0	1	1	0	1	0	1
P2	1	0	0	1	0	1	1	0	1	1	0	0
⋮	⋮	⋮	⋮	⋮	⋮	⋮	⋮	⋮	⋮	⋮	⋮	⋮

Chromosome P1 = [001100110101] means that the MR damper was arranged at positions 3, 4, 7, 8, 10, and 12. Chromosome P2 = [100101101100] indicates that the MR damper was arranged at positions 1, 4, 6, 7, 9, and 10. Through the above coding method, the spatial information of the MR damper arrangement could be transformed into a code that could be recognized by the genetic algorithm.

5.3. Initialization of the Population. After determining the encoding method of the MR damper, the arrangement scheme of the MR damper was coded through population initialization. In the genetic algorithm, the initialization of the population involved generating the initial population of the required individuals through a random method. The initialized population was a two-dimensional array P, with the rows representing each arrangement plan and the columns representing the position of the damper for choosing the arrangement.

$$P = \begin{bmatrix} P_1^1 & \cdots & p_1^n \\ \vdots & \ddots & \vdots \\ P_a^1 & \cdots & p_a^n \end{bmatrix}, \tag{11}$$

where a is the population size and n is the chromosome length, which was equal to the number of optional positions.

The number of dampers to be installed for the space optimization problem of the MR dampers was fixed, so the number of MR dampers in the initialization unit needed to be restricted. According to the coding method, the value of a chromosome was either 0 or 1. If the number of dampers was set to m, the constraint condition could be expressed as follows:

$$\sum_i^n t_i = m, \tag{12}$$

where n is the chromosome length, and t_i is the value on the $i-$th chromosome. Therefore, the constraint conditions could ensure that each individual obtained by initialization contained m dampers, thus ensuring the correctness of the chromosome. The size of the population had a great influence on the performance of genetic algorithms. The population size was too large to increase the calculation time, which caused the competitive advantage over other methods to be lost. The population size was too small, which makes it difficult to satisfy the species diversity. It is possible that the population did not contain the optimal gene at the beginning, and it was difficult to find the potential optimal individual during the evolution process. In that case, the competitiveness between individuals was not great, which caused the genetic algorithm to greatly reduce the optimization ability. Therefore, selecting an appropriate population size was the key starting point for the entire genetic algorithm. This step had to ensure that the initial population cause essentially contain all possible genes in order to find the optimal individual as soon as possible. According to the experience of other researchers [49, 50], the population size was usually set to 20–100.

5.4. Fitness Function. Fitness is an index used to measure the pros and cons of individuals, and it is also the only basis for natural selection. Individuals with high fitness are more likely to be selected and inherited to the next generation. For the optimal placement of the MR dampers in the plant structure, the response of the plant structure was taken as the objective function (see equation (8)) to calculate the fitness value. Therefore, the larger the fitness value, the smaller the objective function value, and the better the individual, which indicated that the optimally arranged MRD had a better vibration damping effect.

The fitness function had to satisfy the conditions of [36, 37]: (1) being single value, continuous, nonnegative, and maximized; (2) being reasonable and consistent; (3) having a small amount of calculation; and (4) having strong versatility. For the minimum objective function, the fitness function is as follows:

$$\{F\} = \begin{cases} \{C_{\max}\} - \{f(x)\}, & \{f(x)\} < \{C_{\max}\}, \\ 0, & \text{other}, \end{cases} \tag{13}$$

$$[K]\{u\} = \{F\}, \tag{14}$$

$$\{u\} = \begin{Bmatrix} v \\ a \end{Bmatrix}, \tag{15}$$

$$\{F\} = c_0\dot{x} + k_0(x - x_0) + \alpha z, \tag{16}$$

$$\{f(x)\} = \{u\} = [K]^{-1}\{F\}, \tag{17}$$

where $\{C_{\max}\}$ is the maximum estimate of $\{f(x)\}$, $[K]$ is the system characteristic matrix, and $\{u\}$ is the state variable contains the velocity and the acceleration. The above fitness function fully reflected the differences between individuals. Among them, good individuals could gain a greater chance of survival, while poor individuals were eliminated with a greater probability.

5.5. Selection, Crossover, and Mutation

5.5.1. Select Operation. Natural selection involves selecting excellent individuals from an old population to form a new population with a certain probability and obtaining the next generation of individuals through reproduction. The probability of an individual being selected is related to fitness. The greater the fitness, the higher the probability of the individual being selected. In this research, the selection operation was performed with the roulette method. The probability P_i of the individual being selected is as follows:

$$P_i = \frac{F_i}{\sum_{j=1}^{N} F_j}, \tag{18}$$

where F_i is the fitness value of individual i and N is the number of individuals in the population.

Figure 11 shows a schematic diagram of the roulette method. The roulette wheel represents the entire population, and the area of each block in the roulette wheel is the ratio of the overall fitness of the individual to the population. For individuals with high fitness, the larger the occupied area, the higher the probability of being selected. The specific algorithm flow is as follows. The first step is to calculate the probability P_i of all individuals being selected according to formula (18). The second step is to generate random numbers between 0 and 1 consistent with the population size and to arrange the random numbers from small to large. The third step is to compare the random number with the probability of the individual being selected. Those who were less than the random number were eliminated, and those who were greater than the random number were left. Through the roulette method, the excellent individuals with high adaptability could be selected, and the individuals with low adaptability could be eliminated.

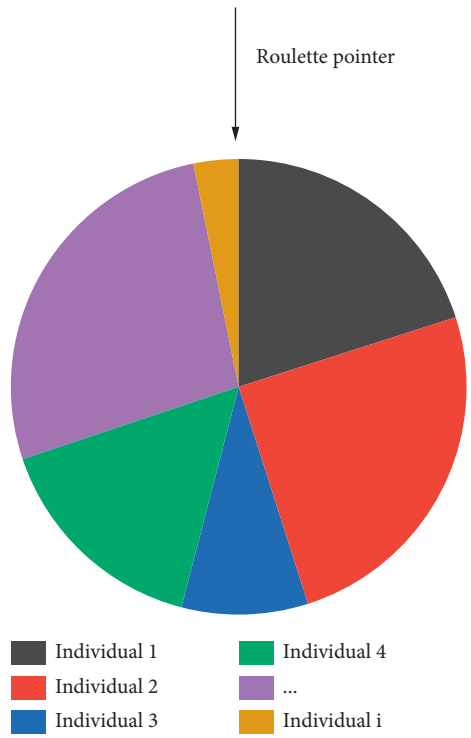

Figure 11: The sketch of the roulette method.

5.5.2. Crossover Operation. The crossover operation involved randomly selecting two individuals from the population, exchanging and combining the chromosomes of the two individuals, and causing the excellent genes of the parent to be inherited by the offspring, thereby forming a better individual. In the optimizing placement of the MR dampers, the new entity obtained by crossover needs to meet the constraint condition of the constant number of dampers. Therefore, the specific crossover algorithm could be described as follows.

It was assumed that the two selected individuals to cross were P1 and P2, for which the individual chromosome length was 12, and the number of MR dampers was 6.

Location / Chromosome	1	2	3	4	5	6	7	8	9	10	11	12
P1	0	0	1	1	0	0	1	1	0	1	0	1
P2	1	0	0	1	0	1	1	0	1	1	0	0

The number of dampers needed to be kept constant for each crossover, so the crossover position needed to be selected correctly. The specific method is as follows. The first step is to accumulate the values of the chromosomes in the individual one by one. Then the accumulation result of P1 and P2 is as follows:

Location / Chromosome	1	2	3	4	5	6	7	8	9	10	11	12
P1	0	0	1	2	2	2	3	4	4	5	5	6
P2	1	1	1	2	2	3	4	4	5	6	6	6

The second step was to compare the cumulative results of two crossover individuals. If the cumulative results were the same at the same position, the position was the crossover position. Therefore, the cross positions of P1 and P2 were 3, 4, 5, and 8, respectively [3–5, 8].

The third step was to randomly select a position among the four optional positions for crossover operation.

The crossover probability determined the frequency of the crossover operation, which had a greater impact on the entire optimization process. If the crossover probability was too high, too many new individuals would be generated, making it difficult for the calculation to converge. If the crossover probability was too small, the newly generated individual would be poor, and the result might fall into the local optimal solution prematurely. Generally, the crossover probability was between 0.4 and 0.9 [49, 50].

5.5.3. Mutation Operation. The purpose of mutation was to maintain the diversity of the population. The mutation involved randomly selecting an individual from the population, selecting a certain gene in the individual to mutate, and producing a new outstanding individual. To solve the problem of optimizing the arrangement of the MR dampers, the constraint condition that the number of MR dampers remained unchanged also needed to be satisfied after the mutation. Therefore, when mutating, two genes needed to be randomly selected: gene 1 and gene 0. During mutation, gene 1 became 0, and gene 0 became 1 to ensure that the number of MR dampers remained unchanged during the mutation process.

The probability of mutation had a greater impact on the optimization process of the genetic algorithm. The selection of the mutation probability was affected by factors such as the population size and the chromosome length. If the mutation probability was too large, it would lead to the instability of the algorithm; if the mutation probability was too small, the ability of the newly generated individual would be poor and the algorithm would become premature. Normally, the probability of mutation was 0.001~0.1 [49, 50].

6. Engineering Case Analysis

6.1. Calculation Model and Parameter Selection. The entire calculation model was gridded into 214,087 units and 52,724 nodes (see Figure 12). The origin of the coordinates is set at the center of the generator floor. The x direction of the coordinate system was the longitudinal axis of the plant; the y direction was the upstream and downstream direction of the plant; and the z direction was the vertical direction. The material parameters of the plant structure are shown in Table 1. Among them, the concrete strength grade of the factory floor, beams, pillars, machine piers, windshield, and spiral casing was C30, and the concrete strength grade of the rest was C25.

Research has shown that under no-load conditions, the damping control effect of MR dampers is poor [51]. Therefore, in this research, this operating condition was selected in order to study the optimal layout of MR dampers. It was assumed that various vibration loads were simple harmonic loads. The position and the magnitude of each load are shown in Table 2.

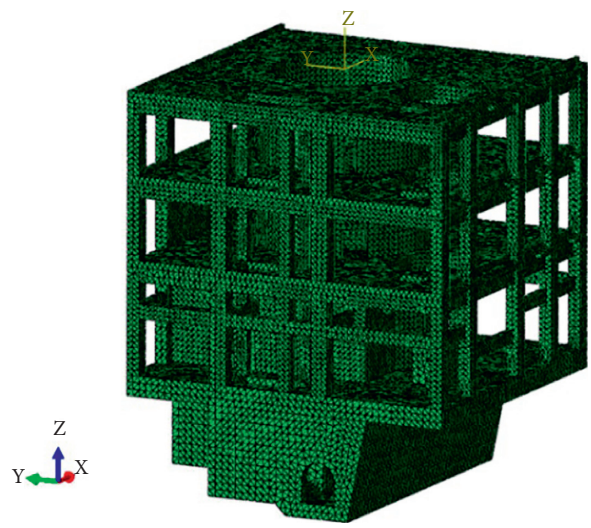

Figure 12: The mesh model of the powerhouse.

The time history of the external force couple is given by $F(t) = f(t) \times F_D$, where the time variation factor $f(t)$ is depicted in Figure 13 and F_D is the standard loading value of the unit.

In this research, the minimization of vertical speed and the acceleration were taken as the optimization objective function. Taking the no-load condition as an example, the multiobjective genetic algorithm was used to optimize the layout of the MR damper on the generator floor. The parameters used in the genetic algorithm are shown in Table 3. The population size was 20; the chromosome length was 22; the maximum number of iterations was 30; and the crossover and mutation probabilities were 0.8 and 0.05, respectively. The objective function was calculated according to formula (10), for which ωA and ωV were both selected as 0.5. When using the compiled program to calculate the optimal layout, taking the calculation efficiency into consideration, the passive-on control method was adopted to optimize the layout of the MR damper in the powerhouse.

In order to obtain a better vibration reduction effect, the MR damper should be installed in the large response area of the structure. At the same time, the principle of symmetry between the center of mass and the center of stiffness should be considered, as well as the requirements of the use of structural space. The MR damper was installed in the midspan position of the beam to control the first vibration mode, in combination with the structural characteristics of the generator floor, as shown in Figure 14. The MR damper parameters are shown in Table 4. In this research, 22 optional MR damper installation positions were selected (the positions are shown in Table 5). Twelve damper installation positions in the optional positions were selected to control the vibration of the powerhouse.

Table 1: The parameters of the powerhouse.

Material	Static elastic modulus (10^4MPa)	Severe ($kN \cdot m^{-3}$)	Poisson's ratio
Steel	20.60	78.0	0.300
C25 concrete	2.80	25.0	0.167
C30 concrete	3.00	25.0	0.167

Table 2: The standard loading value of the unit (units: kN).

Unit		Backfill gravel
Stator	Axially V1	1,379.0
	Tangential T1	0.0
	Radial R1	0.0
Lower bracket	Axially V2	24.5
	Tangential T2	18.9
	Radial R2	18.9
Upper bracket	Radial R3	48.8

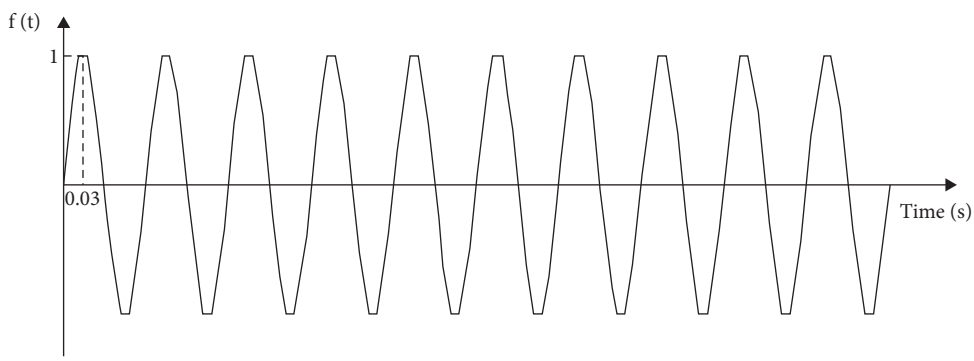

Figure 13: Time variation factor $f(t)$ of force couple.

Table 3: The parameters of the genetic algorithm.

Population size	Chromosome length	Crossover probability	Mutation probability	Maximum number of iterations
20	22	0.8	0.05	30

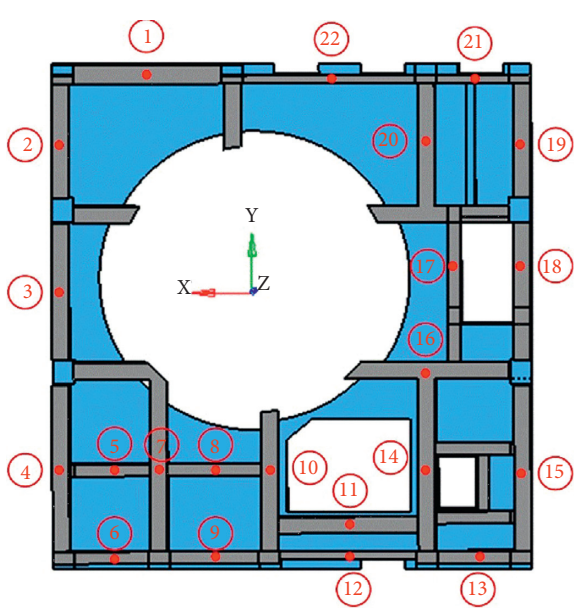

Figure 14: The installation location of the MR dampers.

Table 4: The parameters of the MR dampers.

Parameter	Value
A	53.17
α	862.30
β	36.37
γ	47.46
C_0	2.245
K_0	1.31
n	1.24
x_0	−20.75

6.2. Vibration Reduction Effect after Optimized Layout. Table 6 and Figure 13 illustrate the optimized layout results of the MR dampers on the generator floor. It can be seen from Figure 15 that when the genetic algorithm was iterated to about 16 generations, the optimized solution tended to converge. It can be seen from Table 6 that the target value converged to 1.547, and the subobjective function values of the velocity and the acceleration were 2.493 mm/s and 0.601 m/s^2, respectively. According to the optimized

Table 5: The coordinate of the installation locations of MR dampers.

Structure	Control point	Control point coordinates	Control point	Control point coordinates
Generator floor	1	(5.00, 9.85)	12	(−4.65, −13.10)
	2	(9.10, 6.90)	13	(−10.54, 13.10)
	3	(9.10, 0.00)	14	(−8.10, −9.10)
	4	(9.10, −9.10)	15	(−12.60, −9.10)
	5	(6.96, −9.10)	16	(−8.05, −4.40)
	6	(7.00, −13.10)	17	(−9.10, 0.01)
	7	(4.50, −9.10)	18	(−12.60, 0.01)
	8	(2.14, −9.10)	19	(−12.6, 6.90)
	9	(1.90, −13.10)	20	(−8.10, 6.90)
	10	(−0.01, −9.10)	21	(−10.54, 9.60)
	11	(−4.65, −11.85)	22	(−4.06, 9.60)

Table 6: The results of the optimal placement of the MR dampers.

Optimal position	Objective function value	Speed function objective function value (mm/s)	Acceleration function objective function value (m/s^2)
1, 2, 3, 4, 7, 14, 15, 16, 17, 20, 21, 22	1.547	2.493	0.601

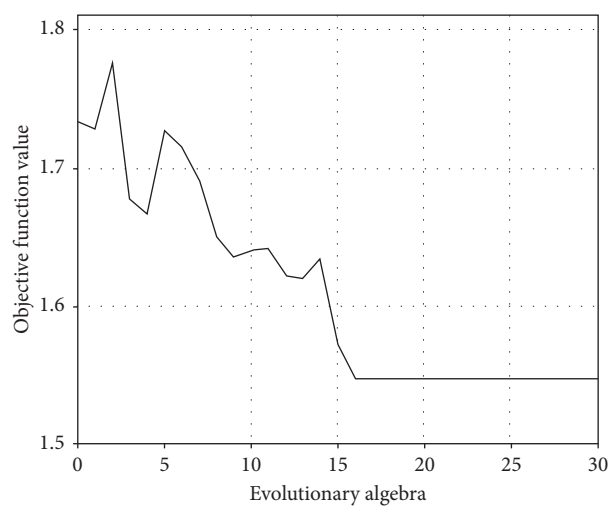

Figure 15: The evolution process of the objective function value.

installation position of the MR damper, the semiactive control methods of improved simple bang-bang were used to control the vibration of the powerhouse.

Table 7 shows the overall maximum response value of the generator floor after the optimized layout. For the vertical velocity, after optimizing the layout, the passive control passive-on and the semiactive control improved simple bang-bang responses were 2.836 mm/s and 2.686 mm/s, respectively, and the responses were reduced by 13.90% and 18.46%, respectively. For the vertical acceleration, the responses of the passive control passive-on and the semiactive control improved simple bang-bang were 0.605 m/s^2 and 0.549 m/s^2, respectively, and the responses were reduced by 11.16% and 19.38%, respectively. Before comparing the optimized layout, the optimized layout of the MR damper installation position was used for the vibration damping control, and the damping effect was improved. In particular, when the improved simple bang-bang control method was adopted, the overall maximum vertical velocity damping effect of the generator floor was increased by 5.56%, and the maximum vertical acceleration damping effect was increased by 8.66%.

In order to better demonstrate the damping effect after the optimized layout, Table 8 shows the response values of the characteristic points of the generator floor after the optimized layout. For the maximum vertical velocity response point after optimization, the vertical speed responses of the passive control passive-on and the semiactive control improved simple bang-bang were 2.493 mm/s and 2.086 mm/s, respectively, and the responses were reduced by 24.32% and 36.67%, respectively. For the maximum vertical acceleration response point, the vertical acceleration responses of the passive control passive-on and the semiactive control improved simple bang-bang responses were 0.601 m/

Table 7: The maximum response of the generator floor after the optimal layout.

Response		No control	Passive-on	Improved simple bang-bang
Vertical velocity (mm/s)	Before optimization	3.294	2.933 (10.96%)	2.869 (12.90%)
	Optimized	—	2.836 (13.90%)	2.686 (18.46%)
	Optimization effect	—	2.94%	5.56%
Vertical acceleration (m/s^2)	Before optimization	0.681	0.617 (9.40%)	0.608 (10.72%)
	Optimized	—	0.605 (11.16%)	0.549 (19.38%)
	Optimization effect	—	1.76%	8.66%

Table 8: The response of the generator floor characteristic points after the optimal layout.

Response		No control	Passive-on	Improved simple bang-bang
The maximum vertical velocity response point (vertical velocity; mm/s)	Before optimization	3.294	2.729 (17.15%)	2.257 (31.48%)
	Optimized	—	2.493 (24.32%)	2.086 (36.67%)
	Optimization effect	—	7.16%	5.19%
The maximum vertical acceleration response point (vertical acceleration; m/s^2)	Before optimization	0.681	0.617 (9.40%)	0.550 (19.24%)
	Optimized	—	0.601 (11.75%)	0.520 (23.64%)
	Optimization effect	—	2.35%	4.41%

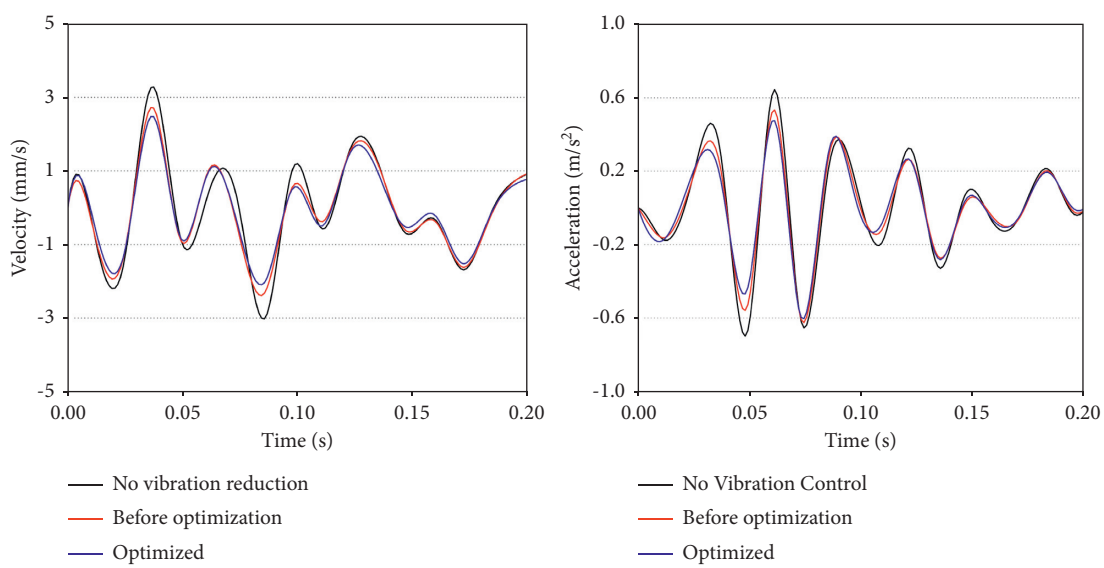

Figure 16: Time-history curve of characteristic points after the optimal layout for the passive-on control.

s^2 and 0.520 m/s^2, respectively, and the responses were reduced by 11.75% and 23.64%, respectively. When the improved simple bang-bang control method was adopted, the vertical velocity vibration reduction effect of the maximum vertical velocity response point of the generator floor was increased by 5.19%, and the vertical acceleration vibration reduction effect of the maximum vertical acceleration response point was increased by 4.41%. In addition, Figures 16 and 17 show the time history curves of the maximum response point of the two control methods. It can also be seen from the figures that the optimized arrangement effectively improved the vibration damping control effect of the MR damper.

In summary, for the no-load conditions, the overall responses of the vertical velocity and the acceleration of the generator floor were reduced by 18.46% and 19.38%, respectively, by optimizing the arrangement of MR dampers. Compared with the optimized layout, the vibration reduction effect was increased by 5.56% and 8.66%, respectively. The vertical velocity at the maximum vertical velocity

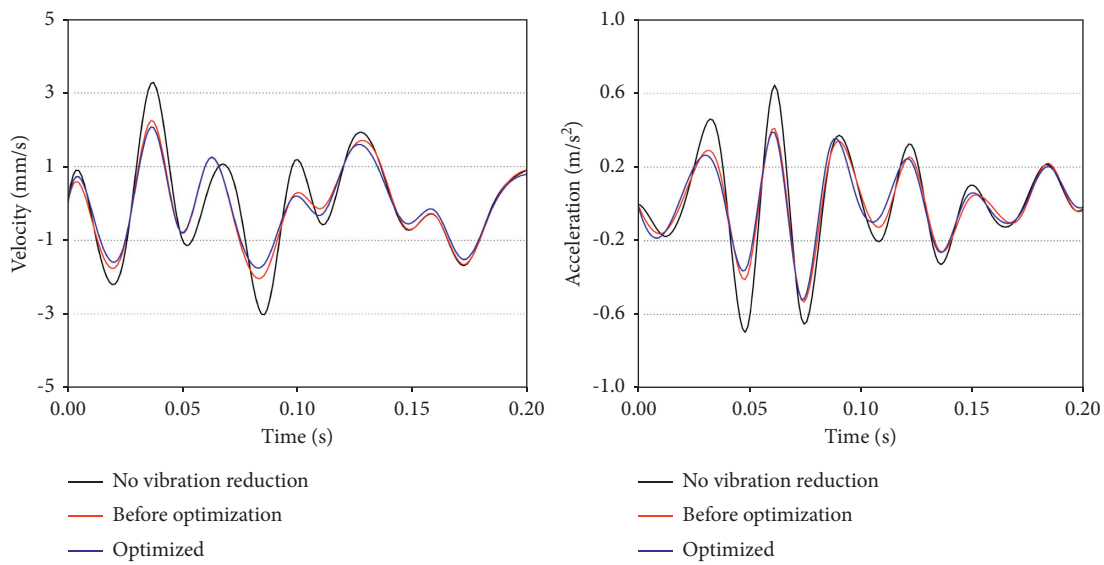

Figure 17: Time-history curve of characteristic points after the optimal layout for the improved bang-bang control.

response point was reduced by 36.67%, and the vertical acceleration at the maximum acceleration response point was reduced by 23.64%. Compared with the optimized layout, the vibration reduction effect was increased by 5.19% and 4.41%, respectively. Therefore, the optimized layout method of the MR dampers for plant buildings proposed in this research could effectively improve the vibration reduction effect of the MR dampers.

7. Conclusions

Based on the engineering background of an existing pumped-storage power plant, in this research, two aspects are mainly discussed and researched: the numerical simulation method of MR damper vibration reduction control and the optimal arrangement of an MR damper. The main conclusions were as follows:

(1) Based on the Bouc–Wen model, we proposed a calculation method for an MR damper that was suitable for large and complex structures. Through the secondary development of the Abaqus platform, the passive control (passive-off and passive-on) and semiactive control of the MRD were realized. The method was simple and easy to implement by simply controlling the current switch of the MR damper. Additionally, the size could achieve the passive control and semiactive control of the MR damper.

(2) In view of the large vertical velocity and acceleration response of the generator floor, we took minimizing the vertical velocity and acceleration as the optimization objective function, and we established a multiobjective optimization problem for the optimal placement of the MR dampers. Based on the multiobjective genetic algorithm, Abaqus was redeveloped through Python and Fortran, and the MR damper on the generator floor of the plant was optimized. The results showed that the optimized layout method of the plant MR damper proposed in this research was effective and feasible, and the damping effect of the damper could be effectively improved through the optimized layout.

Data Availability

The codes used in this paper are available from the author upon request.

Conflicts of Interest

The authors declare that there are no conflicts of interest regarding the publication of this paper.

Acknowledgments

This research was funded by the National Natural Science Foundation of China (51579089).

References

[1] J. Lian, H. Wang, and H. Wang, "Study on vibration transmission among units in underground powerhouse of a hydropower station," *Energies*, vol. 11, no. 11, p. 3015, 2018.

[2] J. Zhang, F. Yang, C. Liang, Y. Zhang, and Y. Li, "An SVDD-based post-processing approach for vibration risk assessment of the hydro-turbine-generator in a large hydropower station," *Journal of Low Frequency Noise, Vibration and Active Control*, vol. 40, no. 3, pp. 1309–1334, 2020.

[3] R. K. Mohanta, T. R. Chelliah, S. Allamsetty, A. Akula, and R. Ghosh, "Sources of vibration and their treatment in hydro power stations—a review," *Engineering Science and Technology, An International Journal*, vol. 20, no. 2, pp. 637–648, 2017.

[4] S. Dyke and B. Spencer, "A comparison of semi-active control strategies for the MR damper," in *Proceedings of the Intelligent Information Systems-IIS'97*, pp. 580–584, IEEE, Grand Bahama Island, Bahamas, December 1997.

[5] N. Mohajer Rahbari, B. Farahmand Azar, S. Talatahari, and H. Safari, "Semi-active direct control method for seismic alleviation of structures using MR dampers," *Structural Control and Health Monitoring*, vol. 20, no. 6, pp. 1021–1042, 2013.

[6] S. Zahrai and H. Salehi, "Semi-active seismic control of mid-rise structures using magneto-rheological dampers and two proposed improving mechanisms," *Iranian Journal of Science and Technology: Transactions of Civil Engineering*, vol. 38, no. C1, p. 21, 2014.

[7] S.-Y. Ok, D.-S. Kim, K.-S. Park, and H.-M. Koh, "Semi-active fuzzy control of cable-stayed bridges using magneto-rheological dampers," *Engineering Structures*, vol. 29, no. 5, pp. 776–788, 2007.

[8] V. Bhaiya, S. Bharti, M. Shrimali, and T. Datta, "Genetic algorithm based optimum semi-active control of building frames using limited number of magneto-rheological dampers and sensors," *Journal of Dynamic Systems, Measurement, and Control*, vol. 140, no. 10, 2018.

[9] M. Abdeddaim, A. Ounis, N. Djedoui, and M. K. Shrimali, "Pounding hazard mitigation between adjacent planar buildings using coupling strategy," *Journal of Civil Structural Health Monitoring*, vol. 6, no. 3, pp. 603–617, 2016.

[10] X. J. Qi, X. J. Li, and J. H. Xiao, "Algorithm comparison and analysis of bridge seismic semi-active control," *Journal of Vibration and Shock*, vol. 25, no. 6, pp. 71–75, 2006.

[11] J. T. P. Yao, "Concept of structural control," *Journal of the Structural Division*, vol. 98, no. 7, pp. 1567–1574, 1972.

[12] W. Zheng, H. Wang, J. Li, and H. Shen, "Parametric study of superelastic-sliding LRB system for seismic response control of continuous bridges," *Journal of Bridge Engineering*, vol. 25, no. 9, Article ID 04020062, 2020.

[13] B. Wang, S. Zhu, and F. Casciati, "Experimental study of novel-centering esismic base isolators incorporating superelastic shape memory alloys," *Journal of Structural Engineering*, vol. 146, no. 7, 2020.

[14] S. Gur, G. N. Frantziskonis, and S. K. Mishra, "Thermally modulated shape memory alloy friction pendulum (tmSMA-FP) for substantial near-fault earthquake structure protection," *Structural Control and Health Monitoring*, vol. 24, no. 11, 2017.

[15] Y. Peng, T. Huang, and J. Chen, "Experimental study of seismic isolated structures with sliding implant-magnetic bearings," *Journal of Earthquake Engineering*, pp. 1–32, 2020.

[16] Y. Peng, L. Ding, J. Chen, and R. Villaverde, "Experimental study of sliding hydromagnetic isolators for seismic protection," *Journal of Structural Engineering*, vol. 145, no. 5, Article ID 04019021, 2019.

[17] P. W. Nugroho, W. Li, H. Du, G. Alici, and J. Yang, "An adaptive neuro fuzzy hybrid control strategy for a semiactive suspension with magneto rheological damper," *Advances in Mechanical Engineering*, vol. 6, Article ID 487312, 2014.

[18] P. J. Gawthrop, S. A. Neild, and D. J. Wagg, "Semi-active damping using a hybrid control approach," *Journal of Intelligent Material Systems and Structures*, vol. 23, no. 18, pp. 2103–2116, 2012.

[19] M. Ahmadian and N. Vahdati, "Transient dynamics of semiactive suspensions with hybrid control," *Journal of Intelligent Material Systems and Structures*, vol. 17, no. 2, pp. 145–153, 2006.

[20] M. Bitaraf, O. E. Ozbulut, S. Hurlebaus, and L. Barroso, "Application of semi-active control strategies for seismic protection of buildings with MR dampers," *Engineering Structures*, vol. 32, no. 10, pp. 3040–3047, 2010.

[21] Z. G. Ying, W. Q. Zhu, and T. T. Soong, "A stochastic optimal semi-active control strategy for ER/MR dampers," *Journal of Sound and Vibration*, vol. 259, no. 1, pp. 45–62, 2003.

[22] R. Alkhatib and M. F. Golnaraghi, "Active structural vibration control: a review," *The Shock and Vibration Digest*, vol. 35, no. 5, pp. 367–383, 2003.

[23] A. Bathaei, S. M. Zahrai, and M. Ramezani, "Semi-active seismic control of an 11-DOF building model with TMD+MR damper using type-1 and -2 fuzzy algorithms," *Journal of Vibration and Control*, vol. 24, no. 13, pp. 2938–2953, 2018.

[24] H. J. Lee, G. Yang, H. J. Jung, B. F. Spencer, and I. W. Lee, "Semi-active neurocontrol of a base-isolated benchmark structure," *Structural Control and Health Monitoring: The Official Journal of the International Association for Structural Control and Monitoring and of the European Association for the Control of Structures*, vol. 13, no. 2-3, pp. 682–692, 2006.

[25] N. K. Hazaveh, J. G. Chase, G. W. Rodgers, and S. Pampanin, "Smart semi-active MR damper to control the structural response," *Bulletin of the New Zealand Society for Earthquake Engineering*, vol. 48, no. 4, pp. 235–244, 2015.

[26] D.-H. Kim and I.-W. Lee, "Neuro-control of seismically excited steel structure through sensitivity evaluation scheme," *Earthquake Engineering & Structural Dynamics*, vol. 30, no. 9, pp. 1361–1377, 2001.

[27] J. Chen, J. Jiang, K. Wang, and F. Zhang, "Optimal placement of actuators for active vibration control using EER and genetic algorithm," in *Proceedings of the 2019 IEEE 10th International Conference on Mechanical and Aerospace Engineering (ICMAE)*, pp. 449–453, IEEE, Brussels, Belgium, July 2019.

[28] M. P. Singh and L. M. Moreschi, "Optimal placement of dampers for passive response control," *Earthquake Engineering & Structural Dynamics*, vol. 31, no. 4, pp. 955–976, 2002.

[29] F. Amini and P. Ghaderi, "Optimal locations for MR dampers in civil structures using improved ant colony algorithm," *Optimal Control Applications and Methods*, vol. 33, no. 2, pp. 232–248, 2012.

[30] G. Agranovich and Y. Ribakov, "A method for efficient placement of active dampers in seismically excited structures," *Structural Control and Health Monitoring*, vol. 17, no. 5, pp. 513–531, 2010.

[31] J. A. Main and S. Krenk, "Efficiency and tuning of viscous dampers on discrete systems," *Journal of Sound and Vibration*, vol. 286, no. 1-2, pp. 97–122, 2005.

[32] R. Lewandowski, "Optimization of the location and damping constants of viscous dampers," in *Proceedings of the Ninth International Conference on Computational Structures Technology*, Athens, Greece, September 2008.

[33] M. P. Singh and L. M. Moreschi, "Optimal seismic response control with dampers," *Earthquake Engineering & Structural Dynamics*, vol. 30, no. 4, pp. 553–572, 2001.

[34] J. Zhang and K. Zhang, "Improved multi-objective sensor optimization method for structural damage identification based on genetic algorithm," *IOP Conference Series: Materials Science and Engineering*, vol. 780, no. 3, Article ID 032022, 2020.

[35] Y.-K. Wen, "Method for random vibration of hysteretic systems," *Journal of the Engineering Mechanics Division*, vol. 102, no. 2, pp. 249–263, 1976.

[36] Y. G. Li, M. Chen, H. Y. Long, and L. Y. Ju, "Identifying the parameters of bouc-wen model for MR damper based on matlab," *Machine Tool & Hydraulics*, vol. 46, no. 5, pp. 97–101, 2019.

[37] N. R. Fisco and H. Adeli, "Smart structures: Part I—active and semi-active control," *Scientia Iranica*, vol. 18, no. 3, pp. 275–284, 2011.

[38] E. Lee, J. Park, K. A. Loparo, C. B. Schrader, and P. H. Chang, "Bang-bang impact control using hybrid impedance/time-delay control," *IEEE/ASME transactions on mechatronics*, vol. 8, no. 2, pp. 272–277, 2003.

[39] K. B. Saad, A. Mbarek, and M. Benrejeb, "Determination of the switching times of the bang-bang control for a linear stepping motor by Lyapunov functions," *Studies in Informatics and Control*, vol. 17, no. 4, p. 393, 2008.

[40] U. Ledzewicz and H. Schättler, "Optimal bang-bang controls for a two-compartment model in cancer chemotherapy," *Journal of Optimization Theory and Applications*, vol. 114, no. 3, pp. 609–637, 2002.

[41] P. Azimzadeh and P. A. Forsyth, "The existence of optimal bang-bang controls for GMxB contracts," *SIAM Journal on Financial Mathematics*, vol. 6, no. 1, pp. 117–139, 2015.

[42] P. Dong and J. Fan, "Semiactive wind response control of 76-story benchmark building with smart piezoelectric friction dampers," in *Advanced Materials Research*, vol. 250–253, pp. 2196–2201, Trans Tech Publications, Freienbach, Switzerland, 2011.

[43] S.-S. Chen and J.-H. Li, "Analyses of semi-active control of earthquake response to building structure by magneto-rheological damper," *Journal of Railway Engineering Society*, vol. 9, 2007.

[44] W. Wang, X. Hua, X. Wang, J. Wu, H. Sun, and G. Song, "Mechanical behavior of magnetorheological dampers after long-term operation in a cable vibration control system," *Structural Control and Health Monitoring*, vol. 26, no. 1, Article ID e2280, 2019.

[45] J. Gené-Badia, G. Escaramis-Babiano, M. Sans-Corrales et al., "Impact of economic incentives on quality of professional life and on end-user satisfaction in primary care," *Health Policy*, vol. 80, no. 1, pp. 2–10, 2007.

[46] H. Natke and T. Soong, "Topological structural optimization under dynamic loads," *WIT Transactions on The Built Environment*, vol. 2, 1970.

[47] Z. Dong, Z. Feng, Y. Chen, K. Yu, and G. Zhang, "Design and multiobjective optimization of magnetorheological damper considering the consistency of magnetic flux density," *Shock and Vibration*, vol. 2020, Article ID 7050356, 12 pages, 2020.

[48] W. Zhu and X.-T. Rui, "Semiactive vibration control using a magnetorheological damper and a magnetorheological elastomer based on the Bouc-Wen model," *Shock and Vibration*, vol. 2014, Article ID 405421, 10 pages, 2014.

[49] X. Zhang, Z. Li, K. Guo, F. Zheng, and Z. Wang, "A novel pumping magnetorheological damper: design, optimization, and evaluation," *Journal of Intelligent Material Systems and Structures*, vol. 28, no. 17, pp. 2339–2348, 2017.

[50] S. Kanarachos, D. Savitski, N. Lagaros, and M. E. Fitzpatrick, "Automotive magnetorheological dampers: modelling and parameter identification using contrast-based fruit fly optimisation," *Soft Computing*, vol. 22, no. 24, pp. 8131–8149, 2018.

[51] C. Su and Y. Yang, "Study on intelligent vibration control of hydropower powerhouse based on magnetorheological damper," *Water Power*, vol. 8, pp. 36–41, 2019.

Hindawi
Mathematical Problems in Engineering
Volume 2021, Article ID 6651215, 23 pages
https://doi.org/10.1155/2021/6651215

Research Article

Influence of Restrainer Piers on the Seismic Performance of Long Bridges with Equal-Height Piers

Yuhu Luo, Yongguang Li, Xu Wang, and Guangping Lu

State Key Laboratory of Mountain Bridge and Tunnel Engineering, Chongqing Jiaotong University, Chongqing 400074, China

Correspondence should be addressed to Xu Wang; xuwang@cqjtu.edu.cn

Received 20 October 2020; Revised 11 April 2021; Accepted 13 May 2021; Published 30 May 2021

Academic Editor: Hao Wang

Pounding may occur between the main girders under the action of strong earthquakes, so as between main girders and abutments. This causes excessive longitudinal displacement of the main girder and unseating damage to bridges. Because long bridges in mountainous areas with high intensity are easy to unseat, the authors studied the influence of restrainer piers, expansion joint spacings (EJSs), and the span on the seismic performance of long bridges. The ABAQUS finite element software was used to simulate a bridge dynamic analysis model considering the elastoplasticity of the pounding effect of the pier and the beam. By inputting El-Centro, Northbridge, and Taft seismic waves, the time-history analysis of the seismic response of long bridges was carried out. The results indicated that a reasonable number of restrainer piers, an appropriate EJS, and a span could effectively reduce the maximum relative displacement of pier-beams. This behavior will improve the seismic performance of bridge structures. Moreover, for a 24-span equal-height beam bridge, the optimum seismic effect was obtained when 3 restrainer piers, an EJS of 70 mm, and a 50 m span were used.

1. Introduction

From a global perspective, China is in a seismically active zone and faces serious earthquake threats [1,2]. For example, in the 2008 Wenchuan earthquake, about 1,400 bridges were in a high-intensity area. Among them, the Baihua Bridge underwent unseating damage due to excessive displacement of the superstructure. Furthermore, many bridges were damaged by the earthquake in Lushan County, Ya'an City, located in Sichuan Province, in 2013. The probability of unseating damage for short- to medium-span bridges in earthquakes is very high [2]. Consequently, transportation systems and modern communication infrastructures may be severely impaired. Hence, an analysis of seismic isolation and pounding during earthquakes is of paramount significance [3–5].

Pounding between bridge decks with insufficient separation distances may result in significant structural damage or even beam unseating, which has been identified as one of the primary causes of bridge damage in many major earthquakes. Li et al. experimentally investigated the influence of spatial variation of ground motions on the pounding behavior of three adjacent bridge segments using three shake tables. The results indicated that the spatially nonuniform ground motions increased the pounding forces [6]. Because a simplified model failed to evaluate the pounding responses, a longitudinal pounding analysis of an isolated continuous beam bridge was carried out under unidirectional ground motions, based on a multiscale simulation scheme [7]. Wei et al. and He and Zhao investigated the seismic performance of bridges based on seismic blocks and pins [8, 9] and found that the pounding between linear bridge structures should be between rigid body pounding and straight bar coaxial pounding. Moreover, the reasonable pounding contact stiffness should be 0.5 times that of the axial stiffness of the shorter main beam [10]. Zhu et al. [11] proposed a 3D contact-friction model to simulate an arbitrary pounding between bridges, combining the advantages of the recovery coefficient method [12–14] and the contact element method [15–17]. The experimental

observations demonstrated that this pounding model can be used to simulate poundings in multiple directions. Li et al. [18] introduced an equivalent Kelvin pounding model, in which the authors presented a parameter determination method for pounding analysis of straight-line bridges. Their research suggested that the range of pounding stiffness for the seismic pounding response analysis of urban bridges was 3E+5 kN/m-6E+5 kN/m. By setting up restrainer piers in a key part of the bridge, the rigidity and strength of the key piers were enhanced, and the overall seismic performance of the bridge was increased accordingly. This was because the excessive displacement of the piers during the earthquake due to insufficient rigidity and strength was avoided [19, 20]. Taking a 32 m simply supported girder bridge as a research object, it was found that the pounding between the shear keys and the bearings restrained the transverse relative displacement between the superstructure and the substructure [21]. The most efficient way to avoid pounding between adjacent structures is to provide sufficient separation distances. However, for bridge structures with conventional expansion joints, complete avoidance of pounding during strong earthquakes is often impossible. Bi et al. proposed a new modular expansion joint (MEJ) and investigated the minimum total gap of a MEJ to avoid pounding at the abutments and between bridge decks [22, 23]. Pounding may be the primary cause of beam unseating. In this study, a 3D contact-friction model was used to simulate bridge pounding.

To dissipate earthquake energy and to decrease damage to the bridge structure, seismic isolation methods have been applied. Seismic isolation is a design strategy to isolate a structure from the ground and thereby protect it from the damaging effects of earthquake motions [24,25]. Moreover, the performance of bridges isolated with shape memory alloy- (SMA-) based FPS bearings at low temperatures was scrutinized. The results showed that the seismic performance could be improved without significantly increasing the base forces at low temperatures [26]. The bridge model supported by four spherically shaped sliding bearings (known as the friction pendulum system or FPS bearings) was tested on a shake table with seismic motions. The experimental results demonstrated a substantial improvement in the ability of the isolated bridge to sustain all levels of seismic excitation under elastic conditions [27]. Seismic performances of bridges installed with a conventional lead rubber bearing (LRB) system and sliding-LRBs were investigated under near-fault excitations [28,29]. By combining SMA wires with sliding-LRBs, thus forming a superelastic-sliding-LRB isolation system, different studies have indicated that the displacement responses can be effectively mitigated [30]. The mechanical parameters of the LRB and viscous damper have been analyzed and optimized and are known to have a positive impact on seismic isolation [31–33]. Xia and Chen [34] proposed a simulation method of restrainer devices and improved the analysis model of high-pier seismic isolation. Several innovative types of piers have been proposed to improve seismic performance, such as rectangular-hollow double-column tall piers with energy dissipation beams, new base rocking isolation bridge piers, and double-deck bridge bents based on a rocking self-centering system [35–37]. Guo et al. [38] presented a new type of multilevel spring restrainer (MLSR) to diminish the seismic responses of a curved bridge and show that the MLSR has high effectiveness in mitigating pier damage to the bridge. Furthermore, other researchers proposed several new isolation systems such as an SMA-based isolation system [39] and a wedge-shaped block [40].

The aim of this research was to study the influence of restrainer piers, EJSs, and the span on the seismic performance of long bridges. A 3D contact-friction model was utilized to simulate bridge pounding using the ABAQUS finite element software. The El-Centro, Northbridge, and Taft seismic waves were selected for the analysis of the dynamic response of long bridges. To reduce the negative effect of pounding and to decrease the relative displacement of pier-beams, different EJSs (30, 50, 70, and 90 mm) and different spans (20, 30, 40, and 50 m) were investigated. The results indicated that the relative displacement of pier-beams could be reduced by increasing the structural stiffness, and the pounding between the pier and beam could likely be avoided. Here, restrainer piers were designed and simulated to increase the structural stiffness and to lessen the relative displacement of the pier-beam under seismic action. Finally, it was concluded that the relative displacement of pier-beams could be significantly decreased when there were three restrainer piers, which could be a falling-off prevention measure.

2. Analytical Model and Algorithm

2.1. Analytical Model. When analyzing the influence of the number of restrainer piers and EJSs on the dynamic response, the span of the bridge was set to 30 m. The bridge consisted of six units, and each unit had four spans. The cross section of the main girder was T-shaped. Figure 1 shows the size parameters of the main girder.

The height of the cap girder was 1.6 m, and its width was 2 m. The length of the transverse cap and main girder was 12.5 m. The bridge adopted a double cylindrical pier, and its height was 10 m. The cross radius of the pier was 0.8 m, and the transverse distance was 7 m. The tie beam size was 1.0 m × 1.3 m. The restrainer pier size was 5.0 m × 4.0 m. The overlapping length of the main girder and restrainer was 1.535 and 1.035 m, respectively. The direction of the falling beam was in the direction of the main girder, deviating from the bearing centerline. The positive direction of the falling beam is shown in Figure 2(a). The bridge was modeled by beam elements except for the cap beam and upper area, which were modeled using solid elements. The local drawing of the restrainer pier is presented in Figure 2(b), and its layout is presented in Table 1.

2.2. 3D Contact-Friction Model. To study the arbitrary contact and pounding between the main girders, Zhu et al. [11] proposed a 3D contact-friction model. The pounding surface contact can be divided into normal and tangential contact methods. The model is based on the point-surface

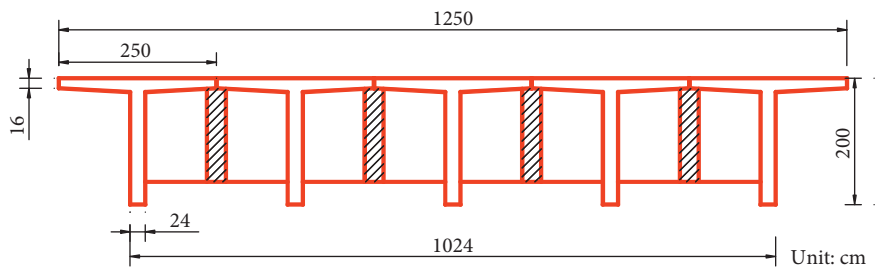

Figure 1: Section size of the main girder.

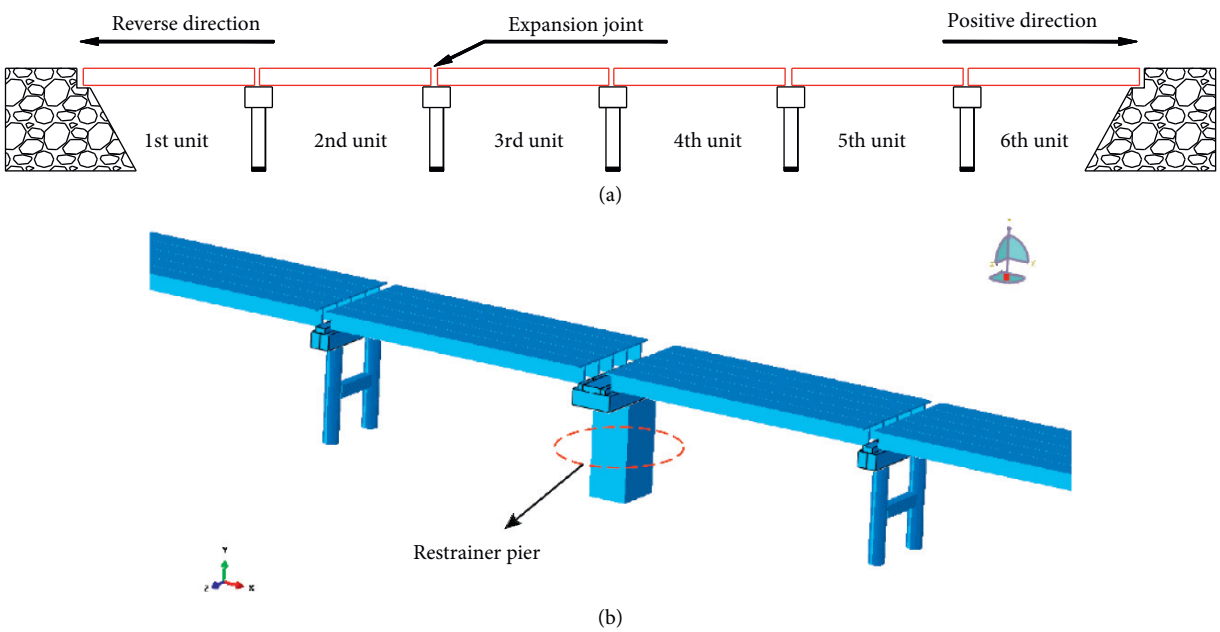

Figure 2: (a) Direction of the falling beam and (b) local drawing of the restrainer pier.

Table 1: The layout of the restrainer pier.

Number of restrainer piers	Pier number
0	–
1	No. 12
2	Nos. 8 and 16
3	Nos. 4, 12, and 20

contact theory, and the boundary interference fit was considered (Figure 3).

The contact surface on the end of the beam on the pounding side is defined as surface *a-b-c-d*, and the contact point is defined as point p. During the pounding, point p contacts surface *a-b-c-d* and invades point k. The relative displacement between point k and p is Δ_k, and their relative velocity is V_P. They are related using

$$\begin{aligned} \Delta_k &= X_P - X_k, \\ V_{kp} &= V_P - V_k, \end{aligned} \tag{1}$$

where X_p and X_k are the displacement of point p and k, respectively, and V_p and V_k are the velocity of point p and k, respectively.

The contact force between point p and k is expressed by the contact stiffnessK_{cnt}, and the force is calculated using

$$F_k = K_{cnt} \cdot \Delta_k, \tag{2}$$

where the contact force F_k can be decomposed into a normal component F_{kn} and a tangential component F_{kt}. The contact states are divided into a sliding and nonsliding state (Figure 3(b)), which are judged using

$$\begin{aligned} \text{adhesive contact } F_{kt} &< \mu_s |F_{kn}|, \\ \text{sliding contact } F_{kt} &\geq \mu_s |F_{kn}|, \end{aligned} \tag{3}$$

where μ_s is the coefficient of static friction.

The energy loss between the contact point p and the intrusion point k is simulated by the normal damping and tangential damping of the contact surface. The damping coefficients are C_n and C_t, and the damping forces are F_{cn} and F_{ct}, respectively. Their relationship is expressed through

$$\begin{aligned} F_{cn} &= -C_n V_{kpn}, \\ F_{ct} &= -C_t V_{kpt}. \end{aligned} \tag{4}$$

The pounding force can be expressed using

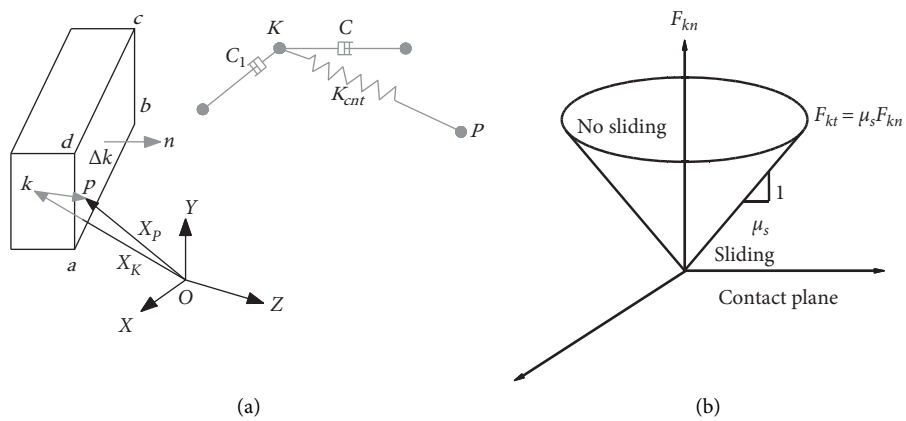

Figure 3: (a) 3D contact-friction model and (b) sliding limit.

$$\begin{aligned} \text{adhesive contact } R_k &= F_k + F_{cn} + F_{ct}, \\ \text{sliding contact } R_k &= F_{kn} + F_{cn} + F_{ft}, \end{aligned} \tag{5}$$

where F_{ft} is the dynamic friction force, which is defined by $F_{ft} = -\mu_k F_{kn}$.

2.3. Explicit Contact Algorithm. The contact algorithm or contact pair algorithm can be employed in contact simulation in ABAQUS/Explicit. To define a contact simulation, we usually need to specify only the contact algorithm and the contact surface. There are some general contact algorithms, including the contact pair algorithm, slip formula, penalty function contact formula, and dynamic contact formula. Pounding between the abutments and the girder or adjacent girder was considered through the surface-to-surface contact in ABAQUS. The problem of seismic pounding in which the pounding point cannot be determined in advance can be solved by an explicit contact algorithm. The interaction between two contact surfaces includes two components of normal contact force and tangential contact force. In this research, the hard contact behavior was set for normal contact behavior [7].

The iterative process is displayed in Figure 4.

2.4. Selection of Seismic Waves. The ground motion was regarded as a random process, and the uncertainty of the ground motion input in the seismic time-history analysis inevitably results in uncertainty regarding the structural response. Analysis of historical ground motion is one of the most effective methods to understand the real response of structures in an earthquake. In analyses of seismic performance, two types of ground motion inputs are generally adopted (i.e., seismic acceleration response spectrum and seismic time history). In the seismic design of bridges, there are three methods to select the seismic time history, namely, using the acceleration time-history record, adopting the artificial acceleration time history, and selecting the standard acceleration time history. The seismic waves are usually simulated as random processes with prescribed spectral patterns [41–43]. The selection of seismic waves generally follows the principle of selecting representative strong earthquake records. Tianjin, El-Centro, Northridge, and Taft waves are commonly utilized to analyze the seismic performance of bridges. According to the above analysis, the representative El-Centro, Northbridge, and Taft waves were chosen based on the site characteristics of bridges in the high-intensity areas in central-western China. The peak ground acceleration (PGA) of selected seismic waves was adjusted to 0.4, 0.7, and 1.0 g.

3. Influence of the Number of Restrainer Piers on the Dynamic Response

3.1. Influence of the Number of Restrainer Piers on the Dynamic Response under the El-Centro Seismic Wave

3.1.1. Dynamic Response under the El-Centro Seismic Wave. The maximum relative displacement of the pier-beam and its percentage reduction are plotted in Figure 5. Under the three different PGAs, the maximum relative displacement of the pier-beam decreased as the number of restrainer piers increased. Meanwhile, the percentage reduction in relative displacement increased with an increase in the number of restrainer piers. When the PGA was 0.4 g and there were three restrainer piers, the maximum reduction in the relative displacement occurred, which was 61.67% (Figure 5(b)). This was mainly because the restrainer pier increased the structural stiffness. Also, the higher the number of restrainer piers, the greater the structural stiffness and the smaller the maximum relative displacement of the pier-beam. These findings show that setting up a restrainer pier could reduce the relative displacement between the pier and beam. Hence, it could be a falling-off prevention measure.

Figure 6 depicts the internal force of the ordinary and the restrainer piers. Figures 6(a) to 6(c) illustrate the internal force of the ordinary pier, and the other figure panels illustrate the internal force of the restrainer pier, where M_O, F_{SO}, and F_{NO} represent the maximum pier bottom moment, maximum pier bottom shear, and maximum pier bottom axial force of the ordinary pier, respectively. M_R, F_{SR}, and F_{NR} represent the maximum pier bottom moment,

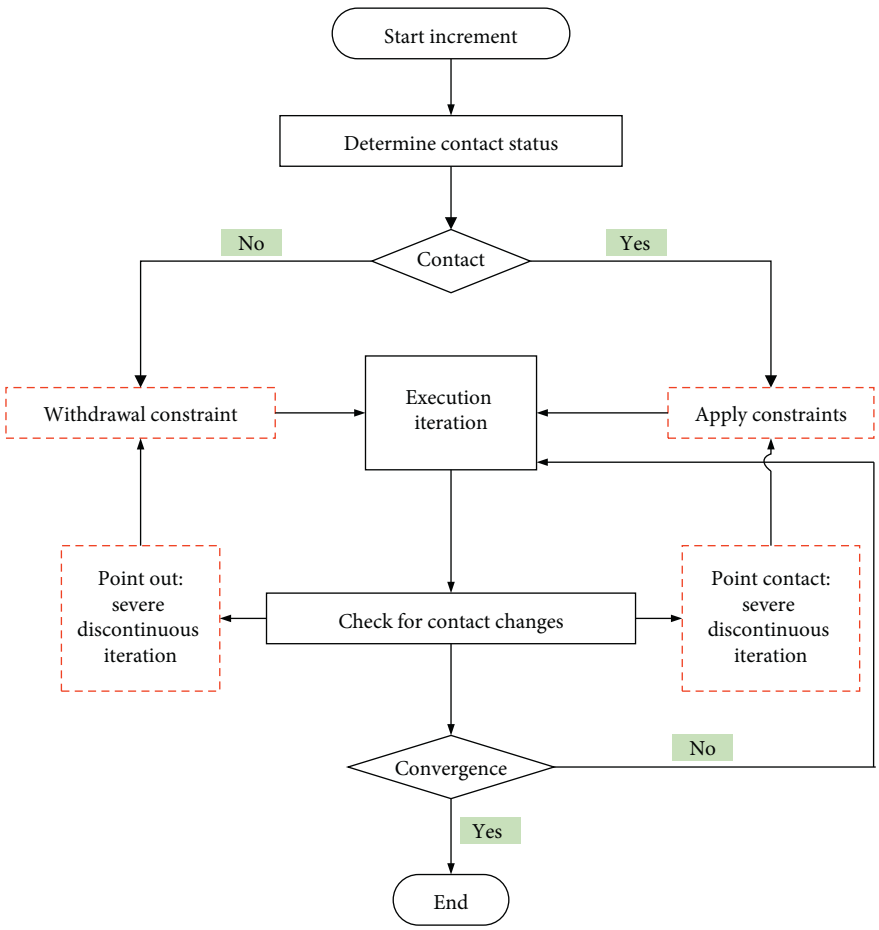

Figure 4: Iterative process.

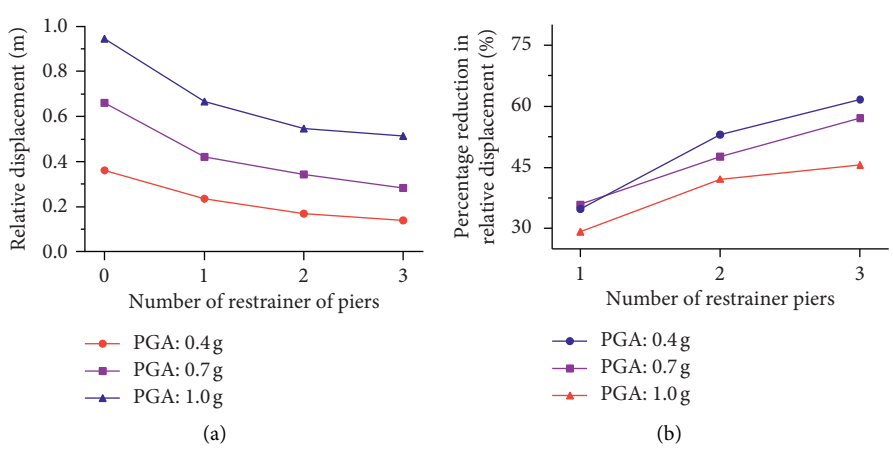

Figure 5: (a) Maximum relative displacement of the pier-beam and (b) percentage reduction in the relative displacement.

maximum pier bottom shear, and maximum pier bottom axial force of the restrainer pier, respectively.

When the PGA was 0.4 g and there were three restrainer piers, the maximum pier bottom moment of the restrainer pier was greater than that of the corresponding ordinary pier (Figures 6(a) and 6(d)). When the PGA was 0.7 or 1.0 g and only one restrainer pier was set up, the maximum pier bottom moment of the ordinary pier was at its minimum. Moreover, under a PGA of 0.7 or 1.0 g, the maximum pier bottom moment of the restrainer pier gradually increased as the number of restrainer piers increased. The maximum pier bottom shear of the restrainer pier was larger than that of the corresponding ordinary pier (Figures 6(b) and 6(e)). When the PGA was 0.4 g, the shear of the ordinary pier gradually

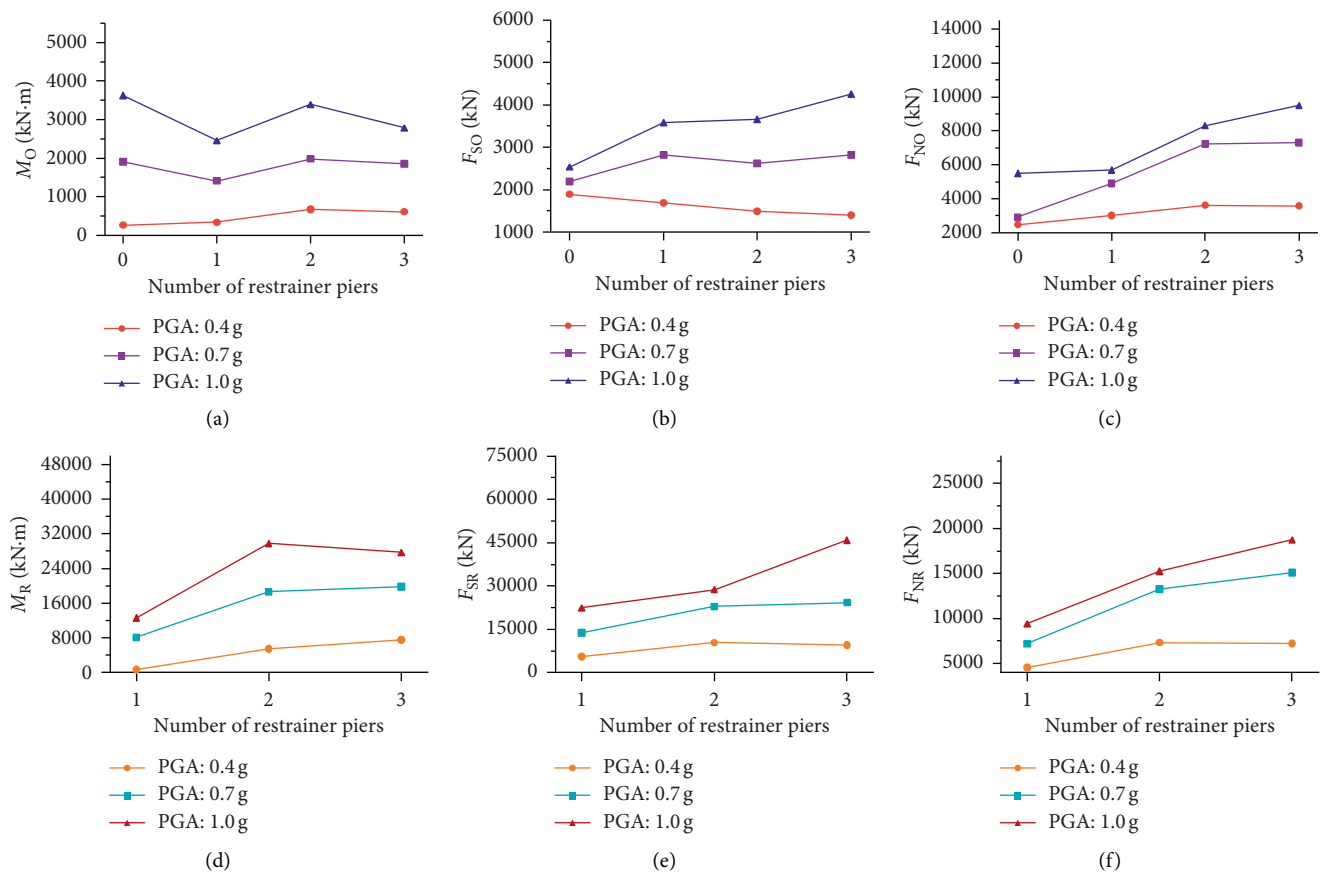

Figure 6: Internal force of the ordinary and restrainer piers.

decreased with an increase in the number of restrainer piers, while the shear tended to increase when the PGA was 0.7 and 1.0 g. Moreover, the shear of the restrainer pier gradually increased with an increase in the number of restrainer piers. The axial force at the bottom of the restrainer pier was larger than the corresponding ordinary pier, especially when the PGA was 1.0 g (Figures 6(c) and 6(f)). The axial force of the ordinary and restrainer piers gradually increased as the number of restrainer piers increased. Finally, when the number of restrainer piers was three, the axial force of both the ordinary and restrainer piers reached their maximum value.

3.1.2. Displacement Response When the El-Centro Seismic Wave PGA Was 0.4 g. As the number of restrainer piers increased, the maximum relative displacement of the pier-beam gradually decreased (Figure 7), and the maximum relative displacement occurred at the abutment. When there were three restrainer piers, displacement was at its minimum; thus, the effect of reducing the relative displacement was the most effective.

3.1.3. Displacement Response When the El-Centro Seismic Wave PGA Was 0.7 g. On the left and right sides of the restrainer pier, because of the pounding between the beam and retaining wall, the maximum relative displacement of the pier-beam on the left and right sides near the restrainer pier increased. As the number of restrainer piers increased, the relative displacement at the abutment gradually decreased. It could be observed that the relative displacement of the pier-beam gradually decreased as the number of restrainers piers increased (Figures 8(a) and 8(b)). Finally, when three restrainer piers were set up, the relative displacement of the pier-beam was at its minimum.

3.1.4. Displacement Response When the El-Centro Seismic Wave PGA Was 1.0 g. Figure 9 reveals the displacement response when the PGA was 1.0 g. As the number of restrainer piers increased, the relative displacement of the pier-beam gradually decreased. When there were no restrainer piers, the maximum relative displacement occurred at the abutment; however, when restrainer piers were set up, the maximum relative displacement occurred close to the restrainer pier. The relative displacement was obviously reduced after setting up a restrainer pier (Figure 9(b)), and the restrainer pier at the Nos. 12 and 20 piers had almost the same role in limiting the relative displacement of the pier-beam when two or three restrainer piers were set up. Finally, after setting up three restrainer piers, the relative displacement of the pier-beam was at its minimum.

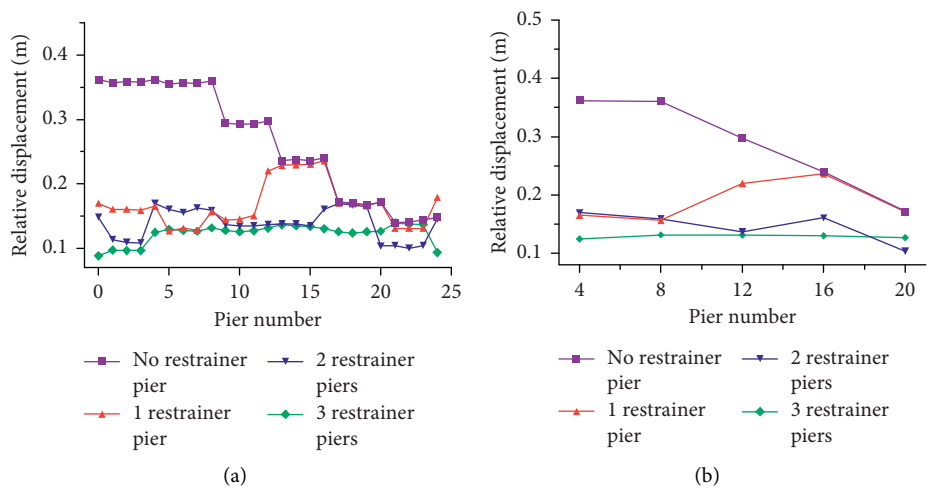

Figure 7: (a) Relative displacement of each pier and (b) trend of relative displacement of the pier-beam.

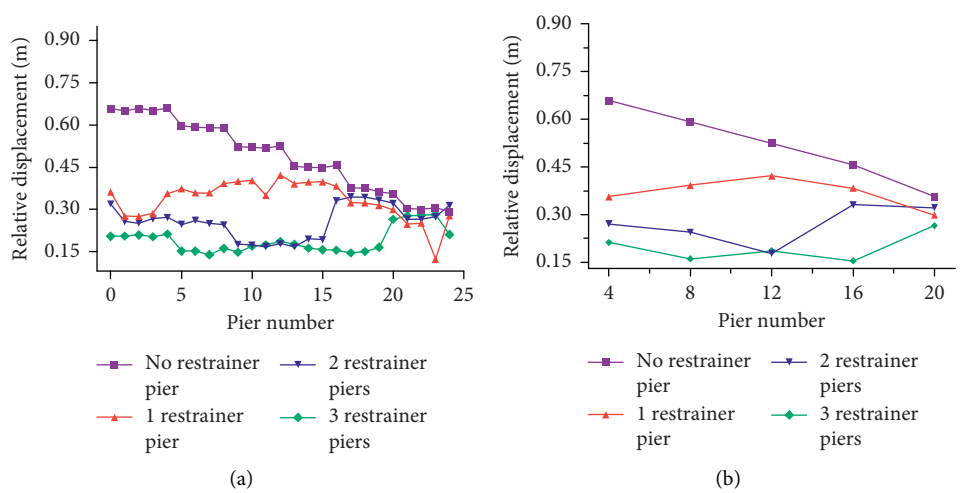

Figure 8: (a) Relative displacement of each pier and (b) trend of relative displacement of the pier-beam.

3.2. Influence of the Number of Restrainer Piers on the Dynamic Response under the Taft Seismic Wave

3.2.1. Dynamic Response under the Taft Seismic Wave. The maximum relative displacement of the pier-beam and its percentage reduction are plotted in Figure 10. It can be observed that the maximum relative displacement of the pier-beam increased with an increase in PGA when the number of restrainer piers was the same. Specifically, the maximum displacement occurred when the PGA was 1.0 g. Furthermore, the maximum relative displacement of the pier-beam decreased with an increase in the number of restrainer piers (Figure 10(a)). Figure 10(b) demonstrates that the more the number of restrainer piers, the greater the percentage reduction. When there were three restrainer piers and the PGA was 0.4 g, the relative displacement of the pier-beam decreased significantly, and the maximum was 62.47%. The analysis above indicates that setting up a restrainer pier could reduce the relative displacement of the pier-beam under the Taft seismic wave. Hence, it could be a falling-off prevention measure.

Figure 11 depicts the internal force of the ordinary and the restrainer piers. Figures 11(a) to 11(c) illustrate the internal force of the ordinary pier, and the other figure panels illustrate the internal force of the restrainer pier. When the number of restrainer piers and PGA were the same, the maximum pier bottom moment of the restrainer pier was greater than that of the corresponding ordinary pier; moreover, the maximum pier bottom moment increased with an increase in PGA. The maximum pier bottom moment of the ordinary pier substantially increased when the number of restrainer pier increased from zero to one under a PGA of 0.7 and 1.0 g, and when the number of restrainer pier was more than one, the maximum pier bottom moment varied little. Besides, when the PGA was 0.4 g, the maximum pier bottom moment of the ordinary and the restrainer piers did not change much. Under a PGA of 0.7 and 1.0 g, the maximum pier bottom moment of the restrainer pier increased with an increase in the number of restrainer piers. It may attribute that the increase in the number of restrainer piers aggravated the pounding between the

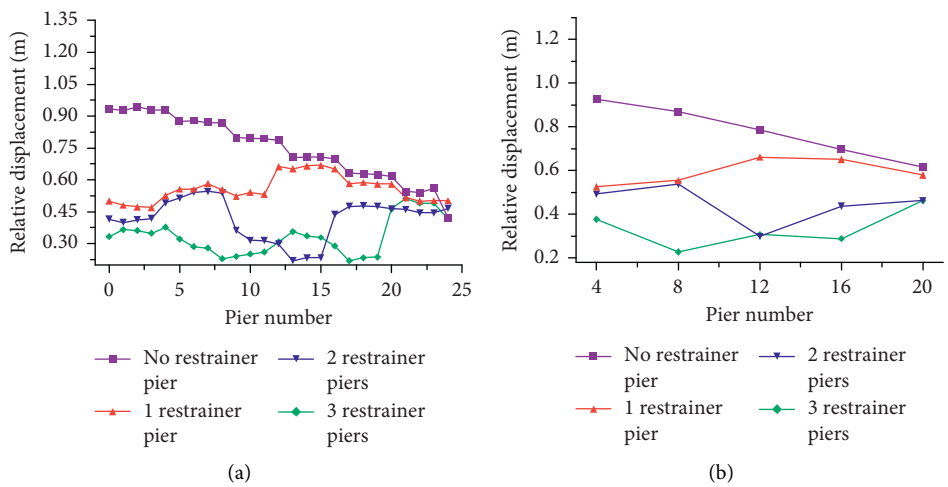

Figure 9: (a) Relative displacement of each pier and (b) trend of relative displacement of the pier-beam.

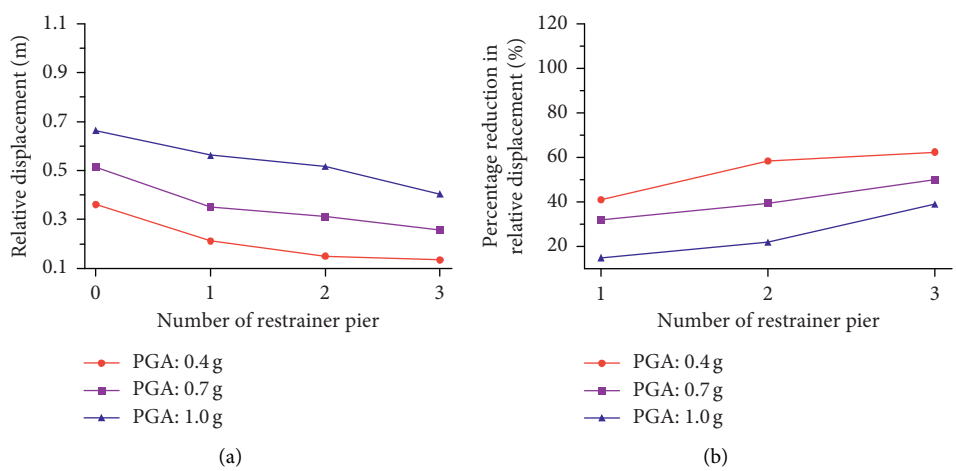

Figure 10: (a) Maximum relative displacement of the pier-beam and (b) percentage reduction in relative displacement.

main girders and between the main girder and the restrainer pier, which eventually led to the increase of the maximum pier bottom moment of the restrainer pier (Figures 11(a) and 11(d)). When the number of restrainer piers was the same, the maximum pier bottom shear increased with an increase in PGA. When the PGA was 0.7 or 1.0 g, the maximum pier bottom shear of the ordinary and the restrainer piers increased with an increasing number of restrainer piers. Moreover, when the PGA was 0.4 g, the maximum pier bottom shear of the ordinary and restrainer piers changed little, and the maximum pier bottom shear of the ordinary pier got the minimum when the number of restrainer pier was three (Figures 11(b) and 11(e)). The axial force at the bottom of the restrainer pier was larger than that of the corresponding ordinary pier. The maximum axial force at the bottom of the pier increased with the PGA when the number of restrainer piers was the same. When the number of the restrainer pier was more than two, the maximum axial force at the bottom of the ordinary pier did not change much (Figure 11(c)). The maximum axial force at the bottom of the restrainer pier increased significantly with an increase in the number of restrainer piers, especially the PGA was 1.0 g (Figure 11(f)).

3.2.2. Displacement Response When the Taft Seismic Wave PGA Was 0.4 g. Figure 12 depicts the displacement response when the Taft seismic wave PGA was 0.4 g. As the number of restrainer piers increased, the maximum relative displacement of the pier-beam gradually decreased, and the maximum relative displacement occurred at the abutment. When there were three restrainer piers, the relative displacement of the pier-beam changed evenly and reached its minimum at most piers. Thus, the setting up of the restrainer pier could effectively reduce the relative displacement.

3.2.3. Displacement Response When the Taft Seismic Wave PGA Was 0.7 g. Figure 13 shows that the maximum relative displacement of the whole pier-beam was the smallest when there were three restrainer piers. Besides, the setting up of restrainer pier had a significant effect on the displacement of

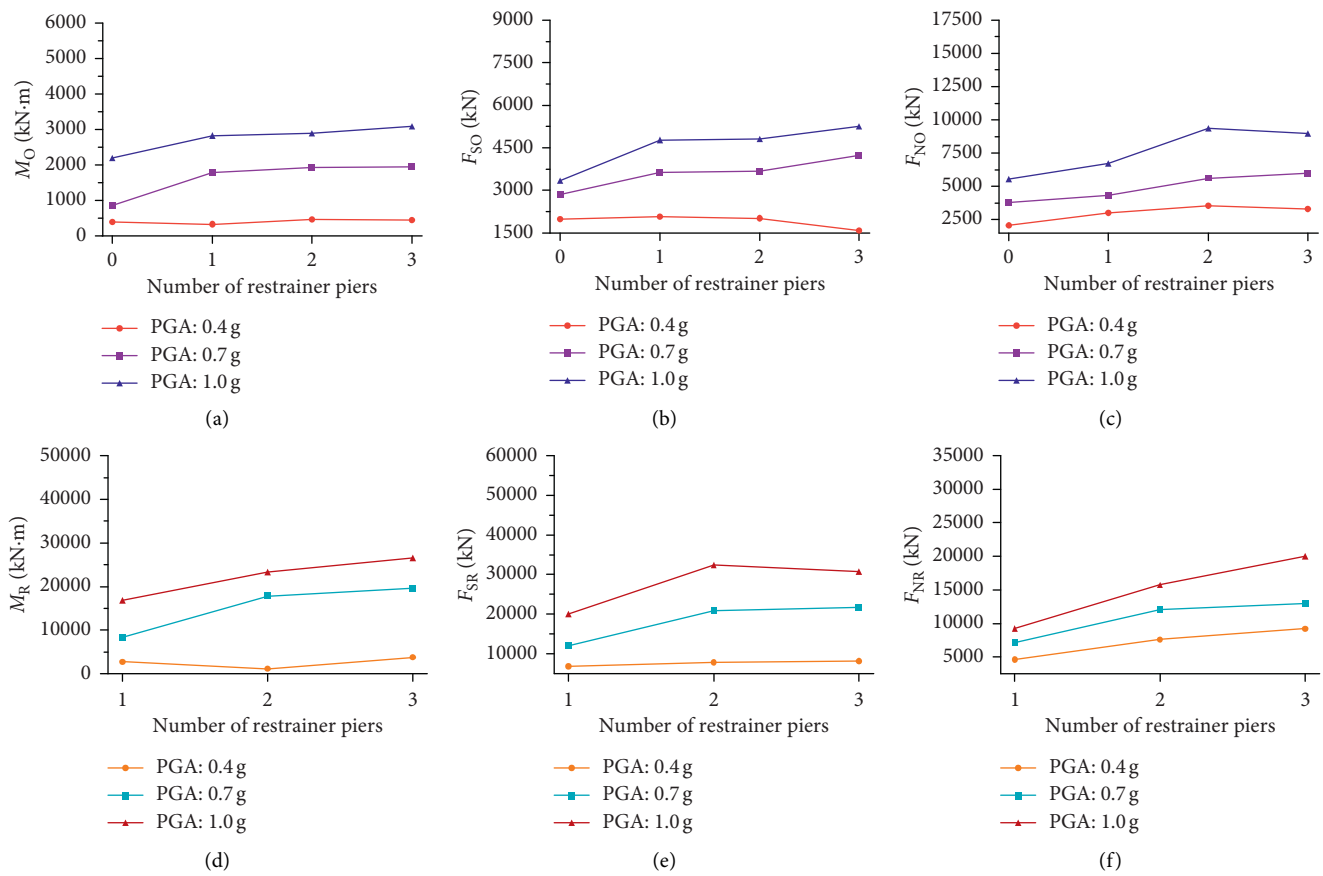

Figure 11: Internal force of the ordinary and restrainer piers.

the abutment. For the abutment of the first unit, when there was no restrainer pier, the relative displacement of the abutment was 0.52 m, and it was 0.29 m when setting up one restrainer pier, which reduced 0.23 m.

3.2.4. Displacement Response When the Taft Seismic Wave PGA Was 1.0 g. Figure 14 depicts the displacement response when the Taft seismic wave PGA was 1.0 g.

When three restrainer piers were set up, the relative displacement of the pier-beam clearly decreased, especially at the abutment. Besides, when there were two restrainer piers (Nos. 8 and 16), the relative displacement of the piers from Nos. 9 to 15 decreased significantly. It was mainly because two restrainer piers limited the displacement of main girders. When the number of the restrainer piers was three, the relative displacement of the pier-beam at most piers was at its minimum.

4. Influence of the EJS on the Dynamic Response

When the moving distance of two beams on the pier is greater than the EJS, the beams will pound at the expansion joint. The smaller the EJS, the greater the chance of pounding. Generally, the displacement of the beam is limited by restricting the pounding between the beam and retaining wall. Here, the EJS was considered to affect the relative displacement of the pier-beam. A single-column restrainer pier was set in the middle of the bridge. In this analysis, the EJS varied in size from 3 to 9 cm in increments of 2 cm. The El-Centro and Taft seismic waves were employed in this analysis. The number of restrainer piers was 0, 1, or 2, and the EJS of the ordinary pier was 7 cm.

4.1. Influence of EJS on the Dynamic Response under the El-Centro Seismic Wave

4.1.1. No Restrainer Piers. Figure 15(a) shows the relative displacement when the PGA was 0.7 g. The relative displacement of the pier-beam was maximum at the No. 0 abutment. With the increase of the EJS, the displacement of the No. 0 abutment increased, and the displacement of the whole bridge gradually decreased along the positive direction. The difference of relative displacement under any cases was small after pier No. 20. In addition, there was little difference between the relative displacement when EJSs of 70 or 90 mm were used.

The maximum internal force of the ordinary pier at the pier bottom when there was no restrainer pier is plotted in Figures 15(b) to 15(d). When the PGA was 0.4 g, the EJS had little impact on the maximum moment. When the PGA was 0.7 g, the maximum moment increased first and then decreased with the increase of the EJS, and when the EJS was greater than 70 mm, the maximum moment changed little (Figure 15(b)). When the PGA was 0.7 g, the EJS had little

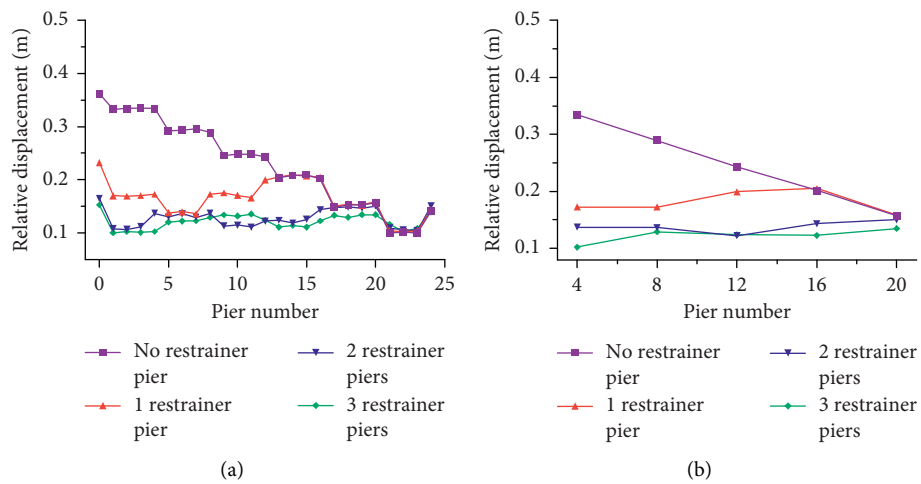

Figure 12: (a) Relative displacement of each pier and (b) trend of relative displacement of the pier-beam.

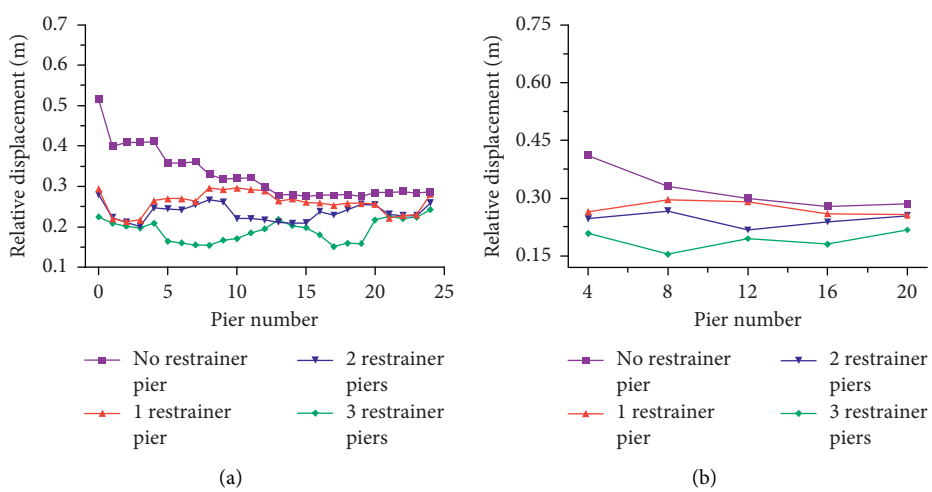

Figure 13: (a) Relative displacement of each pier and (b) trend of relative displacement of the pier-beam.

effect on the maximum shear. When the PGA was 0.4 g, the maximum shear decreased initially, then increased with the increase of the EJS, and reached its minimum when the EJS was 50 mm (Figure 15(c)). The maximum axial force increased firstly and then decreased with the increase of the EJS. When the EJS was greater than 70 mm, the maximum axial force changed little, and the maximum axial force at the pier bottom reached its maximum value when EJS of 50 mm was used. In conclusion, a bridge with an EJS of 70 or 90 mm could obtain better seismic performance.

4.1.2. One Restrainer Pier. Compared with the case of when no restrainer pier was set up, when there was one restrainer pier, the relative displacement of the pier-beam along the positive direction varied widely. Overall, when the EJS was 70 mm, the relative displacement of the pier-beam was more stable (Figure 16(a)). The relative displacement of the pier-beam increased with an increase in the EJS, and when the PGA was 0.7 g, the relative displacement of the pier-beam was larger than that of the pier-beam with the PGA of 0.4 g (Figure 16(b)). The relative displacement of the pier-beam was reduced because of the restrainer pier. When the PGA was 0.4 and 0.7 g and the EJS was 50 and 70 mm, respectively, the relative displacement of the pier-beam decreased significantly, and the maximum was 40.33 and 46.91%, respectively.

Figure 17 depicts the internal force of the ordinary and the restrainer piers. Figures 17(a) to 17(c) illustrate the internal force of the ordinary pier, and the other figure panels illustrate the internal force of the restrainer pier. The maximum pier bottom moment of the ordinary pier gradually decreased with an increase in the EJS. When the PGA was 0.7 g, the maximum pier bottom moment greatly changed, and it reached its minimum when the EJS was 70 mm. However, the EJS had little impact on the maximum pier bottom moment when the PGA was 0.4 g (Figure 17(a)). Under a PGA of 0.4 or 0.7 g, the maximum pier bottom moment of the restrainer pier decreased with the increase of the EJS, and when the EJS was greater than 70 mm, the maximum pier bottom moment changed little (Figure 17(d)). When PGA and EJS were the same, the

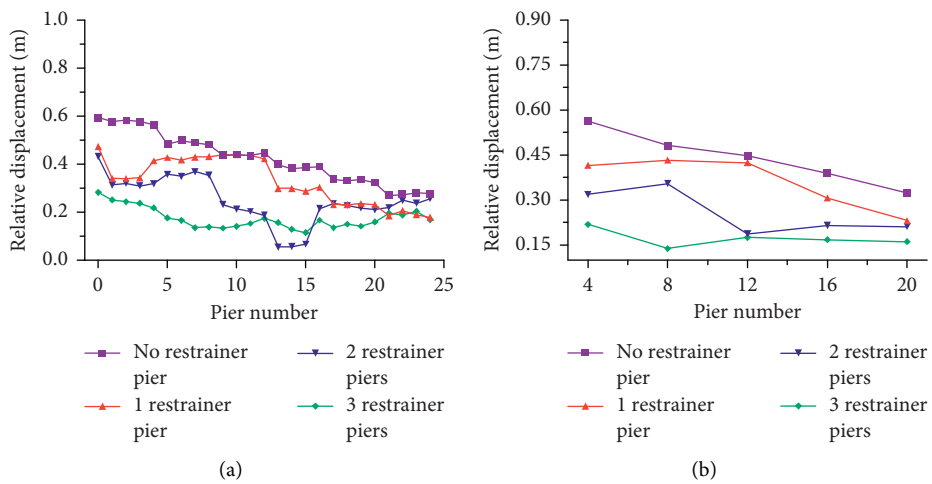

Figure 14: (a) Relative displacement of each pier and (b) trend of relative displacement of the pier-beam.

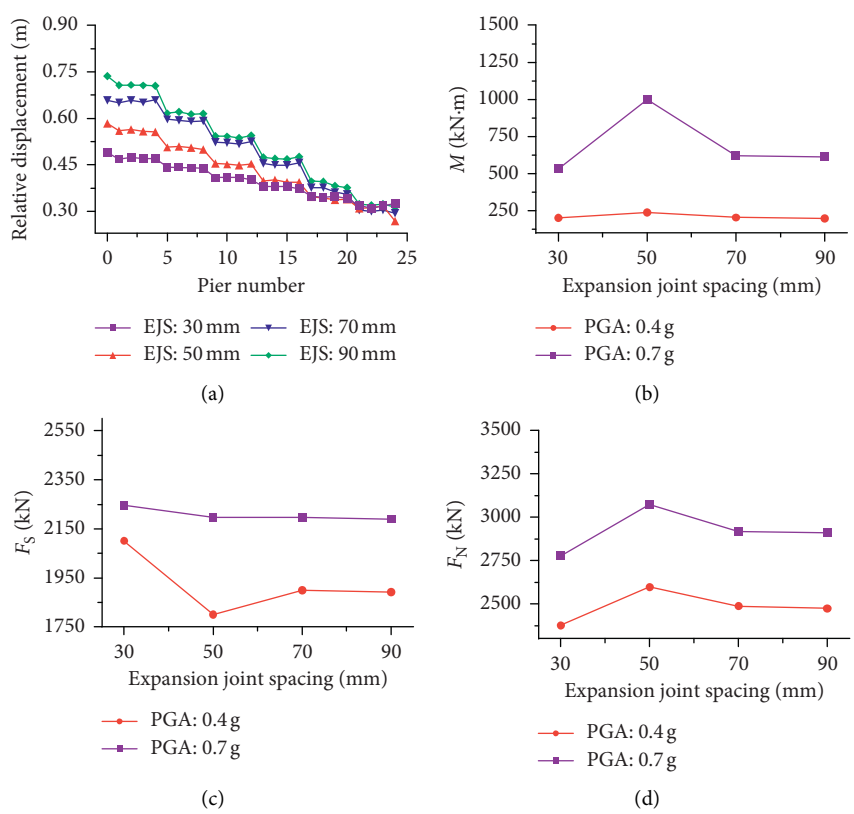

Figure 15: Relative displacement of each pier and maximum internal force.

maximum pier bottom shear of the restrainer pier was greater than that of the corresponding ordinary pier. The maximum pier bottom shear of the restrainer pier decreased with an increase in the EJS; moreover, the maximum pier bottom shear of the restrainer pier changed little when the EJS was greater than 70 mm (Figures 17(b) and 17(e)). The axial force at the pier bottom of the restrainer pier was greater than that of the ordinary pier when the PGA and the EJS were the same. With an increase in the EJS, the maximum axial force at the pier bottom of both piers varied little. The axial force at the pier bottom of the restrainer pier reached its minimum value when the EJS was 70 mm (Figures 17(c) and 17(f)).

4.1.3. Two Restrainer Piers. The relative displacement of the pier-beam under different EJSs changed similarly along the positive direction (Figure 18(a)). When the PGA was 0.7 g, the relative displacement of the pier-beam decreased first and then increased as the EJS increased.

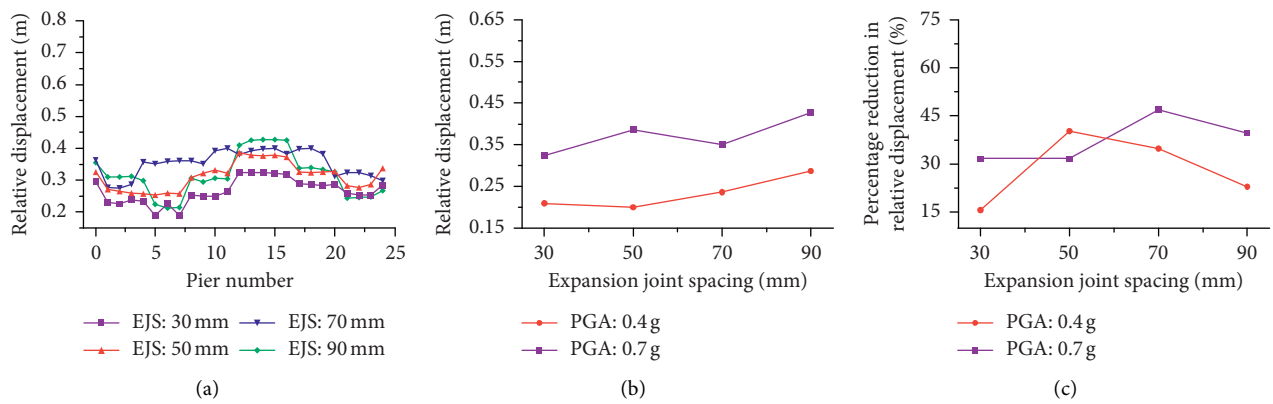

Figure 16: (a) Relative displacement of each pier, (b) maximum relative displacement of the pier-beam, and (c) percentage reduction in relative displacement.

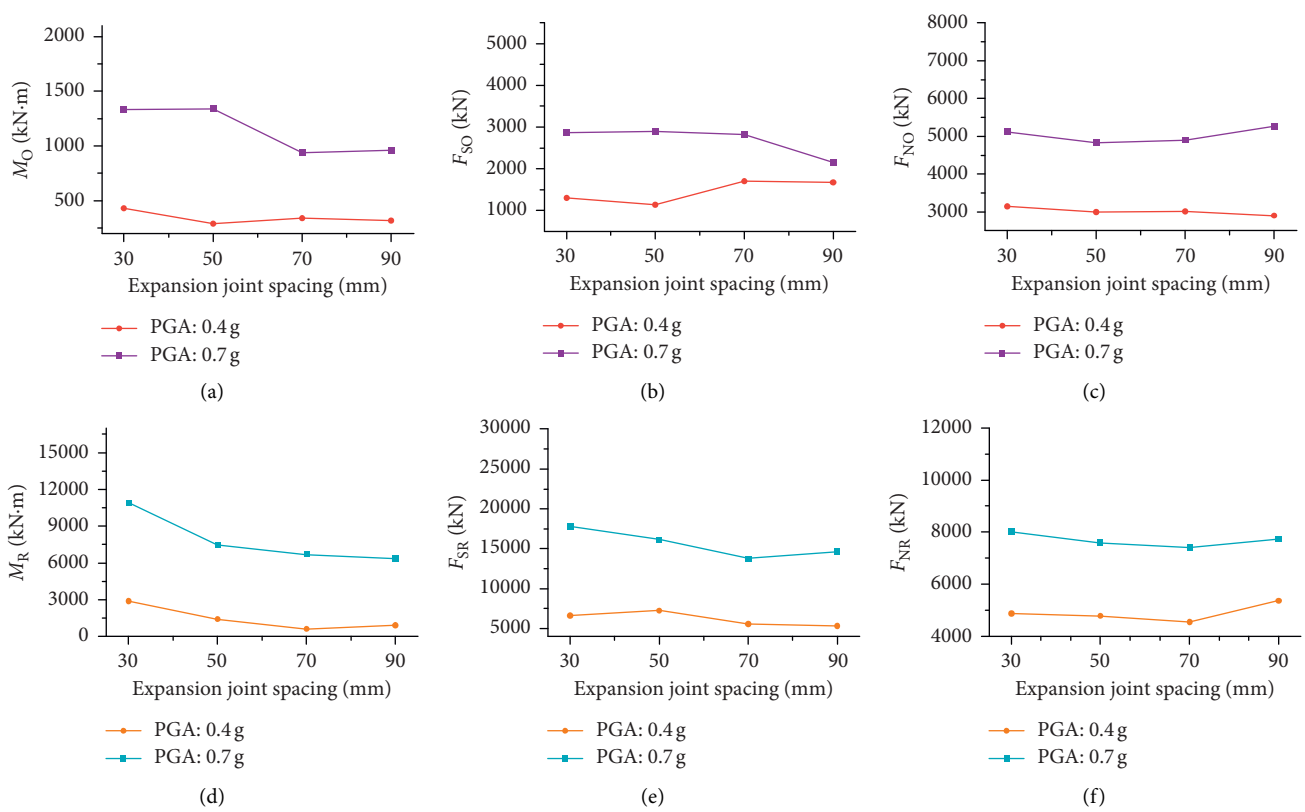

Figure 17: Internal force at the pier bottom of the ordinary and the restrainer piers with one restrainer pier.

When the EJS was 70 mm, the relative displacement of the pier-beam was at its minimum. However, its relative displacement varied little when the PGA was 0.4 g (Figure 18(b)). Under a PGA of 0.4 and 0.7 g, the relative displacement of the pier-beam was reduced maximally (the maximum was 53.06 and 54.33%, respectively) when the EJS was 70 mm, compared with the case of no restrainer pier (Figure 18(c)).

Figure 19 depicts the internal force of the ordinary and restrainer piers. Figures 19(a) to 19(c) illustrate the internal force of the ordinary pier, and the other figure panels illustrate the internal force of the restrainer pier. The maximum pier bottom moment of both the ordinary and restrainer piers gradually decreased as the EJS increased (Figures 19(a) and 19(d)). When the PGA was 0.7 g, the maximum pier bottom shear of the ordinary pier decreased with the increase of the EJS and then varied little after 50 mm. When the PGA was 0.4 g, the EJS had little influence on the maximum pier bottom shear (Figure 19(b)). Under a PGA of 0.4 and 0.7 g, the maximum pier bottom shear of the restrainer pier changed little and reached its minimum value when the EJS was 70 mm (Figure 19(e)). The EJS had little impact on the axial force at the pier bottom of the ordinary pier in

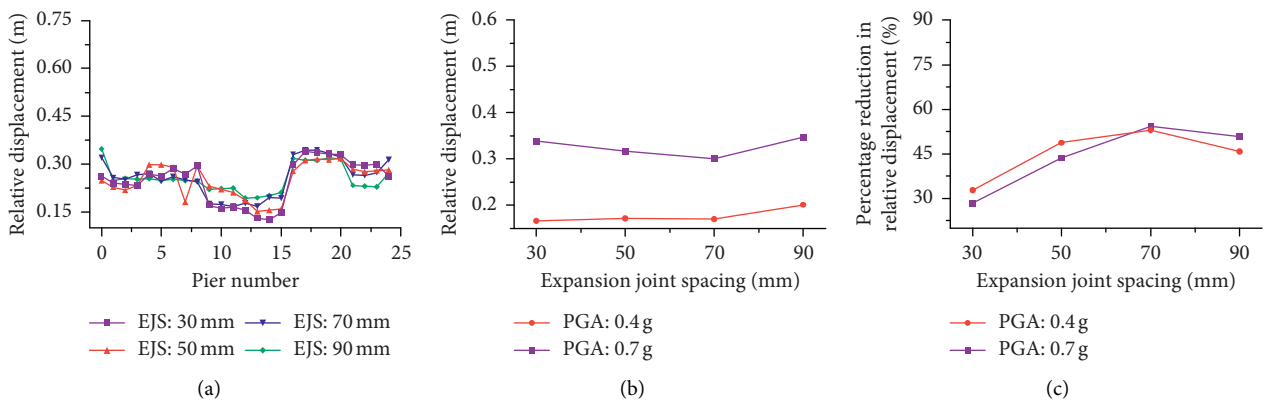

Figure 18: (a) Relative displacement of the pier-beam, (b) maximum relative displacement of the pier-beam, and (c) percentage reduction in relative displacement.

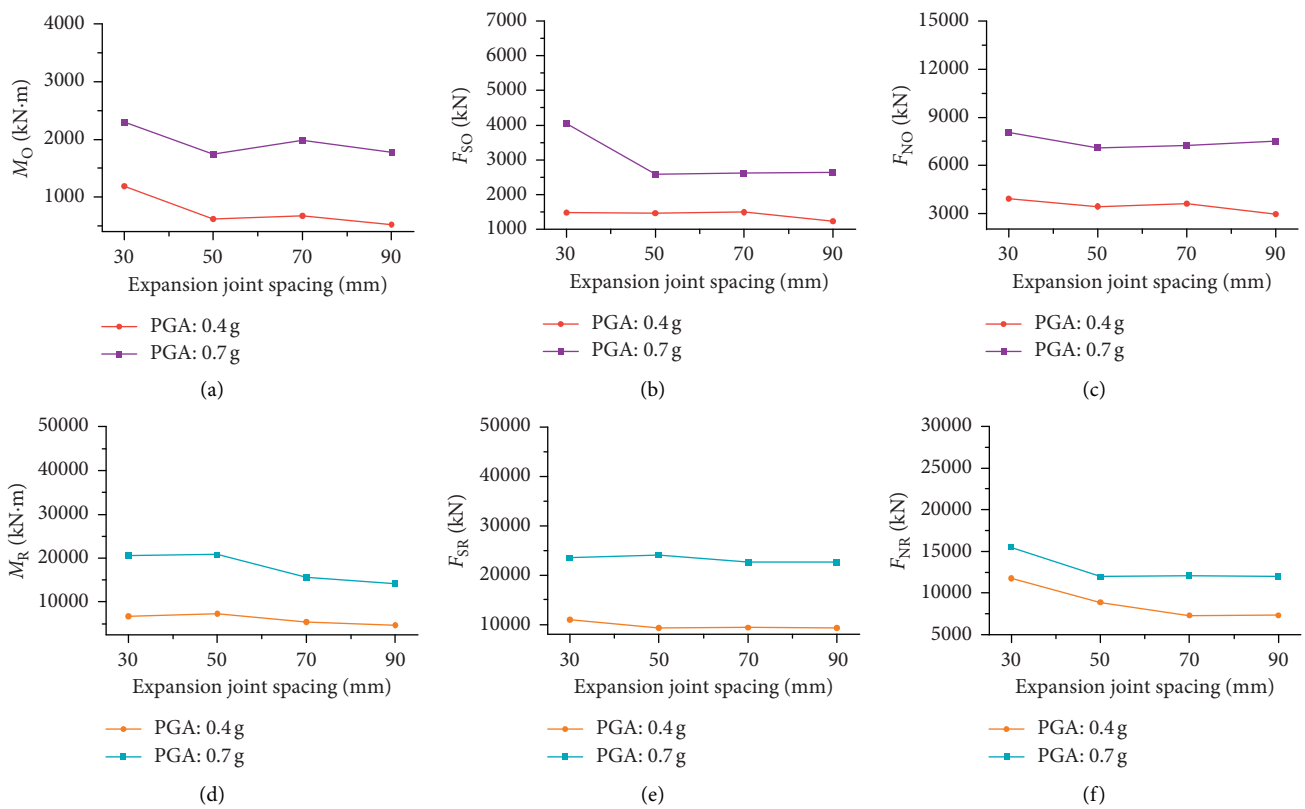

Figure 19: Internal force at the pier bottom of the ordinary and restrainer piers with two restrainer piers.

general. When the PGA was 0.7 g, the axial force at the pier bottom of the ordinary decreased with the increase of the EJS (Figure 19(c)). When the PGA was 0.4 g, the maximum axial force at the pier bottom of the restrainer pier significantly reduced as the EJS increased and reached its minimum value when the EJS was 70 mm. When the PGA was 0.7 g and the EJS was greater than 50 mm, the maximum axial force at the bottom of the restrainer pier changed little (Figure 19(f)).

4.2. Influence of EJS on the Dynamic Response under the Taft Seismic Wave

4.2.1. No Restrainer Piers. Figure 20(a) shows the relative displacement when the PGA was 0.7 g. The maximum relative displacement of the pier-beam occurred at the No. 0 abutment (Figure 20(a)). With an increase in the EJS, the displacement of the No. 0 abutment progressively increased and the displacement of the whole bridge gradually

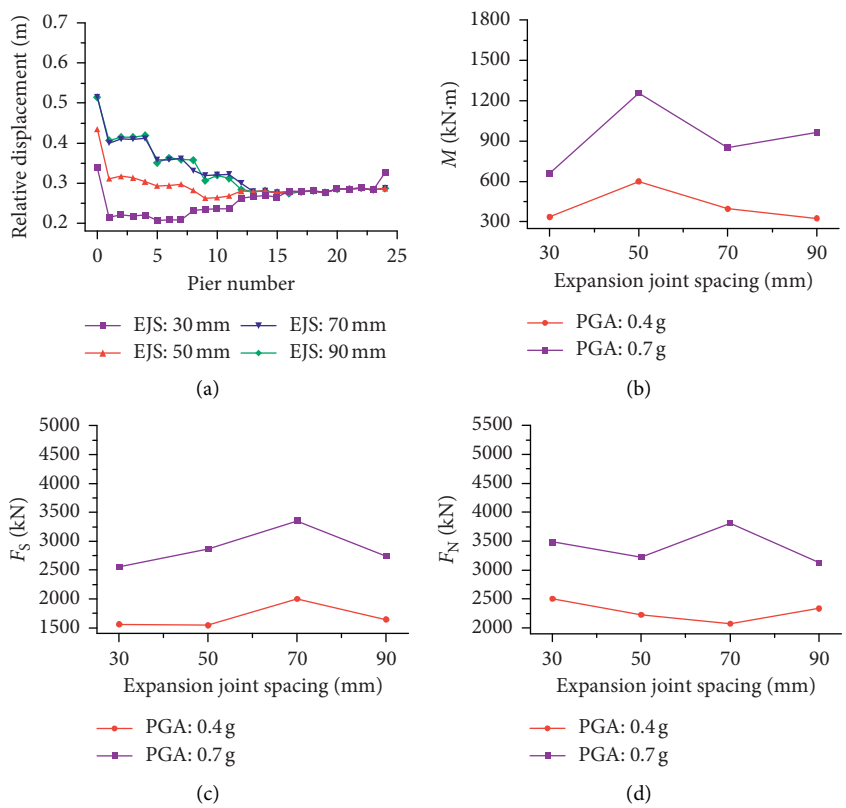

Figure 20: Relative displacement of each pier and maximum internal force.

decreased along the positive direction. However, there was little difference between the relative displacement when EJSs of 70 or 90 mm were used. Also, in pier Nos. 16 to 24, the EJS had little impact on the displacement. An insufficient EJS had a great impact on pounding between the main girders. Small EJSs cause frequent poundings, which leads to local concrete spalling and bearing damage to the bridge. In conclusion, a bridge with an EJS of 70 or 90 mm could obtain better seismic performance.

The maximum internal force of the ordinary pier when there was no restrainer pier is plotted in Figures 20(b) to 20(d). With an increase in the EJS, the maximum moment and the maximum shear at the pier bottom increased initially and then decreased. When the EJS was greater than 70 mm, the maximum moment changed little. When the EJS was 50 or 70 mm, the maximum moment and the maximum shear force at the pier bottom reached their maximum values. However, when the PGA was 0.4 g and the EJS was 70 mm, both the maximum moment and the maximum axial force reached their minimum values.

4.2.2. One Restrainer Pier. When the EJS was 90 mm, the relative displacement of the pier-beam changed suddenly at the No. 12 restrainer pier when the PGA was 0.7 g (Figure 21(a)). When the PGA was 0.4 or 0.7 g, the maximum relative displacement of the pier-beam increased with an increase in the EJS and reached its maximum value at an EJS of 90 mm (Figure 21(b)). When the EJS was 50 and 70 mm, the PGA was 0.4 and 0.7 g, respectively; the percentage reduction of the maximum relative displacement of the pier-beam reached its maximum value of 49.15 and 32.71%, respectively (Figure 21(c)).

The internal force of the ordinary and the restrainer piers is shown in Figure 22 when there was one restrainer pier. The maximum pier bottom moment of the ordinary pier gradually decreased with an increase in the EJS when the PGA was 0.7 g, and it increased first and then decreased when the PGA was 0.4 g; it was at its maximum when the EJS was 50 mm (Figure 22(a)). Moreover, when the PGA was 0.4 g, the maximum pier bottom moment of the restrainer pier first increased and then decreased with an increase in the EJS; it was at its maximum when the EJS was 50 mm. Meanwhile, the maximum moment also reached its maximum value when the PGA was 0.7 g and the EJS was 50 mm (Figure 22(d)). From the shear curve illustrated in Figures 22(b) and 22(e), it can be seen that when the EJS was 70 mm, the maximum pier bottom shear of the ordinary pier reached its maximum value, while that of the restrainer pier reached its minimum value when the PGA and EJS were 0.7 g and 70 mm, respectively. The axial force curves illustrated in Figures 22(c) and 22(f) indicate that when the PGA

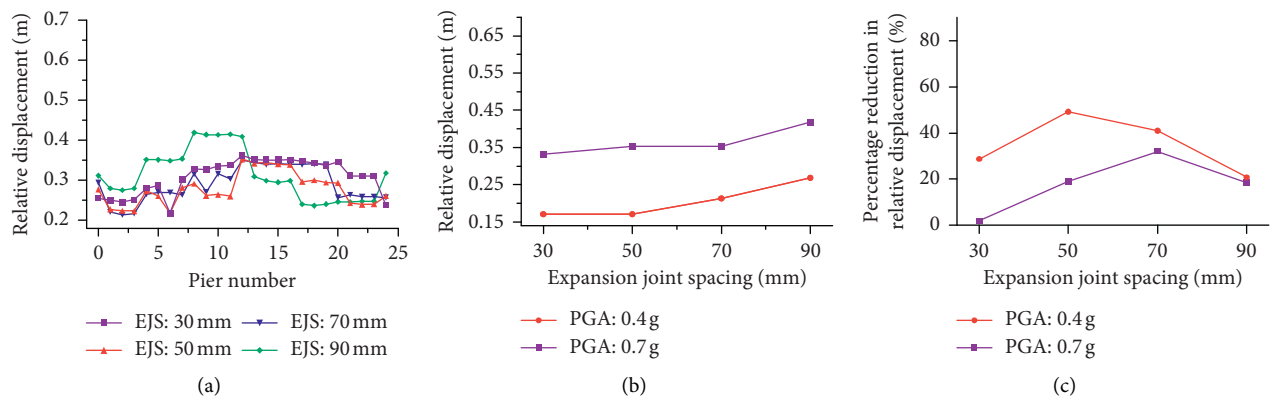

Figure 21: (a) Relative displacement of each pier, (b) maximum relative displacement of the pier-beam, and (c) percentage reduction in relative displacement.

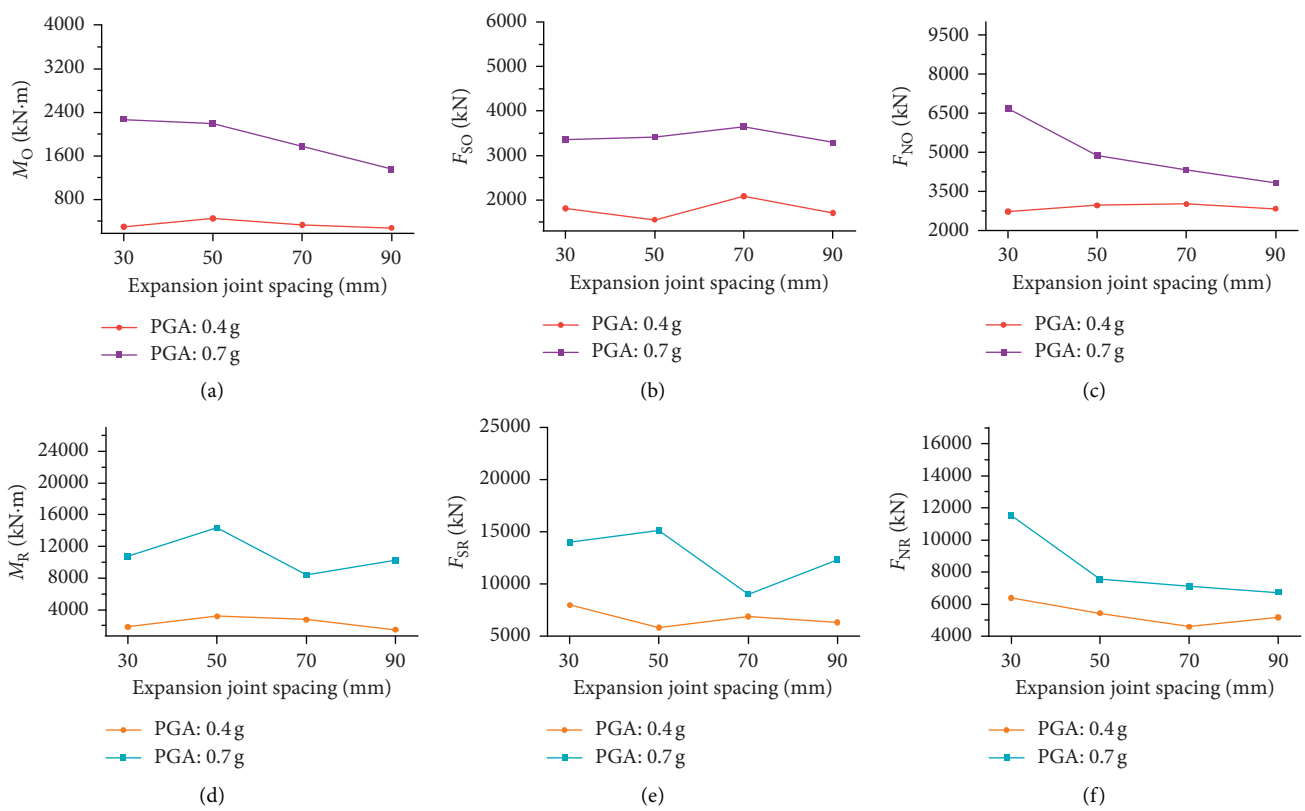

Figure 22: Internal force at the pier bottom of the ordinary and the restrainer piers with one restrainer pier.

was 0.7 g, the maximum pier bottom axial force of the ordinary and the restrainer piers gradually decreased with an increase in the EJS. When the PGA was 0.4 g, the maximum pier bottom axial force of the ordinary pier increased first and then decreased, while the maximum axial force of the restrainer pier decreased first and then increased; its minimum value was obtained at an EJS of 70 mm.

4.2.3. Two Restrainer Piers. The relative displacement of the pier-beam under different EJSs changed similarly along the positive direction (Figure 23(a)). When the EJS was 70 mm and the PGA was 0.4 g, the relative displacement of the pier-beam was reduced maximally (the maximum was 58.33%). It is believed that from a relative displacement perspective, good performance for a six-unit bridge can be achieved with two restrainer piers and an EJS of 70 mm (Figures 23(b) and 23(c)).

The internal force of the ordinary and the restrainer piers when two restrainer piers were set up is plotted in Figure 24. With an increase in the EJS, the maximum pier bottom moment of the ordinary and the restrainer piers generally decreased (Figures 24(a) and 24(d)). For the restrainer pier, the moment changed little when the EJS was greater than 70 mm. The shear

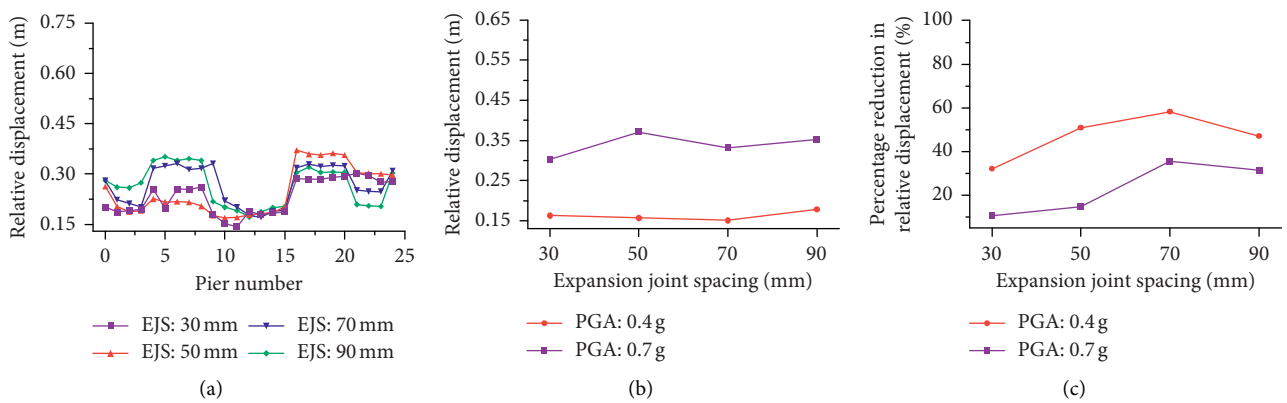

Figure 23: (a) Relative displacement of the pier-beam, (b) maximum relative displacement of the pier-beam, and (c) percentage reduction in relative displacement.

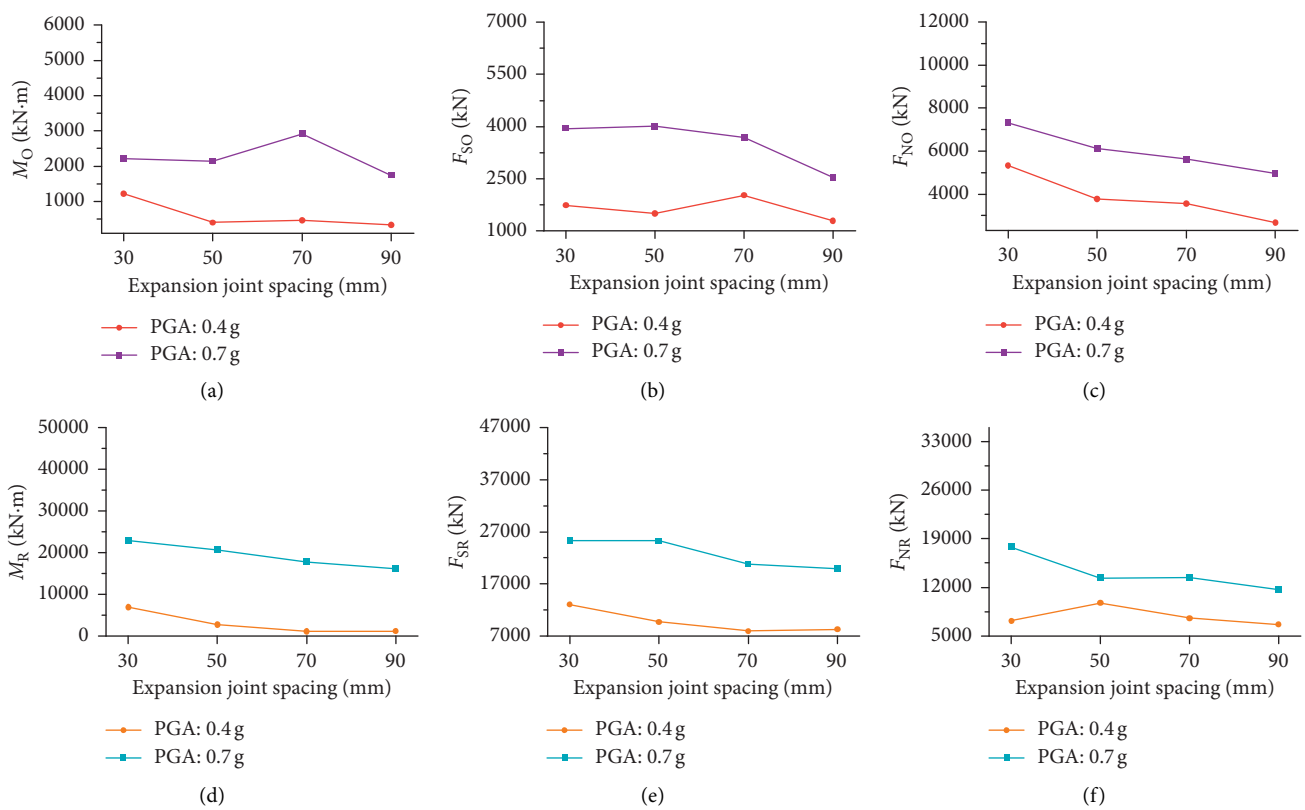

Figure 24: Internal force at the pier bottom of the ordinary and the restrainer piers with two restrainer piers.

curves illustrated in Figures 24(b) and 24(e) indicate that the maximum pier bottom shear of the ordinary and the restrainer piers gradually decreased with an increase in the EJS. However, when the PGA was 0.4 g and the EJS was 70 mm, the maximum pier bottom shear of the ordinary pier increased, and then gradually decreased. The axial force curves illustrated in Figures 24(c) and 24(f) demonstrate that the maximum pier bottom axial force of the ordinary and the restrainer piers gradually decreased with an increase in the EJS, differing only in the rate of change. When the PGA was 0.4 g, the maximum pier bottom axial force of the restrainer pier increased first, then decreased with an increase in the EJS, and reached its maximum value when the EJS was 50 mm. Moreover, when the PGA was 0.4 or 0.7 g and the EJS was greater than 70 mm, the axial force changed little.

5. Influence of Span on the Structural Dynamic Response

5.1. No Restrainer Piers. The maximum relative displacement of the pier-beam under a PGA of 0.4 or 0.7 g reached its maximum value at the No. 0 abutment (Figure 25). With an

increase in the span, the relative displacement at the No. 0 abutment gradually decreased. The relative displacement of the whole bridge in the positive direction decreased gradually. When the PGA was 0.4 g and the span was 50 m, the relative displacement at each pier was the smallest for pier Nos. 1 through to 17. Also, the relative displacement of each span between pier Nos. 17 and 20 was similar under different spans, and there was a big difference after No. 20 pier. When the PGA was 0.7 g and the span was 50 m, the relative displacement of each pier was the smallest for pier Nos. 1 through to 8. After pier No. 8, the relative displacement at a span of 50 m was less different from that of the other spans (although that of the 50 m span was larger).

The internal force of each pier with no restrainer pier is shown in Figure 26, where the subscripts 0.4 and 0.7 indicate a PGA of 0.4 and 0.7 g, respectively. The maximum moment occurred at pier No. 16 when the span was 20 m and at pier No. 12 for all the other spans. When the span was 40 m, the maximum moment at pier Nos. 1 through to 12 was smaller than that of the other spans. After pier No. 12, at a span of 50 m, the maximum moment was smaller than that of the other spans (Figure 26(a)). However, when the PGA was 0.7 g and the span was 50 m, the maximum moment had a smaller value for pier Nos. 1 through to 14 (Figure 26(d)). Figures 26(b) and 26(e) display that the maximum shear occurred at the abutment of both pier Nos. 0 and 24, and the span had little influence on the shear of the No. 0 abutment. However, for the No. 24 abutment, the shear under different spans differed widely. Moreover, when the span was 30 m, the shear of the No. 24 abutment was maximum under a PGA of 0.4 and 0.7 g. However, when the span was 50 m, the shear at the bottom of most piers was at its minimum.

The axial force of the bridge showed an increasing trend along the positive direction (Figures 26(c) and 26(f)). For spans of 20, 30, 40, and 50 m, the maximum axial force occurred from pier Nos. 22 to 24. When the PGA was 0.4 g and the span was 30 m, the axial force at the pier bottom was larger than that of the other spans. When the PGA was 0.7 g and the span was 50 m, the axial force of pier Nos. 0 through to 10 was at its minimum. Under a PGA of 0.4 and 0.7 g, the axial force of each pier showed fewer changes when the span was 50 m.

5.2. One Restrainer Pier. A restrainer pier changes the rigidity of the bridge, resulting in uneven internal force distribution. After setting up one restrainer pier, the relative displacement of the third and fourth unit was large (Figure 27). However, the largest displacement occurred at the No. 0 abutment, and with an increase in the span, the relative displacement along the positive direction decreased first and then increased and was ultimately reduced. When the PGA was 0.7 g, the maximum relative displacement occurred in the middle part of the bridge. For a span of 50 m, the relative displacement varied gently.

The internal force of the ordinary and the restrainer piers with one restrainer pier is plotted in Figure 28. The maximum moment of the ordinary and the restrainer piers gradually decreased with an increase in the span, and its maximum and minimum values were obtained at a span of 20 and 50 m, respectively (Figures 28(a) and 28(d)). The shear curves illustrated in Figures 28(b) and 28(e) reveal that when the PGA was 0.4 g, the maximum shear of the ordinary and the restrainer piers increased first and then decreased with an increase in the span. Its maximum value was obtained at a span of 30 m; a smaller value was obtained at the span of 50 m. When the PGA was 0.7 g and the span was 40 m, the pier bottom shear of the ordinary pier was at its minimum, while the shear of the restrainer pier changed little with an increase in the span. Under a PGA of 0.4 and 0.7 g, when the span was 50 m, the axial force of the ordinary pier bottom was at its minimum (Figures 28(c) and 28(f)). When the PGA was 0.4 g and the span was more than 30 m, the influence of the span on the restrainer pier axial force was insignificant. Therefore, from the perspective of axial force, a 50 m span is suitable for long bridges.

5.3. Two Restrainer Piers. The relative displacement of the pier-beam with two restrainer piers under a PGA of 0.4 or 0.7 g is illustrated in Figure 29. The relative displacement of the pier-beam reached its extremum at the No. 0 abutment, No. 24 abutment, and No. 4 pier. As the span increased, the relative displacement in the positive direction fluctuated substantially. Moreover, when the PGA was 0.7 g, the trend of the relative displacement in the positive direction under each span was essentially the same. The relative displacement in the middle part of the bridge was smaller when the span was 50 m.

The internal force of the ordinary and the restrainer piers is depicted in Figure 30. The moment curves of Figures 30(a) and 30(d) demonstrate that when the PGA was 0.4 g, the maximum moment of the ordinary and the restrainer piers gradually decreased with an increase in the span, reaching its maximum and the minimum values at spans of 20 and 50 m, respectively. However, when the PGA was 0.7 g, the maximum moment of the ordinary and the restrainer piers increased first and then decreased with an increase in the span. Maximum and minimum values were reached at spans of 30 and 50 m, respectively. When the PGA was 0.4 g, the maximum shear of the ordinary pier increased first and then decreased with increases in the span, and its minimum value was reached at a span of 50 m (Figure 30(b)). When the PGA was 0.7 g, its maximum and minimum values were reached at spans of 40 and 50 m, respectively. The shear of the restrainer pier changed little with an increase in the span (Figure 30(e)). When the PGA was 0.4 g, the maximum axial force of the ordinary and the restrainer piers increased first and then decreased with an increase in the span (Figures 30(c) and 30(f)). When the PGA was 0.7 g, the maximum axial force of the ordinary pier gradually decreased with an increase in the span. Finally, under a PGA of 0.4 or 0.7 g, the axial force of the ordinary and the restrainer piers reached its minimum value at a span of 50 m.

5.4. Three Restrainer Piers. The relative displacement of the pier-beam with three restrainer piers under a PGA of 0.4 or 0.7 g is plotted in Figure 31. The relative displacement of the

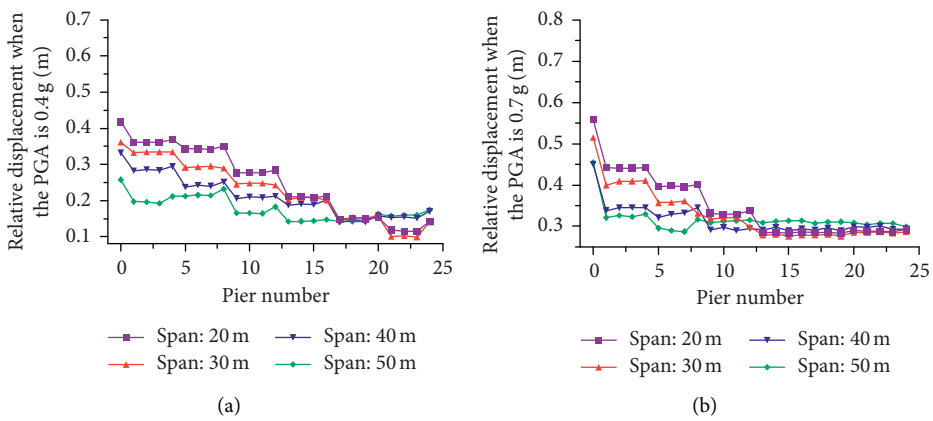

Figure 25: Relative displacement of the pier-beam with no restrainer pier.

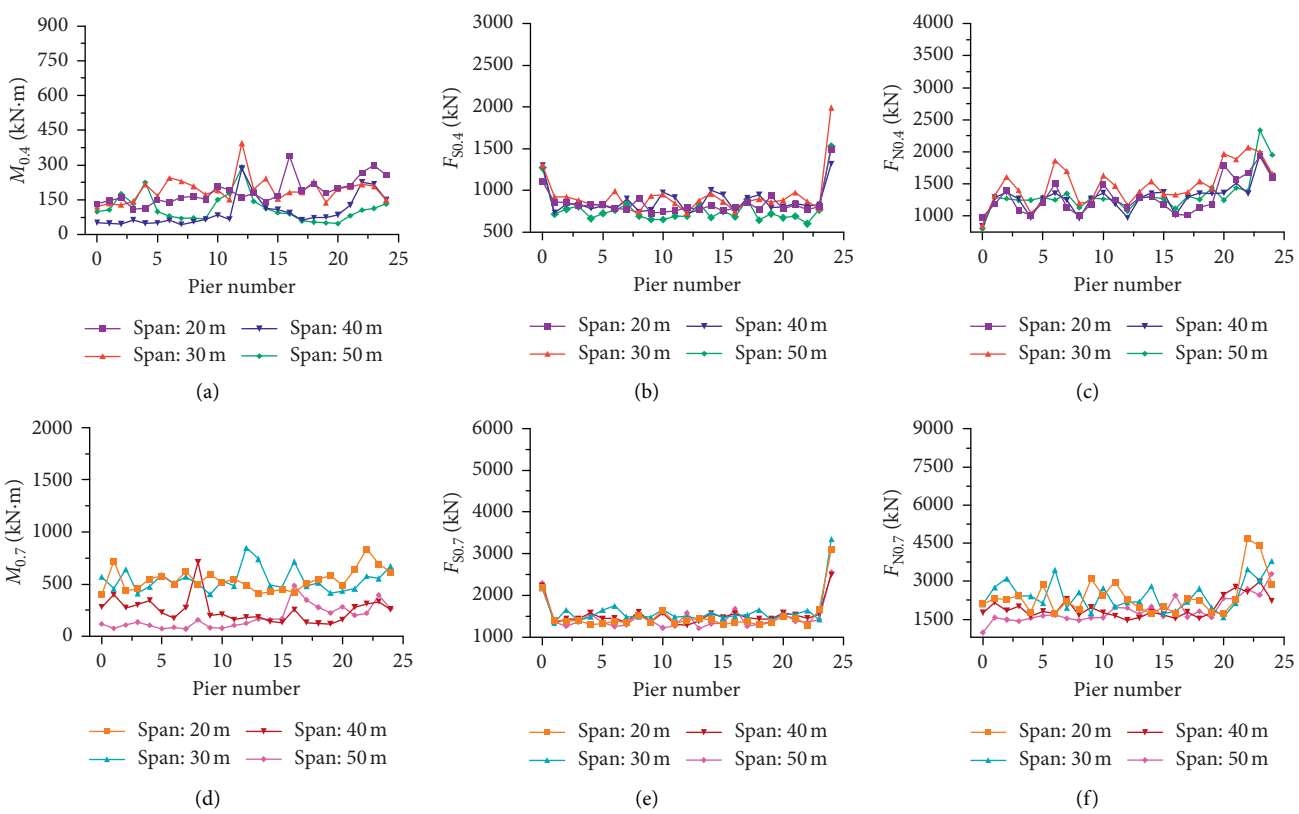

Figure 26: Internal force at the pier bottom of the ordinary pier under different PGAs.

pier-beam from the second unit to the fourth unit was smallest when the PGA was 0.4 g and the span was 50 m. Moreover, when the PGA was 0.7 g, the relative displacement trend of each span was the same in the positive direction, and the first and sixth units had the largest values.

The internal force of the ordinary and the restrainer piers is plotted in Figure 32. The maximum moment of the ordinary and the restrainer piers decreased with an increase in the span (Figures 32(a) and 32(d)). Under a PGA of 0.4 or 0.7 g, the maximum moment of the ordinary and the restrainer piers reached their minimum value at a span of 50 m. The curves of shear illustrated in Figures 32(b) and 32(e) indicate that when the PGA was 0.4 g, with an increase in the span, the maximum and minimum shear of the ordinary pier was reached at spans of 40 and 30 m, respectively. When the PGA was 0.7 g, the maximum shear increased first and then decreased with an increase in the span, and its minimum value was reached at a span of 50 m. The maximum shear of the restrainer pier was less affected by span and was less varied. Under a PGA of 0.4 or 0.7 g, the maximum axial force of the ordinary pier reached its maximum and

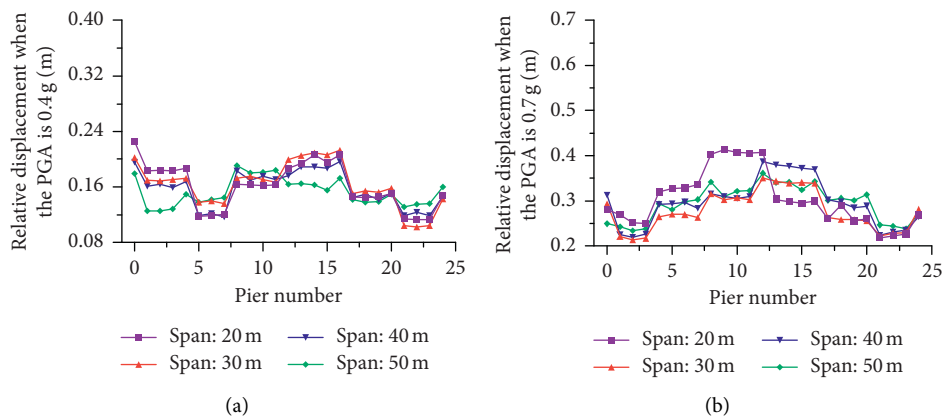

Figure 27: Relative displacement of the pier-beam with one restrainer pier.

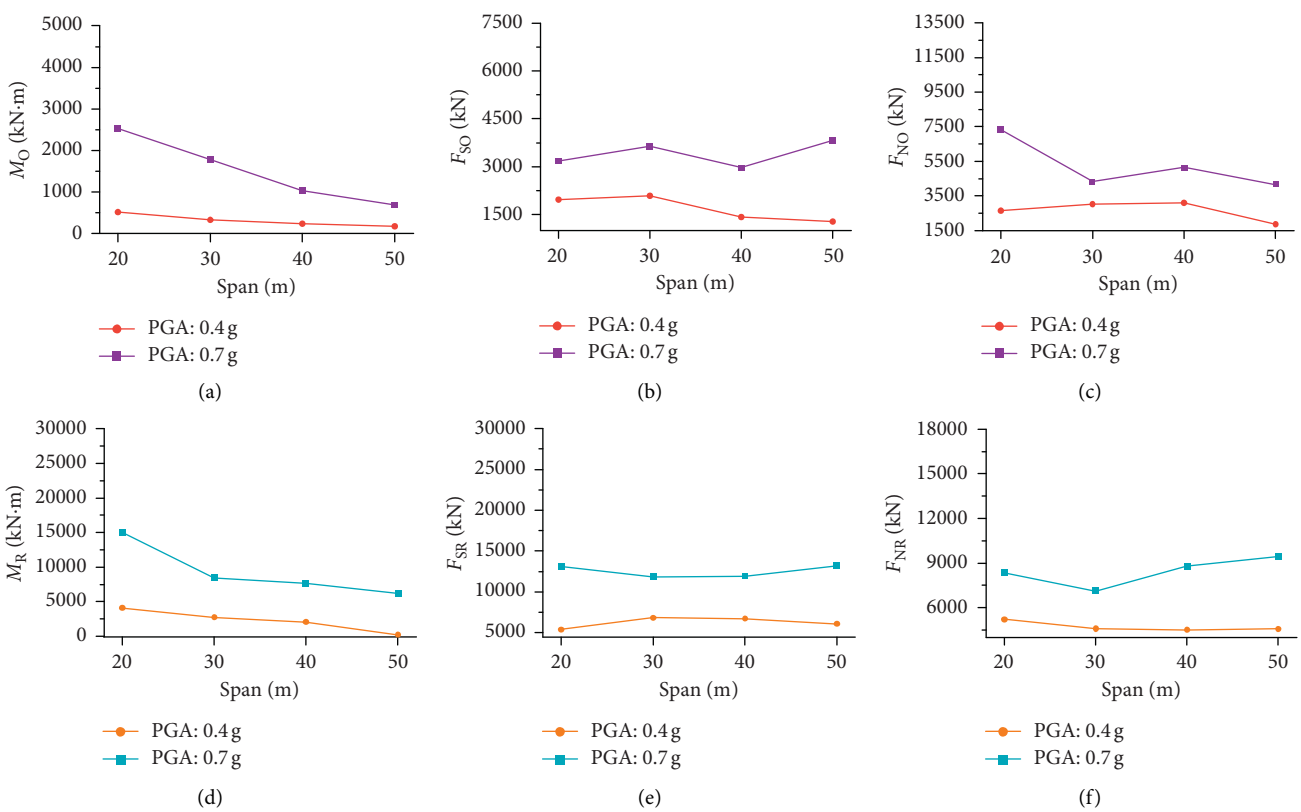

Figure 28: Internal force at the pier bottom of the ordinary and the restrainer piers with one restrainer pier.

minimum values at spans of 40 and 30 m, respectively, with an increase in the span (Figures 32(c) and 32(f)). However, the maximum axial force of the restrainer pier increased with an increase in span, and its maximum and minimum values were reached at spans of 50 and 20 m, respectively.

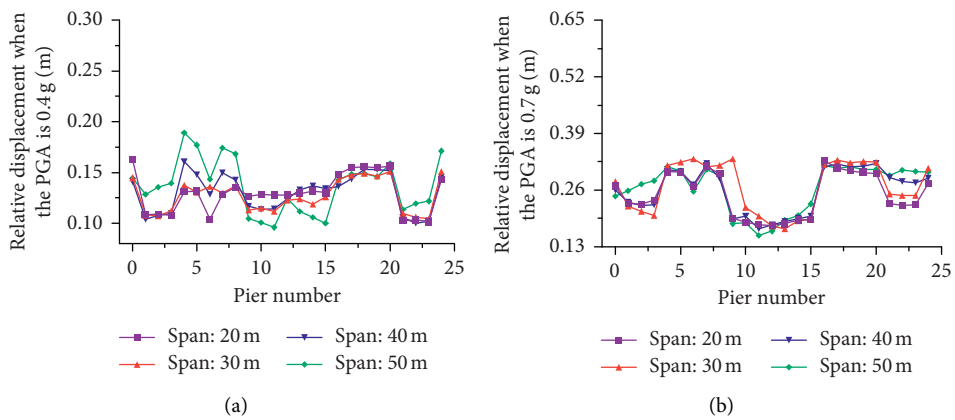

Figure 29: Relative displacement of the pier-beam with two restrainer piers.

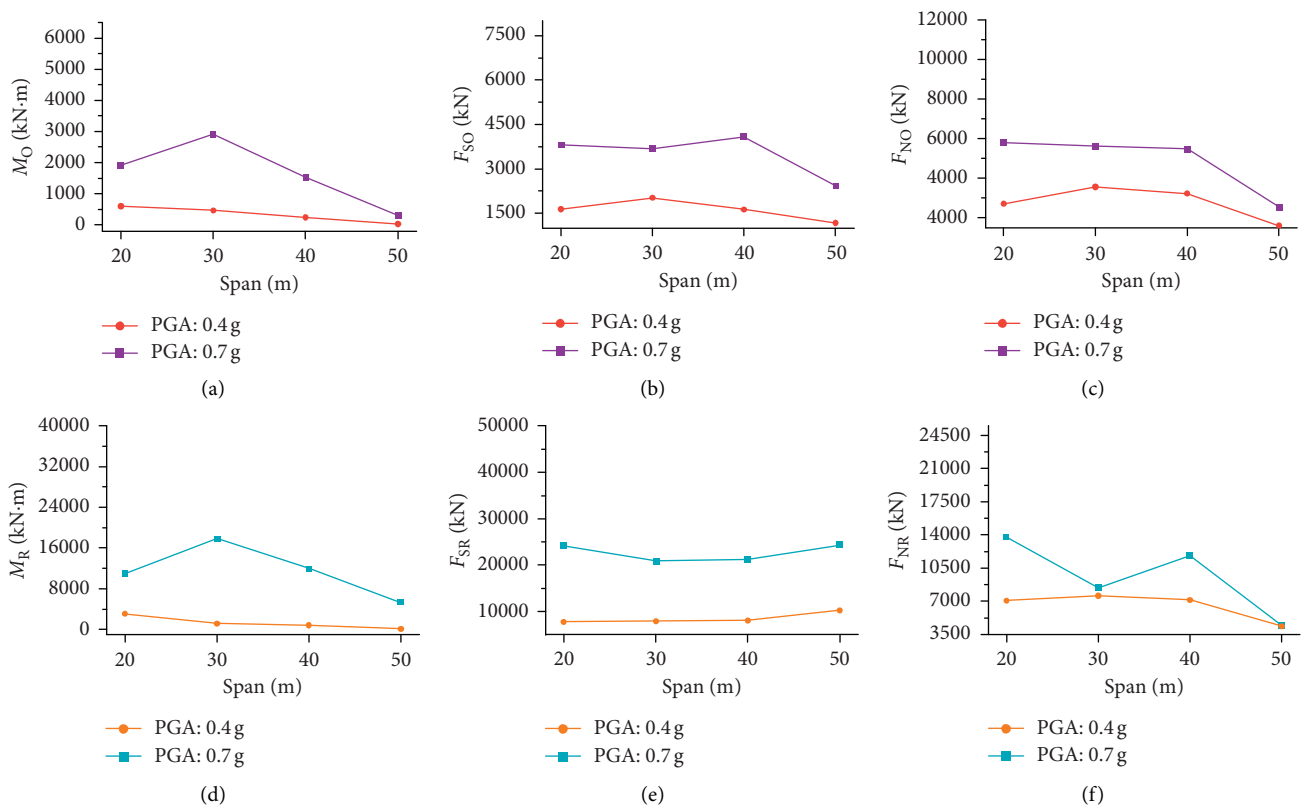

Figure 30: Internal force at the pier bottom of the ordinary and the restrainer piers with two restrainer piers.

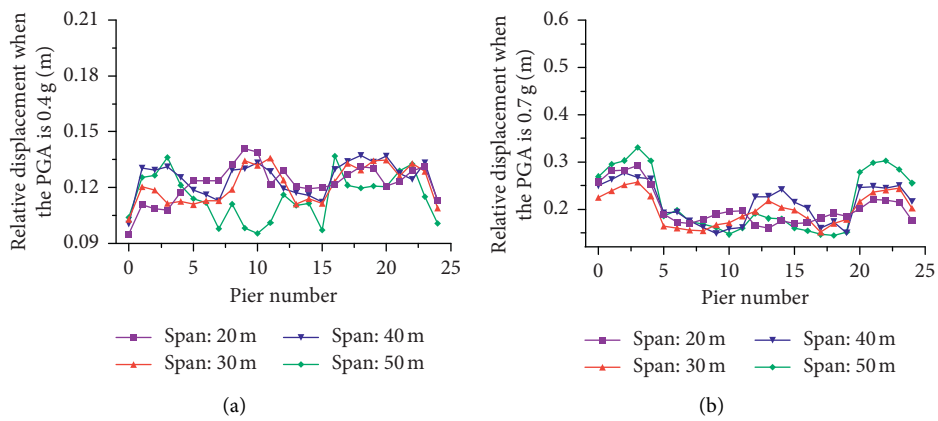

Figure 31: Relative displacement of the pier-beam with three restrainer piers.

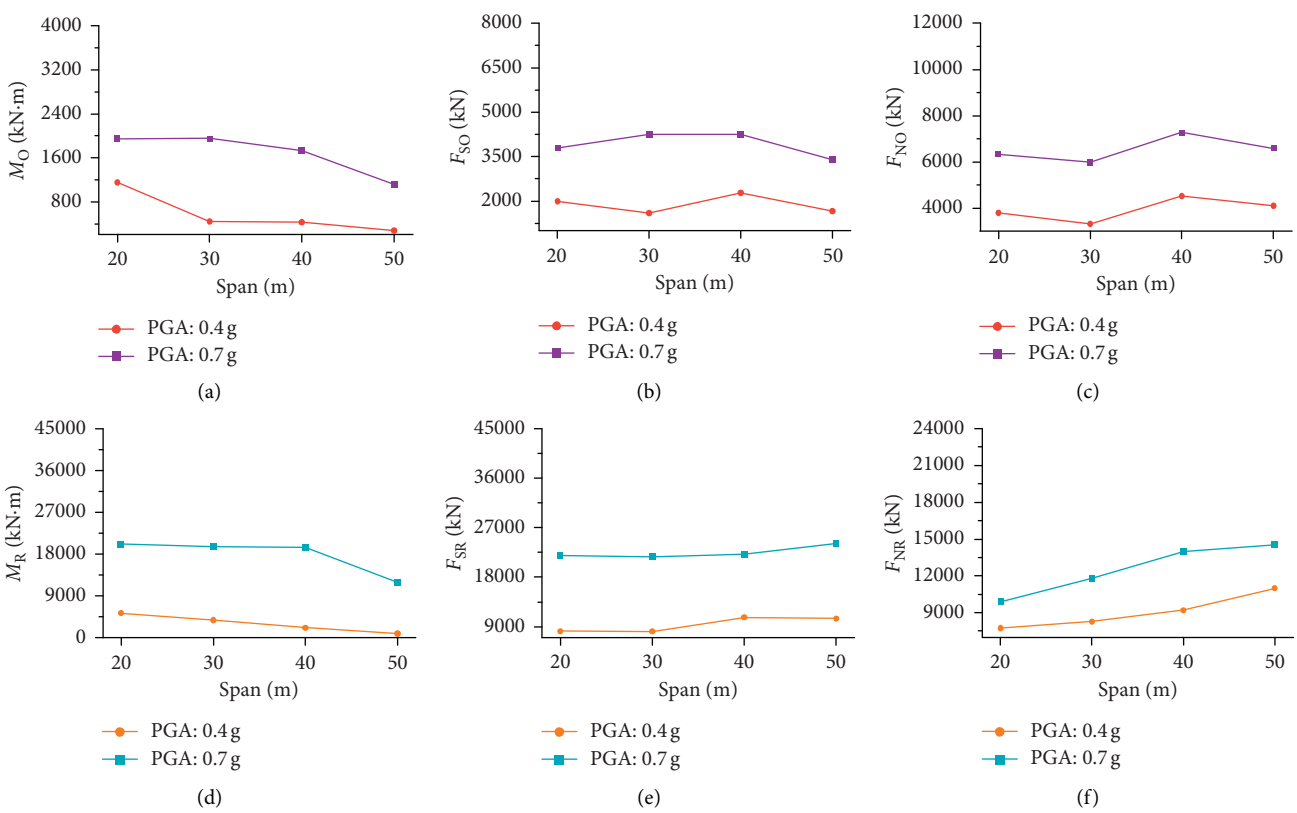

Figure 32: Internal force at the pier bottom of the ordinary and the restrainer piers with three restrainer piers.

6. Conclusion

After inputting some seismic waves, the influence of a varying number of restrainer piers, EJSs, and spans on the dynamic response and seismic performance of long bridges with equal-height piers was scrutinized. The main conclusions of this study can be summarized as follows:

(1) The influence of the number of restrainer piers on the dynamic response showed that the internal force at the bottom of the pier increased for each additional restrainer pier. Moreover, our results also illustrated that the longitudinal antipushing rigidity of the bridge increased with an increase in the number of restrainer piers, which could reduce the maximum relative displacement of the pier-beam in the longitudinal direction. Considering the occurrence of, and cost incurred by, rare earthquakes, it is recommended to use three restrainer piers in bridge engineering.

(2) The influence of the EJS on the dynamic response showed that the pounding had little impact on the internal force of the pier bottom when one or two restrainer piers were set up. Moreover, in terms of the relative displacement, when there were two

restrainer piers and the EJS was 70 mm, the relative displacement of the pier-beam was at their minimum. Therefore, the seismic performance was best when an EJS of 70 mm was used.

(3) The dynamic response analysis of the main girder with different spans indicated that the relative displacement of the pier-beam gradually decreased with an increase in the span on the whole, and the internal force of the whole bridge had the same trend in general. Using a span of 50 m was proposed for areas with frequent strong earthquakes.

(4) The results demonstrated that efficient performance can be achieved for a 24-span equal-height beam bridge under the following parameters: 3 restrainer piers, an EJS of 70 mm, and a 50 m span. However, in other cases, the determination of the optimal number of restrainer piers, the size of EJS, and the span need further investigation.

Data Availability

The data that support the findings of this study are included within the article.

Conflicts of Interest

The authors declare that there are no conflicts of interest regarding the publication of this manuscript.

Acknowledgments

This project was supported by the National Natural Science Foundation of China (Grant Nos. 51708074, 51678544, and 51678452) and the Key Project of Foundation and Frontier Research of Chongqing (Grant No. cstc2017jcyjAX0187). The authors gratefully acknowledge the financial support.

References

[1] S. Y. Zhao, *Earthquake of Ming-Dynasty and Succor after the Disaster—Great Guanzhong Earthquake in Jiajing 34 Year as an Example*, Jiangxi Normal University, Nanchang, China, 2009.

[2] L. S. Chen, *Investigation of Highway Damage in Wenchuan earthquake*, China Communications Press, Beijing, China, 2012.

[3] J. W. Wang, J. Z. Li, and L. C. Fan, "State of art of current studies on the effect of seismic induced pounding between adjacent bridge decks and falling-off prevention measures," *Journal of Highway and Transportation Research and Development*, vol. 24, no. 5, pp. 71–75, 2007.

[4] D. S. Wang, J. Y. Wang, Z. G. Sun et al., "Unseating damage to simply supported bridges during Wenchuan earthquake and design countermeasures," *Journal of Disaster Prevention and Mitigation Engineering*, vol. 31, no. 5, pp. 595–601, 2011.

[5] Y. Gao, Q. Pu, and X. Li, "State-of-arts of earthquake-induced pounding responses of girder bridges and measures for preventing pounding and span collapse," *Dizhen Gongcheng yu Gongcheng Zhendong (Earthquake Engineering and Engineering Vibration)*, vol. 31, no. 1, pp. 80–88, 2011.

[6] B. Li, K. Bi, N. Chouw, J. W. Butterworth, and H. Hao, "Experimental investigation of spatially varying effect of ground motions on bridge pounding," *Earthquake Engineering & Structural Dynamics*, vol. 41, no. 14, pp. 1959–1976, 2012.

[7] B. Sha, T. Tao, C. Xing et al., "Pounding analysis of isolated girder bridge under nonpulse and pulse-like earthquakes," *Journal of Performance of Constructed Facilities*, vol. 34, no. 4, Article ID 04020062, 2020.

[8] H. Wei, X. D. Wei, K. H. Wang et al., "Design of unseating preventing system in Japan," *Journal of World Bridge*, vol. 40, no. 6, pp. 11–14, 2012.

[9] X. L. He and L. Z. Zhao, "Analysis of shear wave velocity based on multiple cross-correlation functions," *Rock and Soil Mechanics*, vol. 31, no. 8, pp. 2541–2545, 2010.

[10] D. S. Wang, Q. M. Feng, and G. X. Wang, "Analysis model of pounding between adjacent bridge girders during earthquakes based on collinear impact between rods," *Engineering Mechanics*, vol. 21, no. 2, pp. 157–166, 2004.

[11] P. Zhu, M. Abe, and Y. Fujino, "Modelling three-dimensional non-linear seismic performance of elevated bridges with emphasis on pounding of girders," *Earthquake Engineering & Structural Dynamics*, vol. 31, no. 11, pp. 1891–1913, 2002.

[12] Y. A. Khulief and A. A. Shabana, "Dynamic analysis of constrained system of rigid and flexible bodies with intermittent motion," *Journal of Mechanisms, Transmissions, and Automation in Design*, vol. 108, no. 1, pp. 38–45, 1986.

[13] J. Rismantab-Sany and A. A. Shabana, "On the use of the momentum balance in the impact analysis of constrained elastic systems," *Journal of Vibration and Acoustics*, vol. 112, no. 1, pp. 119–126, 1990.

[14] A. S. Yigit, "Dynamics of a radially rotating beam with impact, part 1: theoretical and computational model," *Transactions of the ASME Journal of Dynamic Systems Measurement and Control*, vol. 112, no. 1, 1990.

[15] S. A. Anagnostopoulos, "Pounding of buildings in series during earthquakes," *Earthquake Engineering & Structural Dynamics*, vol. 16, no. 3, pp. 443–456, 1988.

[16] R. Jankowski, K. Wilde, and Y. Fujino, "Pounding of superstructure segments in isolated elevated bridge during earthquakes," *Earthquake Engineering & Structural Dynamics*, vol. 27, no. 5, pp. 487–502, 2015.

[17] G. L. Fenves and R. Desroches, *Evaluation of the Response of I-10/215 Interchange Bridge Near San Bernardino in the 1992 Landers and Big Bear Earthquakes*, California Strong Motion Instrumentation Program, Sacramento, CA, USA, 1995.

[18] Z. X. Li, F. Q. Yue, and L. Zhou, "Equivalent kelvin impact model for pounding analysis of bridges during earthquake," *Engineering Mechanics*, vol. 25, no. 4, pp. 128–133, 2008.

[19] K. N. Guo, "Influence of pier height on the seismic behaviors of continuous-beam bridge," *Journal of North China Institute of Water Conservancy and Hydroelectric Power*, vol. 33, no. 5, pp. 53–59, 2012.

[20] Y. L. Xu, "Nonlinear FEA of breaking force distribution of long connected continuous bridge," *Journal of Lanzhou Jiaotong University*, vol. 35, no. 2, pp. 14–18, 2008.

[21] D. L. Meng, Q. Gao, and M. G. Yang, "Shaking table tests on transverse pounding effect of high-speed railway simply-supported girder bridges under earthquake excitations," *Journal of Vibration and Shock*, vol. 38, no. 24, pp. 63–73, 2019.

[22] K. Bi, H. Hao, and N. Chouw, "Influence of ground motion spatial variation, site condition and SSI on the required separation distances of bridge structures to avoid seismic

pounding," *Earthquake Engineering & Structural Dynamics*, vol. 40, no. 9, pp. 1027–1043, 2011.

[23] K. Bi, H. Hao, and N. Chouw, "Required separation distance between decks and at abutments of a bridge crossing a canyon site to avoid seismic pounding," *Earthquake Engineering &Structural Dynamics*, vol. 39, no. 3, pp. 303–323, 2010.

[24] I. G. Buckle and R. L. Mayes, "Seismic isolation: history, application, and performance-A world view," *Earthquake Spectra*, vol. 6, no. 2, pp. 161–201, 1990.

[25] N. Makris, "Seismic isolation: early history," *Earthquake Engineering & Structural Dynamics*, vol. 48, no. 2, pp. 269–283, 2019.

[26] W. Zheng, H. Wang, J. Li, and H. Shen, "Performance evaluation of bridges isolated with SMA-based friction pendulum system at low temperatures," *Soil Dynamics and Earthquake Engineering*, vol. 125, Article ID 105734, 2019.

[27] P. Tsopelas, M. C. Constantinou, Y. S. Kim, and S. Okamoto, "Experimental study of fps system in bridge seismic isolation," *Earthquake Engineering & Structural Dynamics*, vol. 25, no. 1, pp. 65–78, 1996.

[28] H. Wang, W.-Z. Zheng, J. Li, and Y.-Q. Gao, "Effects of temperature and lead core heating on response of seismically isolated bridges under near-fault excitations," *Advances in Structural Engineering*, vol. 22, no. 14, pp. 2966–2981, 2019.

[29] W. Zheng, H. Wang, H. Hao, K. Bi, and H. Shen, "Performance of bridges isolated with sliding-lead rubber bearings subjected to near-fault earthquakes," *International Journal of Structural Stability and Dynamics*, vol. 20, no. 2, Article ID 2050023, 2020.

[30] W. Zheng, H. Wang, J. Li et al., "Parametric study of superelastic-sliding LRB system for seismic response control of continuous bridges," *Journal of Bridge Engineering*, vol. 25, no. 9, Article ID 04020062, 2020.

[31] H. Wang, H. J. Shen, H. Zhang et al., "Parameter optimization analysis of viscous dampers for isolated continuous curved girder bridges," *Journal of Harbin Engineering University*, vol. 41, no. 2, pp. 282–288, 2020.

[32] R. J. Liang, H. Wang, W. Z. Zheng et al., "Parameter optimization of lead rubber bearings of an isolated curved girder bridge," *Engineering Mechanics*, vol. 36, no. 11, pp. 83–90, 2019.

[33] W. Z. Zheng, H. Wang, and H. J. Shen, "Thermal effects on response of seismic isolated bridges subjected to strong ground motions," *Engineering Mechanics*, vol. 36, no. 4, pp. 188–195+205, 2019.

[34] X. S. Xia and X. C. Chen, "Restrainer effect on rocking response of tall pier with pile foundations," *Journal of Tongji University*, vol. 41, no. 10, pp. 1470–1475, 2013.

[35] Z. G. Sun, T. Y. Zhao, D. S. Wang et al., "Seismic damage control design for double-deck bridge bents based on rocking self-centering system," *China Journal of Highway and Transport*, vol. 33, no. 3, pp. 97–106, 2020.

[36] Y. Wang, T. Q. Wang, L. M. Sun et al., "Experimental investigation on seismic performance of rectangular-hollow double-column tall piers with energy dissipation beams," *Engineering Mechanics*, vol. 37, no. 7, pp. 159–167, 2020.

[37] Z. Guo, X. C. Chen, M. B. Ding et al., "Experimental study and analysis on the seismic performance of new base rocking isolation bridge piers," *Journal of Vibration and Shock*, vol. 39, no. 4, pp. 69–87, 2020.

[38] J.-j. Guo, J. Zhong, X.-z. Dang, and W.-c. Yuan, "Seismic performance assessment of a curved bridge equipped with a new type spring restrainer," *Engineering Structures*, vol. 151, no. 15, pp. 105–114, 2017.

[39] S. S. Cao, S. W. Wu, Z. Sun et al., "A multi-level performance SMA-based isolation system in girder bridges," *Journal of Vibration and Shock*, vol. 38, no. 24, pp. 209–217, 2019.

[40] J. Zhao, C. S. Xiang, Y. Zhou et al., "Effect of wedge block on the transverse seismic performance," *China Earthquake Engineering Journal*, vol. 42, no. 1, pp. 22–31, 2020.

[41] T. Tao, P. Shi, and H. Wang, "Spectral modelling of typhoon winds considering nexus between longitudinal and lateral components," *Renewable Energy*, vol. 162, pp. 2019–2030, 2020.

[42] T. Y. Tao, H. Wang, and K. Y. Zhao, "Efficient simulation of fully non-stationary random wind field based on reduced 2Dhermite interpolation," *Mechanical Systems and Signal Processing*, vol. 150, Article ID 107265, 2021.

[43] T. Y. Tao, H. Wang, L. Hu et al., "Error analysis of multivariate windfield simulated by interpolation-enhanced spectral representation method," *Journal of Engineering Mechanics*, vol. 146, no. 6, Article ID 04020049, 2020.

Hindawi
Mathematical Problems in Engineering
Volume 2021, Article ID 6647303, 13 pages
https://doi.org/10.1155/2021/6647303

Research Article

Seismic Vibration Mitigation of a Cable-Stayed Bridge with Asymmetric Pounding Tuned Mass Damper

Peng Zhang,[1] **Jie Tan**,[2,3] **Haitao Liu**,[1] **Gang Yang**,[1] **and Chunyi Cui**[1]

[1]*Institute of Road and Bridge Engineering, Dalian Maritime University, Dalian 116023, China*
[2]*Hubei Key Laboratory of Earthquake Early Warning, Institute of Seismology, China Earthquake Administration, Wuhan 430071, China*
[3]*Wuhan Institute of Earthquake Engineering, Wuhan 430071, China*

Correspondence should be addressed to Chunyi Cui; cuichunyi@dlmu.edu.cn

Received 21 December 2020; Revised 27 March 2021; Accepted 19 April 2021; Published 29 April 2021

Academic Editor: Hao Wang

In order to mitigate the seismic response of a cable-stayed bridge, a new type damping device named asymmetric pounding tuned mass damper (APTMD) is developed in this paper on the basis of the traditional symmetric pounding tuned mass damper. The novel APTMD has three parameters to be determined: the left-side gap, the right-side gap, and the frequency ratio. A numerical model of the APTMD damping system is established with consideration of both the computational efficiency and accuracy to enable the parametric optimization of the damper. The numerical model is based on a simplified model of the cable-stayed bridge and a nonlinear pounding force model. The genetic algorithm is utilized for the optimization of the damper. Afterwards, the cable-stayed bridge is subjected to 20 recorded ground motions to evaluate the vibration control effectiveness of the APTMD. Four systems are considered: (1) without dampers; (2) with a TMD; (3) with a PTMD; and (4) with an APTMD. Time history analysis reveals the following: (1) those dampers can all effectively suppress the vibration of the bridge and (2) the vibration control effectiveness of the APTMD is slightly better than the TMD and the PTMD.

1. Introduction

Cable-stayed bridges, typical long-span structures used in modern traffic and transportation systems, are featured by their large flexibility and low damping. During the past decades, structural damage induced by earthquakes has been extensively reported and investigated [1–4]. Therefore, it is of great necessity to reduce the seismic responses of a bridge and so as to improve its safety and reliability.

The seismic isolation technique is one of the most efficient vibration control techniques and its effectiveness has been verified by numerous numerical simulations and experimental investigations. The seismic isolation technique often employs flexible bearings to isolate the superstructure from its foundations and consequently interrupt the energy transfer between the superstructure and substructure. The most commonly adopted base isolators include lead rubber bearings (LRB) and friction pendulum systems (FPS), both exhibiting large vertical stiffness and low horizontal stiffness. Due to the large lateral flexibility, the isolating system often suffers from large displacements under earthquakes. Therefore, additional damping was introduced to the isolating systems to reduce the displacement of the isolators. Peng and Huang proposed to implant permanent magnets and elastomer fillings to the regular isolators. This new isolator was named the implant-magnetic bearing (IMB) and had been proved effective in mitigating the story accelerations and interstory drifts via both numerical studies [5] and experimental tests [6, 7]. Zheng [8] introduced the shape memory alloys (SMA) into the LRB system and proposed a superelastic-sliding lead rubber bearing (SSLRB) isolation system. Compared with the conventional LRBs, the SSLRB further reduce the residual displacement and the seismic demand of the piers. De Domenico et al. [9]combined the low-friction curved surface sliders (CSSs) with SMA gap

dampers. The combined isolating system is featured by the negligible residual displacement under small earthquakes and reduced displacement demand under large earthquakes. Wang et al. [10] proposed a novel self-centering (SC) base isolating system by incorporating SMA U-shaped dampers (SMA-UD). The superelasticity behavior of the SMA-UDs provides sufficient energy dissipation and excellent SC force. Additionally, the hysteresis characteristics of the SMA-UD are nearly isotropic, indicating that these isolators can be effective in any horizontal direction. Another drawback of the FPS system is that the sliding friction coefficient is sensitive to the surrounding temperatures and may lose recentering capability at low temperature. Zheng et al. [11] proposed a shape memory alloys (SMA) based FPS system to address this issue. Analytical results demonstrate that the residual displacement of the regular FPB system can be effectively reduced without significantly increasing the base forces of the bridge piers. In a following parametric study [12], the influence of the SMA wire properties on the response of the bridge to be controlled was investigated and optimal design can be obtained. A case study further demonstrated that the SMA-based FPB system can reduce the residual displacement and peak displacement when subjected to near-fault ground motions. Gur et al. [13] proposed to incorporate the base isolators with thermally modulated SMA damper, of which the temperature is altered during loading-unloading cycles to improve the energy dissipation. It is demonstrated by a numerical simulation that the thermally modulated shape memory alloy friction pendulum (tmSMA-FP) showed improved control efficiency compared with the regular FPS and SMA-FPS.

The tuned mass damper (TMD) is another commonly adapted damping device for bridge structures. In concept, the TMD is a dynamic absorber, often installed at the place of the main structure where the largest motion occurs. When the TMD is tuned to the target frequency of the main structure, it can effectively absorb the kinetic energy of the primary structure and thus reduce its vibration [14]. However, the TMD often suffers from a limited energy dissipation capacity and a relatively narrow band of effective frequency. Therefore, a variety of damping elements are introduced to the TMD to improve vibration control efficiency and robustness, such as friction dampers [15, 16], eddy-current components [17–20], inerters [21–24], particle dampers [25, 26], and shape memory alloys [27–29]. Most of these damping elements are expensive in cost and difficult in maintenance.

Recently, a new passive damping device named pounding tuned mass damper (PTMD) was proposed for vibration control of flexible structures such as power transmission towers [30, 31], high-rise buildings [32], subsea pipelines [33, 34], and bridges [35–37]. The PTMD consists of a tuned mass whose stroke is restrained by a pair of delimiters covered with viscoelastic materials. When the tuned mass impacts on the viscoelastic delimiter, large amounts of energy can be dissipated via collision. Therefore, the PTMD has an additional energy consumption pattern compared with a regular TMD and thus has better vibration control effectiveness. Furthermore, this additional damping mechanism can also improve the robustness of the PTMD. Even if the PTMD is off-tuned from the target frequency by 15%, it still can effectively mitigate the vibration of the primary structure [33, 38].

In early studies of the PTMD [30], the mass block is located in the middle of the two delimiters, which implies that the gap of the left side is the same as the right side. Parametric studies revealed that the gap is the key parameter that influences the vibration control effectiveness [39, 40]. The optimal gap is sensitive to the input amplitude and mass. To avoid the design complexity, a single-sided pounding tuned mass damper (SSPTMD) is proposed [37, 41]. In the SSPTMD, the mass block is placed aside the delimiter, which means that the gap equals zero. The frequency of the SSPTMD is tuned to half of the value of the target frequency to achieve the optimal design. Numerical studies and experimental results also validated the effectiveness of the SSPTMD.

With the inspiration of the SSPTMD, a novel damper called asymmetric pounding tuned mass damper (APTMD) is proposed in this paper. Compared with the former symmetric PTMD, the two gaps of the APTMD can be set to different values. Additionally, the frequency ratio, which is defined as the frequency of the damper over that of the primary structure, is another parameter to be determined. In order to achieve the optimal vibration mitigation effectiveness for a realistic bridge, the genetic algorithm (GA) is employed, with the left-side gap, right-side gap, and frequency ratio defined as the optimal variables and the average value of dynamic responses under 20 ground motions taken as the objective function. Even though the finite element (FE) model of the cable-stayed bridge equipped with an APTMD can be established in ANSYS, it is time-consuming to perform a time history analysis of this numerical model. Therefore, a simplified model of the bridge is developed and utilized to calculate the fitness of each individual in the GA optimization process. Finally, a time history analysis is conducted on the FE model of the cable-stayed bridge damped by the optimized APTMD. A TMD and a PTMD with the same mass ratio are also attached to the bridge to compare their damping effect with the APTMD.

The remainder of this paper is arranged as follows: in Section 2, the damping mechanism of the APTMD will be further explained by comparison with the classical TMD and the previously proposed symmetric PTMD. Motion equations of the APTMD damping system will be established on the basis of a nonlinear pounding force model in MATLAB/Simulink environment. Afterwards, a simplified model of a real cable-stayed bridge is established in Section 3. Optimal design of the APTMD will be achieved using the genetic algorithm in Section 4. Then, in Section 5, the dynamic responses of the bridge equipped with optimal APTMD, former PTMD, and traditional TMD will be compared to evaluate the performance of the proposed APTMD. Finally, this paper concludes with a discussion of the overall results and suggestion for future studies.

2. Development of APTMD Damping System

2.1. Introduction of APTMD. In order to demonstrate the damping mechanism of the proposed APTMD, the schematics of the classical TMD, the previously proposed symmetric PTMD, and the APTMD, as well as the undamped system, are compared in Figure 1. In Figure 1(a), a mass block, m_1, which is connected to the base by a spring, k_1, and a dashpot, c_1, represents the primary structure with being controlled. x_1 denotes the displacement of m_1.

In Figure 1(b), an auxiliary mass, m_2, is connected to m_2 by a spring, k_2, and a dashpot c_2, composing a classical TMD. If optimally designed, the additional mass, m_2, can generate an initial force toward the equilibrium position to damp the oscillation of the primary structure m_1. However, the classical TMD suffers a deterioration in vibration control effectiveness when its parameters shift away from the optimal values. Additionally, the added mass often has an overlarge stroke, causing impacts between the added mass and the primary structure, which makes the TMD not applicable for structures with confined space. Therefore, the PTMDs are proposed to address these issues.

Figure 1(c) illustrates the previously proposed PTMD, which can be regarded as a restricted TMD. In the PTMD damping system, the motions of the additional mass m_2 are restrained within a range of two delimiters (as illustrated by the two blue triangles in Figure 1(c)). The delimiters are covered with viscoelastic materials for two purposes: firstly, to dissipate the kinetic energy when m_2 collides with the delimiter and, secondly, to reduce the noise and excessive acceleration induced by the collision. In Figure 1(c), gp_l denotes the gap between the m_2 and the left delimiter, while $gp_r$is the gap of the right side. In the previous PTMD, gp_l equals gp_r. It is reported in much literature that there is an optimal gap for each given loading amplitude and mass ratio. For a severe dynamic excitation and relatively small mass ratio, a large gap shall be provided to allow for enough motion of the added mass, m_2. Otherwise, the energy dissipation during impact will be limited due to a small relative velocity between the added mass and the delimiter. However, if the gap is exceedingly large, the added mass will not impact on the two delimiters. In this case, the PTMD degrades to a spring-mass type dynamic absorber as Frahm invented in the 1900s.

Figure 1(d) shows the proposed APTMD. The major difference between the previous PTMD and the APTMD is that the gp_l and gp_r can be set to different values in the APTMD, which may further improve the vibration control effectiveness of the damper. Three key parameters of the APTMD are gp_l, gp_r, and the frequency ratio of the APTMD over that of the primary structure. These parameters can be optimized using the genetic algorithm in this paper.

2.2. Nonlinear Pounding Force Model. Since the APTMD relies on the poundings between the added mass and the nonsymmetrically designed delimiters to dissipate energy, an accurate pounding force model is necessary to enable numerical study. In previous studies, the nonlinear pounding force model [42] based on the Hertz contact element and a nonlinear damping element has been proved to be relatively accurate and computationally efficient [30]. The mathematical expression of the pounding force is as follows:

$$F = \begin{cases} \beta\delta^{1.5} + c\dot{\delta}, & \dot{\delta} > 0, \\ \beta\delta^{1.5}, & \dot{\delta} < 0, \end{cases} \tag{1}$$

in which F denotes the nonlinear pounding force; δ and $\dot{\delta}$ are the deformation and velocity of deformation, respectively; β is the pounding stiffness; and c is the pounding damping, which can be determined by

$$c = 2\xi\sqrt{\beta\delta^{0.5}\frac{m_1 m_2}{m_1 + m_2}}, \tag{2}$$

where m_1 and m_2 are the two colliding bodies and ξ is the pounding damping ratio:

$$\xi = \frac{9\sqrt{5}}{2}\frac{1 - e^2}{e(e(9\pi - 16) + 16)}, \tag{3}$$

where e is the restitution coefficient of the viscoelastic material. It can be obtained by dropping a sphere on the viscoelastic material, observing the initial height h_0 and rebound height h_1:

$$e = \sqrt{\frac{h_1}{h_0}}. \tag{4}$$

2.3. Governing Equation of APTMD Damping System. Based on the nonlinear pounding force model, the governing equations of a single degree of freedom (DOF) structure equipped with an APTMD are

$$\begin{bmatrix} m_s & \\ & m_d \end{bmatrix}\begin{Bmatrix} \ddot{x}_s \\ \ddot{x}_d \end{Bmatrix} + \begin{bmatrix} c_s & 0 \\ 0 & 0 \end{bmatrix}\begin{Bmatrix} \dot{x}_s \\ \dot{x}_d \end{Bmatrix} + \begin{bmatrix} k_s + k_d & -k_d \\ -k_d & k_d \end{bmatrix}\begin{Bmatrix} x_s \\ x_d \end{Bmatrix} = -\begin{bmatrix} m_s & \\ & m_d \end{bmatrix}\begin{Bmatrix} 1 \\ 1 \end{Bmatrix}\ddot{x}_g + \begin{bmatrix} 1 \\ -1 \end{bmatrix}F_p, \tag{5}$$

where m_s, c_s, and k_s are the mass, damping, and stiffness of the primary structure, respectively; and m_d and k_d are the mass and stiffness of the APTMD. $\ddot{x}_s$, $\dot{x}_s$, and x_s denote the acceleration, velocity, and displacement of the primary structure, while $\ddot{x}_d$, $\dot{x}_d$, and $x_d$correspond to those quantities of the damper. In equation (5), $\ddot{x}_g$is the recorded ground motion and F_p is the pounding force computed by equation (1).

Here, the deformation, δ, and its velocity, $\dot{\delta}$, can be obtained by the relative displacement and velocity:

$$\delta = \begin{cases} x_d - x_s - gp_r, & x_d - x_s - gp_r > 0, \\ |x_d - x_s + gp_l|, & x_d - x_s + gp_l < 0, \\ 0, & \text{otherwise}, \end{cases} \tag{6}$$

$$\dot{\delta} = \dot{x}_d - \dot{x}_s,$$

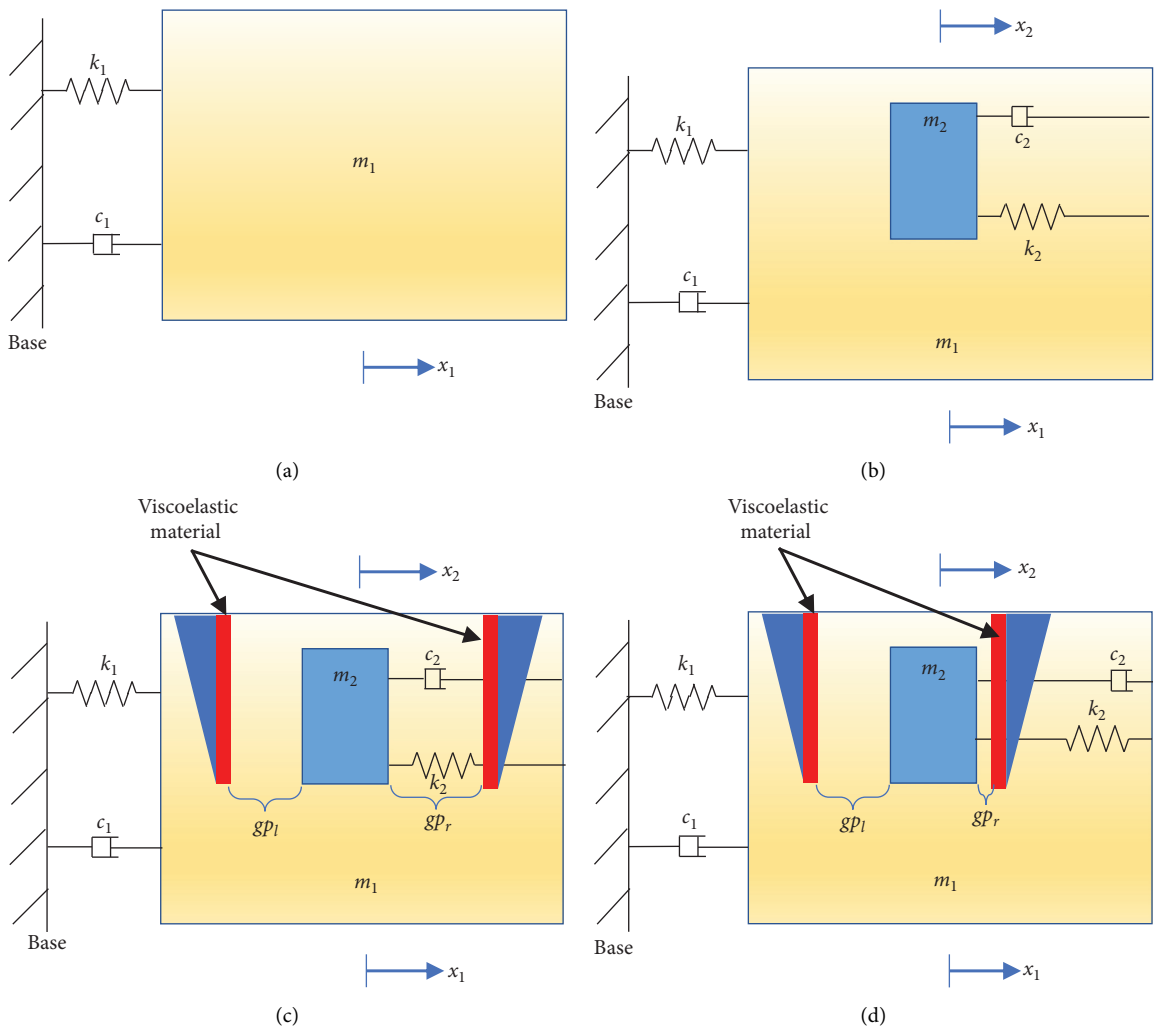

Figure 1: Schematics of the damping system: (a) primary structure without additional damping; (b) TMD damping system; (c) symmetric PTMD damping system; and (d) APTMD damping system.

where gp_l and gp_r are the gap of the left side and right side (as shown in Figure 2). In this equation, $x_d - x_s - gp_r > 0$ implies that collisions occur on the right-side delimiter, while $x_d - x_s + gp_l < 0$ implies that the collisions take place on the left-side delimiter. Otherwise, no collisions happen indicating $\delta = 0$.

Introducing the following mass, damping, and stiffness matrices,

$$M = \begin{bmatrix} m_s & \\ & m_d \end{bmatrix}, \quad C = \begin{bmatrix} c_s & 0 \\ 0 & 0 \end{bmatrix}, \quad K = \begin{bmatrix} k_s + k_d & -k_d \\ -k_d & k_d \end{bmatrix}, \tag{7}$$

and acceleration, velocity, and displacement vector,

$$\ddot{X} = \begin{Bmatrix} \ddot{x}_s \\ \ddot{x}_d \end{Bmatrix}, \quad \dot{X} = \begin{Bmatrix} \dot{x}_s \\ \dot{x}_d \end{Bmatrix}, \quad X = \begin{Bmatrix} x_s \\ x_d \end{Bmatrix}, \tag{8}$$

and vectors indicating the location of the ground motion and pounding force.

$$L_e = \begin{Bmatrix} 1 \\ 1 \end{Bmatrix}, \quad L_p = \begin{Bmatrix} 1 \\ -1 \end{Bmatrix}. \tag{9}$$

Equation (5) can be simplified as

$$M\ddot{X} + C\dot{X} + KX = -M\begin{Bmatrix} 1 \\ 1 \end{Bmatrix}\ddot{x}_g + \begin{bmatrix} 1 \\ -1 \end{bmatrix}F_p. \tag{10}$$

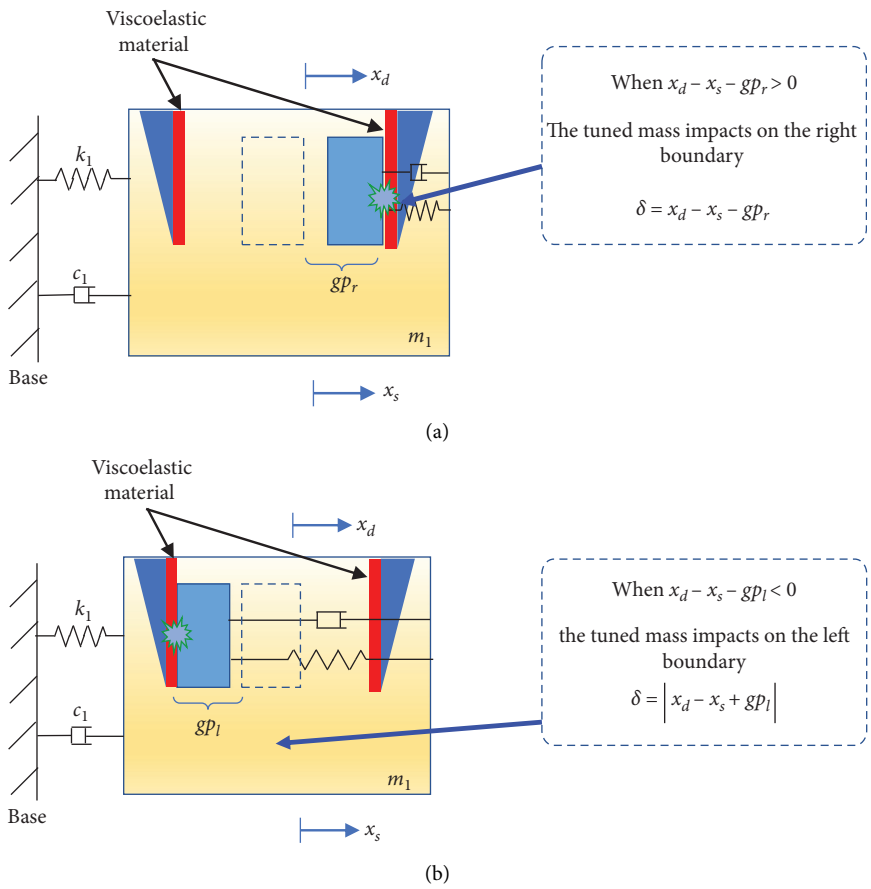

Figure 2: Determination of the impact deformation δ: (a) impacting on the right boundary and (b) impacting the left boundary.

Introducing a state vector Z and the external force vector U, equation (10) can be expressed as

$$Z = AZ + BU, \tag{11}$$

where

$$Z = \begin{Bmatrix} X \\ \dot{X} \end{Bmatrix},$$
$$\dot{Z} = \begin{Bmatrix} \dot{X} \\ \ddot{X} \end{Bmatrix},$$
$$U = \begin{Bmatrix} x_g \\ F_p \end{Bmatrix}, \tag{12}$$
$$A = \begin{bmatrix} 0 & I \\ -M^{-1}K & -M^{-1}C \end{bmatrix},$$
$$B = \begin{bmatrix} 0 & 0 \\ -ML_e & L_p \end{bmatrix}.$$

Equation (11) can be solved using MATLAB/Simulink environment. Figure 3 demonstrates how equation (11) is established in Simulink. The Runge–Kutta method, which is already embedded in Simulink, is employed to solve this equation. Automatic solver selection and default settings of the software were applied.

3. Modelling of the Cable-Stayed Bridge

In order to demonstrate the vibration control effectiveness of the APTMD, a real cable-stayed bridge located in Dalian, Liaoning, China, is selected as the primary structure to be controlled. Figure 4 and 5 illustrate the configuration and appearance of the bridge. As shown in the figures, this bridge is a typical extradosed cable-stayed bridge, with a span of 140 m + 260 m + 140 m and a width of 25 m. The main girder is a continuous box girder with a variable cross section, supported by twin pylon and double-plane fan-type cables. The main pylon is 37.4 m high above the bridge deck. Concretes used for the main girder are C55 type concrete; those for the main pylon and piers are C50 and C40, respectively. The stay cables are made of Φ_s 15.2 type high yield steel strand. Properties of the concretes and cables are listed in Table 1 and 2.

Every table must have a descriptive title and if numerical measurements are given, the units should be included in the column heading. Vertical rules should not be used (see Table 1). Tables should be cited consecutively in the text.

E denotes the elastic modulus of the concrete; μ is Poisson's ratio; G is the shear modulus; f_c is the design value of axial compressive strength; and f_t is the design value of axial tensile strength.

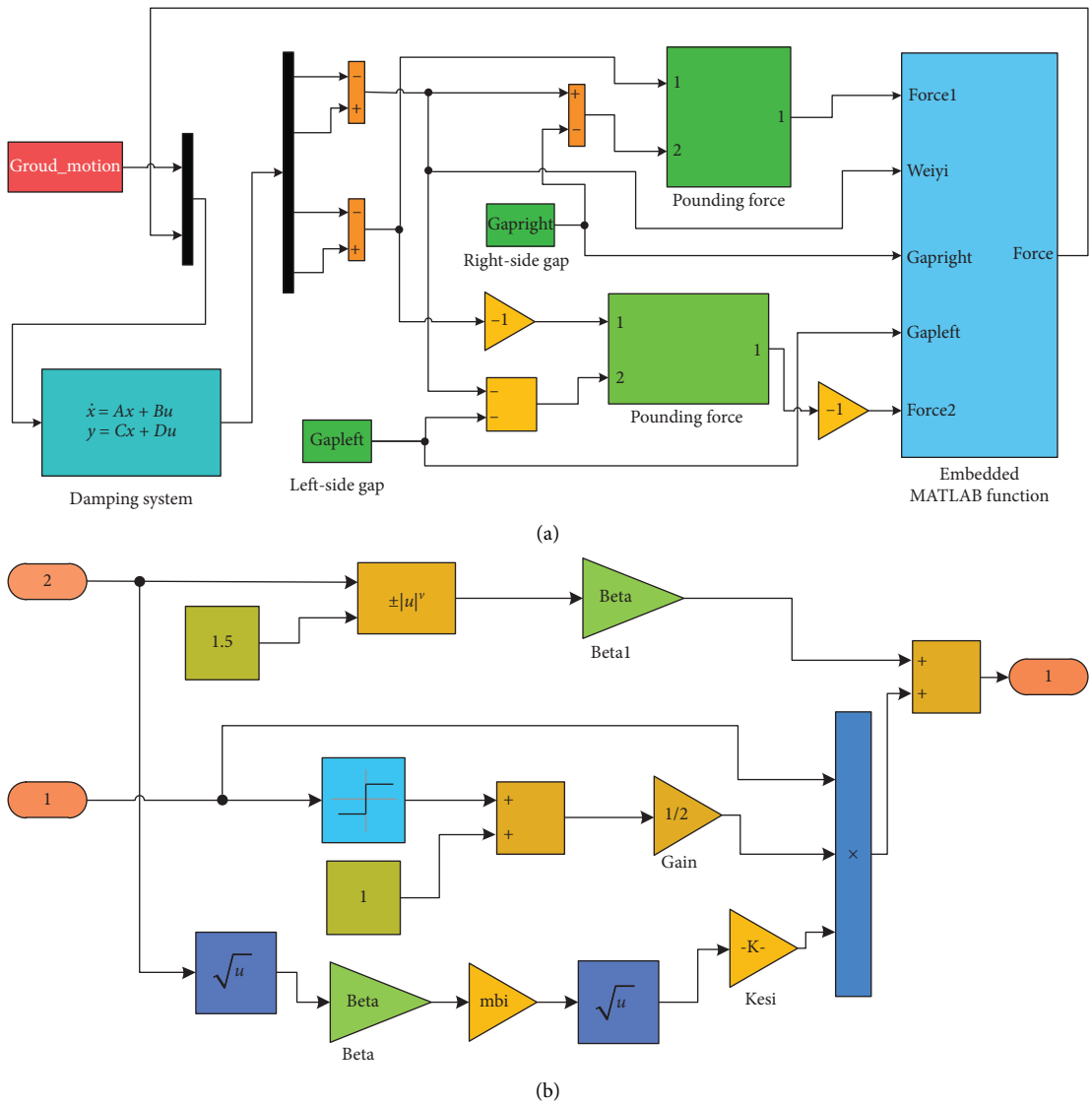

Figure 3: Model of APTMD damping system established in Simulink: (a) SDOF structure controlled by an APTMD and (b) subsystem for calculating the pounding force.

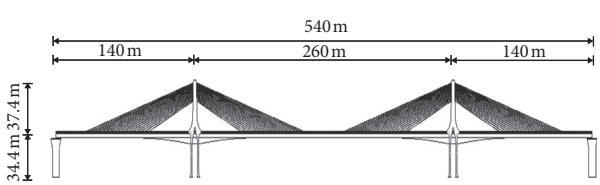

Figure 4: Configuration of Dalian Changshan Bridge.

3.1. FE Model. A finite element model of the bridge is established in ANSYS. The FE model consists of 869 nodes and 639 elements (Figure 6). The main girder, pylons, and piers are modeled using BEAM188 element; the stay cables are modeled by the LINK10 element. Furthermore, the second phase loads, that is, the loads of pavements and other facilities, are modeled by MASS21 elements.

In order to verify the FE model, a modal analysis was conducted using Block Lanczos method. The frequencies of the first 10 orders are listed in Table 3 and the first 3 modal shapes are presented in Figure 7. Compared with the technical report of the bridge, errors of the 1st and 2nd order frequencies are 1.3% and 2%, implying that the FE model can be used for time history analysis.

3.2. Simplified Model. Although the aforementioned nonlinear pounding force model can be simulated in ANSYS software using its APDL module, it is still time-consuming to conduct a time history analysis of the FE model of 5214 DOF. Consequently, a simplified model of the bridge is necessary to enable massive numerical studies and parametric optimization. In this paper, the bridge is represented by a concentrate mass connected to the ground with a spring and a damping element. The stiffness of the spring can be calculated using the FE model. The mass of the simplified model is 7.20×10^{7} kg and the stiffness of the spring is

(a) (b)

Figure 5: On-site photographs of Dalian Changshan Bridge.

Table 1: Properties of prestressed concrete (unit: MPa).

Type	E	μ	G	f_c	f_t
C55	35500	0.2	14200	24.4	1.89
C50	34500	0.2	13800	22.4	1.83
C40	32500	0.2	13000	18.4	1.65

Table 2: Properties of the strand.

Type	Elastic modulus (MPa)	Standard tensile strength (MPa)	Thermal expansion coefficient (°C)
Strand	195 000	1860	1.2×10^{-5}

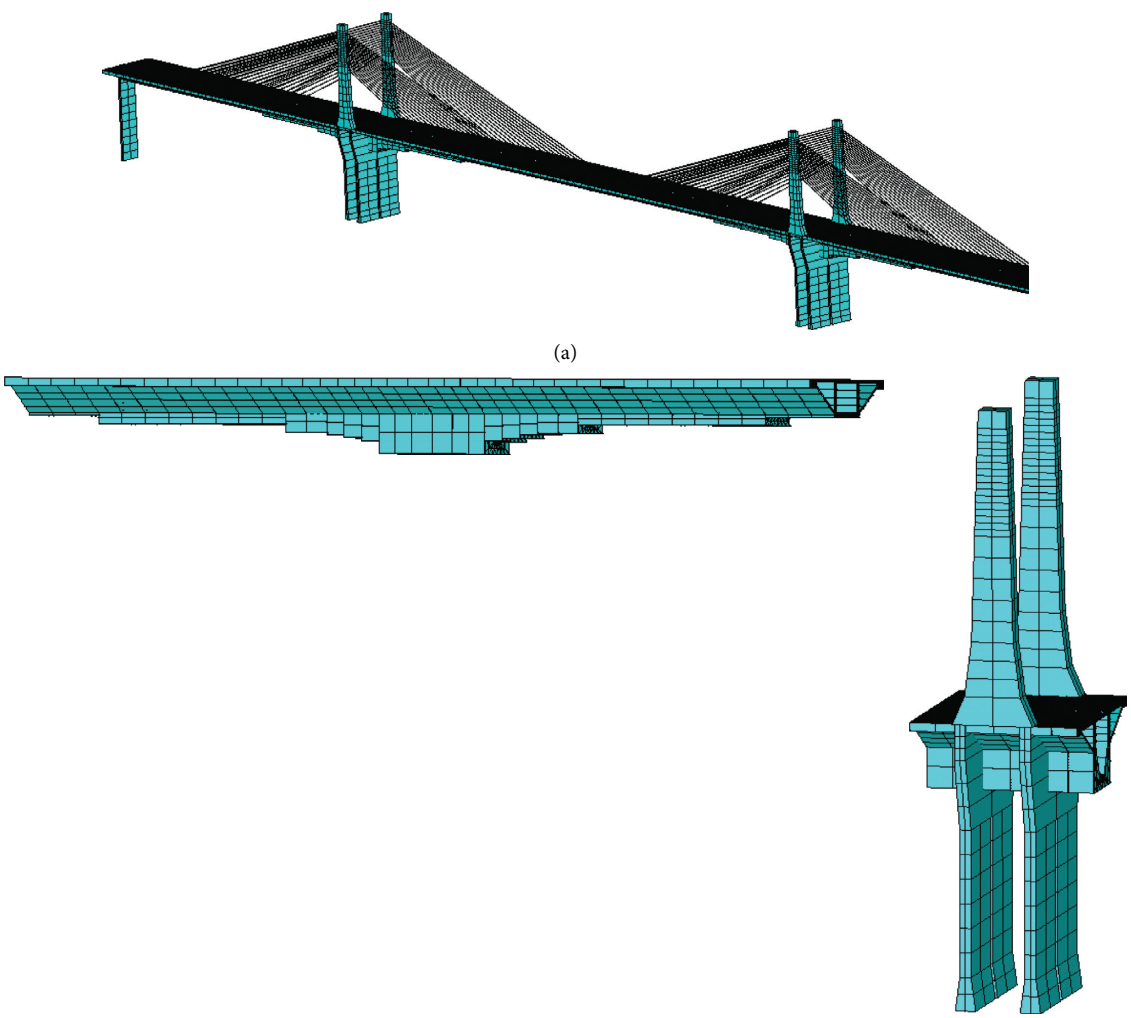

(a)

(b) (c)

Figure 6: FE model of the bridge: (a) the whole bridge; (b) the girder; and (c) the pylon and pier.

Table 3: The first 10 vibration modes of the bridge.

Number of the mode	Frequency (Hz)	Description of modal shape
1st	0.239	Floating of the girder in the longitudinal direction
2nd	0.448	Symmetric bending of the girder in the vertical direction
3rd	0.566	Symmetric bending of the girder in the lateral direction
4th	0.608	Floating of the side piers in the longitudinal direction
5th	0.608	Floating of the side piers in the longitudinal direction
6th	0.654	The tower bends asymmetrically in the lateral direction
7th	0.666	Bending of the girder in the vertical direction (second order)
8th	0.680	Symmetric bending of the girder in the lateral direction (second order)
9th	0.815	Bending of the pylon toward the inside direction
10th	0.815	Bending of the pylon toward the outside direction

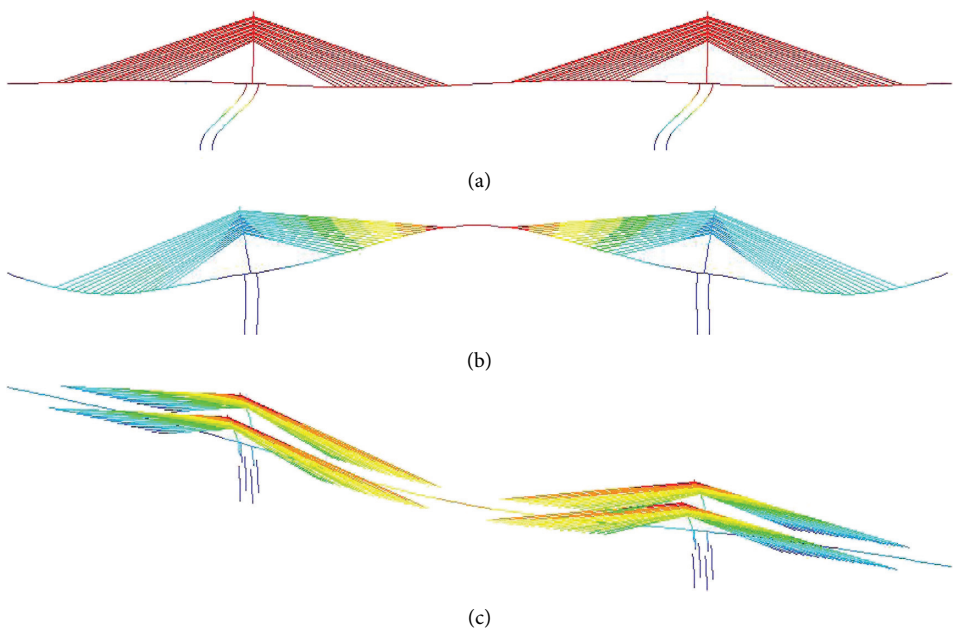

Figure 7: The first 3 modal shapes of the bridge: (a) 1st order; (b) 2nd order; and (c) 3rd order.

1.62×10^8 N/m. Figure 8 shows the displacement response of the simplified model and the FE model subjected to 2 recorded earthquakes. It can be observed that the dynamic responses of the two models are in satisfying agreement.

3.3. Selection of Earthquakes. According to the seismic design code of China [43], three earthquakes are adequate for time history analysis of an infrastructure. In order to fully consider the uncertainties of ground motions, a group of 20 seismic records (as listed in Table 4) are obtained from Pacific Earthquake Engineering Research Center (PEER). Peak accelerations are set to 139 gal, in accordance with the geological report and design manual of the bridge.

4. Optimization of the APTMD with Genetic Algorithm

In order to evaluate the vibration control effectiveness of the proposed APTMD, the vibration reduction ratio is defined as

$$\eta_d = \frac{D_0 - D_{\text{ctrl}}}{D_0}, \tag{13}$$

where D_0 and D_{ctrl} are the average value of the relative displacement of the bridge deck without and with damper and η_d is the vibration reduction ratio of the displacement.

There are three parameters to be determined to achieve the optimal design of the APTMD, that is, the left gap, gp_l, right gap, gp_r, and the frequency ratio, f_d. The genetic algorithm is employed to obtain the optimum values of these parameters. The displacement reduction ratio η_d is defined as the objective function or fitness function of the genetic algorithm. The three parameters gp_l, gp_r, and f_d are the optimal variables. The range of gp_l and gp_r is from 0.005 m to 0.1 m at an interval of 0.005 m. The range of f_d is from 0.5 to 1.5 at an interval of 0.05. Other parameters of the genetic algorithm, such as reproduction coefficient, mutation coefficient, crossover coefficient are set to the default value. The optimal individual of the final population yields the optimum APTMD: $gp_l = 0.03$ m, $gp_r = 0.09$ m, and $f_d = 1$.

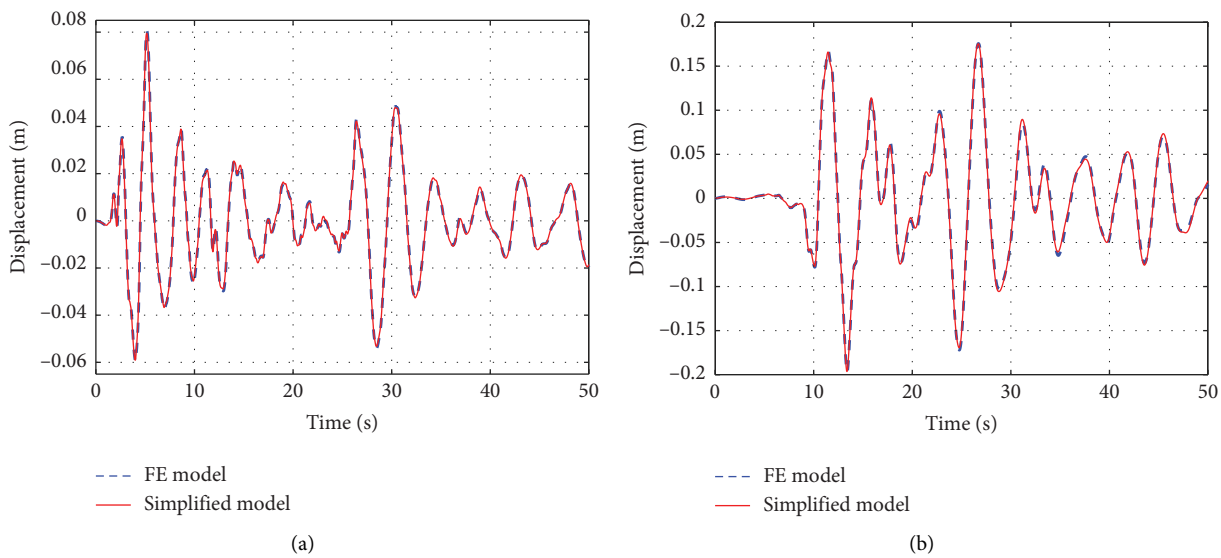

Figure 8: Comparison of dynamic responses computed by the simplified model and FE model: (a) displacement under El Centro earthquake and (b) displacement under Kobe earthquake.

Table 4: Selected ground motions.

Number	Earthquake			Station
	Name	Magnitude	Year	
1	San Fernando	6.6	1971	Pacoima Dam
2	Coyote Lake	5.7	1979	Gilroy Array #6
3	Imperial Valley-06	6.5	1979	El Centro Array #4
4	Imperial Valley-06	6.5	1979	El Centro Array #10
5	Mammoth Lakes-06	5.9	1980	Long Valley Dam
6	Irpinia, Italy-01	6.9	1980	Sturno
7	Morgan Hill	6.2	1984	Gilroy Array #6
8	N. Palm Springs	6.1a	1986	North Palm Springs
9	Whittier Narrows-01	6.0	1987	LB-Orange Ave
10	Loma Prieta	6.4	1989	Gilroy Array #2
11	Loma Prieta	6.4	1989	Saratoga-Aloha Ave
12	Erzincan, Turkey	6.7	1992	Erzincan
13	Landers	7.3	1992	Lucerne
14	Northridge-01	6.7	1994	LA Dam
15	Northridge-01	6.7	1994	Rinaldi Receiving Station
16	Kobe, Japan	6.9	1995	Takarazuka
17	Kobe, Japan	6.9	1995	Takatori
18	Kocaeli, Turkey	7.5	1999	Gebze
19	Chi-Chi, Taiwan	7.6	1999	TCU075
20	Chi-Chi, Taiwan	7.6	1999	TCU076

An optimal PTMD is also designed to compare the vibration control effectiveness. The PTMD has two parameters to be designed, that is, the gap and the frequency ratio. This parameter is optimized by an enumeration algorithm. The value of the gap varies from 0.005 m to 0.1 m at an interval of 0.005 m. The range of f_d is from 0.5 to 1.5 at an interval of 0.05. The optimized gap and frequency ratio are 0.095 m and 1, respectively.

Considering that the TMD, the PTMD, and the APTMD all belong to the dynamic absorber family, these dampers shall be installed at the place where the largest motion occurs to achieve the best vibration control effectiveness. As shown in Figure 7, the largest motion happens at the deck of the bridge. Therefore, the dampers shall be installed inside the hollowed girder, which is spacious to accommodate these dampers.

5. Performance Evaluation of APTMD System

In order to validate the vibration control effectiveness of the APTMD, the seismic responses of the following systems are compared:

(i) Undamped bridge

(ii) Bridge equipped with TMD

(iii) Bridge equipped with symmetric PTMD ($gp = 0.095$ m, $f_d = 1$)

(iv) Bridge equipped with APTMD ($gp_l = 0.03$ m, $gp_r = 0.09$ m, $f_d = 1$)

For these damping systems, the mass ratio μ is all set to 5%, since increasement of mass ratio can slightly improve the vibration control effectiveness, after a certain value (normally 3%), as previous studies revealed [30, 39]. The damping ratio and frequency ratio of the TMD is determined using the following equations [14]:

$$f_{\mathrm{TMD}} = \frac{1}{1+\mu}, \qquad \xi_{\mathrm{TMD}} = \sqrt{\frac{3\mu}{8(1+\mu)}}, \tag{14}$$

in which f_{TMD} and ξ_{TMD} are the frequency ratio and the damping ratio of the TMD. The pounding stiffness β and restitution coefficient e are set to 17259 N/m$^{1.5}$ and 0.2 based on experimental data of a previous study [30].

Figure 9–11 present the seismic response of the bridge under the Kobe earthquake. Due to the length limitation of the paper, the dynamic response corresponding to other ground motions is not plotted. The reduction ratios are listed in Table 5. It can be observed from these figures that all three dampers can effectively suppress the displacement, shear force, and bending moment of the bridge. However, the acceleration response is not satisfyingly reduced. The vibration reduction efficiency of the APTMD is slightly better than TMD and symmetric PTMD.

Considering that the ground motions are with unignorable uncertainties, the bridges are subjected to 20 ground motions and the average vibration reduction ratios are listed in Table 5. This table also demonstrates the effectiveness of the TMD, symmetric PTMD, and APTMD. In terms of the maximum displacement, shear force, and bending moment, the vibration reduction ratios of these three dampers are very close. In terms of the root mean square (RMS) value of these responses, the APTMD is better than the TMD and PTMD.

6. Conclusions

In this paper, a novel damping device, the asymmetric pounding tuned mass damper, is proposed to control the seismic-induced vibrations of a cable-stayed bridge. Compared with traditional symmetric PTMD, the APTMD has unsymmetrical gaps to be designed. A simplified model of the APTMD damping system with sufficient computation efficiency is established to enable optimization. GA is utilized in this paper to search for the optimal gaps and frequency ratio. Finally, time history analysis is conducted on the FE model of the bridge using ANSYS. Based on the numerical results, the following findings can be concluded:

(1) The SDOF model can simulate the behavior of the cable-stayed bridge under earthquakes with satisfying accuracy and efficiency. Computation-intense tasks such as parametric study or optimization can be performed with this model.

(2) The vibrations of the bridge are effectively mitigated by TMD, symmetric PTMD, and APTMD, indicating that impact damping can provide sufficient energy dissipation. Moreover, the impact damping is simple in design, installation, and maintenance, compared with other damping elements such as viscous dampers, SMA dampers, and eddy-current dampers. Therefore, the PTMD and APTMD are very promising for practical applications.

(3) In this paper, the left-side gap, right-side gap, and frequency ratio were selected as the parameters to be designed. These parameters are optimized using GA. The vibration reduction ratio of the optimized APTMD is slightly better than the traditional symmetric PTMD.

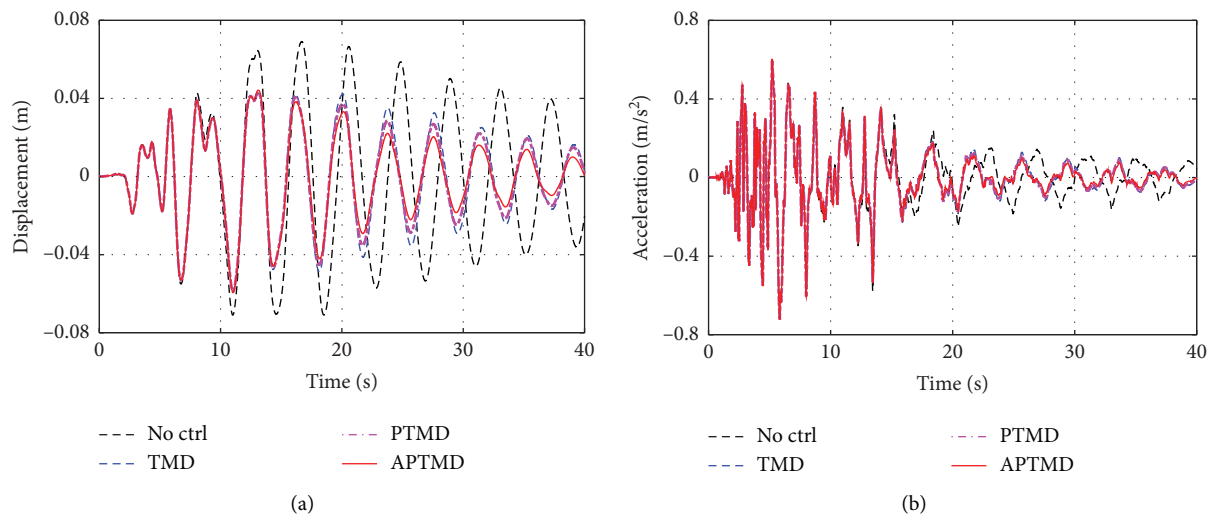

Figure 9: Seismic response at the midspan of the bridge when subjected to Kobe earthquake: (a) displacement and (b) acceleration.

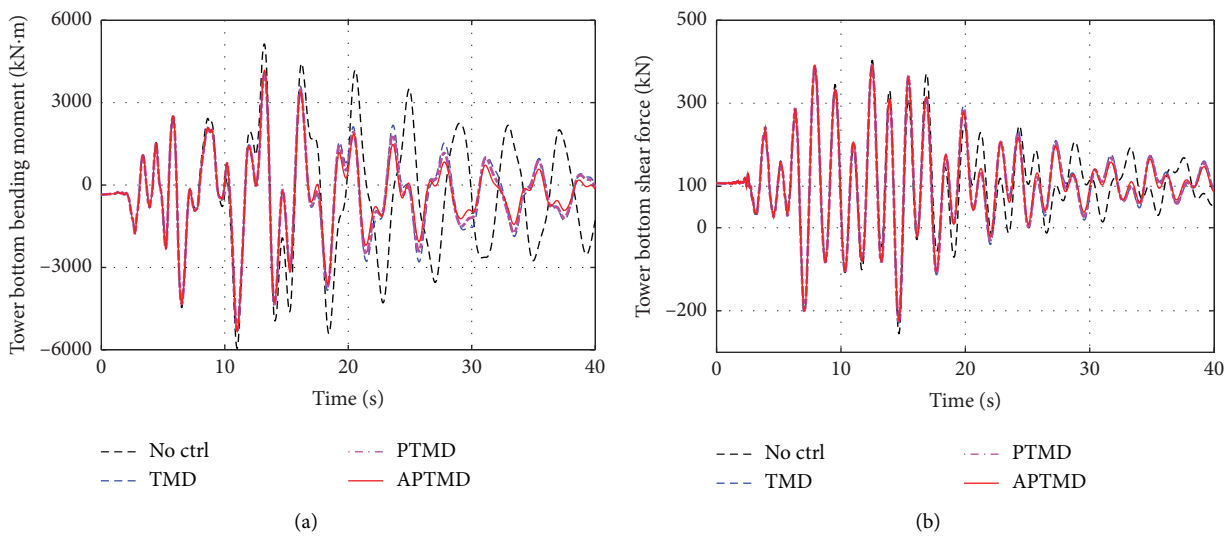

Figure 10: Seismic response at the bottom of the pylon when subjected to Kobe earthquake: (a) bending moment and (b) shear force.

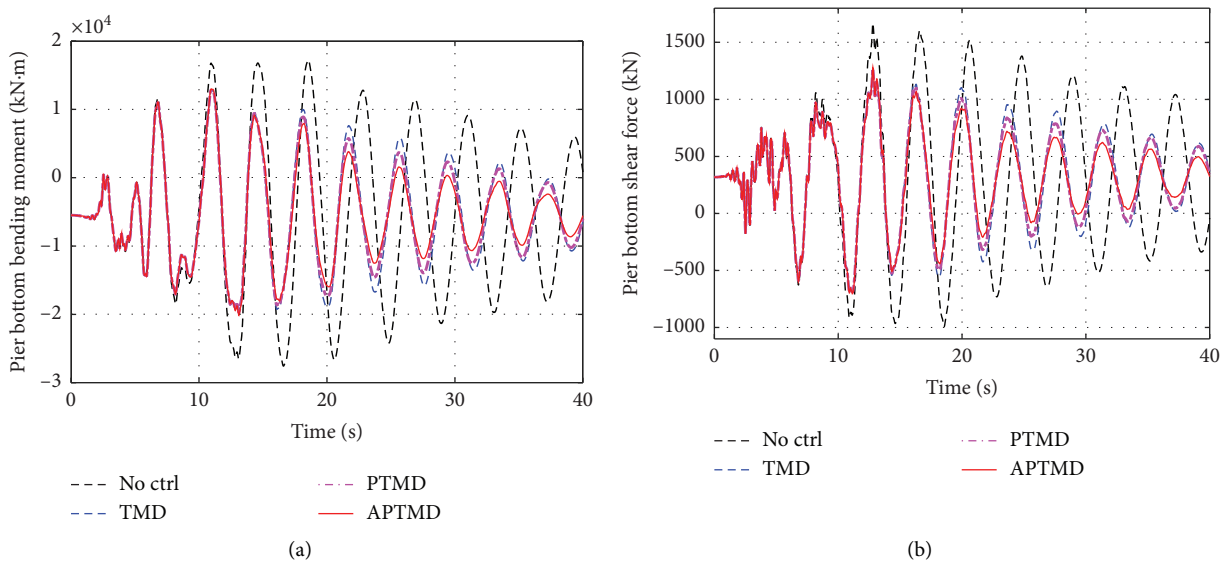

Figure 11: Seismic response at the bottom of the pier when subjected to Kobe earthquake: (a) bending moment and (b) shear force.

Table 5: Vibration reduction ratio of different damping systems.

Structural response	Peak value			R.M.S. value		
	TMD	PTMD	APTMD	TMD	PTMD	APTMD
Midspan displacement	14.70%	15.52%	15.65%	21.13%	27.80%	37.65%
Midspan acceleration	−0.03%	−0.03%	−0.48%	3.89%	4.68%	5.35%
Shear force at pylon bottom	1.51%	1.66%	1.89%	0.86%	1.35%	2.01%
Shear force at pier bottom	20.80%	20.85%	20.52%	21.18%	23.75%	26.77%
Bending moment at pylon bottom	9.52%	9.51%	9.26%	26.20%	28.87%	31.81%
Bending moment at pier bottom	28.29%	28.23%	28.46%	21.42%	24.00%	27.03%
Bending moment at the junction of pier and beam	26.48%	26.46%	26.52%	20.31%	22.69%	25.44%

Data Availability

The data used to support the findings of this study are available from the corresponding author upon request.

Conflicts of Interest

The authors declare that there are no conflicts of interest regarding the publication of this paper.

Acknowledgments

This research was funded by National Natural Science Foundation of China (no. 51808092) and the United Navigation Foundation of Liaoning Province (No. 2020-HYLH-48). The financial supports are gratefully acknowledged.

References

[1] W. Guo, "Seismic performance evaluation of typical piers of China's high-speed railway bridge line using pushover analysis," *Mathematical Problems in Engineering*, vol. 2019, Article ID 9514769, 17 pages, 2019.

[2] X. Liu and Y. Wang, "A novel seismic risk analysis method for structures with both random and convex set mixed variables: case study of a RC bridge," *Mathematical Problems in Engineering*, vol. 2019, Article ID 3613651, 14 pages, 2019.

[3] K. Meng, "A new approach for longitudinal vibration of a large-diameter floating pipe pile in visco-elastic soil considering the three-dimensional wave effects," *Computers and Geotechnics*, vol. 128, Article ID 103840, 2020.

[4] K. Meng, C. Cui, and H. Li, "An ontology framework for pile integrity evaluation based on analytical methodology," *IEEE Access*, vol. 8, pp. 75158–75168, 2020.

[5] Y. Peng and T. Huang, "Sliding implant-magnetic bearing for adaptive seismic mitigation of base-isolated structures," *Structural Control and Health Monitoring*, vol. 26, no. 10, 2019.

[6] Y. Peng, T. Huang, and J. Chen, "Experimental study of seismic isolated structures with sliding implant-magnetic bearings," *Journal of Earthquake Engineering*, vol. 23, pp. 1–32, 2020.

[7] Y. Peng, "Experimental study of sliding hydromagnetic isolators for seismic protection," *Journal of Structural Engineering (United States)*, vol. 145, no. 5, 2019.

[8] W. Zheng, "Parametric study of superelastic-sliding LRB system for seismic response control of continuous bridges," *Journal of Bridge Engineering*, vol. 9, no. 25, 2020.

[9] D. De Domenico, E. Gandelli, and V. Quaglini, "Adaptive isolation system combining low-friction sliding pendulum

bearings and SMA-based gap dampers," *Engineering Structures*, vol. 212, Article ID 110536, 2020.

[10] B. Wang, S. Zhu, and F. Casciati, "Experimental study of novel self-centering seismic base isolators incorporating superelastic shape memory alloys," *Journal of Structural Engineering*, vol. 146, Article ID 040201297, 2020.

[11] W. Zheng, H. Wang, J. Li, and H. Shen, "Performance evaluation of bridges isolated with SMA-based friction pendulum system at low temperatures," *Soil Dynamics and Earthquake Engineering*, vol. 125, Article ID 105734, 2019.

[12] W.-Z. Zheng, H. Wang, J. Li, and H.-J. Shen, "Parametric study of SMA-based friction pendulum system for response control of bridges under near-fault ground motions," *Journal of Earthquake Engineering*, vol. 12, pp. 1–19, 2019.

[13] S. Gur, G. N. Frantziskonis, and S. K. Mishra, "Thermally modulated shape memory alloy friction pendulum (tmSMA-FP) for substantial near-fault earthquake structure protection," *Structural Control and Health Monitoring*, vol. 24, no. 11, p. e2021, 2017.

[14] R. Rana and T. T. Soong, "Parametric study and simplified design of tuned mass dampers," *Engineering Structures*, vol. 20, no. 3, pp. 193–204, 1998.

[15] J. Jiang, S. Ho, N. J. Markle, N. Wang, and G. Song, "Design and control performance of a frictional tuned mass damper with bearing-shaft assemblies," *Journal of Vibration and Control*, vol. 25, no. 12, pp. 1812–1822, 2019.

[16] E. Matta, "A novel bidirectional pendulum tuned mass damper using variable homogeneous friction to achieve amplitude-independent control," *Earthquake Engineering & Structural Dynamics*, vol. 48, no. 6, pp. 653–677, 2019.

[17] S. Liu, "Shaking table test and numerical simulation of eddy-current tuned mass damper for structural seismic control considering soil-structure interaction," *Engineering Structures*, vol. 212, Article ID 110531, 2020.

[18] X. Lu, Q. Zhang, W. Wu, and J. Shan, "Data-driven two-level performance evaluation of eddy-current tuned mass damper for building structures using shaking table and field testing," *Computer-Aided Civil and Infrastructure Engineering*, vol. 34, no. 1, pp. 38–57, 2019.

[19] L. Wang, "Study on adaptive-passive eddy current pendulum tuned mass damper for wind-induced vibration control," *Structural Design of Tall and Special Buildings*, vol. 29, no. 15, 2020.

[20] Z. Wang, "Optimization design and model tests for a pendulum eddy-current tuned mass damper TMD," *Zhendong Yu Chongji/Journal of Vibration and Shock*, vol. 37, no. 9, pp. 1–7, 2018.

[21] H. Gao, H. Wang, J. Li et al., "Optimum design of viscous inerter damper targeting multi-mode vibration mitigation of stay cables," *Engineering Structures*, vol. 226, Article ID 111375, 2021.

[22] R. Ma, K. Bi, and H. Hao, "Heave motion mitigation of semi-submersible platform using inerter-based vibration isolation system (IVIS)," *Engineering Structures*, vol. 219, Article ID 110833, 2020.

[23] H. Zuo, "Influences of ground motion parameters and structural damping on the optimum design of inerter-based tuned mass dampers," *Engineering Structures*, vol. 227, Article ID 111422, 2021.

[24] K. Xu, K. Bi, Q. Han, X. Li, and X. Du, "Using tuned mass damper inerter to mitigate vortex-induced vibration of long-span bridges: analytical study," *Engineering Structures*, vol. 182, pp. 101–111, 2019.

[25] Z. Lu, X. Chen, and Y. Zhou, "An equivalent method for optimization of particle tuned mass damper based on experimental parametric study," *Journal of Sound and Vibration*, vol. 419, pp. 571–584, 2018.

[26] K. Rong and Z. Lu, "An improved esm-fem method for seismic control of particle tuned mass damper in mdof system," *Applied Acoustics*, vol. 172, 2021.

[27] L. Tian, "Seismic response control of transmission tower-line system using SMA-based TMD," *Structural Engineering and Mechanics*, vol. 74, no. 1, pp. 129–143, 2020.

[28] N. D. Tiwari, "A shape memory alloy-tuned mass damper inerter system for passive control of linked-SDOF structural systems under seismic excitation," *Journal of Sound and Vibration*, vol. 494, Article ID 115893, 2021.

[29] M. R. Ghasemi, N. Shabakhty, and M. H. Enferadi, "Vibration control of offshore jacket platforms through shape memory alloy pounding tuned mass damper (SMA-PTMD)," *Ocean Engineering*, vol. 191, Article ID 106348, 2019.

[30] P. Zhang, G. Song, H.-N. Li, and Y.-X. Lin, "Seismic control of power transmission tower using pounding TMD," *Journal of Engineering Mechanics*, vol. 139, no. 10, pp. 1395–1406, 2013.

[31] L. Tian and X. Gai, "Wind-induced vibration control of power transmission tower using pounding tuned mass damper," *Journal of Vibroengineering*, vol. 17, no. 7, pp. 3693–3701, 2015.

[32] W. Lin, "Shaking table test of pounding tuned mass damper (PTMD) on a frame structure under earthquake excitation," *Computers and Concrete*, vol. 20, no. 5, pp. 545–553, 2017.

[33] J. Jiang, "Experimental studies on the effectiveness and robustness of a pounding tuned mass damper for vibration suppression of a submerged cylindrical pipe," *Structural Control and Health Monitoring*, vol. 24, no. 12, p. e2027, 2017.

[34] G. B. Song, "Vibration control of a pipeline structure using pounding tuned mass damper," *Journal of Engineering Mechanics*, vol. 142, no. 6, p. 1, 2016.

[35] X. Yin, G. Song, and Y. Liu, "Vibration suppression of wind/traffic/bridge coupled system using multiple pounding tuned mass dampers (MPTMD)," *Sensors*, vol. 19, no. 5, p. 1133, 2019.

[36] X. Yin, "Suppression of bridge vibration induced by moving vehicles using pounding tuned mass dampers," *Journal of Bridge Engineering*, vol. 23, no. 7, 2018.

[37] W. Wang, X. Wang, X. Hua, G. Song, and Z. Chen, "Vibration control of vortex-induced vibrations of a bridge deck by a single-side pounding tuned mass damper," *Engineering Structures*, vol. 173, pp. 61–75, 2018.

[38] H. Li, "Robustness study of the pounding tuned mass damper for vibration control of subsea jumpers," *Smart Materials and Structures*, vol. 24, Article ID 0950019, 2015.

[39] P. Zhang, "Parametric study of pounding tuned mass damper for subsea jumpers," *Smart Materials and Structures*, vol. 25, no. 1, Article ID 015028, 2015.

[40] W. Wang, "Optimum design of a novel pounding tuned mass damper under harmonic excitation," *Smart Materials and Structures*, vol. 26, 2017.

[41] W. Wang, X. Hua, X. Wang, Z. Chen, and G. Song, "Numerical modeling and experimental study on a novel pounding tuned mass damper," *Journal of Vibration and Control*, vol. 24, no. 17, pp. 4023–4036, 2017.

[42] R. Jankowski, "Non-linear viscoelastic modelling of earthquake-induced structural pounding," *Earthquake Engineering & Structural Dynamics*, vol. 34, no. 6, pp. 595–611, 2005.

[43] Mohurd and Aqsiq, *Code for Seismic Design of Buildings in GB 50011-2010*, China Architecture & Building Press, Beijing, China, 2016.

Hindawi
Mathematical Problems in Engineering
Volume 2020, Article ID 6617976, 14 pages
https://doi.org/10.1155/2020/6617976

Research Article

A Novel Contact Tunnel Profile Monitoring System: Concept and Application

Yang Han,[1,2] Shikun Pu,[1] Lei Gao,[1] Jianli Duan,[1] and Erbing Li[3]

[1]*College of Defense Engineering, Army Engineering University of PLA, Nanjing, Jiangsu 210007, China*
[2]*Nanjing Urban Construction Management Group Co., Ltd., Nanjing, Jiangsu 210006, China*
[3]*College of Field Engineering, Army Engineering University of PLA, Nanjing, Jiangsu 210007, China*

Correspondence should be addressed to Erbing Li; lebingest@126.com

Received 29 October 2020; Revised 13 November 2020; Accepted 12 December 2020; Published 19 December 2020

Academic Editor: Hao Wang

The displacement of the cross section directly reflects the stress state and stability of the surrounding rock and structure, so the monitoring of it is essential during the construction and operation of the tunnel and underground engineering, particularly under the conditions of earthquake and other geological disasters. This paper introduces a new contact tunnel profile monitoring system (TPMS) in detail that uses a tilt sensor and a displacement sensor as data acquisition devices. According to the relation between the sensing physical quantity and displacement change, the displacement calculation formulas of the tunnel cross section measuring points based on the two-dimensional plane coordinate system were deduced, and in order to eliminate the actual installation and positioning deviation of the monitoring system, the method of obtaining the optimal monitoring plane and converting coordinates of the measuring points was proposed, thus establishing the theoretical basis for the application of the TPMS. With the Beishan exploration tunnel (BET) in China as the test platform, the TPMS was successfully applied for long-term monitoring. The application experience showed that the TPMS can realize continuous monitoring, automatic collection and transmission of the monitoring data, remote access whenever necessary, without affecting the transportation in the tunnel, and high accuracy, which reaches 0.01 mm. This system provides a new simple and effective method with good generality and applicability for the deformation monitoring of the tunnel and underground engineering.

1. Introduction

During the construction and operation of the tunnel and underground engineering, it is crucial to guarantee the safety and stability of the surrounding rock and structure. The convergence displacement of the surrounding rock directly reflects the stability of a rock mass after excavation [1, 2] and also provides support for the inversion of the rock mechanics parameters and the determination of a reasonable support time. Therefore, convergence displacement monitoring of the surrounding rock and structure is an essential item for underground engineering deformation monitoring, and the applicability of monitoring methods and systems is of vital importance to guaranteeing safety during tunnel and underground engineering construction and operation.

At present, the monitoring methods for the convergence displacement of the surrounding rock are mainly divided into two categories: noncontact and contact monitoring. Noncontact monitoring methods mainly include the automatic tracking total station measurement method, three-dimensional (3D) laser scanning, and close-range photography [3–9]. The above researchers have conducted many studies with respect to the monitoring principle, the feasibility of monitoring, and the proposal of monitoring programs [10, 11]. The advantages of the total station method are the high measurement accuracy and low light requirements during the measurement process; however, this method is easily affected by the dust generated in the construction process, and the layout of the total station in the full-length of the tunnel is relatively

expensive. The advantages of 3D scanning are fast measurement speed, complete and accurate measurement data, and low light requirements for the test environment, but the registration, denoising, splicing of the point cloud data obtained, and slice after 3D modeling still have errors and reliability issues. The advantage of close-range photography is that the measurement is convenient and fast, but the measurement accuracy is greatly affected by the lighting condition. Specifically, the light source cannot work when light is limited, so an artificial light source should be used as a supplement. The above noncontact measurement methods are mainly based on optical principles, and its measurement accuracy can only reach the millimeter level. For real-time monitoring in long-term health diagnosis [12], the system equipment needs to be fixed near the center of the tunnel section, which will affect normal operation.

Contact monitoring methods that are used to measure the convergence displacement mainly include a convergence meter and a convergence measurement system [13–16]. The convergence meter is a measurement instrument specially used to monitor the distance change (i.e., convergence value) between any two points on the wall of the tunnel or other engineering surrounding rock. This instrument has a digital display and vibrating-wire convergence meter and is widely used to measure the convergence deformation of tunnels and underground engineering. The Bassett convergence system (BCS) is a representative convergence measurement system that uses a tilt sensor and a long and short arm structure to transfer the displacement between measuring points in order to obtain the relative displacement between these points. With the development of optical fiber technology, in recent years, some scholars have used a fiber Bragg grating for convergence displacement contact measurements [17, 18]. Among them, the convergence meter has now realized automatic measurements with an accuracy reaching 0.01 mm, but there are some problems, such as the large interference effects in the construction and operation of the project. The BCS has high precision and automation, but it is fixed and not suitable for large-scale layouts because of high cost. As a new method for measuring the convergence displacement of surrounding rock, fiber Bragg gratings are not yet mature, with some issues, such as difficult laying and obvious influence of temperature change.

In terms of the disadvantages of the methods mentioned above, a new-type contact tunnel profile monitoring system (TPMS) was developed to monitor the long-term deformation and performance of the tunnel surrounding rock and structure. The operating principle of this monitoring system is similar to that of the BCS; that is, it can realize the automation and continuity of the measurement process. Additionally, this system is simple in structure, relatively cheap, suitable for different sections, and reusable.

2. Basic Principles of the TPMS

2.1. Composition of the TPMS. The TPMS is composed of a series of linked arms that are fixed to the tunnel wall. Each arm is fitted with a high-accuracy displacement sensor and precision tilt sensor to monitor the deformation, and a data logging system is available to automatically collect the real-time displacement and transmit it to a computer. A typical measurement unit of the TPMS is shown in Figure 1, including the sensor, rod end, extension tube, and fixed anchor. The length of the measuring arm between two adjacent measuring points can be adjusted on the spot using extension tubes. As an independent working part, the number of TPMS measurement units can be increased and decreased according to the size of the tunnel section and the number of measuring points. The TPMS can be applied to various section forms and can be set up on unsupported bare rock. In addition, the system can be modularly assembled. After the measurement unit is disassembled, it can be reused in many cases except for the fixed anchor.

The sensors of the TPMS include a tilt sensor and a displacement sensor (Figure 2). The tilt sensor is a capacitive sensor, the displacement sensor is a resistive sensor, and the main specifications of the tilt and displacement sensors are shown in Table 1. Both of these sensors produce a signal that can be converted to a change in the microvoltage according to the change in the physical quantity of the sensor. The data logging system of the TPMS is composed of a data collector and data processing software. The data collector model is CR800 produced by Campbell Scientific company, which is a research-level data collector characterized by low cost, small size, and different channels (Figure 3). When TPMS monitoring is conducted, the transducer transfers signals to the data collector, which is connected to the remote-control computer using an RS-232 communication mode. Using the measurement and control software, automatic real-time monitoring can be realized.

As shown in Figure 4, the TPMS is available in either an open or closed loop structure around the inside of the tunnel. Compared with a closed loop structure, an open loop structure omits the linked measuring arm AH. The closed loop structure is analogous to that of conventional closed end survey techniques, while the open loop structure must be referenced to a reference point. Variations from the relative displacements between adjacent measuring points are measured, and after they are transmitted to the reference point, the displacement variations at each measuring point relative to the reference point can be obtained.

2.2. Calculation Principle for the TPMS. A position change between adjacent measuring points will cause the length and angle of the measuring arm to change. Through the displacement and tilt sensors, the change in the length and angle can be obtained, giving the relative displacement between the measuring points. With any measuring point on the monitoring section taken as a reference point, the relative displacement of each measuring point relative to the reference point can be obtained through recursion. Generally, the engineering datum point is located in a region with stable deformation, and it is believed that the displacement caused by that is negligible. The relative displacements of the two measuring points are obtained by the sensor variation values between the two measuring points, and the absolute displacement of each measuring point

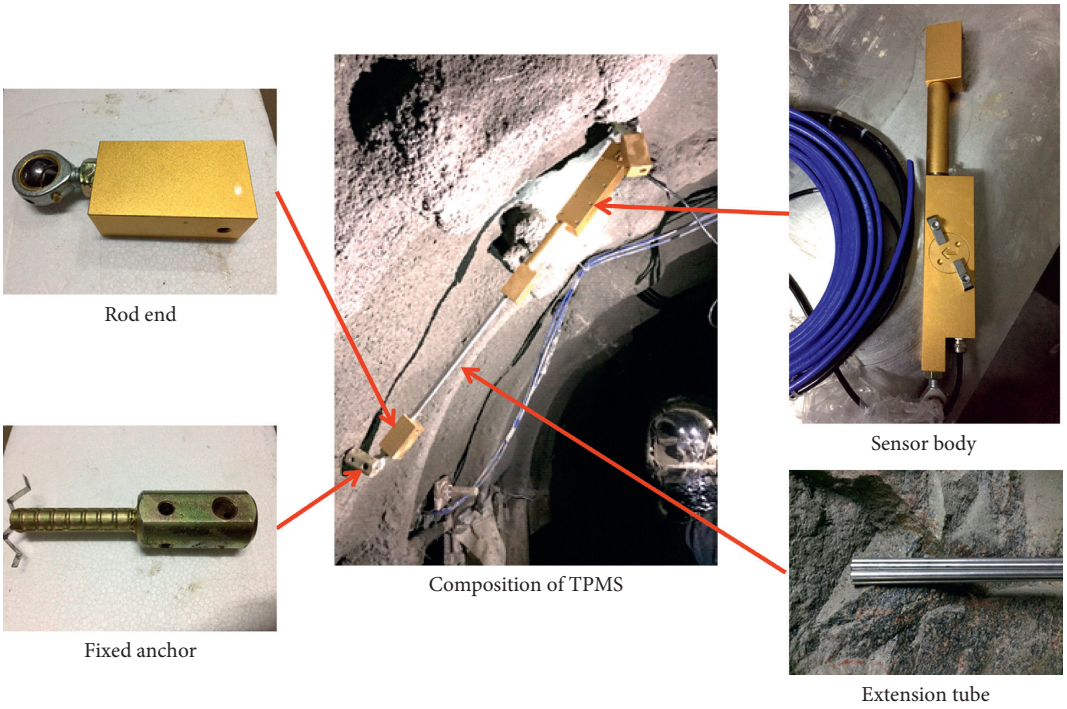

Figure 1: Typical measurement unit of the TPMS.

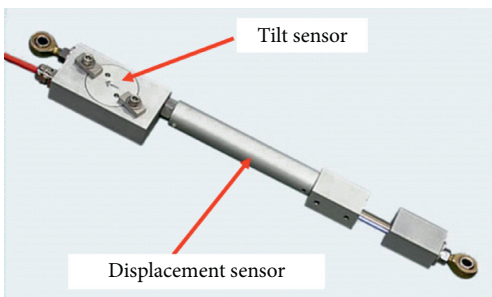

Figure 2: Composition of the TPMS sensor.

Table 1: Main technical specifications of TPMS sensors.

Specification	Tilt sensor	Displacement sensor
Manufacturer	VI Tec (USA)	Honeywell (USA)
Sensor model	MEMS(micro-electro-mechanical systems)	MLT-38000101
Range	±5°	0~50 mm
Accuracy	0.003°	0.01 mm
Input voltage	5.5~15 Vdc	5.5~15 Vdc
Output voltage	±2.5 Vdc	±2.5 Vdc
Operating temperature	−40~+85°C	−40~+80°C

relative to the engineering datum point is obtained via calculation.

It is assumed that the measuring points are serially numbered to 0, 1, 2, . . ., n starting from the reference point. Under the global coordinate system for the monitoring plane, the initial coordinate for each measuring point is $(x_{0,0}^G, y_{0,0}^G)$, $(x_{1,0}^G, y_{1,0}^G)$, $(x_{2,0}^G, y_{2,0}^G)$, . . ., $(x_{i,j}^G, y_{i,j}^G)$, $i, j = 0, 1, 2, \ldots, n$ (Figure 5). Superscript G on the coordinates denotes the global coordinate system; the first subscript i denotes the serial number of the measuring points; the second subscript j denotes the measurement times; and 0 denotes the initial position of measuring points. In the local coordinate system of adjacent measuring points, the initial coordinate of each measuring point is $(x_{0,0}^L, y_{0,0}^L)$, $(x_{1,0}^L, y_{1,0}^L)$, $(x_{2,0}^L, y_{2,0}^L)$, . . ., $(x_{i,j}^L, y_{i,j}^L)$, $i, j = 0, 1, 2, \ldots, n$. The superscript L on the coordinates denotes the local coordinate system, and the

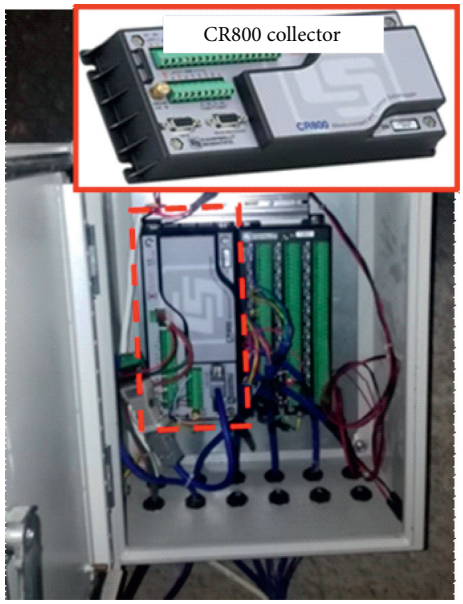

Figure 3: Data collection box.

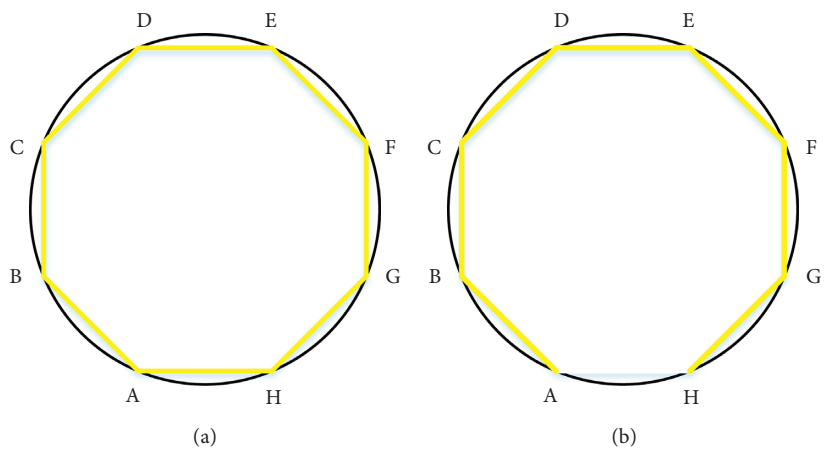

Figure 4: Schematic diagram of the TPMS monitoring configurations: (a) closed loop structure; (b) open loop structure.

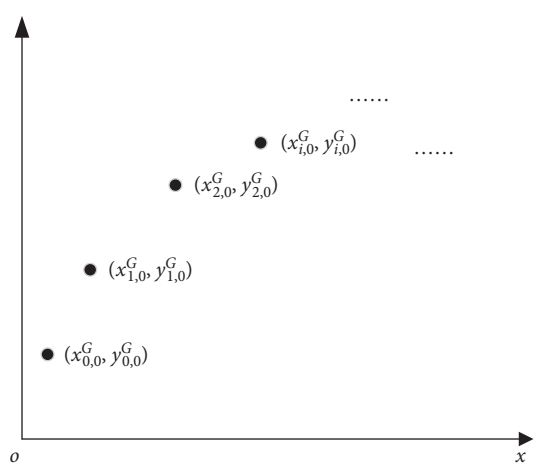

Figure 5: Initial coordinates of each measuring point in the global coordinate system.

subscripts are the same as above. The main symbols and their basic meanings in the text are shown in abbrevations section.

To analyze the relative displacement between adjacent measuring points, a random measuring point $i-1$ is taken to build a local coordinate system relative to the measuring point i (Figure 6). During the actual measurement, the measuring points $i-1$ and i both move, so the relative position of the measuring arm at any time can be obtained by translating the measuring arm between two points with the initial position of point $i-1$ as the origin point. In Figure 6, the initial length of the measuring arm between point i and point $i-1$ is L_i, the rotation angle of the measuring arm is $\Delta\theta_{ij}$, and the length variation is ΔL_{ij} during the jth measurement.

Initial local coordinate for measuring point i is as follows:

$$\left.\begin{aligned} x_{i,0}^{L} &= x_{i,0}^{G} - x_{i-1,0}^{G} \\ y_{i,0}^{L} &= y_{i,0}^{G} - y_{i-1,0}^{G} \end{aligned}\right\}. \tag{1}$$

The initial length of the measuring arm is

$$L_i = \sqrt{\left(x_{i,0}^{L}\right)^2 + \left(y_{i,0}^{L}\right)^2}. \tag{2}$$

Horizontal and vertical coordinates for the point with the length equal to the initial length on the measuring bar under $i-1$ local coordinates are as follows:

$$\left.\begin{aligned} x_{i,j}^{R} &= x_{i,0}^{L}\cos\Delta\theta_{ij} + y_{i,0}^{L}\sin\Delta\theta_{ij} \\ y_{i,j}^{R} &= -x_{i,0}^{L}\sin\Delta\theta_{ij} + y_{i,0}^{L}\cos\Delta\theta_{ij} \end{aligned}\right\}. \tag{3}$$

Thus, according to the geometrical relationship between the elongation ΔL_{ij} of the measuring bar arm and the initial measuring arm length L_i, the horizontal and vertical coordinates for measuring point i during the jth measurement under a local coordinate system for $i-1$ are as follows:

$$\left.\begin{aligned} x_{i,j}^{L} &= \frac{L_i + \Delta L_{ij}}{L_i} x_{i,j}^{R} \\ y_{i,j}^{L} &= \frac{L_i + \Delta L_{ij}}{L_i} y_{i,j}^{R} \end{aligned}\right\}. \tag{4}$$

The global coordinate for measuring point i during the jth measurement is

$$\left.\begin{aligned} x_{i,j}^{G} &= \frac{L_i + \Delta L_{ij}}{L_i}\left(x_{i,j}^{L}\cos\Delta\theta_{ij} + y_{i,j}^{L}\sin\Delta\theta_{ij}\right) + x_{i-1,j}^{G} \\ y_{i,j}^{G} &= \frac{L_i + \Delta L_{ij}}{L_i}\left(-x_{i,j}^{L}\sin\Delta\theta_{ij} + y_{i,j}^{L}\cos\Delta\theta_{ij}\right) + y_{i-1,j}^{G} \end{aligned}\right\}. \tag{5}$$

By taking $i = 1$, the coordinates of measuring point 1 relative to reference point 0 in the jth measurement can be obtained:

$$\left.\begin{aligned} x_{1,j}^{G} &= x_{1,j}^{L} + x_{0,j}^{G} \\ y_{1,j}^{G} &= y_{1,j}^{L} + y_{0,j}^{G} \end{aligned}\right\}. \tag{6}$$

When constructing the global coordinate system in the measurement section, it is often considered that the reference point does not move; that is, $x_{0,0}^{G} = x_{0,1}^{G} = \ldots = x_{0,j}^{G}$ and $y_{0,0}^{G} = y_{0,1}^{G} = \ldots = y_{0,j}^{G}$. Therefore, the global coordinates of each measuring point in the jth measurement can be obtained by recurrence from measuring point 1.

The displacement is generated by subtracting the corresponding initial global coordinates from the global coordinates obtained by each measurement:

$$\left.\begin{aligned} \Delta x_{i,j} &= x_{i,j}^{G} - x_{i,0}^{G} \\ \Delta y_{i,j} &= y_{i,j}^{G} - y_{i,0}^{G} \end{aligned}\right\}. \tag{7}$$

Thus far, the corresponding displacement changes in each measuring point can be calculated by the initial global coordinates and the variation in the measuring arm obtained by the tilt and displacement sensors.

2.3. Calculation of the Variation in the Rotation Angle and Length of the Measuring Arm. The data logging system converts the changes in the sensor angle and displacement into electrical signals, and the conversion of the angle and displacement to an output voltage is as follows.

There is a polynomial relationship between the inclination of the tilt sensor and the output voltage as follows:

$$\theta = C_0 + C_1 V_t + C_2 V_t^2 + C_3 V_t^3 + C_4 V_t^4 + C_5 V_t^5, \tag{8}$$

where θ is the inclination of the tilt sensor; V_t is the output voltage of the tilt sensor; and $C_0, C_1, \ldots, C_5$ are calibration constants for the tilt sensor.

The displacement measured by the displacement sensor has a linear relationship with its output voltage:

$$L = K_d V_d + b, \tag{9}$$

where L is the displacement of the displacement sensor, V_d is the output voltage of the displacement sensor, and K_d and b are calibration constants for the displacement sensor.

After the TPMS is installed, the initial measurement is carried out to record the initial output voltages (V_t^0 and V_d^0) of the tilt and displacement sensors for each measuring arm. Then, the initial values of inclination (θ_0) and displacement (L_0) are obtained according to equations (8) and (9), respectively.

After the TPMS works normally, the change in the rotation angle and length of the corresponding measuring arm can be obtained by subtracting the initial values of the inclination and displacement measured by the tilt and displacement sensors:

$$\left.\begin{aligned} \Delta\theta &= \theta - \theta_0 \\ \Delta L &= L - L_0 \end{aligned}\right\}. \tag{10}$$

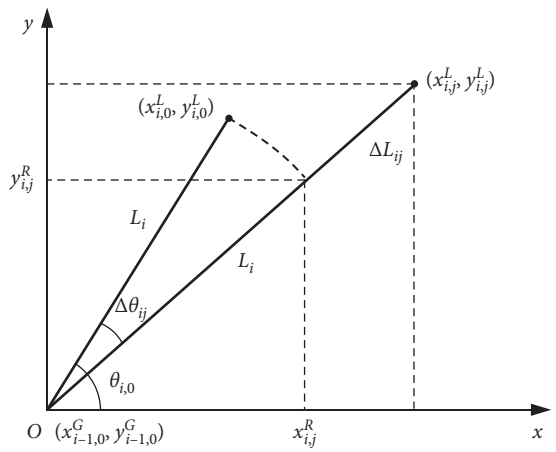

Figure 6: Local coordinate system between adjacent measuring points.

2.4. Optimization of the Monitoring Plane and 2D Coordinate Transformation. After TPMS installation, the initial coordinate for each measuring point measured using a total station is a 3D space coordinate under a geodetic coordinate system, which requires transformation into planar two-dimensional (2D) coordinates for monitoring the section. When fixed anchor measuring points are used, it is difficult to keep all fixed anchors in the same plane, which introduces the problem of how to determine the optimal monitoring plane.

During actual monitoring, the monitoring plane should be perpendicular to the horizontal plane. Thus, the positional relationships between the initial 3D space coordinates (X_i, Y_i, Z_i) $(i = 0, 1, \ldots, n)$ of each measuring point and optimal monitoring plane Ω are as follows (Figure 7).

Suppose the equation of the plane for the optimal monitoring plane is as follows:

$$F(X, Y, Z)_\Omega = 0. \tag{11}$$

Because the optimal monitoring plane is parallel to the Z-axis of the geodetic coordinate system, equation (11) can be expressed as

$$a_0 + a_1 X + a_2 Y = 0, \tag{12}$$

where a_0, a_1, and a_2 are all plane equation parameters.

With the minimum sum of the distance from each measuring point to the plane, the optimized objective function is established as

$$\min f(X, Y, Z) = \sum_{i=0}^{n} d_i = \sum_{i=0}^{n} \frac{\left|a_0 + a_1 X_i + a_2 Y_i\right|}{\sqrt{a_1^2 + a_2^2}}, \tag{13}$$

where $f(X, Y, Z)$ is the objective function and d_i is the distance between measuring point i and the optimal monitoring plane.

After the optimal monitoring plane is determined using the computing method above, the 3D spatial coordinates for measuring points need to be transformed into a 2D coordinate in the plane. The optimal monitoring plane is perpendicular to the horizontal plane (Figure 7). The Y-axis of the established 2D coordinate system is parallel to the Z-axis of the geodetic coordinate system. When the transformation of the X-axis and Y-axis coordinates for each measuring point is conducted, the points can be investigated in the XOY planes of the geodetic coordinate system (Figure 8).

The projection point of the reference point (X_0, Y_0, Z_0) in the optimal monitoring plane is taken as the origin of the 2D coordinate system; thus, the 3D coordinate for the projection point (X_0^T, Y_0^T, Z_0^T) can be obtained using the following equation:

$$\left.\begin{aligned} & a_0 + a_1 X_0^T + a_2 Y_0^T = 0 \\ & \frac{X_0 - X_0^T}{a_1} = \frac{Y_0 - Y_0^T}{a_2} \\ & Z_0^T = Z_0 \end{aligned}\right\}. \tag{14}$$

According to the space vector method, the 2D coordinate for the projection point of any measuring point in the optimal monitoring plane is

$$\left.\begin{aligned} & x_{i,0}^G = \frac{-a_2\left(X_i - X_0^T\right) + a_1\left(Y_i - Y_0^T\right)}{\sqrt{a_1^2 + a_2^2}} \\ & y_{i,0}^G = Z_i - Z_0^T \end{aligned}\right\}. \tag{15}$$

3. Practical Application of the TPMS

3.1. Engineering Background. The new contact TPMS was successfully used in the Beishan exploration tunnel (BET). Figure 9 shows photographs of the entrance and the internal tunnel of the BET. The BET was constructed as a small pilot underground facility for the proposed underground research laboratory of the geological disposal of high-level radioactive waste in China.

The BET is located in the Jiujing site of the Beishan area, which is located approximately 80 km northwest of Yumen City, Gansu Province, PR China. As shown in Figure 10, the BET is mainly composed of 5 parts: a ramp (with a slope of 20°, a vertical depth of 50 m, a length of 146.19 m, a height of 2.64 m, and a width of 2.8 m), a horizontal tunnel (with an L shape, a length of 110 m, a height of 3.0 m, and a width of 2.8 m), underground test chambers (with a total length of approximately 90 m, a height of 3.033 m, and a width of 4.0 m), a water sump, and a ventilation shaft [19, 20].

The surrounding rock of the BET is mainly granite with good integrity, except for the Shiyuejing Fault, and the rock of the BET is a typical hard rock with a uniaxial compressive strength above 190 MPa [20]. The main unfavorable geology of the BET is the Shiyuejing Fault, which has an inclination of approximately 70–80°. The rocks in the fault zone are strongly fractured, with the various well-developed dikes.

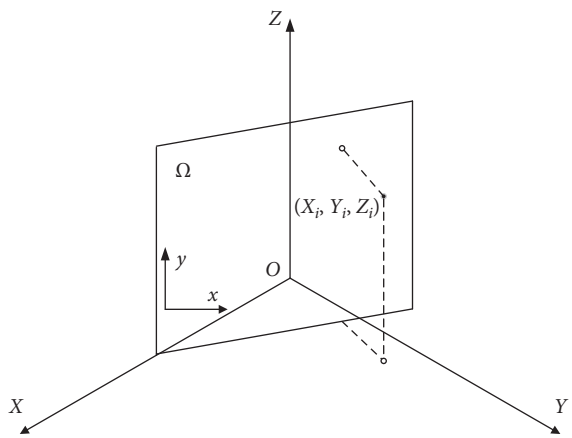

Figure 7: Relationships between global coordinate of measuring points and the optimal monitoring plane.

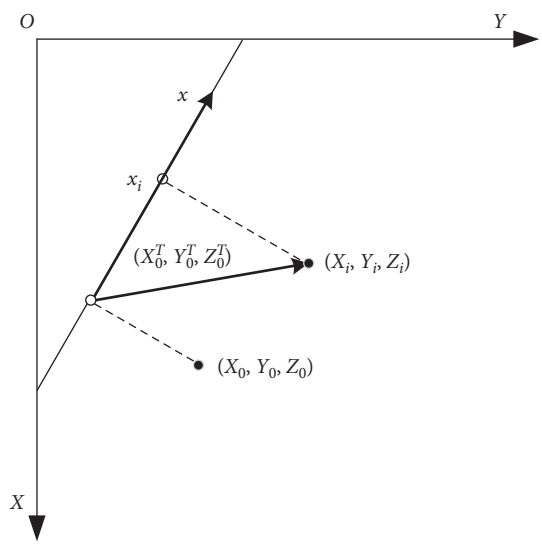

Figure 8: Projection plane of global coordinates and the optimal monitoring plane.

(a) (b)

Figure 9: Photographs of the entrance and internal tunnel of the BET.

The BET was excavated by full-face smooth blasting, and it took 18 months to complete the excavation. To obtain the peripheral displacement of the BET surrounding rock, the TPMS was adopted immediately after excavation.

3.2. In Situ Measurement Scheme. The measuring section of the TPMS was set in the supporting test area of the BET, which is located in the Shiyuejing Fault zone (Figure 11). Before excavation, advanced pipe shed support in the arch

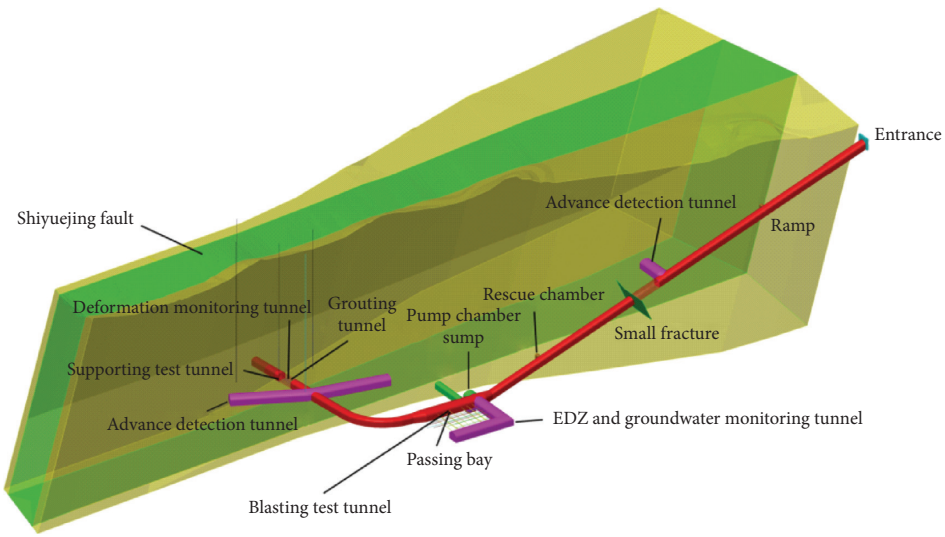

Figure 10: Spatial structure of the BET [19].

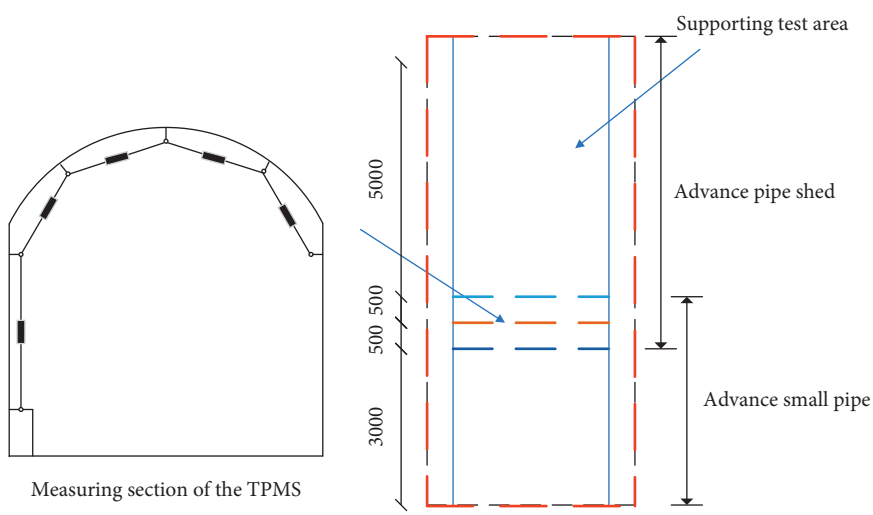

Figure 11: Schematic diagram of measuring section location (unit: mm).

top was conducted for this area, with the length set as 6 m. After the pipe shed section was tunneled 5 m, 4 m of the advanced small pipe support in the arch top was set up forward. When the advanced small pipe support was completed, tunneling stopped after 3 m of forward construction. Afterwards, the mesh shotcrete and the steel arch supports were installed with an arch spacing of 0.5 m. After the shotcrete was completed, the TPMS was installed, and the TPMS was located at the junction between the advance pipe shed and the advance small pipe, where the support was relatively weak.

As shown in Figure 12, the chamber span was 4.0 m, the height of the arch apex was 3.0 m, and the straight-wall section had a three-centered arch shape. There were 6 measuring points arranged in the measuring section with an open loop system. Except for measuring point 0, which was set on the ground as a reference point, the other 5 measuring points were all arranged on the arch, with measuring point 3 at the apex of the arch, points 1 and 5 in the arch foot, and points 2 and 4 located on the hance.

3.3. Section Optimization and Coordinate Transformation. According to the optimization and transformation method described in Section 2.4, the optimal plane corresponding to each measuring point of the in situ monitoring test is solved, and the initial 2D coordinates of each point are established.

By total station measurements, the initial 3D coordinates in the geodetic coordinate system of each measuring point in the field test are shown in Table 2. As shown in Table 2, the numerical values of the measuring points in 3D geodetic coordinates are all relatively great, and numerical overflow may occur during optimization. However, the origin position of the geodetic coordinate system does not affect the obtainment of the optimal plane and coordinate transformation. Therefore, the geodetic coordinate system origin is

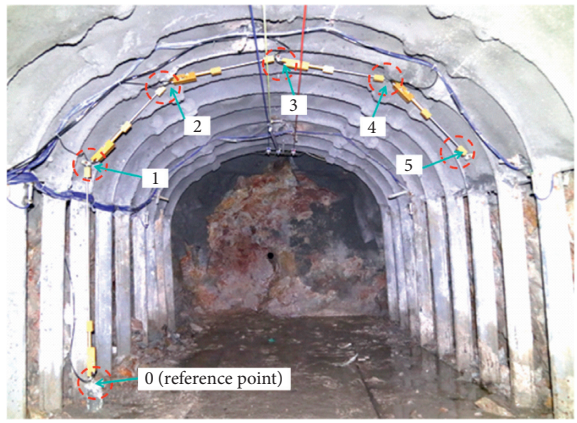

Figure 12: Distribution of measuring points.

Table 2: Initial 3D coordinates of TPMS measuring points.

Measuring point	X (m)	Y (m)	Z (m)	X_d (m)	Y_d (m)	Z_d (m)
0	4524349.584	360613.163	1606.893	1.584	3.163	0.893
1	4524349.582	360613.173	1608.374	1.582	3.173	2.374
2	4524349.399	360612.651	1608.933	1.399	2.651	2.933
3	4524349.137	360611.909	1609.084	1.137	1.909	3.084
4	4524348.889	360611.183	1608.920	0.889	1.183	2.920
5	4524348.688	360610.693	1608.309	0.688	0.693	2.309

translated to point (4524348, 360610, 1606), and the corresponding initial 3D coordinates of each measuring point are transformed into (X_d, Y_d, Z_d) coordinates. According to the objective function for equation (13), the optimal monitoring plane determined by all the measuring points is calculated. When parameters $a0$, $a1$, and $a2$ in equation (12) are multiplied by any nonzero constant that can still meet the equation, only the proportional relations between the parameters of the plane equations need to be obtained. Therefore, set $a1 = 1$ and the Levenberg–Marquardt (LM) integration algorithm and particle swarm optimization (PSO) may be used, where LM is a least squares fitting algorithm and PSO is an iterative optimization algorithm. Via calculations using MATLAB software, the plane parameters $a0 = -0.4629$ and $a2 = -0.3531$ can be obtained. Then, equation (14) is solved, and the 3D coordinate of the projection point for the reference point in the optimal monitoring plane is (1.5802541, 3.1643227, 0.893). Finally, according to equation (15), the 2D coordinate of each measuring point on the optimal monitoring plane (x, y) can be obtained (Table 3).

3.4. Analysis of the Long-Term Monitoring Results. After installation and debugging of the test instruments and with December 18th, 2016, as the start time for monitoring, 561 days of test data were obtained by July 2nd, 2018. As convergence and deformation monitoring was mainly focused on local variations in the section, in subsequent data processing, the displacement of the reference point was returned to zero, and the relative displacement of each monitoring point was obtained. Time-history curves for the x and y directions and the total displacement of each measuring point relative to the reference point are shown in Figure 13.

As shown in Figure 13, in the initial monitoring stage, the total displacement of each measuring point increased almost linearly with time, and the displacement increase rate of each measuring point showed a tendency to significantly decrease around the 30th day, and the displacement increased slowly after the 30th day and showed a tendency to converge to fixed values. The monitoring data of the surrounding rock indicated the following phenomena: there was mainly a horizontal displacement at measuring points 1 and 5, while the vertical displacement was small. In contrast, a vertical displacement mainly occurred, while the horizontal displacement could be ignored in the case of point 3. Because of the symmetrical location of measuring points 2 and 4, their displacement variation laws were similar. The horizontal displacement of the tunnel was larger than the vertical displacement, mainly because the tunnel was located in the Shiyuejing Fault zone, the rock lithology was poor, the in situ stress condition was complex, and the tunnel vault was presupported. The surrounding rock deformation was mainly controlled by the horizontal stress.

The direction of the total displacement of each measuring point can be obtained by the ratio of the displacement value in the x direction to the displacement value in the y direction:

$$\tan \varphi = \frac{d_y}{d_x}, \tag{16}$$

where φ is the angle between the displacement of the measuring point and the horizontal direction and d_x and d_y

Table 3: 2D coordinates of each measuring point in the optimal plane.

Measuring point	x (m)	y (m)
0	0	0
1	−0.00826	1.481
2	0.51332	2.040
3	1.25532	2.191
4	1.97870	2.027
5	2.47749	1.416

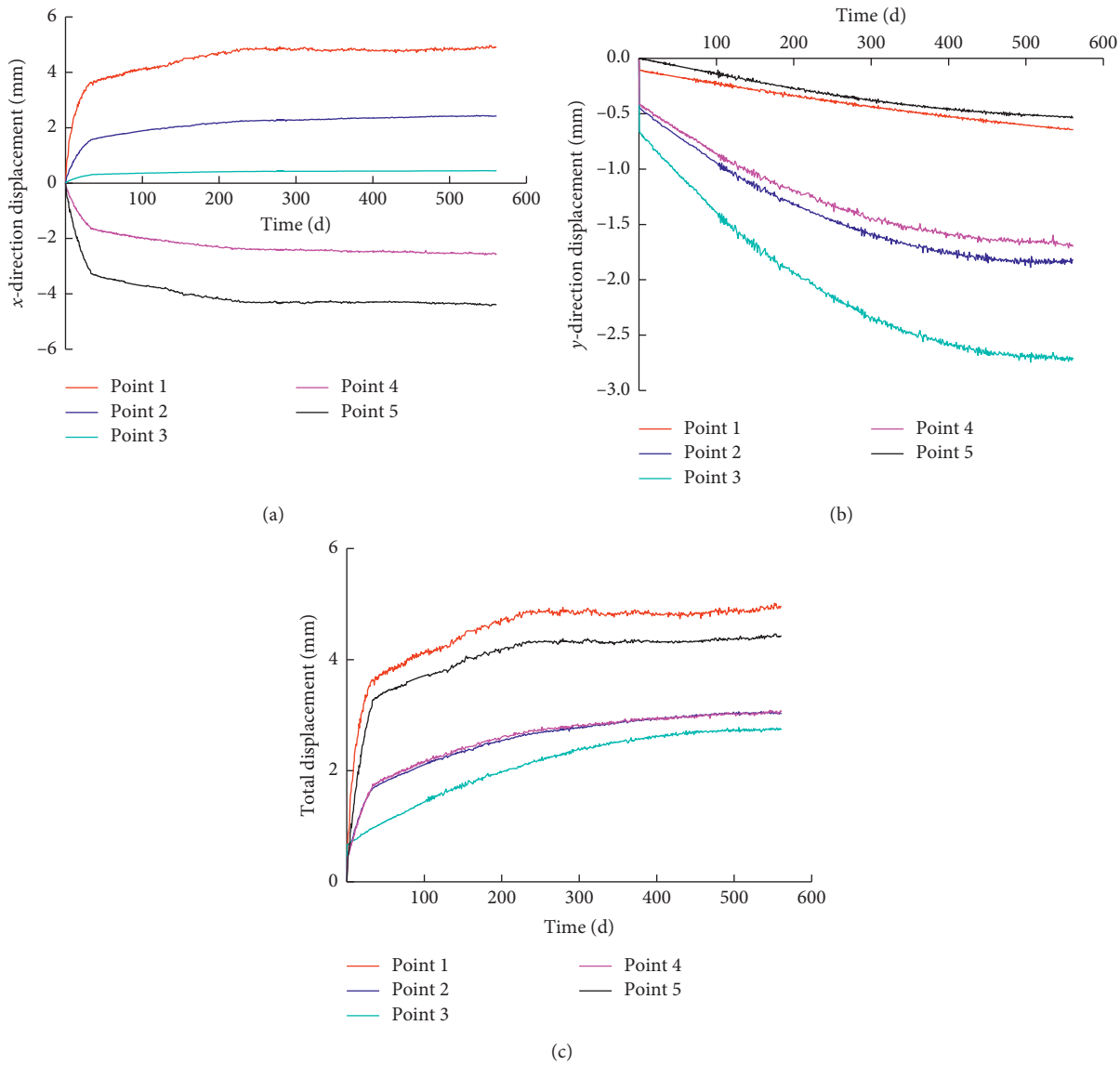

Figure 13: Time-history curves of the displacement of each measuring point: (a) x-direction displacement; (b) y-direction displacement; (c) total displacement.

are the displacement values of the measuring point in the horizontal and vertical directions, respectively.

According to equation (16) and the data of Figure 13, the displacement direction angle of each measuring point at different times could be obtained, as shown in Table 4. Based on the obtained displacement direction angle, the displacement trend diagrams of the measurement section at 30, 200, 400, and 561 days after monitoring were given, that is, the displacement envelope diagram, as shown in Figure 14.

Table 4: Displacement direction angle of each measuring point at different times.

Measuring point	30 d			200 d			400 d			561 d		
	d_x (mm)	d_y (mm)	φ (°)	d_x (mm)	d_y (mm)	φ (°)	d_x (mm)	d_y (mm)	φ (°)	d_x (mm)	d_y (mm)	φ (°)
1	3.514	0.148	2.41	4.683	0.344	4.20	4.802	0.532	6.32	4.914	0.645	7.48
2	1.496	0.611	22.22	2.174	1.324	31.34	2.339	1.766	37.05	2.425	1.820	36.89
3	0.281	0.907	72.79	0.408	1.940	78.12	0.431	2.587	80.54	0.445	2.716	80.70
4	1.521	0.565	20.38	2.318	1.192	27.21	2.439	1.587	33.05	2.546	1.701	33.75
5	3.064	0.040	0.75	4.183	0.268	3.67	4.280	0.453	6.04	4.393	0.536	6.96

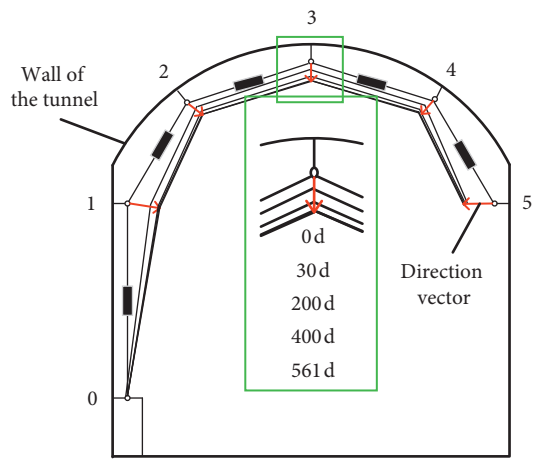

Figure 14: Displacement envelope diagrams and direction vector of the displacements.

4. Discussion and Suggestions

4.1. Comparative Analysis of the TPMS and Artificial Convergence. The TPMS is a new-type convergence displacement monitoring device. To verify the feasibility and accuracy of monitoring results, especially after TPMS installation is completed, the convergence displacement is measured manually using a convergence gauge. The results are compared and analyzed with the TPMS data. The convergence gauge is a 30 m digital convergence gauge manufactured by Jiangsu Haiyan Engineering Material and Instrument Co., Ltd. The horizontal measuring line is the connected line between measuring points 1 and 5 on the TPMS; the measurement time lasts 17 days, from December 18th, 2016 to January 3rd, 2017. The relative displacement of measuring points 1 and 5 of the TPMS in the horizontal direction is just the convergence displacement of the 1–5 measuring line. The measurement results from the TPMS and artificial convergence monitoring are shown in Figure 15.

A linear function is used to conduct a linear fitting on the TPMS and manually measured data, and the fitting equations are

$$y_1 = 0.27297t + 0.80094, \tag{17}$$

$$y_2 = 0.28189t + 0.7726, \tag{18}$$

where y_1 denotes the measured results from the TPMS, y_2 denotes the measured results from the artificial convergence gauge, and t denotes the measurement time. The measured data from the TPMS are in better agreement with those from the artificial convergence gauge, verifying the accuracy of the TPMS data and the feasibility of using the TPMS as a new-type monitoring method for tunnel section convergence.

Compared with traditional convergence monitoring methods, such as the convergence meter, the TPMS can realize the continuous monitoring, automatic collection and transmission of monitoring data, and remote access whenever necessary, without affecting the transportation in the tunnel. Furthermore, the monitoring frequency of the TPMS can be set freely according to the need. The measurement accuracy of the TPMS relates to the accuracy of the tilt sensor and displacement sensor, which reach 0.003° and 0.01 mm, respectively.

4.2. Comparative Analysis of the TPMS and BCS. As a representative convergence measurement system, the BCS measurement schematic diagram is shown in Figure 16. From Figures 1 and 16, similarities are evident between the TPMS and the BCS, such as the structure of the measurement system and relative displacement measurement between two measuring points. However, the measurement principles of the TPMS and BCS are clearly different; the BCS obtains the relative displacement of adjacent measuring points by two tilt sensors and the length of the measuring arm, and the TPMS obtains the relative displacement of adjacent measuring points through tilt and displacement sensors. Compared with the BCS, the TPMS integrates both the displacement sensor and the tilt sensor so that only one

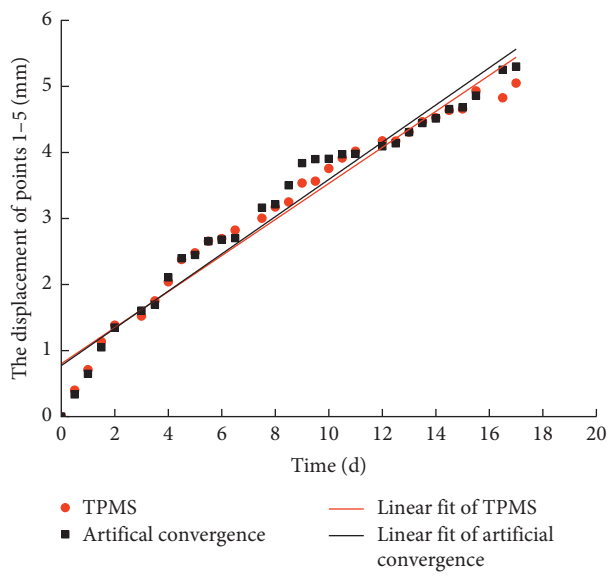

Figure 15: Data diagram of the TPMS and artificial convergence monitoring.

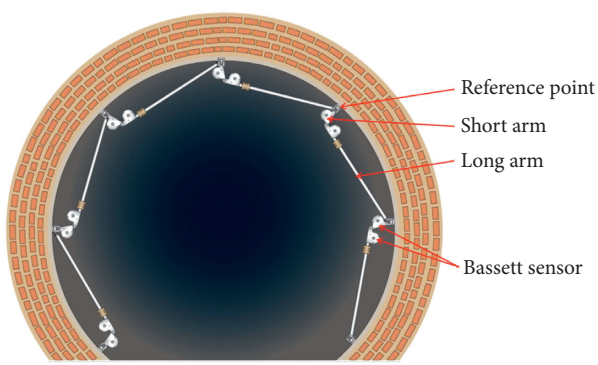

Figure 16: Measurement schematic diagram of the BCS.

measuring arm can transmit the angle and displacement between two measuring points. Therefore, the TPMS simplifies the long arm and short arm structure of the BCS and avoids the errors introduced in calculating the displacement by using a fixed length long arm and short arm, thus forming a simple and effective measurement method for the convergence displacement of the tunnel.

4.3. Suggestions for the TPMS. Through the practical application of in situ monitoring, the following three suggestions for improvement are summarized. First, the long-term stability of the displacement sensor used in the TPMS monitoring unit is worse than that of the tilt sensor, and data floating sometimes occurs when the acquisition frequency is dense. If the displacement sensor is changed from the voltage sensor to the vibrating-wire sensor, the error caused by the sensor itself can be reduced. Second, although the open loop structure can reduce interference in the use of the tunnel, the monitoring configuration should be made up of a closed loop structure so that the closure error can be effectively reduced. Third, to obtain the absolute deformation of each measuring point, it is necessary to regularly measure the spatial coordinates of the reference point through engineering datum point guidance. In addition, since this project monitors the tunnel after the support, the displacement is small. To ensure the accuracy of the measurement, we chose a small range of the sensor. When monitoring a large deformation tunnel, it is necessary to select a sensor of the appropriate range according to the actual situation.

5. Conclusions

A new contact TPMS was introduced in detail, and the method of obtaining the optimal monitoring plane and converting coordinates of the measuring points was established to eliminate the actual installation and positioning deviation of the monitoring system. The displacement calculation formulas of the tunnel cross section measuring points based on the two-dimensional plane coordinate system were proposed, providing a theoretical basis for the popularization and application of this monitoring system.

Through long-term monitoring of the convergence displacement of the surrounding rock in the BET, the time-history curves of each measuring point and displacement envelope diagrams for the measurement section were obtained. Monitoring application practice and results show that the TPMS can realize continuous monitoring, automatic collection and transmission of monitoring data, remote access whenever necessary, without affecting the transportation in the tunnel, and high accuracy, which can reach 0.01 mm, and can be applied to the long-term health monitoring of the lining or envelope of the tunnel and underground engineering.

The reliability of TPMS monitoring is verified by comparing with the monitoring data of a convergence meter. To better apply the TPMS, three further research directions for improvement are proposed. Additionally, the convergence monitoring method such as the TPMS and the BCS can be used in the same measurement section for comparative analysis.

Abbrevations

x, y:	The initial 2D coordinates of measuring point (m)
X, Y, Z:	The initial 3D coordinates of measuring point (m)
$\Delta\theta_{ij}$:	The rotation angle of the measuring arm (°)
ΔL_i:	The length variation h of the measuring arm (m)
θ:	The inclination of the tilt sensor (°)
L:	The displacement of the displacement sensor (m)
V_t:	The output voltage of the tilt sensor (V)
C:	The calibration constants for the tilt sensor
V_d:	The output voltage of the displacement sensor (V)
K_d:	The calibration constants for the displacement sensor (mm/V)
b:	The calibration constants for the displacement sensor (mm)
a_0, a_1, a_2:	The plane equation parameters
d_x, d_y:	The displacement values of the measuring point in the horizontal and vertical directions
φ:	The angle between the displacement of the measuring point and the horizontal direction
t:	Time.

Data Availability

The data used to support the findings of this study are included within the article.

Conflicts of Interest

The authors declare that they have no conflicts of interest regarding the publication of this paper.

Acknowledgments

The authors wish to extend their sincere thanks for the support from the China Atomic Energy Authority (CAEA) for China's URL Development Program and the Geological Disposal Program. This work was supported by the China Atomic Energy Authority (grant no. FZ1402) and National Natural Science Foundation of China (grant no. 51408605).

References

[1] P. P. Oreste and D. Dias, "Stabilisation of the excavation face in shallow tunnels using fibreglass dowels," *Rock Mechanics and Rock Engineering*, vol. 45, no. 4, pp. 499–517, 2012.

[2] L. Qiao, S. Li, Z. Wang, H. Tian, and L. Bi, "Geotechnical monitoring on the stability of a pilot underground crude-oil storage facility during the construction phase in China," *Measurement*, vol. 82, pp. 421–431, 2016.

[3] S. Yang, W. Liu, H. Shi, and F. Huang, "A study on the theory and method of non-contact monitoring for tunnel rock deformation based on free stationing of a total station," *China Civil Engineering Journal*, vol. 39, no. 4, pp. 100–104, 2006.

[4] A. Berberan, M. Machado, and S. Batista, "Automatic multi total station monitoring of a tunnel," *Survey Review*, vol. 39, no. 305, pp. 203–211, 2007.

[5] Y. Luo, J. Chen, W. Xi et al., "Application of a total station with RDM to monitor tunnel displacement," *Journal of Performance of Constructed Facilities*, vol. 31, no. 4, 2017.

[6] S. Slob and R. Hack, "3D terrestrial laser scanning as a new field measurement and monitoring technique," in *Engineering Geology for Infrastructure Planning in Europe: A European Perspective*, H. Robert, A. Rafig, and C. Robert, Eds., pp. 179–189, Springer, Berlin, Germany, 2004.

[7] X. Xie and X. Lu, "Development of a 3D modeling algorithm for tunnel deformation monitoring based on terrestrial laser scanning," *Underground Space*, vol. 2, no. 1, pp. 16–29, 2007.

[8] G. Walton, D. Delaloye, and M. S. Diederichs, "Development of an elliptical fitting algorithm to improve change detection capabilities with applications for deformation monitoring in circular tunnels and shafts," *Tunnelling and Underground Space Technology*, vol. 43, pp. 336–349, 2014.

[9] Y.-H. Li, S.-D. Xu, and J.-P. Liu, "A new convergence monitoring system for tunnel or drift based on draw-wire displacement sensors," *Tunnelling and Underground Space Technology*, vol. 49, pp. 92–97, 2015.

[10] T. Tao and H. Wang, "Modelling of longitudinal evolutionary power spectral density of typhoon winds considering high-frequency subrange," *Journal of Wind Engineering and Industrial Aerodynamics*, vol. 193, Article ID 103957, 2019.

[11] T. Tao, Y. L. Xu, and Z. F. Huang, "Buffeting analysis of long-span bridges under typhoon winds with time-varying spectra and coherences," *Journal of Structural Engineering*, vol. 146, no. 2, Article ID 4020255, 2020.

[12] T. Tao, P. Shi, and H. Wang, "Spectral modelling of typhoon winds considering nexus between longitudinal and lateral components," *Renewable Energy*, vol. 162, pp. 2019–2030, 2020.

[13] R. H. Bassett, J. P. Kimmance, and C. Rasmussen, "An automated electrolevel deformation monitoring system for tunnels," *Proceedings of the Institution of Civil Engineers - Geotechnical Engineering*, vol. 137, no. 3, pp. 117–125, 1999.

[14] L. Simeoni and L. Zanei, "A method for estimating the accuracy of tunnel convergence measurements using tape distometers," *International Journal of Rock Mechanics and Mining Sciences*, vol. 46, no. 4, pp. 796–802, 2009.

[15] W. D. Li, N. Lin, and X. Chen, "Research on 3D tunnel modeling based on close-range photogrammetry," *Advanced Materials Research*, vol. 1076, pp. 1934–1940, 2014.

[16] F. Ariznavarreta-Fernández, C. González-Palacio, A. Menéndez-Díaz, and C. Ordoñez, "Measurement system with angular

encoders for continuous monitoring of tunnel convergence," *Tunnelling and Underground Space Technology*, vol. 56, pp. 176–185, 2016.

[17] Q. Liu, J. Chen, P. Huang, X. Pu, Y. Zhao, and X. Yuan, "Multivariate information dynamic monitoring system application of tunnel construction process model test," *Electronic Journal of Geotechnical Engineering*, vol. 21, no. 9, pp. 3519–3533, 2016.

[18] S.-Q. Sun, S.-C. Li, L.-P. Li, S.-S. Shi, Z.-Q. Zhou, and C.-L. Gao, "Design of a displacement monitoring system based on optical grating and numerical verification in geomechanical model test of water leakage of tunnel," *Geotechnical and Geological Engineering*, vol. 36, no. 4, pp. 2097–2108, 2018.

[19] J. Wang, L. Chen, R. Su, and X. Zhao, "The Beishan underground research laboratory for geological disposal of high-level radioactive waste in China: planning, site selection, site characterization and in situ tests," *Journal of Rock Mechanics and Geotechnical Engineering*, vol. 10, no. 3, pp. 411–435, 2018.

[20] J. Wang, E. Li, L. Chen et al., "Measurement and analysis of the internal displacement and spatial effect due to tunnel excavation in hard rock," *Tunnelling and Underground Space Technology*, vol. 84, pp. 151–165, 2019.

Hindawi
Mathematical Problems in Engineering
Volume 2020, Article ID 8822611, 22 pages
https://doi.org/10.1155/2020/8822611

Research Article

Seismic Vibration Mitigation of Wind Turbine Tower Using Bi-Directional Tuned Mass Dampers

Wanrun Li,[1,2,3] **Qing Zhang**,[3] **Zhou Yang**,[3] **Qingxin Zhu**,[4] **and Yongfeng Du**[1,2,3]

[1]*Institute of Earthquake Protection and Disaster Mitigation, Lanzhou University of Technology, Lanzhou 730050, China*
[2]*International Research Base of Seismic Mitigation and Isolation of Gansu Province, Lanzhou University of Technology, Lanzhou 730050, China*
[3]*School of Civil Engineering, Lanzhou University of Technology, Lanzhou 730050, China*
[4]*Key Laboratory of C&PC Structures of Ministry of Education, Southeast University, Nanjing 211189, China*

Correspondence should be addressed to Wanrun Li; ce_wrli@163.com

Received 13 September 2020; Revised 14 October 2020; Accepted 13 November 2020; Published 2 December 2020

Academic Editor: Amr Elsonbaty

Wind turbines have been increasingly erected in earthquake regions to harvest abundant wind energy. However, the wind turbine tower is slender and lightly damping, which exhibits high susceptibility to earthquake-induced vibration. It is challenging to mitigate the seismic vibration of the tower. In this study, a bi-directional tuned mass damper (BTMD) is proposed to mitigate the seismic vibration of the wind turbine tower. Meanwhile, a lumped-mass finite element model (LFEM) and a coupled blade tower finite element model (CBFEM) are used to investigate the vibration mitigation performance of the BTMD. First, the BTMD and corresponding dynamic equilibrium equations are systemically introduced. Accordingly, the optimum stiffness and damping of the BTMD at different mass ratios are investigated. Then, the dynamic prosperities of the LFEM and CBFEM are compared. Subsequently, the seismic responses of the wind turbine with the BTMD are conducted using the LFEM and CBFEM. Meanwhile, the mitigation performances of the BTMD under uni- and bi-directional earthquakes are investigated. The displacement, acceleration, and bending moment of the wind turbine tower are analyzed in time domain and frequency domain. Note that the influential factors, including mass ratio and structural frequency, on the vibration mitigation performance of the BTMD are investigated. Results show that the proposed BTMD can significantly mitigate the peak values of the top displacement and bottom bending moment. However, the blade tower coupling effect and frequency variation of the tower would have influences on the mitigation efficiency of the BTMD. The results enable a better understanding of the seismic vibration mitigation of the wind turbine tower using tuned mass dampers.

1. Introduction

Wind generation overgrows with the merits of fine environment pollution, technology maturation, and sustainability. Numerous wind turbines have been developed in harsh environments and seismic hazard zones to harvest abundant wind energy. These tall and slender wind turbines are vulnerable to wind- and earthquake-induced vibrations, which can be devastating. Numerous vibration control techniques have been developed for building and bridge vibration mitigation, including passive tuned mass damper (PTMD) [1–6], active tuned mass damper (ATMD) [7, 8], semiactive control system [9–11], and hybrid control system [12, 13], which can provide references for the vibration mitigation of the wind turbine. Numerous researchers and engineers devote their attention to the vibration mitigation of wind turbines using enhanced building utilized vibration control devices. In the aspect of using TMD, Stewart and Lackner [14] examined the performance of tuned mass damper (TMD) on the vibration control of wind turbines, and the results demonstrated that the TMD could reduce tower fatigue load efficiently, particularly in side-to-side directions. Altay et al. [15] utilized TMD to mitigate the seismic-induced vibration of the wind turbine tower considering soil-structure interaction. The results showed that TMD could reduce resonant tower vibrations and improve the fatigue life of wind turbines effectively. Zhao et al. [16]

investigated the vibration control effects of a TMD on the monopole offshore wind turbine tower subjected to wind-wave excitations and seismic excitations. The shaking table tests on a 1/13-scaled test model equipped without or with bi-directional TMD, whose mass ratio and frequency ratio were properly designed, are conducted to verify the effectiveness of the bi-directional TMD. It concluded that TMD effectively weakens the dynamic responses of the monopole offshore wind turbine undergoing a variety of earthquake inputs and equivalent wind-wave loads, and the performance is highly dependent on the frequency contents of external excitations.

In addition, tuned liquid column damper (TLCD) and tuned liquid damper (TLD) are employed to mitigate the seismic vibration of wind turbines. Colwell and Basu [17] investigated the performance of the offshore wind turbine with TLCD under wind and wave loadings. It was found that the peak response reductions of the wind turbine with TLCD may be up to 55% of those the wind turbine without TLCD when it is subjected to wind and wave forces. Buckley et al. [18] employed a TLCD to reduce structural vibrations of a wind turbine tower while considering the interaction of the tower and the foundation soil. The efficiency of TLCDs was investigated numerically and experimentally. Results found that soil-structure interaction played a critical role in designing TLCD for wind turbine tower vibration control, and the optimal tuning of the TLCD may need readjustment over the lifespan of turbines. Hemmati et al. [19] conducted TLCD and TMD to study the vibration suppression in offshore wind turbine foundations. Their findings indicated that the standard deviation of the dynamic response could be significantly reduced by using all structural control devices. TMDs were more efficient in operational conditions, and TLCDs showed better performances in parked conditions. Dai et al. [20] studied the performance of the tuned liquid particle damper (TL-PD) on wind turbine vibration, which combines the tuned liquid damping and particle damping technology. The authors concluded that the structural dynamic response could be reduced effectively. Chen et al. [21] proposed a spherical tuned liquid damper (TLD) to reduce the earthquake-induced vibration of wind turbines and investigated its performance of controlling the structural vibration via a 1/20-scale shaking table test. The authors found that the effectiveness of spherical TLDs did not increase linearly as the mass of water in containers and was influenced greatly by the frequency components of earthquake excitations. Zhang et al. [22] utilized real-time hybrid testing to evaluate full-scale tuned liquid dampers (TLDs) in controlling large wind turbine vibration. Van et al. [23] explored vibration isolation in wind turbine structures and proposed vibration isolators for turbine towers, which are mounted below the nacelle. The author demonstrated that implementing an isolation system may be beneficial to reduce certain key parameters of the wind turbine structural response.

As mentioned above, the vibration control system is installed at the location where the peak displacement appears, which is the most effective way to reduce wind-induced vibrations. However, many wind farms are constructed in the areas with high seismic potentials. Seismic load can be another vibration source during their lifetimes in these regions [24]. The higher vibration modes might also be excited as the seismic energy has a broader frequency range, which can further contribute to or even govern the structural responses of the wind turbine. In this case, using a single TMD in the nacelle and tuning it to the fundamental vibration frequency of the tower are not effective, and the damper should be installed at the location where the largest displacement occurs. Researchers employ multiple TMD to mitigate wind turbine tower vibration. Zuo et al. [25] proposed multiple TMDs (MTMDs) to control vibrations of the fundamental and higher modes of offshore wind turbine tower under multiple hazards, and the validity was examined numerically. Hussan et al. [26] installed MTMD at the top and base of the turbine tower corresponding to the mode shapes of the structure to mitigate the first two vibrational modes of jacket-support offshore wind turbine tower under seismic excitations. Gaur et al. [27] compared the control efficiency of the single tuned mass damper (STMD) and distributed multiple tuned mass dampers (d-MTMDs) on the wind turbine with consideration of blade coupling and soil-structure interaction (SSI).

Through the above research works, the same conclusion is obtained where the MTMDs are suitable for multimode control, while STMD is useful for suppressing a single vibration mode. However, due to the limited spare space in the nacelle for additional TMD mass, the control efficiency of the TMD is restrained. Hence, lightweight and small volume are more feasible for the wind turbine. Some scholars proposed an inerter-based TMD system to reduce the physical mass of a conventional TMD system. An inerter device can transform the linear motion into the high-speed rotational motion, which can significantly amplify the physical mass of the system. Hu et al. [28] proposed an inerter-based structural control system, consisting of a parallel connection of a spring, a damper, and an inerter-based network. Three different configurations were employed to constitute the inerter-based network. The effectiveness of the proposed method on controlling the dynamic responses of a barge-type floating offshore wind turbine was investigated numerically by the modified nonlinear FAST-SC code. Results showed that the proposed novel system could effectively mitigate the displacement at the top of the tower while having similar TMD working space as the system without inerter. Zhang et al. [29] conducted the tuned parallel inerter mass system (TPIMS), consisting of a tuned mass, a spring, and parallel inerter subsystem, to mitigate the seismic response of the wind turbine tower. The results found that TPIMS can effectively reduce the seismic response of the wind turbine tower. Furthermore, a much smaller tuned mass of the TPIMS can realize the same target displacement reduction compared with that of the traditional tuned mass dampers done. Although inerter-based structural control system has been verified effectively on wind turbine vibration mitigation, it is in the initial stage and needs to be further studied, such as the working space and parameters of optimal design.

Numerous researches are also explored to use the ATMD and semiactive TMD to control the vibration of the wind turbine. Brodersen et al. [30] employed an ATMD, which is controlled by the feedback of the tower top displacement and the relative velocity of the damper mass to reduce the tower vibration. They concluded that the ATMD provided a considerable decrease in the frequency response, and it was also superior in reducing vibration in transient conditions compared to passive TMD. Sun [31] introduced a semiactive TMD with tuneable natural frequency and damping ratio to control the dynamic response of monopole offshore wind turbines subjected to multihazards consisting of wind, wave, and earthquake. Results showed that, considering the soil effects, damage, and multihazards, the STMD was consistently effective in controlling the response of the tower, whereas the passive TMD may become completely ineffective and induce a potential threat to the structure. Results showed that active structural control could provide better performance than passive control. However, passive structural control has its unique advantages, such as high reliability and low cost, which is particularly essential for offshore wind turbines due to their long lifespan.

Most of the aforementioned references focused on unidirectional response (fore-aft motion) mitigation, while the real wind turbines suffer from bi-directional vibration (fore-aft and side-side) due to wind misalignment, vortex-induced crosswind vibration, and other misaligned loadings, such as earthquakes. The bi-directional vibration control of the wind turbine is relatively scarce. Sun and Jahangiri [32] proposed a three-dimensional pendulum tuned mass damper (3d-PTMD) to mitigate the tower and nacelle dynamic response in the fore-aft and side-side directions. The authors found that the proposed 3d-PTMD was more effective than that of the dual linear TMDs in mitigating the bi-directional vibration of the offshore wind turbine under misaligned loading considering some uncertainty from soil effects. Tong et al. [33] employed two linear TMDs, which shared the same mass component and were installed in both the fore-aft and side-to-side directions of the tower, to reduce the vibration of the tower. The infinite-dimensional model of the monopile wind turbine tower-TMD system was made. The parameters of the TMD were optimized by minimizing the frequency-limited H2-norm of the transfer function matrix. It is concluded that the performance of the optimal TMDs was similar to that of [14]. Although the preliminary exploring works have been done and some researchers have reviewed astate-of-the-art current vibration control techniques and their applications to wind turbines [34, 35], there is still great progress needed to the technology maturation and practical application.

In this study, a bi-directional tuned mass damper (BTMD) is proposed to mitigate the seismic vibration of the wind turbine tower. Meanwhile, a lumped-mass finite element model (LFEM) and a coupled blade tower finite element model (CBFEM) are used to investigate the vibration mitigation performance of the BTMD. First, the BTMD and corresponding dynamic equilibrium equations are systemically introduced. Accordingly, the optimum stiffness and damping of TMD at different mass ratios are investigated. Then, the dynamic prosperities of LFEM and CBFEM are compared. Afterward, the seismic responses of the wind turbine with the BTMD are conducted using the LFEM and CBFEM. Meanwhile, the mitigation performances of the BTMD under uni- and bi-directional earthquakes are investigated. The displacement, acceleration, and bending moment of wind turbine towers are analyzed in time-domain and frequency-domain. Note that the influential factors, including mass ratio and structural frequency variation, on the vibration mitigation performance are investigated. Results show that the proposed BTMD can significantly mitigate the peak values of the top displacement and bottom bending moment. However, the blade tower coupling effect and frequency variation would influence the mitigation efficiency of the BTMD.

2. Bi-Directional Tuned Mass Dampers (BTMDs)

2.1. The BTMD Model. The proposed BTMD is shown in Figure 1, which consists of a mass block, two sets of spring-damping systems, slide rails, and two sets of rollers. The slide rail is set on the inside wall of the device, and the mass block can move along the two directions slide rail independently. The spring-damping system dissipates the kinetic energy of the mass block. Two sets of mutually perpendicular rollers are arranged at the bottom of the device to reduce the friction force between the mass block and bottom plate. The configuration of the BTMD is streamlined, which does not disturb the airflow characteristics of the wind field. The BTMD is installed on the roof of the nacelle. The parameters of the BTMD, including the spring stiffness and the mass of the block, are tuned according to the frequency of controlled structures.

2.2. The Mechanical Model. The mechanical model of the BTMD-equipped wind turbine is shown in Figure 2, and the corresponding equation of motion is written as equation (1). Note that the coupling effect between two directional vibrations is ignored.

$$\begin{bmatrix} M & 0 \\ 0 & m \end{bmatrix} [\ddot{x}_M\ \ddot{x}_d] + \begin{bmatrix} C+c & -c \\ -c & c \end{bmatrix} \begin{bmatrix} \dot{x}_M \\ \dot{x}_d \end{bmatrix} + \begin{bmatrix} K+k & -k \\ -k & k \end{bmatrix} \begin{bmatrix} x_M \\ x_d \end{bmatrix} = \begin{bmatrix} P(t) \\ 0 \end{bmatrix}, \tag{1}$$

where x_M and x_d are the displacements of wind turbine and mass block of the BTMD, respectively; M and m are the mass of the wind turbine and mass block, respectively; C and c are the damping of the wind turbine and BTMD, respectively; K and k are the stiffness of the wind turbine and TMD, respectively; $P(t)$ is the load applied to the wind turbine.

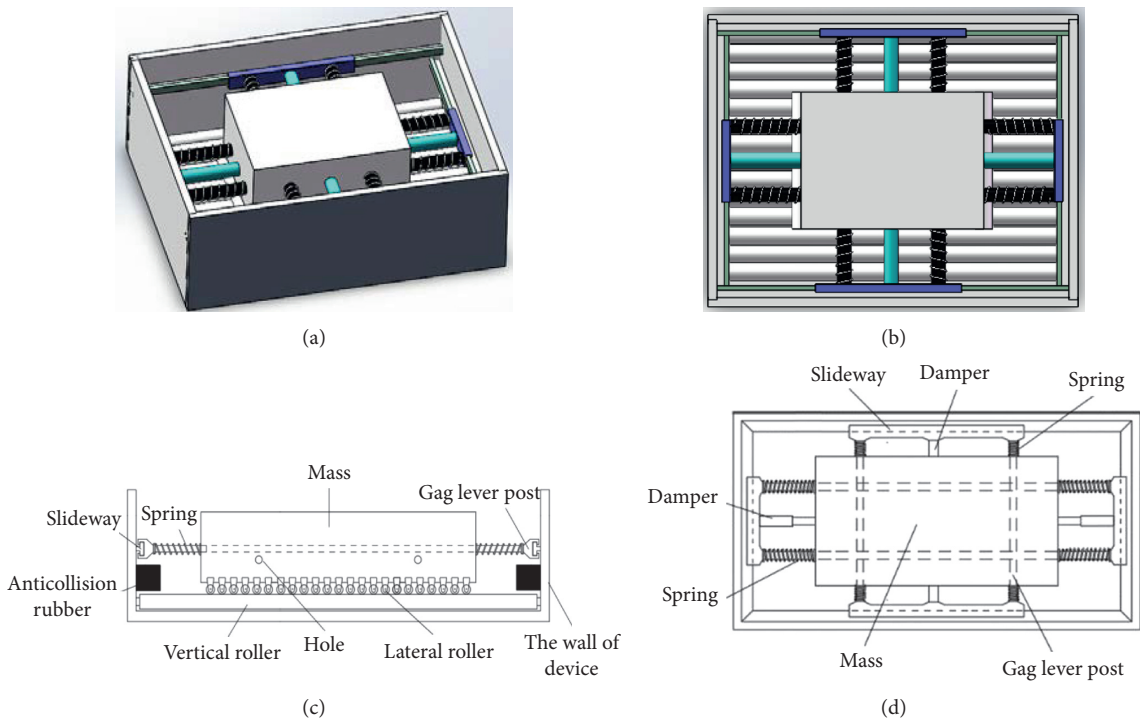

Figure 1: The BTMD model. (a) The diagram of the BTMD. (b) The planform of the BTMD. (c) Lateral view of the BTMD. (d) Aerial view of the BTMD.

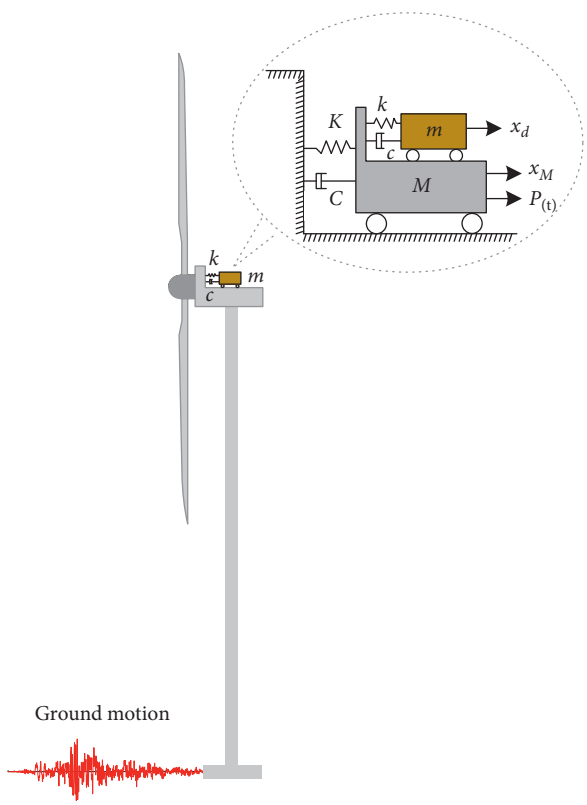

Figure 2: Diagram of the wind turbine with TMD system.

Accordingly, the displacement amplification factor, R, can be calculated using

$$R = \sqrt{\frac{\left(\alpha^2 - \beta^2\right)^2 + (2\zeta\alpha\beta)^2}{\left[\left(\alpha^2 - \beta^2\right)\left(1 - \beta^2\right) - \alpha^2\beta^2\mu\right]^2 + (2\zeta\alpha\beta)^2\left(1 - \beta^2 - \mu\beta^2\right)^2}}, \tag{2}$$

where α is the ratio of the natural frequency of the BTMD to that of the wind turbine, β is the ratio of the frequency of external load to the natural frequency of wind turbine, μ is the mass ratio of BTMD to that of the wind turbine, and ζ is the damping ratio of the wind turbine. The amplification factor, R, reaches the minimum value when α, μ, and ζ satisfy the following equations:

$$\alpha_{\text{opt}} = \frac{1}{1 + \mu}, \tag{3}$$

$$\xi_{\text{opt}} = \sqrt{\frac{3\mu}{8(1 + \mu)}}, \tag{4}$$

where α_{opt} and ξ_{opt} represent the optimal frequency ratio and damping ratio of the BTMD, respectively. Accordingly, the relationships between BTMD parameters and the amplification factor are shown in Figure 3. Note that five mass ratios, varying from 0.01 to 0.05, are utilized to investigate the influence of the mass ratio.

According to Figure 3, the amplification factor decreases with the increase of mass ratio. Meanwhile, the peak amplification ratio is significantly suppressed due to the BTMD. Hence, the optimal mass, stiffness, and damping of the BTMD can be calculated using the following equations:

$$m_d = \mu m_1, \tag{5}$$

$$k_{\text{opt}} = \alpha_{\text{opt}}^2 \omega_1^2 m_d, \tag{6}$$

$$c_{\text{opt}} = 2\xi_{\text{opt}}\alpha_{\text{opt}}\omega_1 m_d, \tag{7}$$

where m_d, k_{opt}, and c_{opt} are the optimal mass, stiffness, and damping of the BTMD, respectively, ω_1 is the first-order natural frequency of the wind turbine, and m_1 is the first-order modal mass of the wind turbine.

3. The Wind Turbine Model

3.1. Description of the Wind Turbine. A 2.5 MW three-blade horizontal wind turbine, which is commonly constructed in the Western of China, is shown in Figure 4. The tower is a cylindrical hollow single steel tube with the wheel hub height of 98.12 m. The diameter and thickness of the tower vary across the height. The diameter and thickness of the bottom tower are 3.9 m and 67 mm, respectively, while the diameter and thickness of the top tower are 2.55 m and 20 mm, respectively. The nacelle is mounted on the tower top where the rotor shaft holding turbine blades is connected. The nacelle height and weight are 3.2 m and 52 tons, respectively. The sum weight of the blade and hub is 31.155 tons.

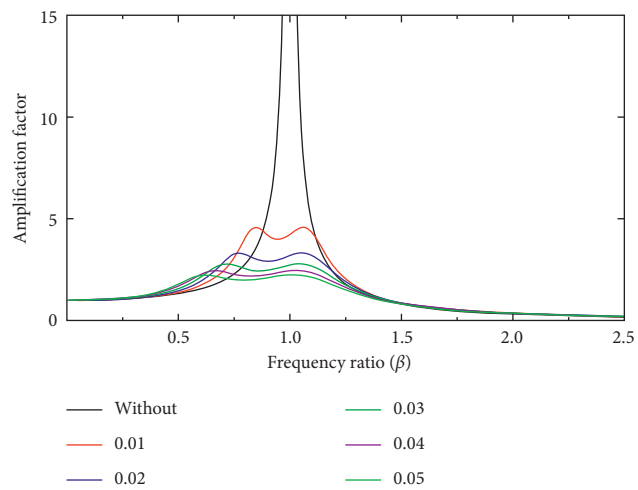

Figure 3: The influence of BTMD parameters on the amplification factor.

3.2. Numerical Model of the Wind Turbine. The finite element model (FEM) of the wind turbine is developed in terms of design drawings. A refined 3D FEM is not economical for the seismic vibration mitigation analysis of numerous wind turbine structures. Hence, a simple FEM is realistic. An acceptable accuracy for seismic performance could be obtained by using simplified models [36, 37]. However, the motion of the tower is strongly associated with the motion of the blades, which reduces the natural frequency and ultimately alters the response of the tower [38]. It may significantly underestimate the structural response [39] and misunderstand the control efficiency of the BTMD without considering the blade tower coupling. Hence, two FEMs of a wind turbine, including an LFEM and a CBFEM, are modeled, as shown in Figure 5. The blades, hub, and nacelle are modeled as a lumped mass of 83.155 tons, whose gravity center shifts by 0.8 m. The tower and lumped mass in the LFEM are modeled using the element Shell 93 and Mass 21, respectively. The connection between the tower and lump mass is modeled using the element MPC 184. The blade and nacelle in the CBFEM are modeled using the element Beam 189. The hub, which connected the blade and nacelle, is modeled as a lumped mass with infinity rigid. Generally, the wind turbine is adjusted to the parked condition (i.e., the rotor rotational speed remains zero and the electric generator does not work) under extreme events using brake rigging to reduce potential rotor motions. Therefore, the parked condition is considered in this work. The Rayleigh damping, which combines the mass and stiffness proportional damping, is used to model the recommended 1% damping [40]. The elasticity modulus of steel is 2×10^5 MPa.

The modal parameters of the first six modes, including frequency and mode shape related to the global flexure of the wind turbine tower and blade coupling, are summarized in Table 1 and Figures 6 and 7. The modal parameters of the LFEM (without blade) are comparable to that of the CBFEM (with blade), especially the first two natural frequencies. However, the blade coupling is obvious in the CBFEM. Note that blade tower coupling effects alter the third and fourth

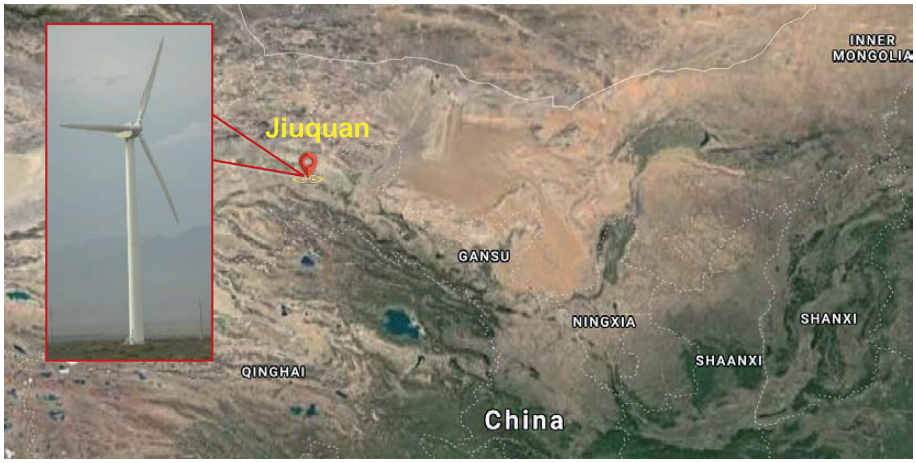

Figure 4: The schematic and location of wind turbine (Map Data © 2020 Google, Imagery © 2020 Maxar Technologies) (image by Wanrun Li).

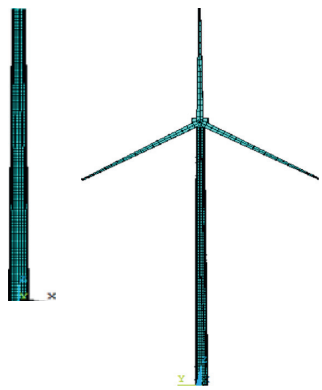

(a) (b)

Figure 5: Numerical models of the wind turbine. (a) The LFEM. (b) The CBFEM.

Table 1: The modal parameters of the LFEM and CBFEM.

Mode	LFEM Mode shape	f (Hz)	Mode	CBFEM Mode shape	f (Hz)
1	1st tower side-to-side	0.3347	1	1st tower side-to-side + 1st blade edgewise	0.3287
2	1st tower fore-aft	0.3348	2	1st tower fore-aft + 1st blade flap-wise	0.3314
3	2nd tower side-to-side	1.7534	3	2nd tower side-to-side + 1st blade edgewise	1.3973
4	2nd tower fore-aft	1.7535	4	1st blade torsion	1.4678
5	3rd tower side-to-side	4.8185	5	2nd tower fore-aft + 1st blade flap-wise	1.5294
6	3rd tower fore-aft	4.8203	6	2st blade torsion	2.7268

natural frequency of the wind turbine. The frequencies decrease from 1.7534 and 1.7535 to 1.3973 and 1.4678, respectively, whose reduction ratios are 20.31% and 16.29%. Hence, the coupling effect would have significant influences on the mitigation efficiency of the BTMD.

3.3. The Finite Element Model of the BTMD. The BTMD is simplified into a bi-directional mass-spring-damper model in the FEM, as shown in Figure 8. The element Combin 14 is selected for modeling the spring-damper of the BTMD, which provides the stiffness and damping. The element Mass 21 is selected for modeling the mass block of the BTMD. Points 1, 2, 3, and 4 represent the connection points, which are located on the wind turbine. The points 5, 6, 7, and 8 represent the connection points which are located on the BTMD. Point 9 represents the mass of the BTMD. The first-order modal mass of the investigated wind turbine is 208.678 tons. Hence, the parameters of BTMD are obtained according to equations (1) to (5), as listed in Table 2.

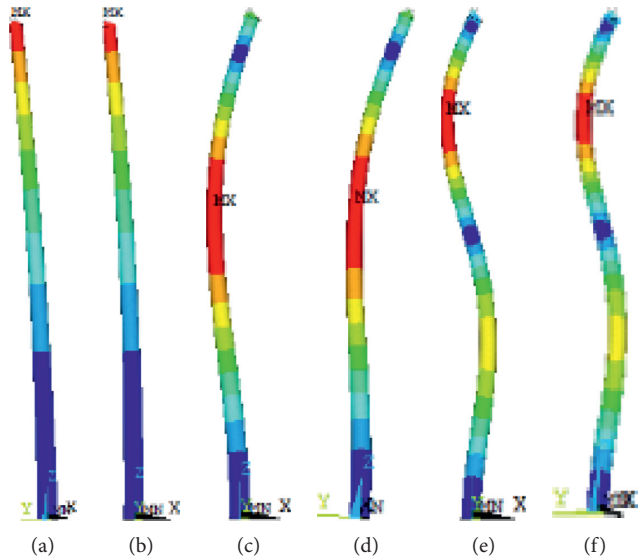

Figure 6: First six vibration mode shapes of the LFEM. (a) Mode 1. (b) Mode 2. (c) Mode 3. (d) Mode 4. (e) Mode 5. (f) Mode 6.

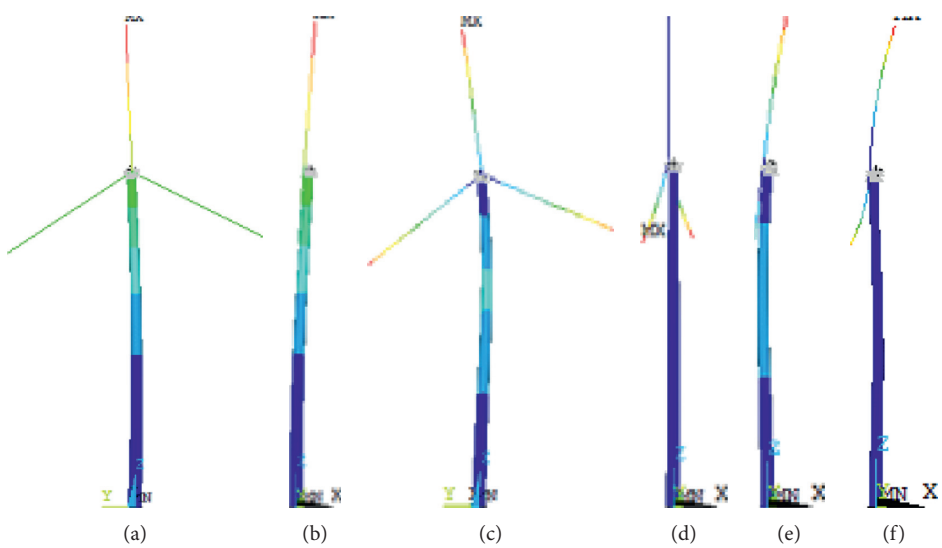

Figure 7: First six vibration mode shapes of the CBFEM. (a) Mode 1. (b) Mode 2. (c) Mode 3. (d) Mode 4. (e) Mode 5. (f) Mode 6.

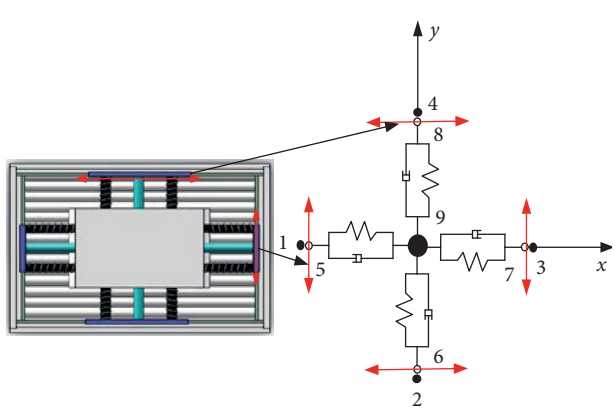

Figure 8: The mechanical model and finite element model of BTMD.

Table 2: Parameters of BTMD.

	Mass ratio	Frequency ratio	Damping ratio (%)	Mass (kg)	Stiffness (N/m)	Damping (N·s/m)
1	0.01	0.9900	6.09	2086.78	9269.53	535.69
2	0.02	0.9804	8.58	4173.56	18181.25	1493.93
3	0.03	0.9709	10.45	6260.34	26744.00	2704.34
4	0.04	0.9615	12.00	8347.12	34974.04	4100.65
5	0.05	0.9523	13.36	10433.90	42884.94	5652.13

4. Structural Responses of Wind Turbines under Uni-Directional Ground Motions

According to the Chinese code for seismic design of buildings GB 50011-2010 [41], the seismic fortification intensity of the region, in which the wind turbine prototype is located, is 8 degrees. The peak acceleration of the design earthquake is 0.2 g. The predominant period of the site is 0.45 s. Several studies have been conducted to investigate the simulations of the stochastic excitations for studying the dynamic responses of infrastructures, e.g., the simulation of stochastic wind field for wind-induced response analysis [42–45] and artificial seismic ground motion simulations [46, 47]. To provide reliable results considering the randomness of the ground motions, two natural waves (El-Centro 1940 and Chalfant 1986) and one artificial wave, which is achieved based on the site conditions of the wind turbine prototype, are selected to investigate the seismic responses and clarify the effectiveness of the BTMD. The time histories of the selected ground motion are shown in Figure 9. The peak acceleration of the three selected ground motions is scaled to 4 m/s^2. Meanwhile, the spectra of these selected ground motions are shown in Figure 10, compared with the design spectrum of Chinese code. The design spectrum and the spectra of these selected ground motion records are statistically compatible. Accordingly, the displacement, acceleration, and bottom bending moment of the wind turbine tower are calculated to evaluate the vibration mitigation performance of the BTMD. The reduction ratio of structural responses is written as

$$\eta = \frac{D_U - D_C}{D_U} \times 100\%, \tag{8}$$

where D_U and D_C are the responses of the wind turbine without and with the BTMD, respectively.

4.1. Displacement of the Wind Turbine Tower. The seismic responses of the wind turbine with different mass ratios BTMD are calculated using the LFEM and CBFEM. The top displacements of the wind turbine with different mass ratios BTMD are shown in Figure 11 and Table 3. Meanwhile, the reduction ratios of peak values and standard deviations with the different mass ratios are shown in Figure 12. The top displacements and corresponding reduction ratio, produced by the CBFEM and LFEM, are similar to each other. The peak value and standard deviation of the displacement significantly decrease with the increase of the mass ratio. However, the increases in the reduction ratio slow down with the increase of mass ratio. The maximum reduction ratios of the peak value and the standard deviation exceed 50% and 40%, respectively. Hence, the BTMD can significantly mitigate the vibration of the tower, and it can be used to depress the fatigue load. Note that the reduction ratio of displacement is dependent on the characteristic of the ground motion, which is mainly influenced by the dominated frequency of the ground motion.

The peak values of the horizontal displacement along the height of the wind turbine are shown in Figure 13. The calculation of the LFEM under different ground motions is similar to that of the CBFEM. The maximum displacement occurs at the top of the wind turbine tower. The displacement of the wind turbine tower is dominated by the first mode. Hence, the reduction ratio reaches the largest when the BTMD is installed on the roof of the nacelle.

4.2. Acceleration of the Wind Turbine Tower. The accelerations of the wind turbine with different mass ratios BTMD are shown in Figure 14 and Table 4. Meanwhile, the reduction ratios of peak value and standard deviation of the top acceleration are shown in Figure 15. Compared with the displacement, the BTMD shows weak efficiency in controlling peak acceleration value, especially in the initial stage. However, the reduction ratio of the standard deviation increases with the increase of mass ratio, which can exceed 20%. Hence, the BTMD can be used to depress the fatigue load.

4.3. The Bottom Bending Moment. The reduction ratios of the bottom bending moment of the wind turbine with different mass ratios BTMD are shown in Figure 16 and Table 5. The reduction ratio variation trend of the bottom bending moment is similar to that of the displacement. The BTMD can significantly mitigate the bottom bending moment, and it can be used to depress the fatigue load.

4.4. The Fourier Spectrum of Wind Turbine Response

4.4.1. The Fourier Spectrum of the Displacement. The Fourier spectra of the top displacement produced by the LFEM and CBFEM with different mass ratios BTMD are shown in Figure 17. The Fourier spectra of the LFEM are similar to those of the CBFEM. The structural response is mainly concentrated around the first natural frequency. One distinct peak around the fundamental frequency can be observed in the Fourier spectrum of the wind turbine without the BTMD. However, there are two peaks in the

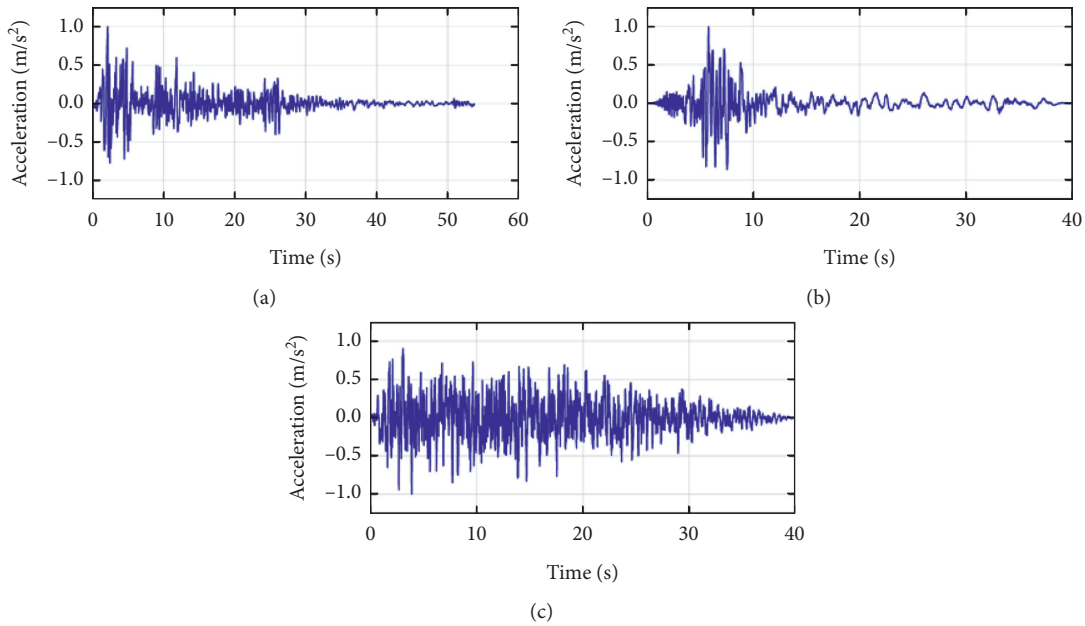

Figure 9: The selected ground motions. (a) El-Centro. (b) Chalfant. (c) Artificial wave.

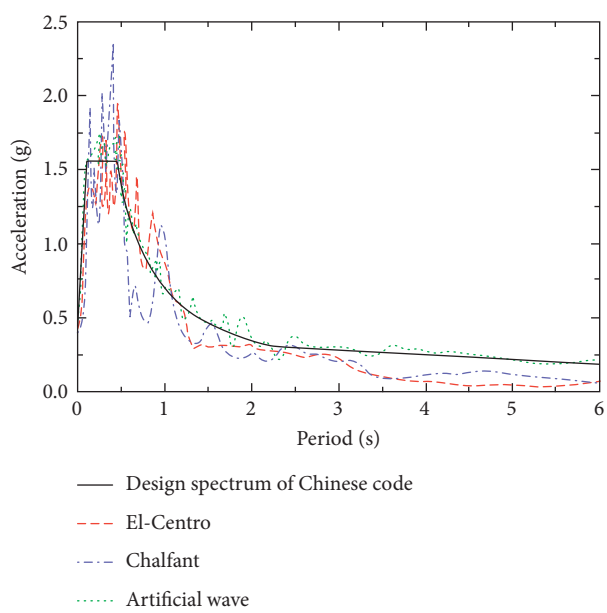

Figure 10: The spectra of the selected ground motions.

Fourier spectra of the wind turbine with the BTMD. The phenomenon is similar to the variation of the amplification factor, as shown in Figure 3. Note that the amplitude of the peak frequency decreases with the increase of mass ratio due to the excellent mitigation performance of the BTMD. The vibration energy of the wind turbine can be dissipated effectively by the BTMD.

4.4.2. The Fourier Spectrum of the Acceleration. The Fourier spectra of the LFEM and CBFEM with different mass ratios of BTMD subjected to different ground motions are shown in Figure 18. The Fourier spectra of the LFEM are similar to those of the CBFEM. Compared with the Fourier spectra of the displacement, the frequency peaks appear around the first two natural frequencies. The amplitude around the first natural frequency decreases significantly with the increase of mass ratio, whereas the amplitude variation around the second natural frequency is small. It may be illustrated by the reason that the BTMD is designed according to the foundational frequency of the wind turbine. Hence, the BTMD can significantly mitigate the amplitude of the controlled frequency. However, it shows weak efficiency on the amplitude mitigation of other frequencies.

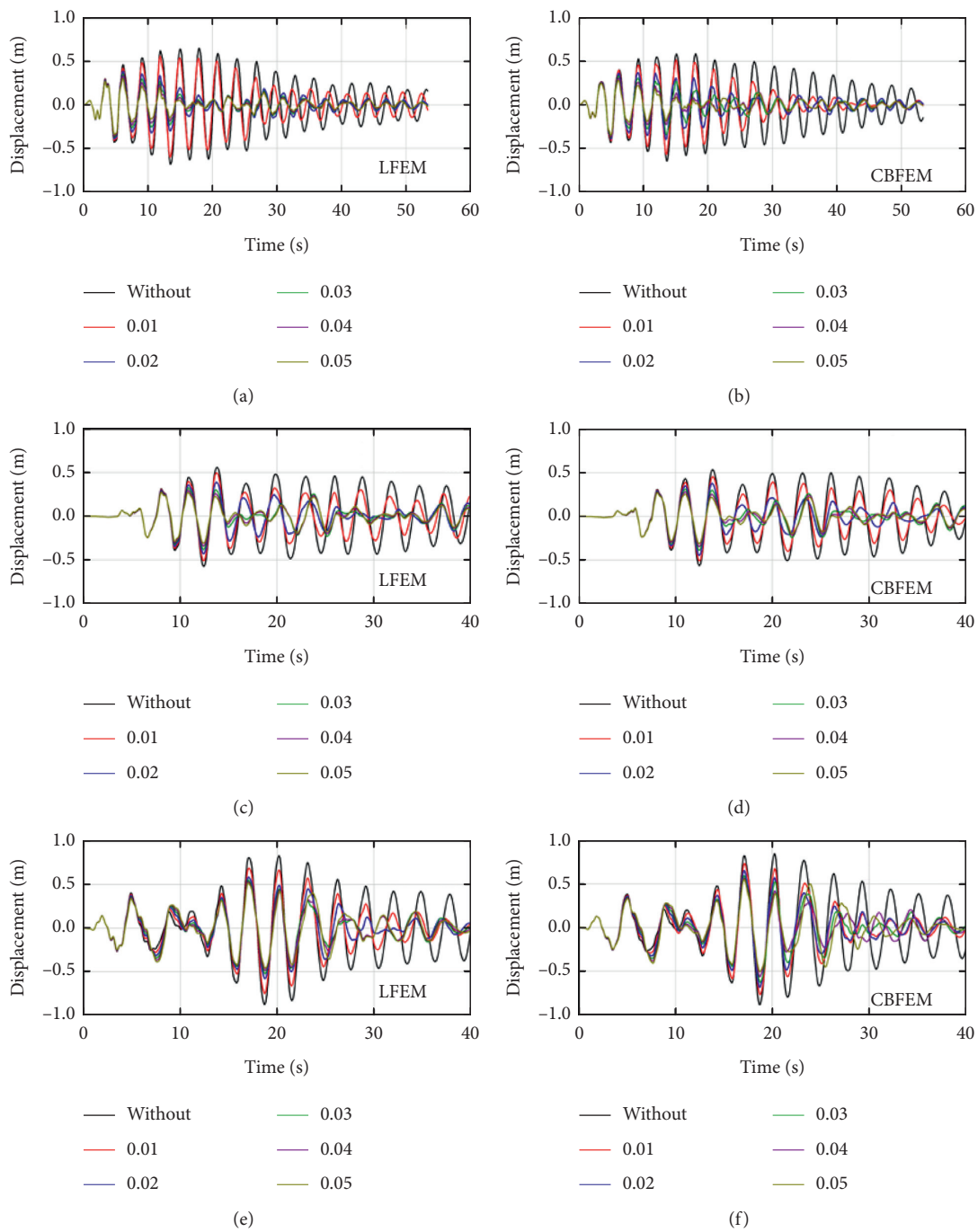

Figure 11: The displacement of wind turbine. (a) LFEM under the El-Centro. (b) CBFEM under the El-Centro. (c) LFEM under the Chalfant. (d) CBFEM under the Chalfant. (e) LFEM under artificial wave. (f) CBFEM under artificial wave.

5. Seismic Response of the Wind Turbine under Bi-Directional Ground Motion

The wind turbine would suffer bi-directional vibration (fore-aft and side-side) due to bi-directional earthquakes. It is meaningful to investigate the effectiveness of the BTMD in the vibration control of wind turbines under bi-directional earthquakes. According to the Chinese code for the seismic design of buildings, the amplitude ratios of two direction ground motions are modulated to 1.0 : 0.85. The seismic responses of the wind turbine under bi-directional ground motion are calculated using the LFEM and CBFEM.

5.1. The Structural Responses Reduction. The reduction ratios of the displacement, acceleration, and bottom bending moment in the two directions calculated using the LFEM and CBFEM are shown in Figures 19–21, respectively. The reduction ratios of the peak value

Table 3: The displacement of the wind turbine with different mass ratios BTMD.

Mass ratio	El-Centro		Chalfant		Artificial wave	
	LFEM	CBFEM	LFEM	CBFEM	LFEM	CBFEM
Without	0.65	0.63	0.56	0.53	0.83	0.81
0.01	0.56	0.52	0.49	0.45	0.69	0.67
0.02	0.38	0.37	0.38	0.37	0.59	0.58
0.03	0.35	0.33	0.31	0.31	0.55	0.54
0.04	0.31	0.30	0.29	0.28	0.53	0.52
0.05	0.30	0.28	0.27	0.27	0.52	0.51

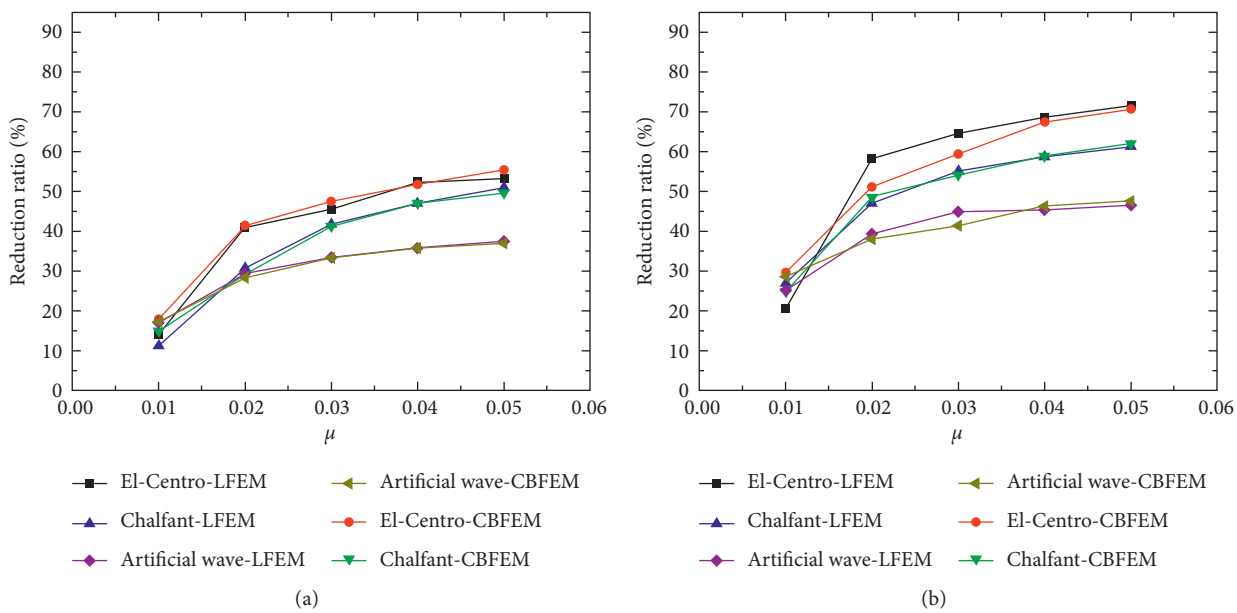

Figure 12: The reduction ratio of displacements. (a) Peak displacement. (b) The standard deviation of displacement.

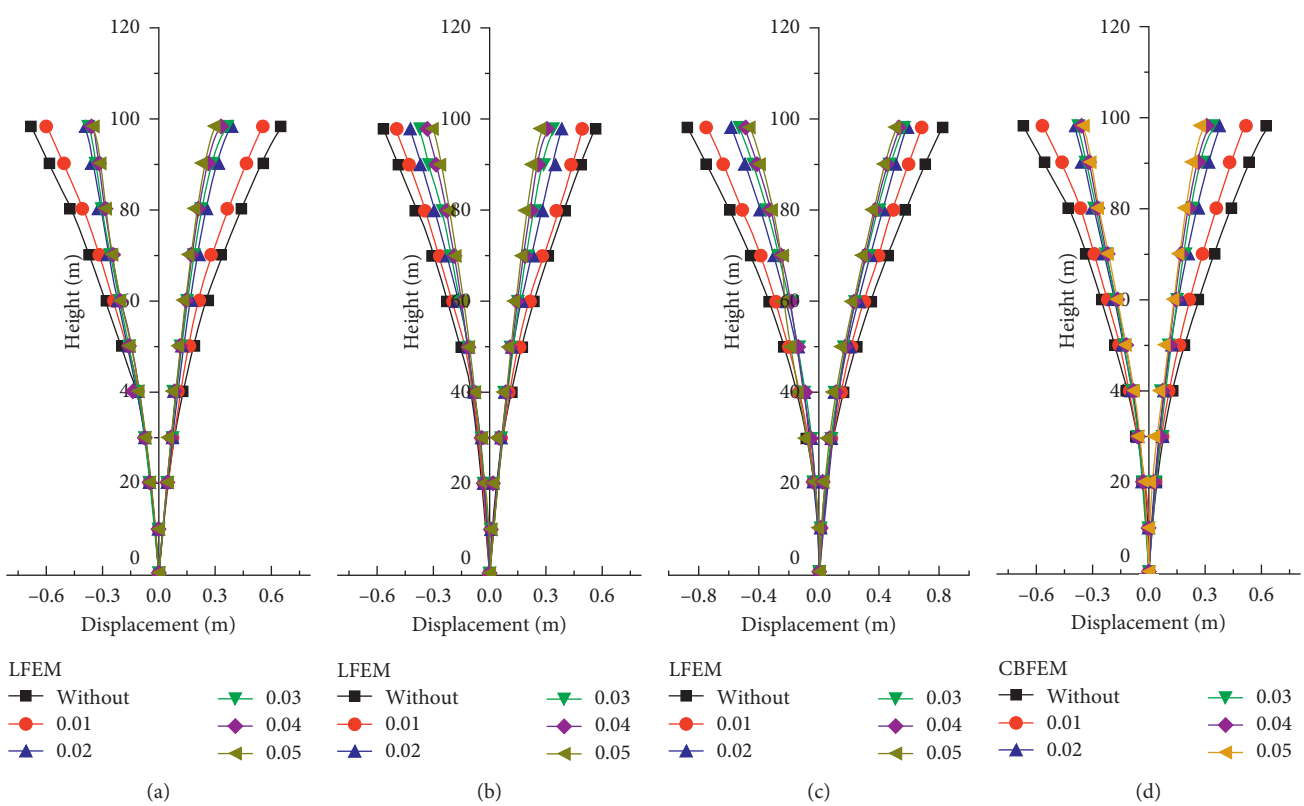

Figure 13: Continued.

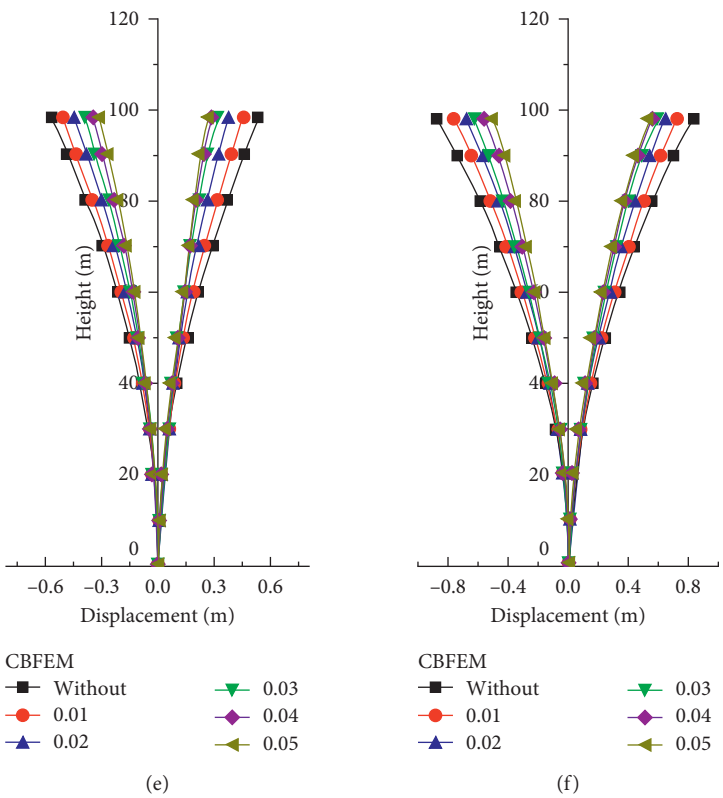

Figure 13: The peak displacement of wind turbine along the height. (a) LFEM under the El-Centro. (b) LFEM under the Chalfant. (c) LFEM under artificial wave. (d) CBFEM under the El-Centro. (e) CBFEM under the Chalfant. (f) CBFEM under artificial wave.

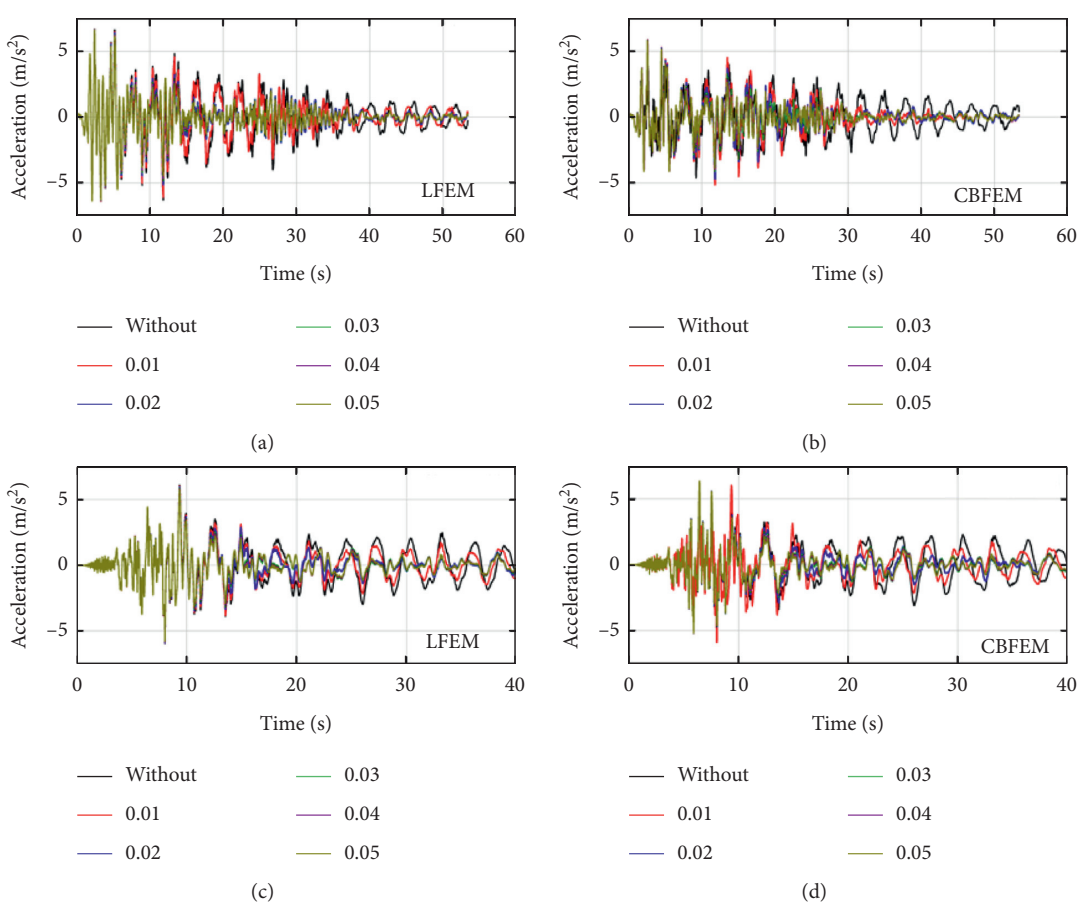

Figure 14: Continued.

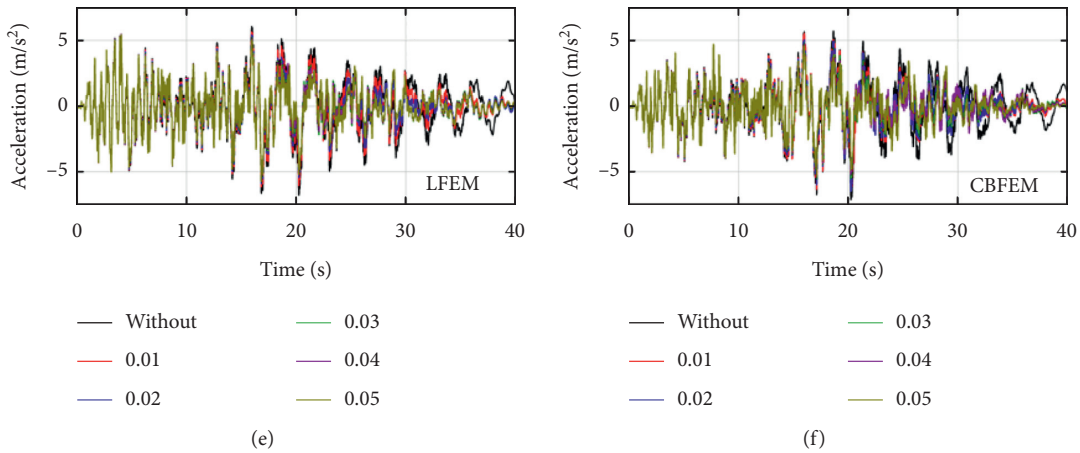

Figure 14: The acceleration of the wind turbine with different mass ratios BTMD. (a) LFEM under El-Centro. (b) CBFEM under the El-Centro. (c) LFEM under the Chalfant. (d) CBFEM under the Chalfant. (e) LFEM under artificial wave. (f) CBFEM under artificial wave.

Table 4: The peak acceleration of the wind turbine with different mass ratios BTMD.

Mass ratio	El-Centro		Chalfant		Artificial wave	
	LFEM	CBFEM	LFEM	CBFEM	LFEM	CBFEM
Without	6.68	5.87	6.12	5.73	6.08	5.71
0.01	6.67	5.85	6.04	5.61	5.66	5.58
0.02	6.66	5.83	5.97	5.52	5.44	5.37
0.03	6.64	5.81	5.90	5.46	5.43	5.13
0.04	6.63	5.80	5.83	5.41	5.43	5.11
0.05	6.62	5.78	5.76	5.37	5.42	5.09

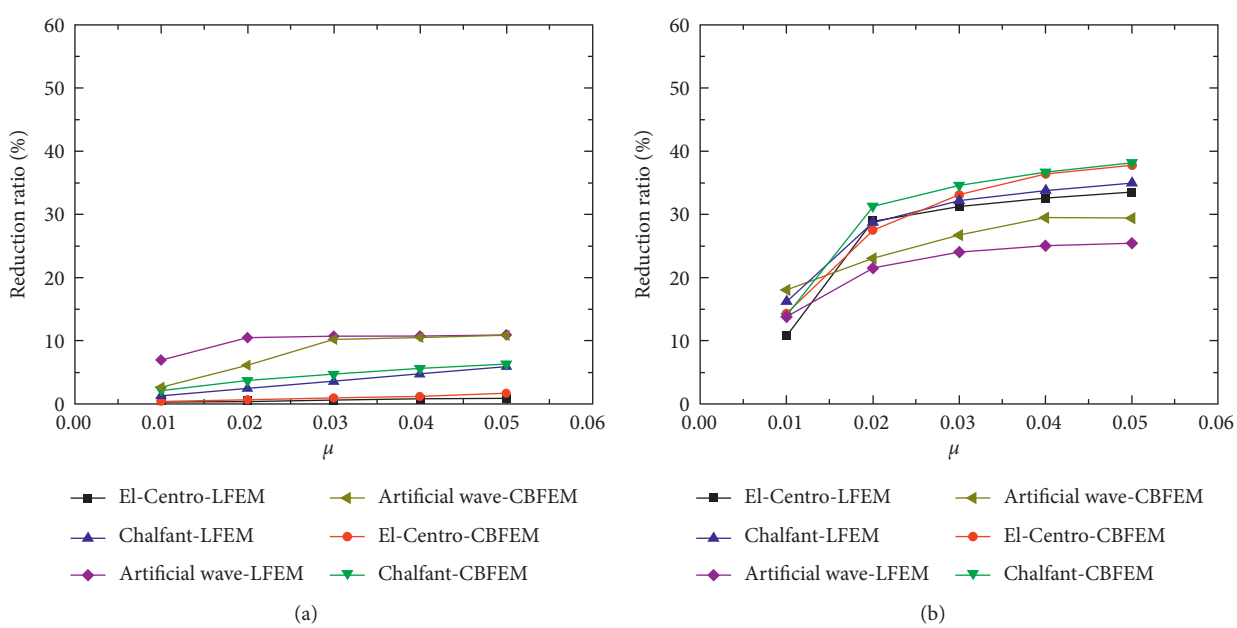

Figure 15: The reduction ratio of (a) the peak acceleration and (b) the peak acceleration standard deviation.

and standard deviation in two directions are similar to each other, which increase with the augment of the mass ratio. The reduction ratio of the peak displacement exceeds 20%. The BTMD can efficiently reduce the bi-directional peak displacement. However, the reduction ratios of peak acceleration are small. It is challenging to reduce the peak acceleration using the BTMD. Meanwhile, the standard deviation reduction ratios of the displacement, acceleration, and bottom bending moment can exceed 40%, 20%, and 30%, respectively. Hence, the proposed BTMD can efficiently depress the fatigue load of wind turbines. Note that the reduction ratio

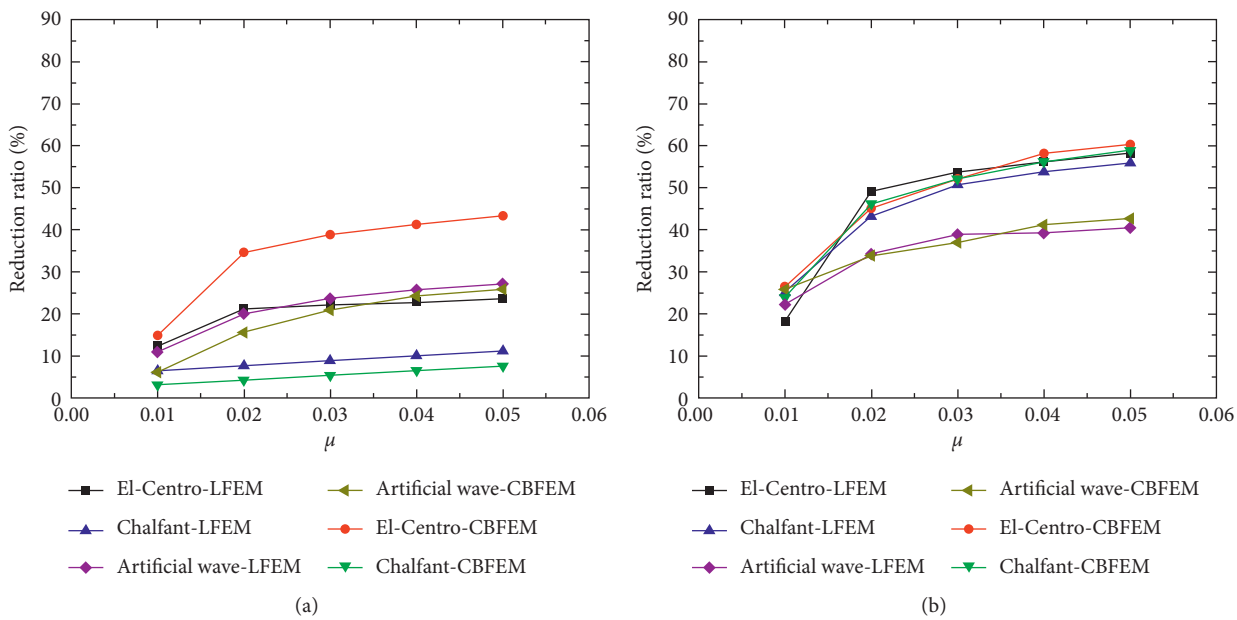

Figure 16: The reduction ratio of (a) the peak bending moment and (b) the standard deviation of bending moment.

Table 5: The bottom bending moment of the wind turbine with different mass ratios of BTMD.

Mass ratio	El-Centro		Chalfant		Artificial wave	
	LFEM	CBFEM	LFEM	CBFEM	LFEM	CBFEM
Without	50989.6	48402.90	39391.70	36431.90	64822.80	62616.90
0.01	44702.4	41204.40	36846.60	35289.10	57728.02	58764.70
0.02	40158.8	31663.20	36374.10	34873.00	51209.89	52848.00
0.03	39741.6	29572.00	35905.60	34463.80	48794.62	49514.90
0.04	39347.7	28437.10	35443.00	34059.20	47383.48	47441.00
0.05	38957.2	27424.70	34987.60	33661.30	46466.11	46423.00

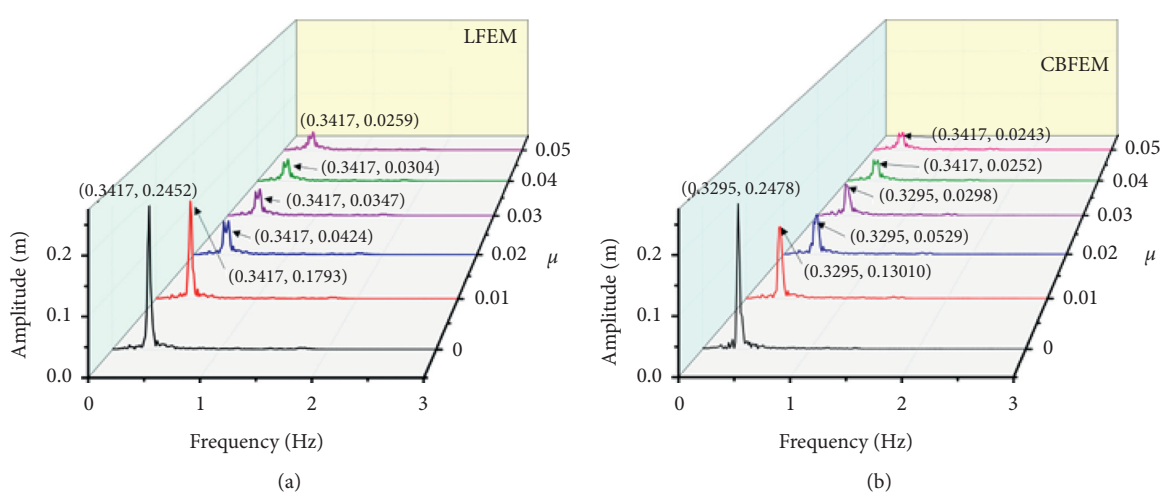

Figure 17: Continued.

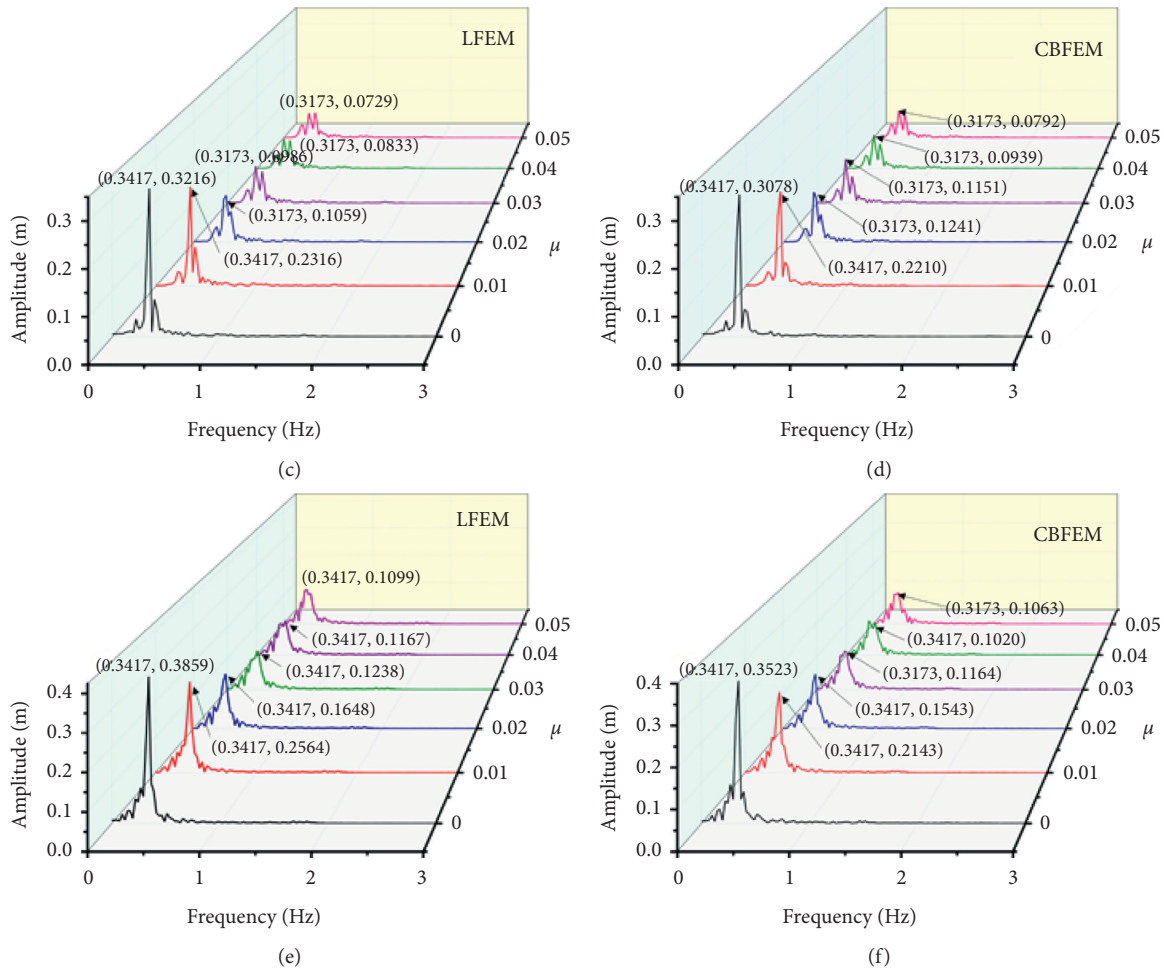

Figure 17: The Fourier spectra of the top displacement. (a) LFEM under the El-Centro. (b) CBFEM under the El-Centro. (c) LFEM under the Chalfant. (d) CBFEM under the Chalfant. (e) LFEM under artificial wave. (f) CBFEM under artificial wave.

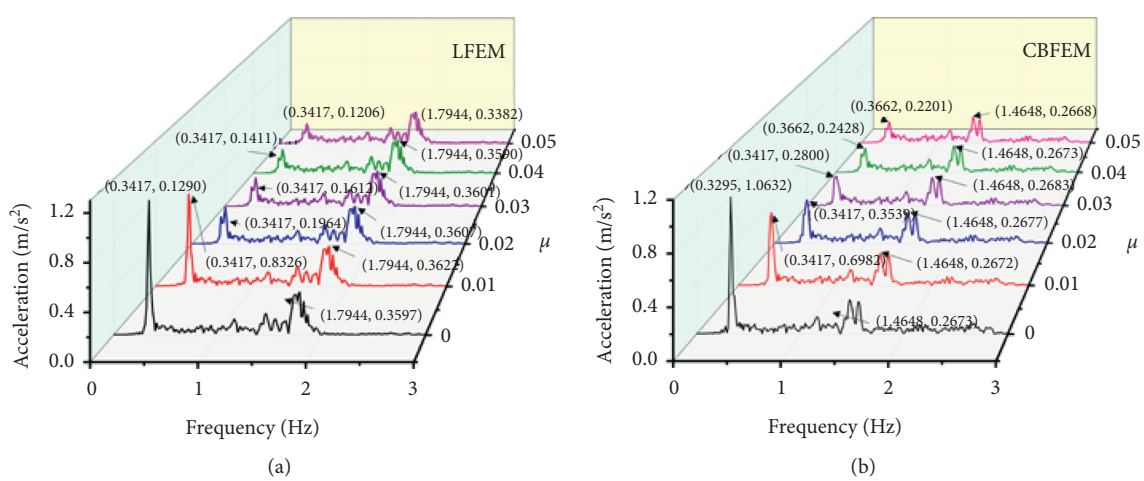

Figure 18: Continued.

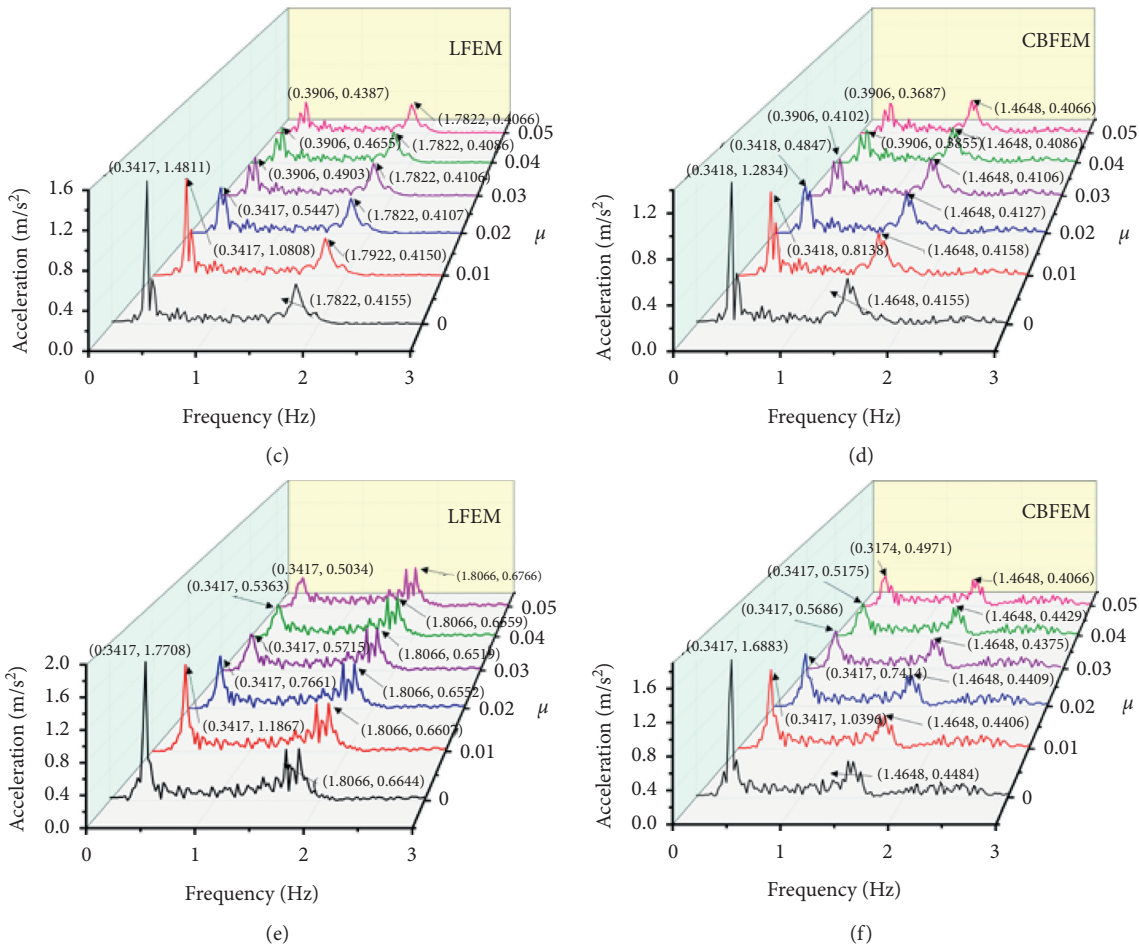

Figure 18: The Fourier spectrum of the top acceleration. (a) LFEM under the El-Centro. (b) CBFEM under the El-Centro. (c) LFEM under the Chalfant. (d) CBFEM under the Chalfant. (e) LFEM under artificial wave. (f) CBFEM under artificial wave.

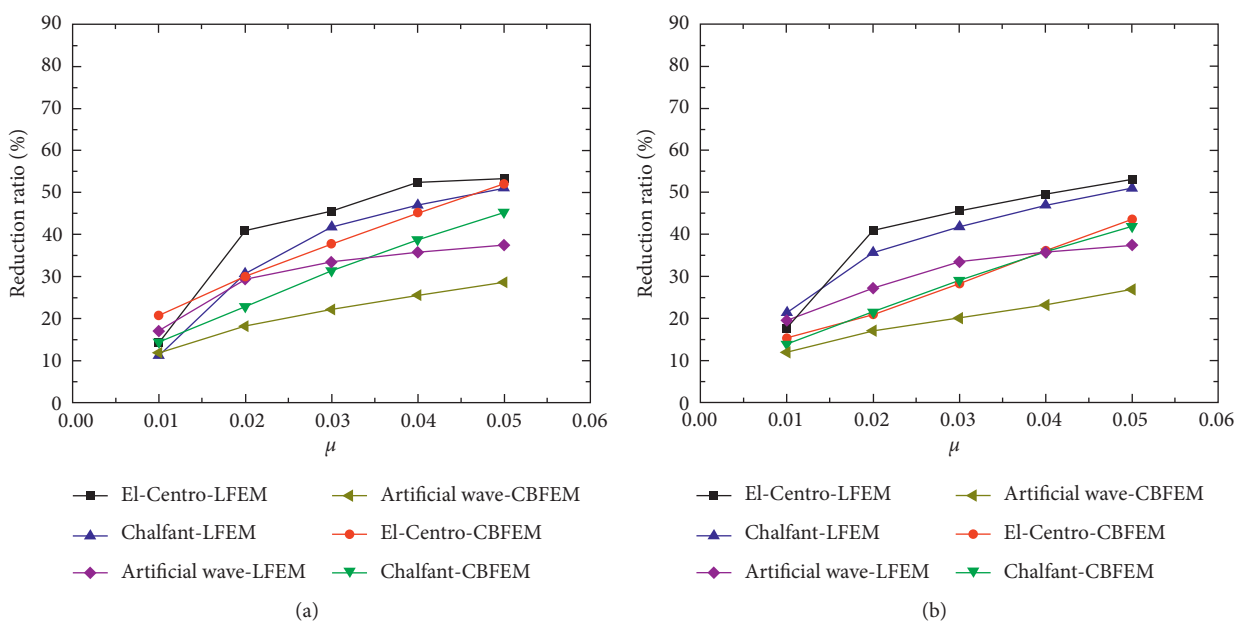

Figure 19: Continued.

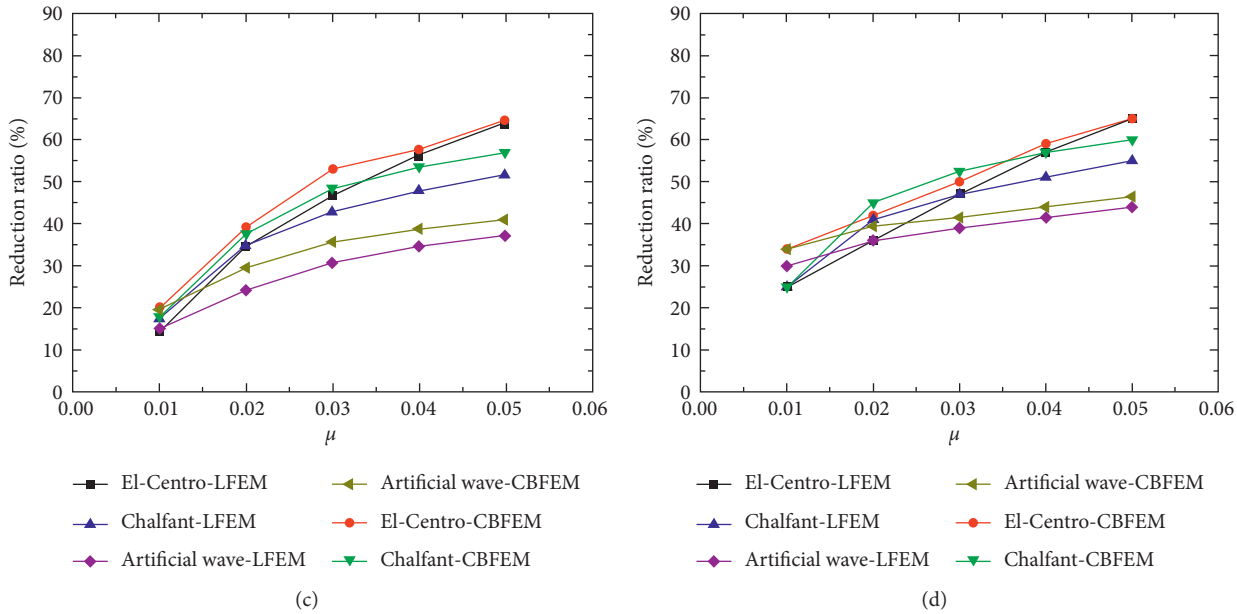

Figure 19: The reduction ratio of displacement produced by bi-directional ground motion. (a) Displacement in fore-aft direction. (b) Displacement in side-side direction. (c) Displacement standard deviation in fore-aft direction. (d) Displacement standard deviation in side-side direction.

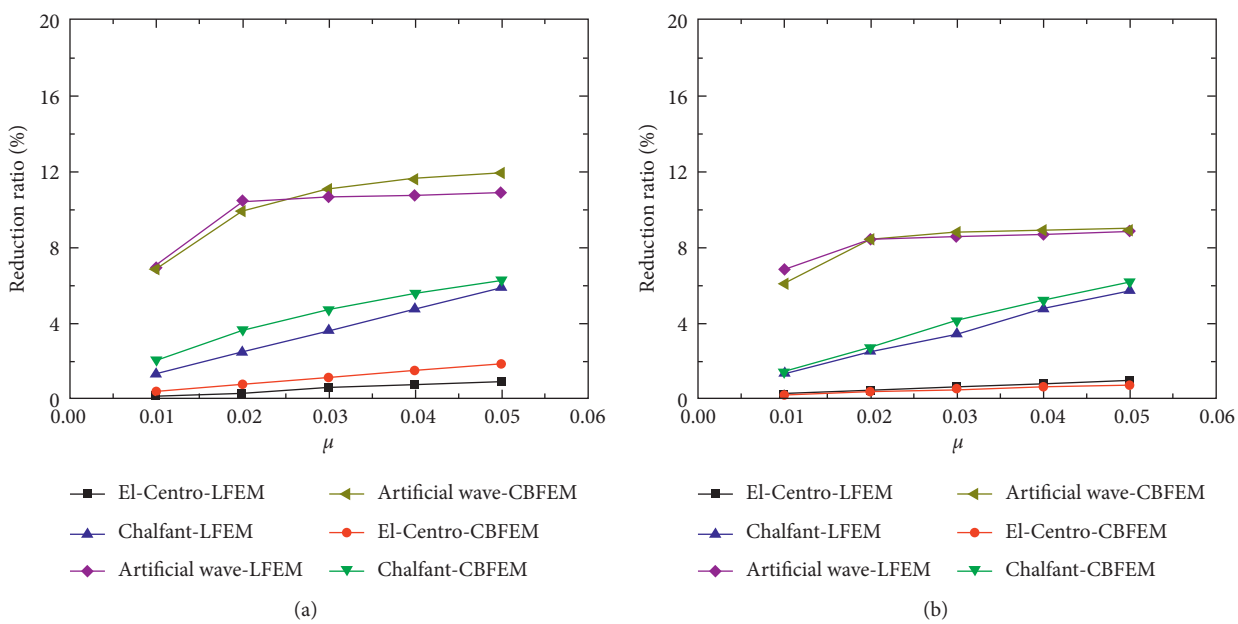

Figure 20: Continued.

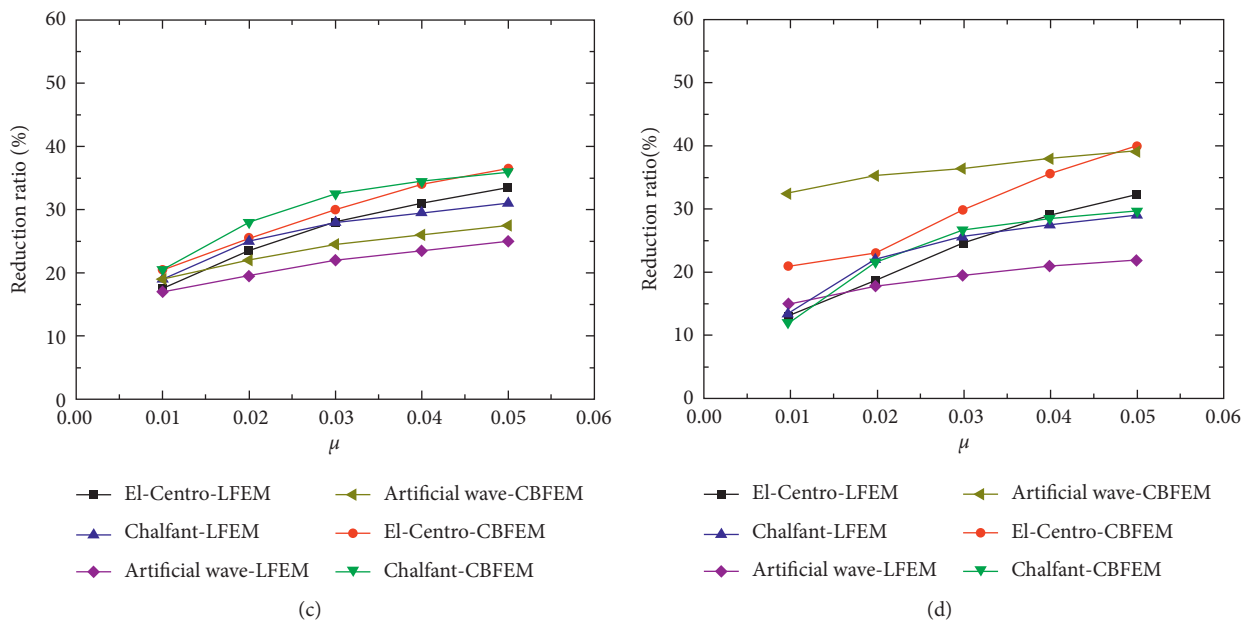

Figure 20: The reduction ratio of acceleration induced by bi-directional earthquakes. (a) Acceleration in fore-aft direction. (b) Acceleration in side-side direction. (c) Acceleration standard deviation in fore-aft direction. (d) Acceleration standard deviation in side-side direction.

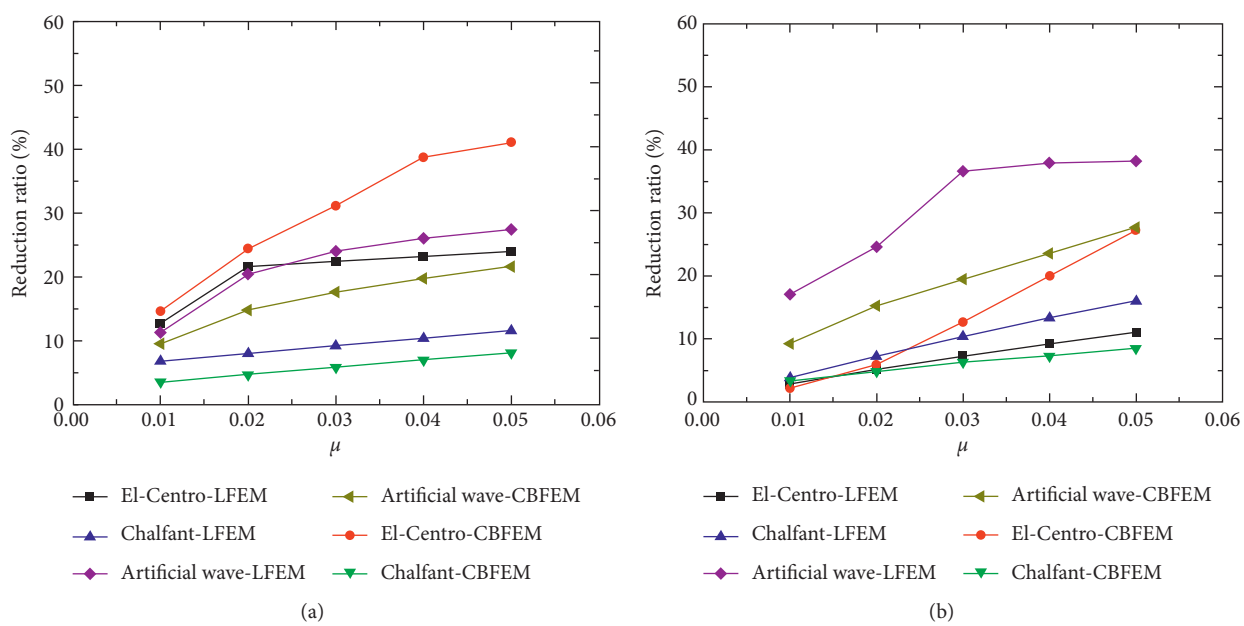

Figure 21: Continued.

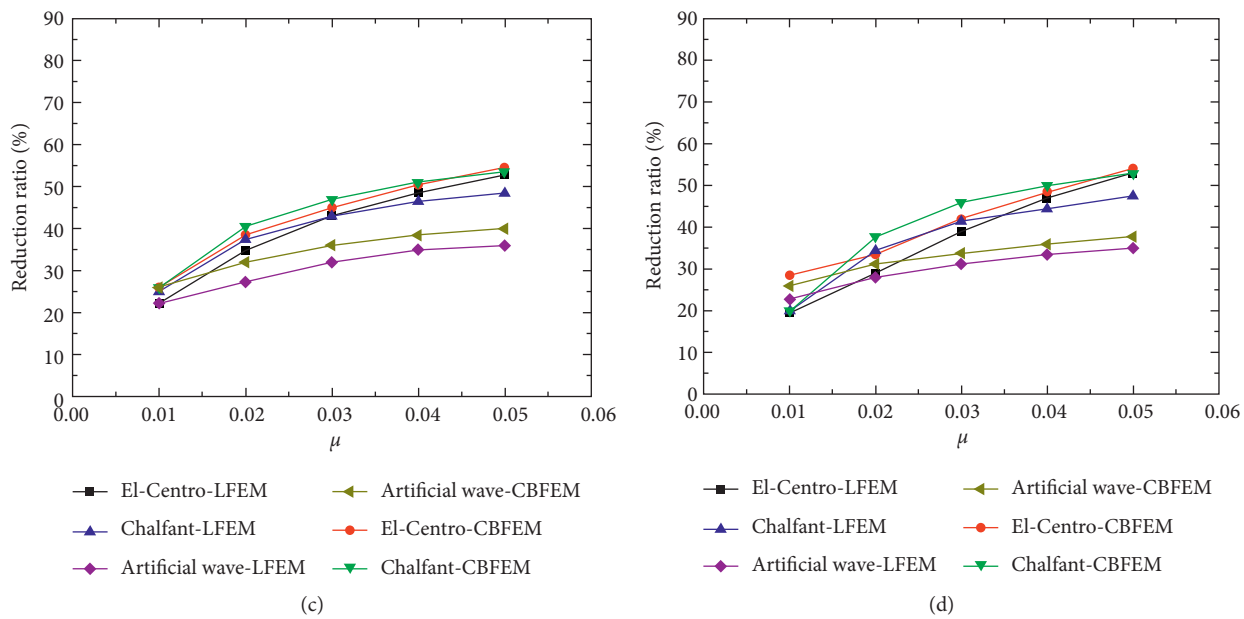

Figure 21: The reduction ratio of the bottom bending moments induced by bi-directional earthquakes. (a) The peak value in fore-aft direction. (b) The peak value in side-side direction. (c) The standard deviation in fore-aft direction. (d) The standard deviation in side-side direction.

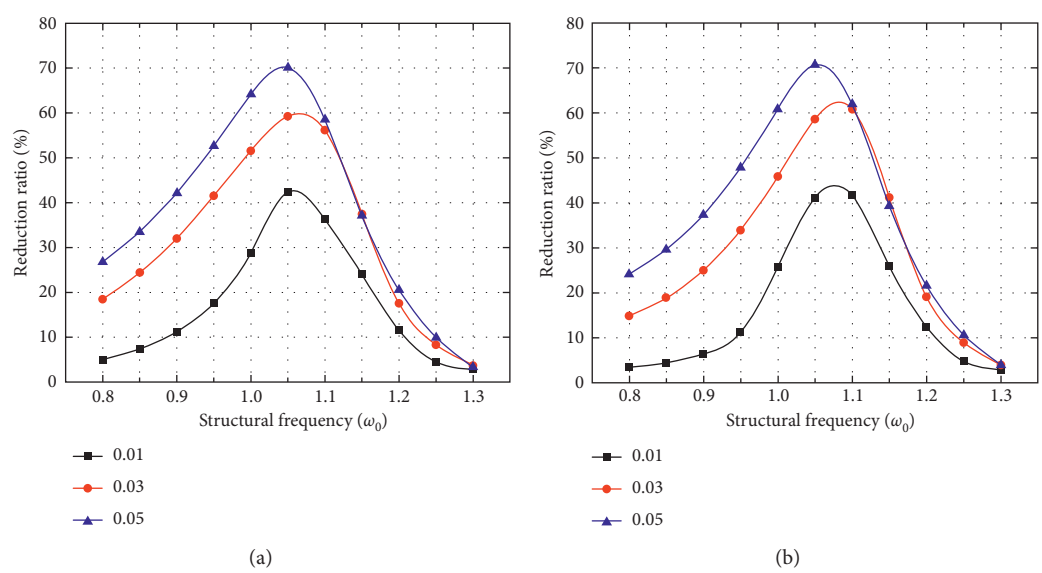

Figure 22: Continued.

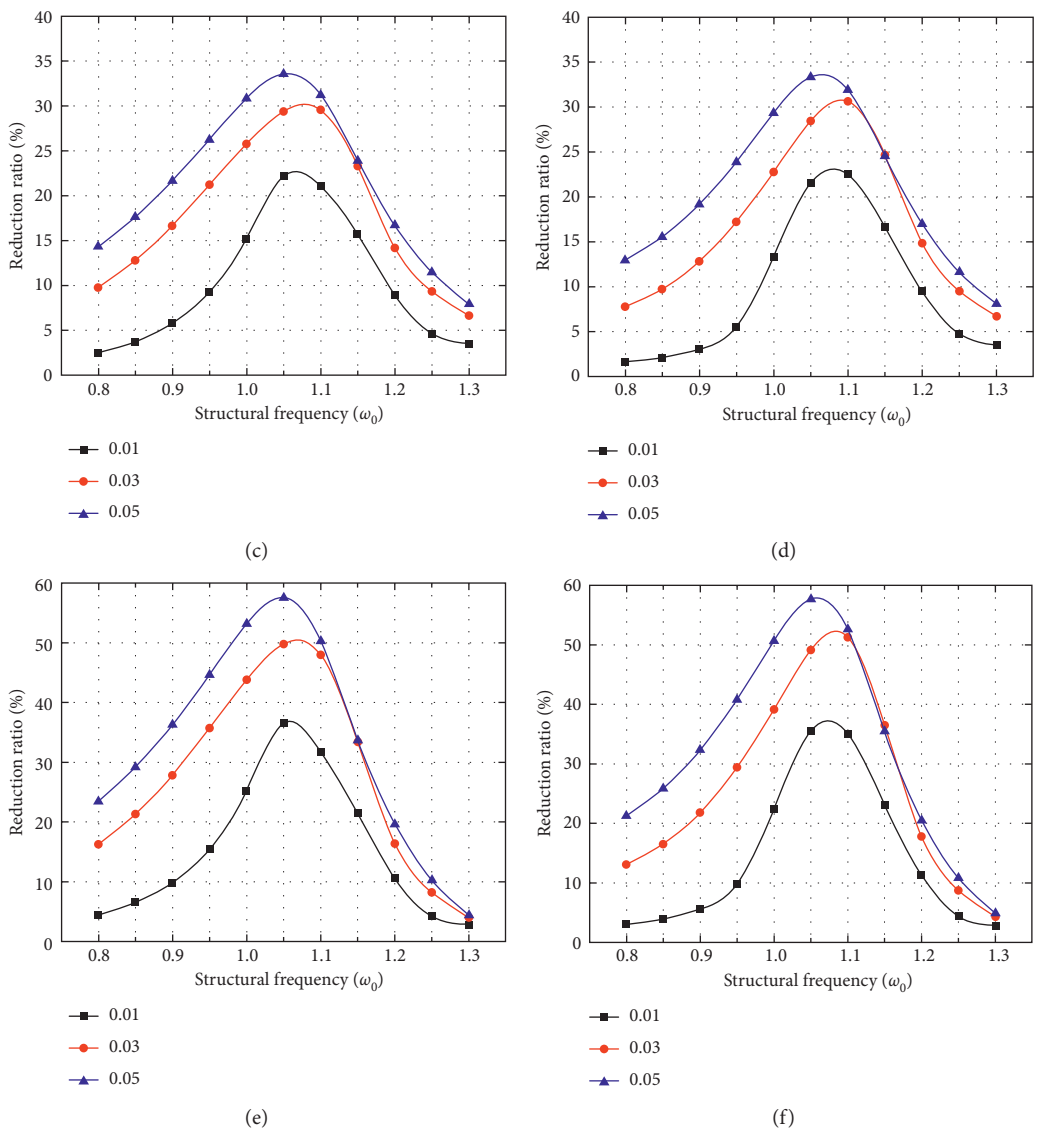

Figure 22: The reduction ratio of structural responses induced by bi-directional earthquakes. (a) Fore-aft direction displacement. (b) Side-side direction displacement. (c) Fore-aft direction acceleration. (d) Side-side direction acceleration. (e) Fore-aft direction moment. (f) Side-side direction moment.

calculated using the CBFEM is lower than those calculated using the LFEM due to the blade tower coupling effect.

5.2. The Influence of Wind Turbine Frequency on the Response Reduction. The natural frequency of the wind turbine is time-varying, which is influenced by many factors, including the centrifugal stiffening effect of the blade, ice, snow, and temperature. The BTMD might be mistuned due to the frequency variation. The mistuning effect would lead to the malfunction of the BTMD, even the amplification of structural responses. Therefore, the influence of frequency variation on the mitigation efficiency of the BTMD is investigated using the LFEM and CBFEM. The fundamental structural frequency varies from 0.8 ω_0 to 1.3 ω_0, where ω_0 is the initial fundamental frequency of the wind turbine. Accordingly, the displacement, acceleration, and bending moment reduction ratios of the wind turbine with different mass ratios BTMD are shown in Figure 22.

The structural response reduction ratios increase with the increase of structural frequency before the structural frequency reaches 1.05 ω_0. The opposite situation applies to the situation that the structural frequency exceeds 1.05 ω_0. The phenomenon is caused by the reason that the system wind turbine and TMD cannot resonate when the structural frequency is far from ω_0, which causes smaller movement of the mass block. Generally, the BTMD can reduce effectively when the wind turbine frequency changed slightly.

6. Conclusions

In this study, a BTMD is proposed to mitigate the seismic vibration of the wind turbine tower. Accordingly, the LFEM and CBFEM are used to investigate the vibration mitigation performance of the proposed BTMD. Afterward, the mitigation performances of the BTMD under uni- and bi-directional earthquakes are investigated. The displacement, acceleration, and bending moment of the wind turbine tower are analyzed in time-domain and frequency-domain. The following conclusions can be drawn from this study:

(1) The first two natural frequencies of the LFEM and CBFEM are similar to each other. However, the other natural frequencies of the LFEM are larger than that of the CBFEM due to the blade tower coupling effect. Meanwhile, the blade coupling effect is evident in the mode shape of the CBFEM. Accordingly, the reduction ratio calculated using the CBFEM is lower than those calculated using the LFEM. Hence, the coupling effect may have significant influences on the mitigation efficiency of the BTMD.

(2) The reduction ratios of the structural responses in two directions are similar to each other, which grow with the increase of the mass ratio. The proposed BTMD can significantly mitigate the peak values of the top displacement and bottom bending moment. However, it shows weak efficiency in controlling the peak acceleration, especially in the initial stage. Note that the BTMD can effectively depress the fatigue load of the wind turbines.

(3) The Fourier spectra of the displacement are mainly concentrated around the first natural frequency. However, the frequency peak of acceleration appears around the first two natural frequencies. The amplitude around the controlled frequency decreases significantly with the increase of the mass ratio. The mitigation efficiency of the BTMD would decrease with the structural frequency far away from the controlled frequency.

Data Availability

The finite element model, the responses data, and the code used to support the findings of this study are available from the corresponding author upon request.

Conflicts of Interest

The authors declare that there are no conflicts of interest regarding the publication of this paper.

Acknowledgments

This research was funded by the National Natural Science Foundation of China (grant numbers 51908266 and 51568041), the Hongliu Excellent Young Scholar Support Program of Lanzhou University of Technology, and the Fund of International Research Based on Seismic Mitigation and Isolation of Gansu Province (grant number GII2018-N04).

References

[1] C.-C. Lin, J.-M. Ueng, and T.-C. Huang, "Seismic response reduction of irregular buildings using passive tuned mass dampers," *Engineering Structures*, vol. 22, no. 5, pp. 513–524, 2000.

[2] C. Li, "Performance of multiple tuned mass dampers for attenuating undesirable oscillations of structures under the ground acceleration," *Earthquake Engineering & Structural Dynamics*, vol. 29, no. 9, pp. 1405–1421, 2000.

[3] C. Xing, H. Wang, A. Li, and Y. Xu, "Study on wind-induced vibration control of a long-span cable-stayed bridge using TMD-type counterweight," *Journal of Bridge Engineering*, vol. 19, no. 1, pp. 141–148, 2014.

[4] J. Ou, X. Long, Q. S. Li, and Y. Q. Xiao, "Vibration control of steel jacket offshore platform structures with damping isolation systems," *Engineering Structures*, vol. 29, no. 7, pp. 1525–1538, 2007.

[5] H. N. Li and X. L. Ni, "Optimization of non-uniformly distributed multiple tuned mass damper," *Journal of Sound and Vibration*, vol. 308, no. 2, pp. 80–97, 2007.

[6] Z. Lu, X. Chen, D. Zhang, and K. Dai, "Experimental and analytical study on the performance of particle tuned mass dampers under seismic excitation," *Earthquake Engineering & Structural Dynamics*, vol. 46, no. 5, pp. 697–714, 2017.

[7] J. C. H. Chang and T. T. Soong, "Structural control using active tuned mass dampers," *Journal of the Engineering Mechanics Division*, vol. 106, no. 6, pp. 1091–1098, 1980.

[8] X. Yan, Z. D. Xu, and Q. X. Shi, "Fuzzy neural network control algorithm for asymmetric building structure with active tuned mass damper," *Journal of Vibration and Control*, vol. 26, no. 21-22, 2020.

[9] M. D. Symans and M. C. Constantinou, "Semi-active control systems for seismic protection of structures: a state-of-the-art review," *Engineering Structures*, vol. 21, no. 6, pp. 469–487, 1999.

[10] T. Pinkaew and Y. Fujino, "Effectiveness of semi-active tuned mass dampers under harmonic excitation," *Engineering Structures*, vol. 23, no. 7, pp. 850–856, 2001.

[11] K. Karami, S. Manie, K. Ghafouri, and S. Nagarajaiah, "Nonlinear structural control using integrated DDA/ISMP and semi-active tuned mass damper," *Engineering Structures*, vol. 181, pp. 589–604, 2019.

[12] T. T. Soong and B. F. Spencer Jr., "Supplemental energy dissipation: state-of-the-art and state-of-the-practice," *Engineering Structures*, vol. 24, no. 3, pp. 243–259, 2002.

[13] H. Kim and H. Adeli, "Wind-induced motion control of 76-story benchmark building using the hybrid damper-TLCD system," *Journal of Structural Engineering*, vol. 131, no. 12, pp. 1794–1802, 2005.

[14] G. M. Stewart and M. A. Lackner, "The impact of passive tuned mass dampers and wind-wave misalignment on offshore wind turbine loads," *Engineering Structures*, vol. 73, pp. 54–61, 2014.

[15] O. Altay, F. Taddei, C. Butenweg, and S. Klinkel, "Vibration mitigation of wind turbine towers with tuned mass dampers," in *Wind Turbine Control and Monitoring*, pp. 337–373, Springer, Cham, Switzerland, 2014.

[16] B. Zhao, H. Gao, Z. Wang, and Z. Lu, "Shaking table test on vibration control effects of a monopile offshore wind turbine

with a tuned mass damper," *Wind Energy*, vol. 21, no. 12, pp. 1309–1328, 2018.

[17] S. Colwell and B. Basu, "Tuned liquid column dampers in offshore wind turbines for structural control," *Engineering Structures*, vol. 31, no. 2, pp. 358–368, 2009.

[18] T. Buckley, P. Watson, P. Cahill, V. Jaksic, and V. Pakrashi, "Mitigating the structural vibrations of wind turbines using tuned liquid column damper considering soil-structure interaction," *Renewable Energy*, vol. 120, pp. 322–341, 2018.

[19] A. Hemmati, E. Oterkus, and M. Khorasanchi, "Vibration suppression of offshore wind turbine foundations using tuned liquid column dampers and tuned mass dampers," *Ocean Engineering*, vol. 172, pp. 286–295, 2019.

[20] K. S. Dai, J. Z. Wang, R. F. Mao, Z. H. Xiang, and Z. Lu, "Wind tunnel test study on a new passive damper TL-PD," *Earthquake Engineering and Engineering Vibration*, vol. 01, no. 5, pp. 35–40, 2015, in Chinese.

[21] J. Chen, G. Zhan, and Y. Zhao, "Application of spherical tuned liquid damper in vibration control of wind turbine due to earthquake excitations," *The Structural Design of Tall and Special Buildings*, vol. 25, no. 10, pp. 431–443, 2016.

[22] Z. Zhang, A. Staino, B. Basu, and S. R. K. Nielsen, "Performance evaluation of full-scale tuned liquid dampers (TLDs) for vibration control of large wind turbines using real-time hybrid testing," *Engineering Structures*, vol. 126, pp. 417–431, 2016.

[23] C. Van der Woude and S. Narasimhan, "A study on vibration isolation for wind turbine structures," *Engineering Structures*, vol. 60, pp. 223–234, 2014.

[24] W. R. Li, J. Huang, and Y. F. Du, "Dynamic response analysis of wind turbines under long-period ground motions," *Data Mining in Structural Dynamic Analysis*, pp. 65–84, Springer, Singapore, 2019.

[25] H. Zuo, K. Bi, and H. Hao, "Using multiple tuned mass dampers to control offshore wind turbine vibrations under multiple hazards," *Engineering Structures*, vol. 141, pp. 303–315, 2017.

[26] M. Hussan, M. S. Rahman, F. Sharmin, D. Kim, and J. Do, "Multiple tuned mass damper for multi-mode vibration reduction of offshore wind turbine under seismic excitation," *Ocean Engineering*, vol. 160, pp. 449–460, 2018.

[27] S. Gaur, S. Elias, T. Höbbel, V. A. Matsagar, and K. Thiele, "Tuned mass dampers in wind response control of wind turbine with soil-structure interaction," *Soil Dynamics and Earthquake Engineering*, vol. 132, Article ID 106071, 2020.

[28] Y. Hu, J. Wang, M. Z. Q. Chen, Z. Li, and Y. Sun, "Load mitigation for a barge-type floating offshore wind turbine via inerter-based passive structural control," *Engineering Structures*, vol. 177, pp. 198–209, 2018.

[29] R. Zhang, Z. Zhao, and K. Dai, "Seismic response mitigation of a wind turbine tower using a tuned parallel inerter mass system," *Engineering Structures*, vol. 180, pp. 29–39, 2019.

[30] M. L. Brodersen, A.-S. Bjørke, and J. Høgsberg, "Active tuned mass damper for damping of offshore wind turbine vibrations," *Wind Energy*, vol. 20, no. 5, pp. 783–796, 2017.

[31] C. Sun, "Semi-active control of monopile offshore wind turbines under multi-hazards," *Mechanical Systems and Signal Processing*, vol. 99, pp. 285–305, 2018.

[32] C. Sun and V. Jahangiri, "Bi-directional vibration control of offshore wind turbines using a 3D pendulum tuned mass damper," *Mechanical Systems and Signal Processing*, vol. 105, pp. 338–360, 2018.

[33] X. Tong, X. Zhao, and S. Zhao, "Load reduction of a monopile wind turbine tower using optimal tuned mass dampers," *International Journal of Control*, vol. 90, no. 7, pp. 1283–1298, 2017.

[34] M. Rahman, Z. C. Ong, W. T. Chong, S. Julai, and S. Y. Khoo, "Performance enhancement of wind turbine systems with vibration control: a review," *Renewable and Sustainable Energy Reviews*, vol. 51, pp. 43–54, 2015.

[35] H. R. Zuo, K. M. Bi, and H. Hao, "A state-of-the-art review on the vibration mitigation of wind turbines," *Renewable and Sustainable Energy Reviews*, vol. 121, Article ID 109710, 2020.

[36] N. Bazeos, G. D. Hatzigeorgiou, I. D. Hondros, H. Karabalis, and D. E. Beskos, "Static, seismic and stability analyses of a prototype wind turbine steel tower," *Engineering Structures*, vol. 24, no. 8, pp. 1015–1025, 2002.

[37] I. Lavassas, G. Nikolaidis, P. Zervas, E. Efthimiou, I. N. Doudoumis, and C. C. Baniotopoulos, "Analysis and design of the prototype of a steel 1-MW wind turbine tower," *Engineering Structures*, vol. 25, no. 8, pp. 1097–1106, 2003.

[38] R. Harrison, E. Hau, and H. Snel, *Large Wind Turbines: Design and Economics*, John Wiley and Sons, Ltd, New York, NY, USA, 2000.

[39] A. Banerjee, T. Chakraborty, V. Matsagar, and M. Achmus, "Dynamic analysis of an offshore wind turbine under random wind and wave excitation with soil-structure interaction and blade tower coupling," *Soil Dynamics and Earthquake Engineering*, vol. 125, Article ID 105699, 2019.

[40] International Electrotechnical Commission (IEC), *Wind Turbines-Part 1: Design Requirements*, International Electrotechnical Commission, Geneva, Switzerland, IEC 61400-1, 3rd edition, 2005.

[41] GB 50011-2010, *Code for Seismic Design of Buildings*, China Ministry of Construction, Beijing, China, 2016, in Chinese.

[42] T. Tao, H. Wang, and K. Zhao, "Efficient simulation of fully non-stationary random wind field based on reduced 2D hermite interpolation," *Mechanical Systems and Signal Processing*, vol. 150, Article ID 107265, 2021.

[43] T. Tao, H. Wang, L. Hu, and A. Kareem, "Error analysis of multivariate wind field simulated by interpolation-enhanced spectral representation method," *Journal of Engineering Mechanics*, vol. 146, no. 6, Article ID 04020049, 2020.

[44] T. Tao and H. Wang, "Modelling of longitudinal evolutionary power spectral density of typhoon winds considering high-frequency subrange," *Journal of Wind Engineering and Industrial Aerodynamics*, vol. 193, Article ID 103957, 2019.

[45] T. Tao, H. Wang, C. Yao, X. He, and A. Kareem, "Buffeting analysis of long-span bridges under typhoon winds with time-varying spectra and coherences," *Journal of Structural Engineering*, vol. 146, no. 2, Article ID 04020255, 2018.

[46] D. Witcher, "Seismic analysis of wind turbines in the time domain," *Wind Energy*, vol. 8, no. 1, pp. 81–91, 2005.

[47] D. H. Kim, S. G. Lee, and I. K. Lee, "Seismic fragility analysis of 5 MW offshore wind turbine," *Renewable Energy*, vol. 65, pp. 250–256, 2014.

Hindawi
Mathematical Problems in Engineering
Volume 2020, Article ID 5453138, 17 pages
https://doi.org/10.1155/2020/5453138

Research Article

Dynamic Response of Composite Lining Tunnel with Buffer Layer: An Analytical and Experimental Investigation

Kaixiang Fan,[1] Yusheng Shen ,[1,2] Shuaishuai Wang,[1,3] Bo Gao,[1] Qing Zheng,[1] Gaoming Yan,[1] and Peng Min[1]

[1]*Key Laboratory of Transportation Tunnel Engineering, Ministry of Education, School of Civil Engineering, Southwest Jiaotong University, Chengdu 610031, China*
[2]*National Engineering Laboratory for Technology of Geological Disaster Prevention in Land Transportation, Southwest Jiaotong University, Chengdu 611756, China*
[3]*CCCC Second Highway Engineering Co., Ltd., Xi'an 710065, China*

Correspondence should be addressed to Yusheng Shen; sys1997@163.com

Received 16 August 2020; Revised 28 September 2020; Accepted 9 November 2020; Published 23 November 2020

Academic Editor: Kaiming Bi

Composite lining is often designed for the mountainous tunnels in high-intensity earthquake areas. The application of the buffer layer will bring more advantages, while the shock-absorbing mechanism is still unclear currently. In this paper, based on the Fourier-Bessel series expansion method, the dynamic stress concentration factor of composite lining tunnel with buffer layer subjected to plane SV waves in the half-space is obtained. Then, the influence of geometric and mechanical parameters of the buffer layer on composite lining was systematically analyzed. Finally, the correctness of the analytical solutions is verified by series shaking table tests and numerical simulations. Results suggest that the buffer layer can play the role of "redistributing" the seismic load, and it can effectively reduce the dynamic responses of secondary lining but amplify in primary support. There is an optimal interval of the stiffness and thickness for the buffer layer. When the stiffness ratio of the buffer layer to surrounding rock is 1/10 ~ 1/50 or the ratio of buffer layer thickness to inner diameters of secondary lining is 1/40 ~ 1/20, the shock-absorbing performance is remarkable. The general damage observations in tests show that the crown, arch springing, and invert of composite lining in case of no buffer layer are prone to cracking under a strong earthquake. The invert of the composite lining is more susceptible to be damaged after adopting the buffer layer. In general, the analytical results were consistent with experimental and numerical results. The above study results may provide theoretical support and experimental data for the seismic design of composite lining tunnels.

1. Introduction

Generally, the underground structure has been considered to have better seismic performance compared with surface structure. However, regarding the Kobe earthquake in Japan in 1995, a large number of underground structures suffered severe damage [1], which overturns the traditional concepts. Underground facilities are often used as lifeline engineering, the repair of earthquake damage comes at a high cost, and seismic fortification measures have drawn great attention [2].

Generally, antiseismic and shock absorption measures are two kinds for seismic design of tunnel [3]. The antiseismic measures are mainly to strengthen the surrounding rock (grouting around the lining, drainage, installation of anchor rods, etc.) or to improve the stiffness of the lining structure (using high-performance concrete, increasing the thickness, increasing the reinforcement, etc.) [4, 5]. The shock absorption measures are usually to design buffer layers with thinner thickness and smaller stiffness around the outer lining. The most common buffer layers are simple plate-type and injection-type; the former is represented by rubber, while the latter is represented by foamed concrete, polymer [6–11]. The buffer layer is much softer than the surrounding rock and lining; thus, the interaction

between the lining and surrounding rock could be improved [12, 13]. Compared with antiseismic measures, it is simple and effective to adopt buffer layers [14]. Surely, antiseismic measures and shock absorption measures can both be adopted in the seismic design of tunnels, under some special adverse geological conditions [15]. In practical engineering, the buffer layer mainly consists of rubber material and compressible foamed concrete. Rubber material is a typical superelastic material, its shear modulus is lower than the lining, and it can bear large deformation. Foam concrete is relatively widely used for the following reasons [16]: (1) foamed concrete has good deformation performance due to the presence of a large number of pores; (2) the mix ratio and casting thickness of foamed concrete can be adjusted quantitatively; (3) foamed concrete is easy to adapt to the geological environment and site construction requirements.

Different kinds of methods have been employed for seismic design of tunnels, such as field prototype observation [17–19], shaking table tests [20–24], numerical simulations [25–29], and analytical methods. Field prototype observation data for earthquake damage are scarce. Therefore, the mechanism and measures of antiseismic and shock absorption are mainly explored by analytical methods, shaking table tests, and numerical simulations. Analytical methods play an irreplaceable role compared with the numerical method; besides, it is also an important means to verify the accuracy of numerical methods [30]. Shaking table test can reproduce various seismic waves in the lab, directly reappear the earthquake damage phenomenon, and obtain the dynamic response of the structure, so it is an effective method to solve the complex seismic engineering problems [31].

In terms of analytical methods, wave function expansion has been widely used in the dynamic stress concentration of tunnel structures, which can reveal the mechanical response mechanism of composite lining tunnel with buffer layer in essence and can be used to verify the numerical calculation and test results. Separation of variables is adopted to get the ordinary differential equations in the Fourier-Bessel series expansion method, then the general solutions can be expanded into the Fourier-Bessel series, and finally, the closed solution of the potential function can be solved in given boundary conditions. The key to wave function expansion method is to establish a special coordinate system that can describe the geometry of the scatterer, so it is only applicable to some simple and regular geometry, such as circular, elliptic, or parabolic cross section. In addition, the wave function expansion method is suitable for low-frequency incident wave in the near field. Pao [32] pioneeringly studied the problem of dynamic stress concentration of hollow cavities and lining tunnels in infinite space under elastic wave incidence. Davis [33] and Lee [30, 34–36] deduced the dynamic stress concentration of circular lining tunnel under SH and SV waves incidence and analyzed the dynamic response law of flexible pipe subjected to real seismic wave. Xu et al. [37] gave the series solution of a semispace circular tunnel under subjected to P waves. Kara [38] studied the diffraction of plane SH waves in a cylindrical tunnel in a homogeneous and isotropic elastic 1/4 space. Lin [39] proposed analytical solutions for semispace surfaces on stress-free boundary conditions and relaxed boundary conditions. Fan [40] introduced a linear spring model to describe the imperfect contact surface between rock mass and lining and then studied the dynamic response of circular lining tunnel to plane SV waves.

However, most of the literature focuses on monolayer lining and lacking theoretical analysis on the dynamic response of the composite lining. What is more, there is a general lack of experimental demonstration, which makes analytical solutions difficult to apply widely. Hence, in this paper, the wave function expansion method is adopted to study the dynamic stress concentration of composite lining tunnel with buffer layer subjected to plane SV waves at different incident angles in elastic half-space. The influence of Young's modulus and thickness of the buffer layer on the dynamic stress of the composite lining is systematically analyzed. First, the series solutions of stress and displacement of composite lining are obtained by the Fourier-Bessel series expansion. Then, the linear equations of wave function coefficients are solved by MATLAB software, and the dynamic stress concentration factors (DSCF) of composite lining are obtained. The influences of angle of incidence, Young's modulus, and thickness of the buffer layer on DSCF are discussed. Finally, the correctness and reliability of the analytical solution are verified by shaking table tests and numerical simulation. Such studies could provide a reference for the seismic design of shallow-buried composite lining tunnel in high-intensity area.

2. Model of Composite Lining Tunnel with Buffer Layer

The model of "Primary Support-Buffer Layer-Secondary Lining" for composite lining tunnel in half-space is depicted in Figure 1.

The distance between the tunnel center and the half-space surface is h. The outer radius of primary support, buffer layer, and the secondary lining is R_1, R_2, and R_3 respectively. The inner radius of the secondary lining is R_4. The half-space and the composite lining are assumed to be isotropic, homogeneous, and elastic. The mechanical parameters are determined by Ramey's constants λ_i, G_i and density ρ_i, and the compression and shear wave velocities are denoted by $c_{\alpha,i}$ and $c_{\beta,i}$, where $i = s, p, b, l$, respectively, representing the surrounding rock, primary support, buffer layer, and secondary lining.

The equations of the scattering waves in the rectangular coordinate system are complicated. To simplify, a large arc is adopted to simulate the surface of half-space; then the scattering waves in half-space can be transformed from rectangular coordinate o to polar coordinate o_2. The large arc radius $b = 10000R_1$, where the center is located at o_2 and D is the distance between o_1 and o_2. Studies indicate that the solution converges to the exact solution when the arc is large enough [30]. In this section, the influence of initial stress is not considered in theoretical analysis, and the contact between surrounding rock and tunnel is ignored. It is assumed that the stress and displacement are continuous at the interfaces between the composite lining tunnel and the half-space.

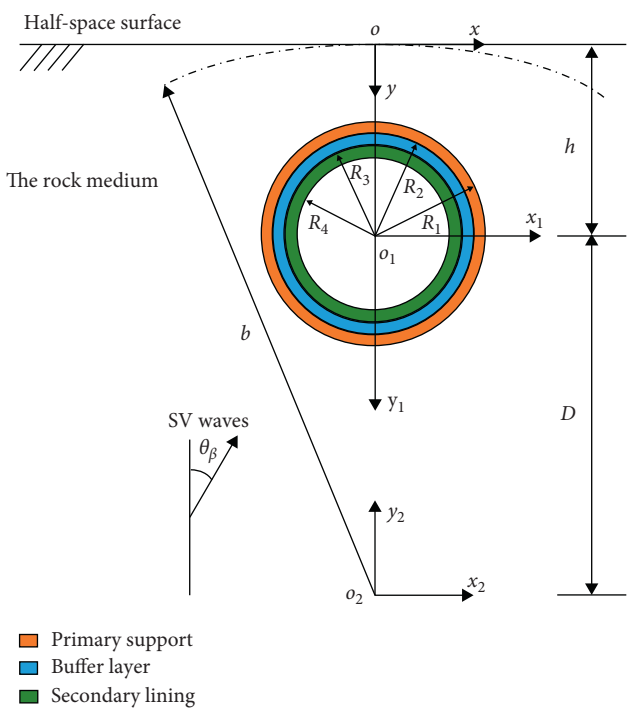

Figure 1: Model of composite lining with buffer layer in half-space.

2.1. Wave Function of Free Field in Half-Space. Planar harmonic SV waves are incident at θ_β, regardless of the dissipation during propagation; then the displacement potential function of steady-state incident waves can be expressed in rectangular coordinate $o(x, y)$ as [30]

$$\psi^{(i)}(x, y) = B_0 \exp\left[ik_{s\beta}(x\sin\theta_0 + y\cos\theta_0)\right]e^{-i\omega t}. \quad (1)$$

Waveform transition of the incident SV waves will occur on the half-space surface, generating reflected SV and P waves. The displacement potential function of reflected SV waves is

$$\psi^{(r)}(x, y) = B_1 \exp\left[ik_{s\beta}\left(x\sin\theta_\beta - y\cos\theta_\beta\right)\right]e^{-i\omega t}. \quad (2)$$

When the angle of incidence is larger than the critical angle, the reflected P waves will no longer be planar, but surface waves [41]. The critical angle is $\theta_{cr} = \sin^{-1}(c_{\beta,s}/c_{\alpha,s})$. Thus, two ways are analyzed through whether the angle of incidence is larger than the critical angle.

2.1.1. The Angle of Incidence Is Less Than the Critical Angle: $\theta_\beta < \theta_{cr}$. As a result, the reflected P waves are planar; the displacement potential function is as follows:

$$\phi^{(r)}(x, y) = B_2 \exp\left[ik_{s\alpha}(x\sin\theta_\alpha - y\cos\theta_\alpha)\right]e^{-i\omega t}, \quad (3)$$

where B_0, B_1, and B_2 are the amplitude of incident plane SV waves and reflected plane SV and P waves, respectively. $k_{s\alpha} = (\omega/c_{\alpha,s})$ is the number of P waves; $k_{s\beta} = (\omega/c_{\beta,s})$ is the number of SV waves. θ_β is the incidence and reflected angle of SV waves, and θ_α is the reflected angle of P waves. Ignoring the time item $e^{-i\omega t}$ and using Fourier-Bessel series, the displacement potential functions of the incident and reflected SV waves and reflected P waves in o_1, the coordinate system, are expanded as follows [30]:

$$\begin{aligned}\psi^{(i+r)}(r_1, \theta_1) &= \sum_{n=0}^{\infty} J_n\left(k_{s\beta}r_1\right)\left(C_{0,n}\sin n\theta_1 + D_{0,n}\cos n\theta_1\right),\\ \phi^{(r)}(r_1, \theta_1) &= \sum_{n=0}^{\infty} J_n\left(k_{s\alpha}r_1\right)\left(A_{0,n}\cos n\theta_1 + B_{0,n}\sin n\theta_1\right),\end{aligned} \quad (4)$$

where $J_n()$ is the Bessel function of the first kind and represent converging standing waves.

The coefficients $A_{0,n}$, $B_{0,n}$, $C_{0,n}$, and $D_{0,n}$ in the potential function are expressed as

$$\begin{aligned}\begin{Bmatrix} A_{0,n} \\ B_{0,n} \end{Bmatrix} &= \varepsilon_n i^n \begin{Bmatrix} \cos n\theta_\alpha \\ \sin n\theta_\alpha \end{Bmatrix} k_1 \exp\left(ik_{s\alpha}h\cos\theta_\alpha\right),\\ \begin{Bmatrix} C_{0,n} \\ D_{0,n} \end{Bmatrix} &= \varepsilon_n i^n \begin{Bmatrix} \sin n\theta_\beta \\ \cos n\theta_\beta \end{Bmatrix} \left[\mp(-1)^n \exp\left(-ik_{s\beta}h\cos\theta_\beta\right)\right.\\ &\quad \left. + k_2 \exp\left(ik_{s\beta}h\cos\theta_\beta\right)\right],\end{aligned} \quad (5)$$

where $k_{sa}\sin\theta_\alpha = k_{s\beta}\sin\theta_\beta$; $\varepsilon_n = 1$, for $n = 0$; $\varepsilon_n = 2$, for $n \geq 1$. The values of ε_n are derived from the Bessel function equation, which is transformed from $n = -\infty \longrightarrow \infty$ to $n = 0 \longrightarrow \infty$; k_1 and k_2 are the reflection coefficients of the incident wave on the half-space surface:

$$\left.\begin{aligned} k_1 &= \frac{2\left(c_{p,s}/c_{s,s}\right)^2 \sin 2\theta_\beta \cos 2\theta_\beta}{\sin 2\theta_\alpha \cos 2\theta_\beta + \left(c_{p,s}/c_{s,s}\right)^2 \cos^2\left(2\theta_\beta\right)}\\ k_2 &= \frac{\sin 2\theta_\alpha \cos 2\theta_\beta - \left(c_{p,s}/c_{s,s}\right)^2 \cos^2\left(2\theta_\beta\right)}{\sin 2\theta_\alpha \cos 2\theta_\beta + \left(c_{p,s}/c_{s,s}\right)^2 \cos^2\left(2\theta_\beta\right)}\end{aligned}\right\}, \quad (6)$$

where $c_{p,s}$ and $c_{s,s}$ are the wave velocities of P and SV in half-space, respectively.

2.1.2. When the Angle of Incidence of Plane SV Waves Is Larger Than the Critical Angle: $\theta_\beta > \theta_{cr}$. The reflected angle of reflected P waves satisfies Snell's law: $\sin\theta_\alpha = (c_{\alpha,s}/c_{\beta,s})\sin\theta_\beta > 1$; however, the reflected angle θ_α has no real solution, thus introducing a real number Φ_α to make the following equation hold [42]:

$$1 < \left(\frac{c_{\alpha,s}}{c_{\beta,s}}\right)\sin\theta_\beta = \cosh\Phi_\alpha = \cos i\Phi_\alpha = \sin\left(\frac{\pi}{2} - i\Phi_\alpha\right) = \sin\theta_\alpha, \quad (7)$$

where $\theta_\alpha = (\pi/2) - i\Phi_\alpha$ is a complex angle. Defining two real numbers to simplify the equations: $k = k_{s\alpha}\sin\theta_\alpha = k_{s\beta}\sin\theta_{s\beta}$; $\gamma = -ik_{s\alpha}\cos\theta_\alpha$.

By transformation, the reflected P waves in the coordinate (x, y) can be expressed as

$$\phi^{(r)}(x, y) = B_2 \exp(-\gamma y + ikx), \quad (8)$$

which can be expressed in cylindrical coordinates, $o_1(r_1, \theta_1)$:

$$\phi^{(r)}(r_1,\theta_1)=k_1\exp(-\gamma h)\exp(-\gamma r_1\cos\theta_1+ikr_1\sin\theta_1). \quad (9)$$

Further, expanding it in Fourier-Bessel series and for $\theta_\beta>\theta_{cr}$, it can also be solved according to the case of $\theta_\beta<\theta_{cr}$:

$$\phi^{(r)}(r_1,\theta_1)=\sum_{n=0}^{\infty}J_n(k_{s\alpha}r_1)\left(A_{0,n}\cos n\theta_1+B_{0,n}\sin n\theta_1\right),$$
$$\left.\begin{aligned}A_{0,n}&=\frac{1}{N}\sum_{l=0}^{2N-1}\frac{\phi^*(r_1,(\pi l/N))\cos((\pi l/N)n)}{J_n(k_{sa}r_1)}\\ B_{0,n}&=\frac{1}{N}\sum_{l=0}^{2N-1}\frac{\phi^*(r_1,(\pi l/N))\sin((\pi l/N)n)}{J_n(k_{sa}r_1)}\end{aligned}\right\}, \quad (10)$$

When the incident SV waves and reflected SV and P waves in free field encounter the tunnel, radial dispersed scattering P waves $\phi_{s1}(r_1,\theta_1)$ and SV waves $\psi_{s1}(r_1,\theta_1)$ will be generated. The Fourier-Bessel series expansion of the displacement potential function is as follows:

$$\begin{cases}\phi_{s1}(r_1,\theta_1)=\sum_{n=0}^{\infty}H_n^{(1)}(k_{s\alpha}r_1)\left(A_{s1,n}\cos n\theta_1+B_{s1,n}\sin n\theta_1\right),\\ \psi_{s1}(r_1,\theta_1)=\sum_{n=0}^{\infty}H_n^{(1)}\left(k_{s\beta}r_1\right)\left(C_{s1,n}\sin n\theta_1+D_{s1,n}\cos n\theta_1\right),\end{cases} \quad (11)$$

where $H_n^{(1)}$ represents the Hankel functions of the first kind, which satisfies the Sommerfeld radiation condition and can represent a diverging standing wave. $A_{s1,n},B_{s1,n},\ldots,A_{s1,m},B_{s1,m},\ldots$ are the undetermined coefficients in the wave potential function.

In addition, the scattering P and SV waves on the tunnel surface will generate radial cohesive scattering P waves $\phi_{s2}(r_2,\theta_2)$ and scattering SV waves $\psi_{s2}(r_2,\theta_2)$ on the arc surface of half-space. The Fourier-Bessel series expansion of the displacement potential function is as follows:

$$\begin{cases}\phi_{s2}(r_2,\theta_2)=\sum_{m=0}^{\infty}J_m(k_{sa}r_2)\left(A_{s2,m}\cos m\theta_2+B_{s2,m}\sin m\theta_2\right),\\ \psi_{s2}(r_2,\theta_2)=\sum_{m=0}^{\infty}J_m\left(k_{s\beta}r_2\right)\left(C_{s2,m}\sin m\theta_2+D_{s2,m}\cos m\theta_2\right),\end{cases} \quad (12)$$

where $J_m()$ is the Bessel function of the first kind and $A_{s2,n},B_{s2,n},\ldots,A_{s2,m},B_{s2,m},\ldots$ are the coefficients to be determined in the wave potential function.

In summary, the total wave potential functions of SV and P waves in the free field are

$$\begin{cases}\phi_s=\phi^r+\phi_{s1}+\phi_{s2},\\ \psi_s=\psi^{(i+r)}+\psi_{s1}+\psi_{s2}.\end{cases} \quad (13)$$

2.2. Wave Function of Scattering Field in Primary Support. When the P and SV waves in the free field encounter the primary support, it will lead to radial cohesive scattering P waves $\phi_{p1}(r_1,\theta_1)$ and SV waves $\psi_{p1}(r_1,\theta_1)$ and radial dispersed scattering P waves $\phi_{p2}(r_1,\theta_1)$ and SV waves $\psi_{p2}(r_1,\theta_1)$ in primary support:

$$\begin{cases}\phi_{p1}(r_1,\theta_1)=\sum_{n=0}^{\infty}J_n\left(k_{p\alpha}r_1\right)\left(A_{p1,n}\cos n\theta_1+B_{p1,n}\sin n\theta_1\right)\\ \psi_{p1}(r_1,\theta_1)=\sum_{n=0}^{\infty}J_n\left(k_{p\beta}r_1\right)\left(C_{p1,n}\sin n\theta_1+D_{p1,n}\cos n\theta_1\right),\end{cases}$$
$$\begin{cases}\phi_{p2}(r_1,\theta_1)=\sum_{n=0}^{\infty}H_n^{(1)}\left(k_{a_1}r_1\right)\left(A_{p2,n}\cos n\theta_1+B_{p2,n}\sin n\theta_1\right),\\ \psi_{p2}(r_1,\theta_1)=\sum_{n=0}^{\infty}H_n^{(1)}\left(k_{\beta_1}r_1\right)\left(C_{p2,n}\sin n\theta_1+D_{p2,n}\cos n\theta_1\right),\end{cases} \quad (14)$$

where $A_{p1,n},B_{p1,n},\ldots,A_{p2,n},B_{p2,n},\ldots$ are the unknown coefficients. $k_{p\alpha}$ and $k_{p\beta}$ are the P and SV waves number, respectively, in the primary support. The total potential functions in the primary support are

$$\begin{cases}\phi_p=\phi_{p1}+\phi_{p2},\\ \psi_p=\psi_{p1}+\psi_{p2}.\end{cases} \quad (15)$$

2.3. Wave Function of Scattering Field in Buffer Layer. When P and SV waves in the primary support encounter the buffer layer, a transmission wave will occur at the interface. Then radial cohesive scattering P waves $\phi_{m1}(r_1,\theta_1)$ and SV waves $\psi_{m1}(r_1,\theta_1)$ and radial dispersed scattering P waves $\phi_{m2}(r_1,\theta_1)$ and SV waves $\psi_{m2}(r_1,\theta_1)$ will be led inside the buffer layer. The displacement of potential functions is

$$\begin{cases}\phi_{b1}(r_1,\theta_1)=\sum_{n=0}^{\infty}J_n(k_{b\alpha}r_1)\left(A_{b1,n}\cos n\theta_1+B_{b1,n}\sin n\theta_1\right),\\ \psi_{b2}(r_1,\theta_1)=\sum_{n=0}^{\infty}J_n\left(k_{b\beta}r_1\right)\left(C_{b2,n}\sin n\theta_1+D_{b2,n}\cos n\theta_1\right),\end{cases}$$
$$\begin{cases}\phi_{b2}(r_1,\theta_1)=\sum_{n=0}^{\infty}H_n^{(1)}(k_{b\alpha}r_1)\left(A_{b2,n}\cos n\theta_1+B_{b2,n}\sin n\theta_1\right),\\ \psi_{b2}(r_1,\theta_1)=\sum_{n=0}^{\infty}H_n^{(1)}\left(k_{b\beta}r_1\right)\left(C_{b2,n}\sin n\theta_1+D_{b2,n}\cos n\theta_1\right),\end{cases} \quad (16)$$

where $A_{b1,n},B_{b1,n},\ldots,A_{b2,n},B_{b2,n},\ldots$ are the undetermined coefficients. $k_{b\alpha}$ and $k_{b\beta}$ are the P and SV waves number, respectively, in the buffer layer. Thus, the total potential functions in the buffer layer are

$$\begin{cases}\phi_b=\phi_{b1}+\phi_{b2},\\ \psi_b=\psi_{b1}+\psi_{b2}.\end{cases} \quad (17)$$

2.4. Wave Function of Scattering Field in Secondary Lining. When P and SV waves in the buffer layer encounter the secondary lining, transmission wave will occur at the interface. Then radial cohesive scattering P waves $\phi_{l1}(r_1,\theta_1)$

and SV waves $\psi_{l1}(r_1,\theta_1)$ and radial dispersed scattering P waves $\phi_{l2}(r_1,\theta_1)$ and SV waves $\psi_{l2}(r_1,\theta_1)$ will be led inside the secondary lining. The displacement of potential functions is

$$\begin{cases} \phi_{l1}(r_1,\theta_1) = \sum_{n=0}^{\infty} J_n(k_{l\alpha}r_1)\left(A_{l1,n}\cos n\theta_1 + B_{l1,n}\sin n\theta_1\right), \\ \psi_{l2}(r_1,\theta_1) = \sum_{n=0}^{\infty} J_n\left(k_{l\beta}r_1\right)\left(C_{l2,n}\sin n\theta_1 + D_{l2,n}\cos n\theta_1\right), \end{cases}$$
$$\begin{cases} \phi_{l2}(r_1,\theta_1) = \sum_{n=0}^{\infty} H_n^{(1)}(k_{l\alpha}r_1)\left(A_{l2,n}\cos n\theta_1 + B_{l2,n}\sin n\theta_1\right), \\ \psi_{l2}(r_1,\theta_1) = \sum_{n=0}^{\infty} H_n^{(1)}\left(k_{l\beta}r_1\right)\left(C_{l2,n}\sin n\theta_1 + D_{l2,n}\cos n\theta_1\right). \end{cases} \tag{18}$$

where $A_{l1,n}, B_{l1,n}, \ldots, A_{l2,n}, B_{l2,n}, \ldots$ are the undetermined coefficients. $k_{l\alpha}$ and $k_{l\beta}$ are the P and SV waves number, respectively, in the secondary lining. Thus, the total potential functions in the secondary lining are

$$\begin{cases} \phi_l = \phi_{l1} + \phi_{l2}, \\ \psi_l = \psi_{l1} + \psi_{l2}. \end{cases} \tag{19}$$

2.5. Boundary Conditions. Based on the assumption of plane strain, there are two kinds of similar boundary conditions: (1) the radial and shear stress at the surface of half-space and the inner surface of secondary lining are zero; (2) the stress and displacement are continuous at the interface of a different medium. Thus, we can obtain the following:

(1) Zero stress at the surface of half-space:

$$\begin{aligned} &\sigma_{rr}^s = 0, \\ &\tau_{r\theta}^s = 0, \\ &(r_2 = b). \end{aligned} \tag{20}$$

(2) Continuous stress and displacement at the interface between primary support and half-space:

$$\begin{cases} \sigma_{rr}^p = \sigma_{rr}^s, \tau_{r\theta}^p = \tau_{r\theta}^s, \quad (r_1 = R_1), \\ u_r^p = u_r^s, u_\theta^p = u_\theta^s, \quad (r_1 = R_1). \end{cases} \tag{21}$$

(3) Continuous stress and displacement at the interface between primary support and buffer layer:

$$\begin{cases} \sigma_{rr}^b = \sigma_{rr}^p, \tau_{r\theta}^b = \tau_{r\theta}^p, \quad (r_1 = R_2), \\ u_r^b = u_r^p, u_\theta^b = u_\theta^p, \quad (r_1 = R_2). \end{cases} \tag{22}$$

(4) Continuous stress and displacement at the interface between buffer layer and secondary lining:

$$\begin{cases} \sigma_{rr}^l = \sigma_{rr}^b, \tau_{r\theta}^l = \tau_{r\theta}^b, \quad (r_1 = R_3), \\ u_r^l = u_r^b, u_\theta^l = u_\theta^b, \quad (r_1 = R_3). \end{cases} \tag{23}$$

(5) Zero stress at the inner surface of the secondary lining:

$$\begin{aligned} &\sigma_{rr}^l = 0, \\ &\tau_{r\theta}^l = 0, \\ &(r_1 = R_4), \end{aligned} \tag{24}$$

where the superscripts s, p, b, and l correspond to the medium of half-space, primary support, buffer layer, and secondary lining, respectively, in equations (20)~(24).

The dynamic stress concentration of composite lining tunnel in half-space subjected to plane SV waves is a plane strain problem. According to the potential functions of displacement and stress in elastic medium, they can be expressed as follows:

$$\begin{cases} u_r = \dfrac{\partial\phi}{\partial r} + \dfrac{1}{r}\dfrac{\partial\psi}{\partial\theta}, \\ u_\theta = \dfrac{1}{r}\dfrac{\partial\phi}{\partial\theta} - \dfrac{\partial\psi}{\partial r}, \end{cases} \tag{25}$$

$$\begin{cases} \sigma_{rr} = \lambda\nabla^2\phi + 2\mu\left[\dfrac{\partial^2\phi}{\partial r^2} + \dfrac{\partial}{\partial r}\left(\dfrac{1}{r}\dfrac{\partial\psi}{\partial\theta}\right)\right], \\ \sigma_{\theta\theta} = \lambda\nabla^2\phi + 2\mu\left[\dfrac{1}{r}\left(\dfrac{\partial^2\phi}{\partial r^2} + \dfrac{1}{r}\dfrac{\partial^2\psi}{\partial\theta^2}\right) + \dfrac{1}{r}\left(\dfrac{1}{r}\dfrac{\partial\psi}{\partial\theta} - \dfrac{\partial^2\psi}{\partial r\partial\theta}\right)\right], \\ \tau_{r\theta} = 2\mu\dfrac{\partial}{\partial r}\left(\dfrac{1}{r}\dfrac{\partial\phi}{\partial\theta}\right) + \mu\left[\dfrac{1}{r^2}\dfrac{\partial^2\varphi}{\partial\theta^2} - r\dfrac{\partial}{\partial r}\left(\dfrac{1}{r}\dfrac{\partial\varphi}{\partial\theta}\right)\right], \end{cases} \tag{26}$$

where $\nabla^2\phi = ((\partial^2\phi)/(\partial r^2)) + (1/r)((\partial\phi)/\partial r^2) + (1/r)((\partial^2\phi)/\partial\theta^2)$.

The above equations can be solved in three steps. (1) The total wave potential functions of each medium (equations (13), (15), (17), and (19)) can be substituted into equations (25) and (26); then the potential functions of stress and displacement with undetermined coefficients can be obtained. (2) The potential functions of stress and displacement obtained in the first step are substituted into the boundary conditions of the model (equations (20)~(24)), a set of linear infinite series equations can be obtained, and the undetermined coefficients can be solved in MATLAB. (3) The solved coefficients are substituted back into the potential functions of stress and displacement obtained in the first step, and finally, the analytical solutions of dynamic stress in composite lining can be solved. Here, different terms are truncated for numerical calculation, and the error between adjacent calculation terms is verified. When the error is less than the preset accuracy, this term number is used as the actual convergent calculation terms. In this paper, the satisfactory results can be obtained when the number of finite terms n or m is 12.

3. Numerical Examples and Analysis Results

The stress distribution of lining subjected to harmonic wave incidence is usually described by the dynamic stress concentration factor (DSCF), which is defined as the ratio of the maximum dynamic stress in the medium to the standard

local stress based on the simple principle [32]. The circumferential dynamic stress concentration factor (DSCF) of composite lining can be expressed as

$$\sigma_{\theta\theta}^{*} = \left|\frac{\sigma_{\theta\theta}}{\sigma_{\theta\theta}^{0}}\right|, \tag{27}$$

where $\sigma_{\theta\theta}^{0} = k_{s\beta}^{2} G_s$ is the standard local stress in the surrounding rock. representing.

The geometric and mechanical parameters simultaneously determine the seismic absorption performances of buffer layer [14]. In addition, the low-frequency seismic waves have the significant influence on the underground structure [37]. Therefore, the influence of stiffness and thickness of buffer layer on composite lining subjected to low-frequency SV waves at different angles of incidence is analyzed.

3.1. Effect of Buffer Layer Stiffness on the Dynamic Stress Concentration Factor of Composite Lining. Young's modulus of buffer layer is a measure of the stiffness. The effect of changing Young's modulus of buffer layer on DSCF in the composite linings, when subjected to different SV waves angle of incidences, is analyzed.

First, the dimensionless frequency (η) is defined as the ratio of inner diameter of the secondary lining to the incident wavelength [43]:

$$\eta = \frac{2R_4}{\lambda_{s\beta}}, \tag{28}$$

where $\lambda_{s\beta}$ is the wavelength of the incident SV waves in half-space.

Based on existing literature [17, 41], Poisson's ratio of surrounding rocks and composite lining in half-space is 0.25, and the velocity of compressional wave in each medium is 1.73 times that of the shear wave. The thickness of the primary support and secondary lining is $0.2R_4$, the thickness ratio of the two is 2 : 3, and the thickness of the buffer layer is $0.05R_4$. The dimensionless frequency η is 0.25. The buried depth of tunnel center (h) is $2R_4$. To be as accurate as possible, the radius of the great arc surface (b) is $10000R_1$. The angle of incidence is 0°, 30°, 60°, and 85°. Young's modulus ratio (E_b/E_s) of buffer layer to surrounding rock is designed as 1/1, 1/10, and 1/50, respectively, which represents that the relative stiffness of buffer layer decreases step by step. The analytical results of DSCF in composite lining are presented in Figure 2.

Figure 2 shows that the stiffness of buffer layer significantly affects the amplitude of DSCF in composite lining but does not obviously change the distribution at the same incident angle. When the stiffness of buffer layer is constant, the DSCF distribution of composite lining became more complex with the increase of incident angle, but the amplitude tends to decrease, indicating that the DSCF of composite lining is higher when subjected to vertical incidence than to oblique incidence, which is also verified by the existing studies [30]. The DSCF of secondary lining and primary support subjected to vertical incidence is emphatically analyzed.

First, we focus on the maximum stiffness of buffer layer ($E_b/E_s = 1$), as shown in Figure 2(a). The maximum DSCF of the secondary lining and primary support is 33.1 and 13.4, both occurring in the direction of conjugate ±45°, which indicates that the secondary lining is bearing the main dynamic load.

Then, the stiffness reduction of buffer layer ($E_b/E_s = 1/10$) is analyzed, as shown in Figure 2(b). Compared with the maximum stiffness of buffer layer ($E_b/E_s = 1$), the maximum DSCF of secondary lining decreases by −23%, while the primary support increases by 49%. It suggests that the buffer layer can reduce the dynamic stress of the secondary lining, but it will increase the dynamic stress of primary support greatly. However, across the board, the DSCF of primary support and the secondary lining is close to each other. The results show that the dynamic responses of the two are consistent, which is beneficial to the coordinated deformation for the composite lining.

Continue to reduce the stiffness of buffer layer ($E_b/E_s = 1/50$), as shown in Figure 2(c). Compared with the maximum buffer layer stiffness ($E_b/E_s = 1$), the DSCF of secondary lining is further reduced by −39.6%, while that of primary support is further increased by 115.6%. It indicates that, within a certain range, the lower the buffer layer stiffness is, the higher the primary support dynamic stress is and the lower the secondary lining dynamic stress is.

For further analyses for two reasons, on the one hand, the interaction between primary support and secondary lining will be weakened when the stiffness of buffer layer is reduced, but the interaction between primary support and surrounding rock will be strengthened. On the other hand, the reduction of the buffer layer stiffness will lead to an increase in the damping ratio, which will further increase the shock-absorbing performance in the buffer layer. Thus, it has an ideal shock-absorbing effect on the secondary lining.

In summary, changing the stiffness of the buffer layer in the composite lining plays the role of "redistributing" the seismic load. Reducing the stiffness of buffer layer is beneficial to protect secondary lining, but it will increase the dynamic stress of primary support. Therefore, the stiffness of buffer layer should not be too low. It is suggested that the stiffness ratio of buffer layer to surrounding rock is $E_b/E_s = 1/10 \sim 1/50$.

3.2. Effect of Thickness of Buffer Layer on the Dynamic Stress Concentration Factor of Composite Lining. To explore the influence of thickness of buffer layer on the dynamic stress of composite lining, three cases were considered that the ratio of thickness of the buffer layers to inner radius of the secondary lining ($(R_2 - R_3)/2R_4$) is, respectively, 1/100, 1/40, and 1/20, which indicates that the relative thickness of buffer layer increases step by step. The parameters are the same as Section 3.1. The DSCF of composite lining are shown in Figure 3.

As seen in Figure 3, at the same angle of incidence, the thickness of buffer layer significantly affects the DSCF amplitude of composite lining but does not change the distribution pattern. When the thickness of buffer layer is constant, the DSCF distribution of composite lining

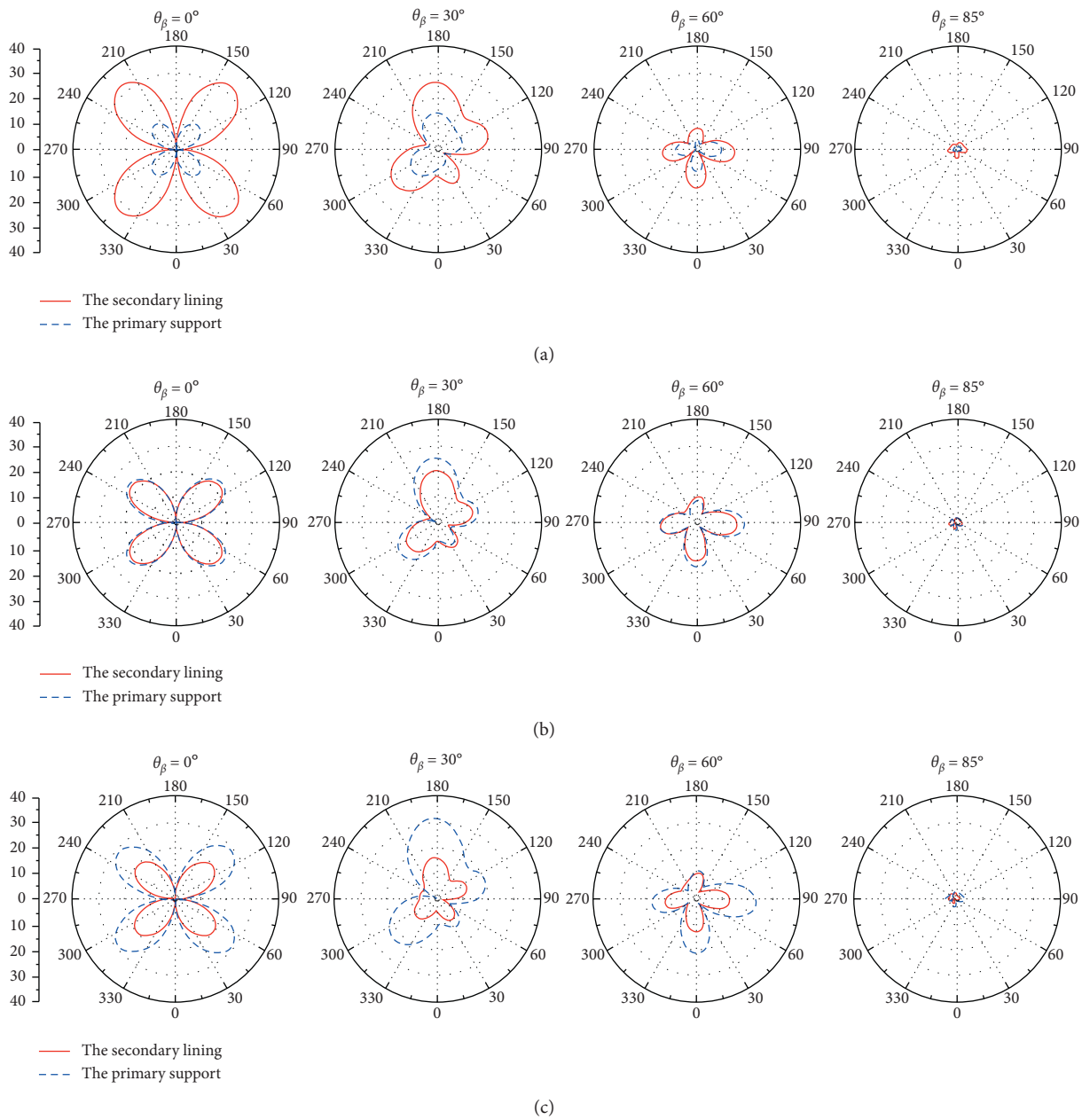

Figure 2: DSCF distribution of composite lining with different buffer layer stiffness. (a) E_b/E_s=1. (b) E_b/E_s=1/10. (c) E_b/E_s=1/50.

becomes more complex with the increase of incident angle, but the amplitude tends to decrease, indicating that the DSCF of composite lining subjected to vertical incidence is higher than that to oblique incidence, which is consistent with the analysis of the stiffness above.

First, we focus on the minimum thickness of buffer layer $((R_2 - R_3)/(2R_4) = 1/100)$, as shown in Figure 3(a). The maximum DSCF of the secondary lining and the primary support is 35.1 and 11.8, both occurring in the direction of conjugate ±45°. It suggests that the secondary lining is bearing the most of dynamic load.

Then, increasing the thickness of buffer layer $((R_2 - R_3)/(2R_4) = 1/40)$ is analyzed, as shown in Figure 3(b). Compared with the minimum thickness of buffer layer $((R_2 - R_3)/(2R_4) = 1/100)$, the maximum DSCF of secondary lining decreases by −43%, while the primary support increases by 60.7%. It suggests that increasing the thickness of buffer layer can significantly change the DSCF amplitude of the composite lining in a certain range.

Further, the thickness of buffer layer increases $((R_2 - R_3)/(2R_4) = 1/20)$, as shown in Figure 3(c). Compared with the thickness of buffer layer $((R_2 - R_3)/(2R_4) = 1/40)$, the DSCF of secondary lining increased by 55%, while the DSCF of primary support decreased a little. This indicates that when the thickness of buffer layer increases, the dynamic stress of secondary lining decreases first and then increases, while the dynamic stress of primary support gradually increases. Thus, it is concluded

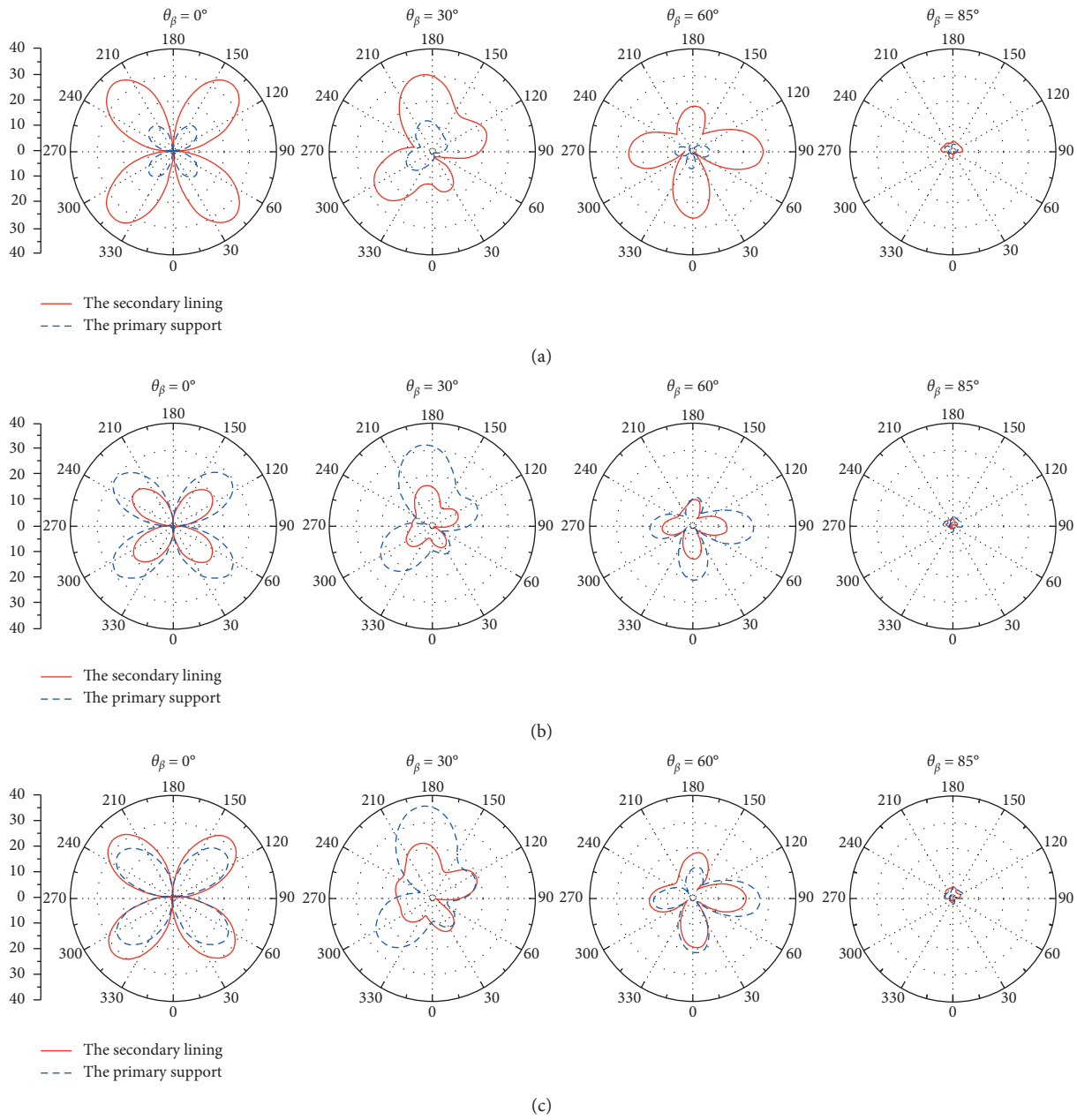

Figure 3: DSCF distribution of composite lining with different thickness of buffer layer. (a) $(R_2 - R_3) / (2R_4)$=1 / 100. (b) $(R_2 - R_3) / (2R_4)$= 1 / 40. (c) $(R_2 - R_3) / (2R_4)$=1 / 20.

that increasing the thickness of buffer layer does not necessarily increase the effect of shock absorption. The dynamic stress and deformation characteristics of the composite lining should be comprehensively analyzed to design the thickness of buffer layer. Based on the results, this paper will propose that the ratio of thickness of buffer layer to the inner diameter of secondary lining is 1/40 ~ 1/20.

4. Shaking Table Test and Numerical Simulation

Shaking table test is undoubtedly a direct and effective method to verify the correctness and applicability of analytical solutions. Three cases of tests were conducted to explore the dynamic response of composite lining with or without buffer layer: (1) without buffer layer; (2) the thickness of buffer layer which is 1 cm (about 1/30 of the inner diameter of secondary lining); (3) the thickness of buffer layer which is 2 cm (about 1/15 of the inner diameter of secondary lining).

4.1. Test Facilities. The series shaking table tests were conducted at the National Engineering Laboratory for Technology of Geological Disaster Prevention in Land Transportation, Southwest Jiaotong University, as shown in Figure 4. Technical items and parameters are shown in Table 1.

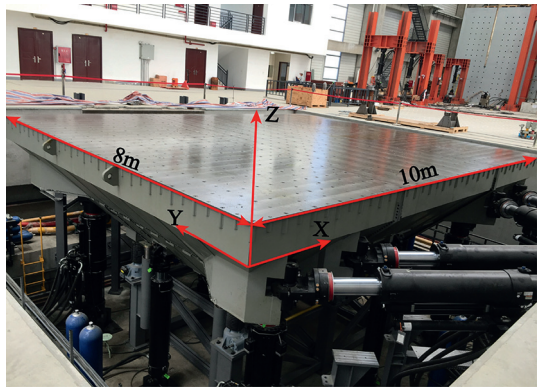

Figure 4: Shaking table (8 m × 10 m).

Table 1: Parameters of shaking table.

Items	Parameters
Table size (unit: m × m)	8.0 × 10.0
Frequency range (Hz)	0.1–50
Degrees of freedom	6
Maximum weight (t)	160
Maximum displacement (mm)	Horizontal direction: ±800; vertical direction: ±400
Maximum velocity (mm/s)	Horizontal direction: ±1200; vertical direction: ±1000
Maximum acceleration (g)	Horizontal direction: 1.2; vertical direction: 1.0
Maximum overturning moment (t·m)	600

4.2. Law of Similarity and Model Materials. To describe the dynamic interaction between the composite lining and surrounding rock accurately, the similarity between the model and prototype was derived based on the Buckingham-π theorem. The basic physical quantities were geometry, Young's modulus, and density, and the other physical quantities were derived from the basic physical quantities. The similarity is shown in Table 2.

Table 2: Similarity relationship for model tests.

Physical quantity	Similarity relation	Similarity ratio
Length	C_l	1/30
Density	C_ρ	1/1.5
Young's modulus	C_E	1/45
Strain	C_ε	1
Time	$C_t = C_l(C_p/C_E)^{1/2}$	1/5.5
Acceleration	$C_a = (C_E/(C_l C_p))$	1
Friction angle	C_φ	1

4.2.1. The Similar Materials of Tunnel Lining. The mechanical parameters of composite lining were obtained from practical engineering [44]. After a series of material tests, water, plaster, diatomite, quartz sand, and barite were adopted to simulate the composite lining with the ratio of 1 : 0.6 : 0.2 : 0.1 : 0.4 [45]. Table 3 lists the parameters of the lining structure for the prototype and model.

4.2.2. Similar Materials of Surrounding Rock. A mixture of fly ash, river, sand, and machine oil was selected to simulate the similar materials of surrounding rocks [44–46]. The ratio of hard rock was fly ash:river sand:oil = 50 : 40 : 10, and the ratio of soft rock was fly ash:river sand:oil = 45 : 40 : 15. Table 4 lists the physical parameters of the surrounding rocks for the prototype and model.

4.2.3. Similar Materials of Buffer Layer. According to the above results, when the stiffness ratio of buffer layer to surrounding rock E_b/E_s was 1/10 ~ 1/50, the shock-absorbing performance was ideal. Therefore, the optimal Young's modulus of the buffer layer was about 2 MPa, based on the similarity relationship and the mechanical parameters of similar materials. The B1 rubber sponge was selected as buffer layer, which has stable mechanical properties and was easy to process and cheap. The density was 60 kg/m^3, Young's modulus was 2.3 MPa, and Poisson's ratio was 0.3, which can satisfy the similarity relationship. The fabrication process of composite lining with buffer layer is shown in Figure 5. It was mainly fabricated in four steps: (a) cutting the buffer layer according to the geometric conditions of the composite lining; (b) laying the buffer layer around the secondary lining; (c) installing the shaping formwork and wire net around buffer layer; (d) casting primary lining. The buffer layer was bonded to the composite lining by glue to achieve the rigid connection. The contact principle of the two was neither slack nor tight, so as to ensure that the buffer layer was in complete contact with the composite lining and no additional stress was generated.

4.3. Model Box Design. The model box was the container of the shaking table test, which requires sufficient strength and

Table 3: Physical parameters of lining structure in the prototype and model.

Name	Density (kg/m^3)	Young's modulus (GPa)	Compression strength (MPa)	Poisson's ratio
Prototype	2400	30	20.1	0.25
Model	1600	0.67	0.45	0.25

Table 4: Physical parameters of surrounding rock in the prototype and model.

Physical quantity		Density (kg/m3)	Cohesion (kPa)	Friction angle (°)	Young's modulus (GPa)
Hard rock	Prototype	2100	135	38	10
	Model	1400	3	38	0.22
Soft rock	Prototype	1700	50	27	1.5
	Model	1133	1.1	27	0.03

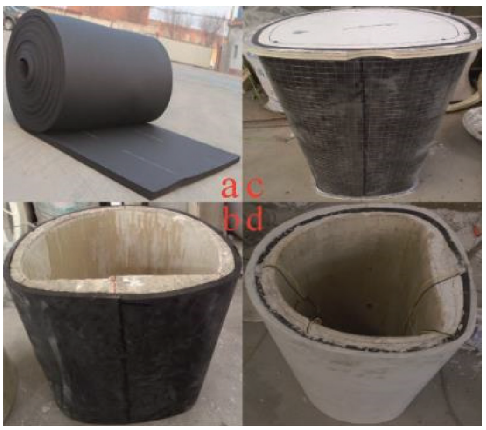

Figure 5: Fabrication of composite lining with buffer layer.

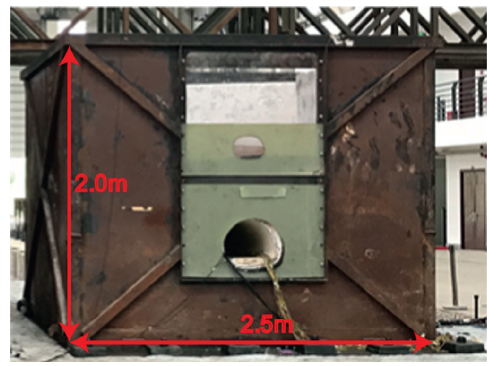

Figure 6: Model box.

stiffness. The natural frequency of box should not resonate with that of the model soil and structure. The model box was made of welded steel plate and angle steel. The size of model box was 2.5 m × 2.5 m × 2.0 m, as shown in Figure 6. The sidewall of model box has a restraint effect on the soil, and the seismic wave will reflect on the sidewall for many times during shaking table test. Thus, a 10 cm EPS-foam was fixed on each sidewall around the model box to simulate the free-field boundary, which can absorb the reflected and scattering seismic wave to reduce the boundary effect.

4.4. Data Acquisition and Sensor Layout. Figure 7 illustrates the sensor locations. The monitoring cross sections were divided into main monitoring sections and auxiliary monitoring sections. The segments of the linings were denoted as *A*, *B*, *C*, and *D*, respectively. Four monitoring sections were designed during the test. Attention has focused on the difference of dynamic response of composite linings with or without buffer layer subjected to strong seismic wave, shown in Figures 7(b) and 7(c).

The main monitoring sections were 2-2 and 3-3, which were designed to monitor the dynamic response of the composite linings in hard rock and soft rock respectively. The auxiliary monitoring sections were 1-1 and 4-4, which were designed to verify the effectiveness of the EPS-foam boundary. The sensors were mainly accelerometers and strain gauges. Accelerometers *A*2 and *A*3 were adopted to monitor the primary support and secondary lining in hard rock, and accelerometers *A*4 and *A*5 were adopted to monitor the primary support and secondary lining in soft rock, respectively. A1 was designed to monitor the surface of the surrounding rock. *A*6 was designed to monitor the input acceleration on the shaking table. The strain gauges were stuck on each monitoring section with both the inner and outer of the linings, as illustrated in Figure 7(a).

4.5. Seismic Wave Input. The acceleration time history of the serials tests was based on the EW-component of seismic waves monitored by bedrock monitoring stations in Mao County during the Wenchuan earthquake in 2008. The peak ground acceleration (PGA) was 0.4 g and the duration time was compressed according to the time similarity ratio 1 : 5.5. The acceleration time history and Fourier spectrum are shown in Figure 8. The input seismic waves were horizontal shear waves perpendicular to the tunnel axis.

4.6. Boundary Effect Validation. To compare with the test data, numerical simulations of three cases were conducted with the finite difference software FLAC^{3D}, as shown in Figure 9. The model geometry, material parameters, and monitoring points layout were the same as the tests. Solid elements were selected to simulate the surrounding rock, lining, and buffer layer. Mohr-Coulomb constitutive model was adopted for surrounding rock, and the elastic constitutive

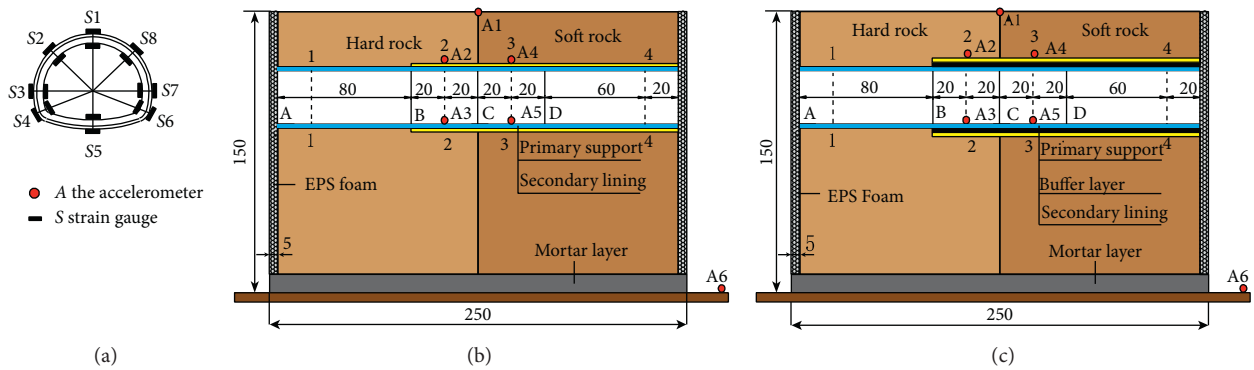

Figure 7: Instrumentation for seismic damage tests: (a) cross-sectional monitoring point, (b) layout of sensors in the longitudinal sections without buffer layer, and (c) layout of sensors in the longitudinal sections with a buffer layer (units: cm).

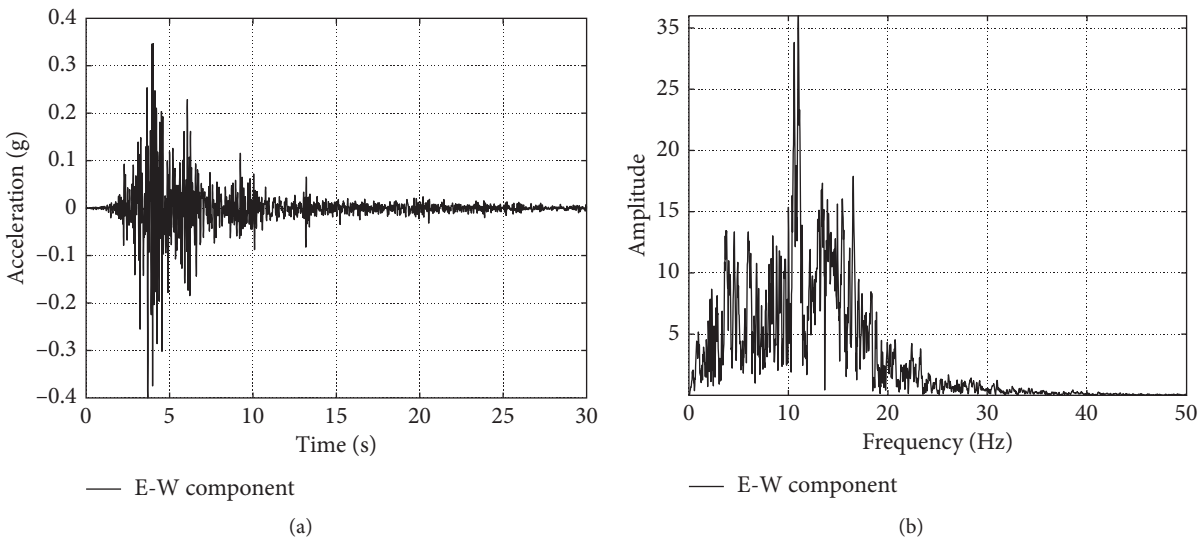

Figure 8: (a) Acceleration time history of E-W component; (b) Fourier spectrum of E-W component.

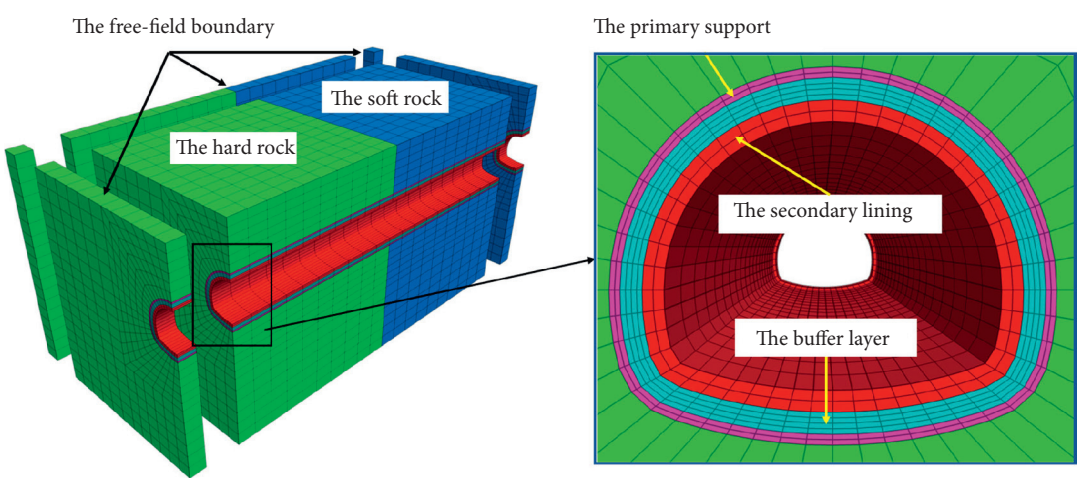

Figure 9: Numerical simulation model (1/2 model).

model was adopted for lining and buffer layer. Free-field boundary was designed and a viscous boundary was applied on the bottom. Seismic waves were perpendicular to the axial of the tunnel and realized by applying shear stress waves at the bottom of the model. Rayleigh damping was adopted, and the critical damping ratio was 5%.

Since free-field boundary was adopted in numerical simulation, the effectiveness of EPS-foam boundary can be verified by comparing the monitored acceleration spectrum of A2 and A4 in tests with the numerical simulation. As shown in Figures 10 and 11, the monitored acceleration spectrum of A2 and A4 were in good agreement with the numerical simulation, which indicated that the rigid sidewall boundary effect of the model box was effectively eliminated by the EPS-foam. It was suggested that the EPS-foam could be adopted to simulate the free-field boundary in tests.

4.7. Acceleration Response of Composite Linings. Figure 12 shows the acceleration time history of A3 and A5 in three cases. It can be seen that the acceleration of the secondary lining without buffer layer was the highest, followed by that when the thickness is 2 cm, and the lowest when the thickness is 1 cm. PGA of A3 (A5) in three cases were 0.31 (0.25) g > 0.25 (0.22) g > 0.15 (0.17) g. It suggested that buffer layer can effectively reduce the acceleration of secondary lining, and with the increase of the thickness of buffer layer, acceleration of secondary lining first decreased and then increased. This indicated that there was an optimal interval for the thickness of buffer layer. When the thickness exceeded the optimal interval, the dynamic response of the secondary lining will be amplified to different degrees.

Figure 13 shows the peak acceleration at invert of secondary lining and crown of primary support in soft and hard surrounding rock under three cases. By comparison, when there was no buffer layer, the difference of PGA between A3 and A5 was 0.05 g, and that between A2 and A4 was 0.06 g. When the thickness of buffer layer was 1 cm, the difference of PGA between A3 and A5 was 0.02 g, and that between A2 and A4 was 0.04 g. When the thickness of buffer layer was 2 cm, the difference of PGA between A3 and A5 PGA was 0.03 g, and that between A2 and A4 was 0.01 g. It is suggested that increasing the thickness of buffer layer will reduce the difference of PGA crossing the soft and hard surrounding rock and make the dynamic response of the composite lining tend to be consistent, but it will amplify the PGA.

4.8. Dynamic Stress Concentration of Composite Linings. The dynamic stress of composite lining was monitored by the strain gauge in the tests. The circumferential dynamic stress of each monitoring point can be calculated through Young's modulus and strains. Figure 14 shows the dynamic stress amplitude of each monitoring point of Section 3 in tests and numerical simulation.

It can be seen that the dynamic stress of secondary lining at each monitoring point was higher than that of primary support in case of no buffer layer, and the amplitude of dynamic stress at arch springing of secondary lining and spandrel of primary support was relatively high, as shown in Figure 14(a).

When the thickness of buffer layer was 1 cm, the dynamic stress of secondary lining decreased remarkably, while the dynamic stress of primary supporting increased, especially at the arch springing. When the thickness of buffer layer was 2 cm, the dynamic stress of the secondary lining increased on the whole, especially at the arch springing and invert. The dynamic stress of the primary support was unchanged except that the crown increased dramatically. Figure 14(b) shows the results of numerical calculation, and it presented a similar rule with the test data, but it was 30 ~ 50% higher in amplitude.

According to the numerical and experimental results, the dynamic stress value of the secondary lining was 2~3 times

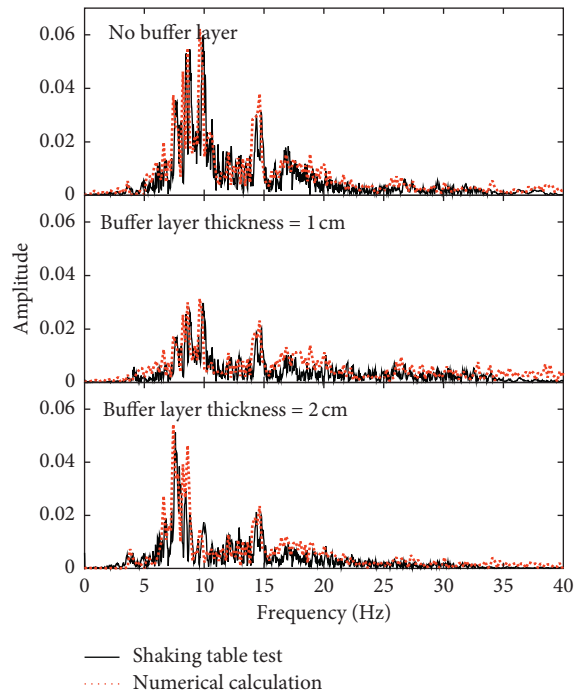

Figure 10: Acceleration spectrum of A2.

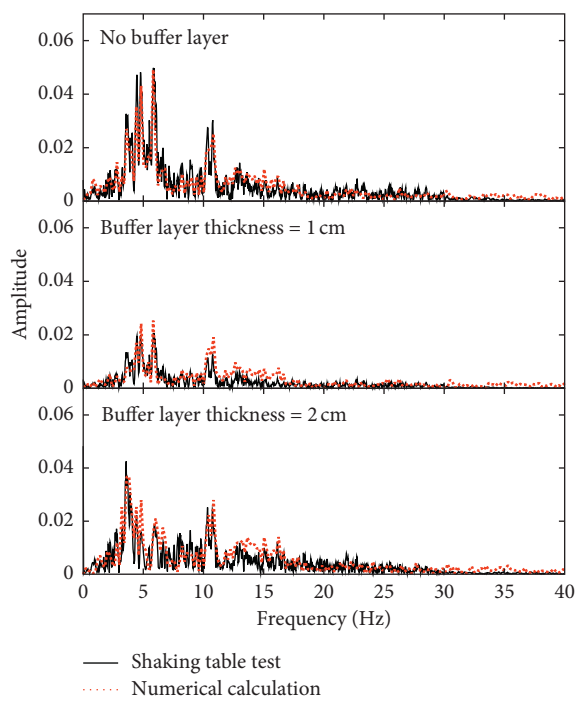

Figure 11: Acceleration spectrum of A4.

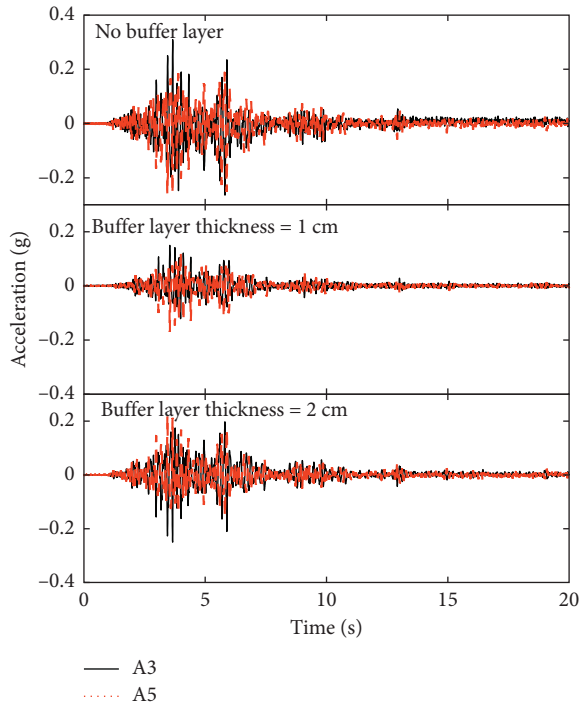

Figure 12: Acceleration time history of A3 and A5.

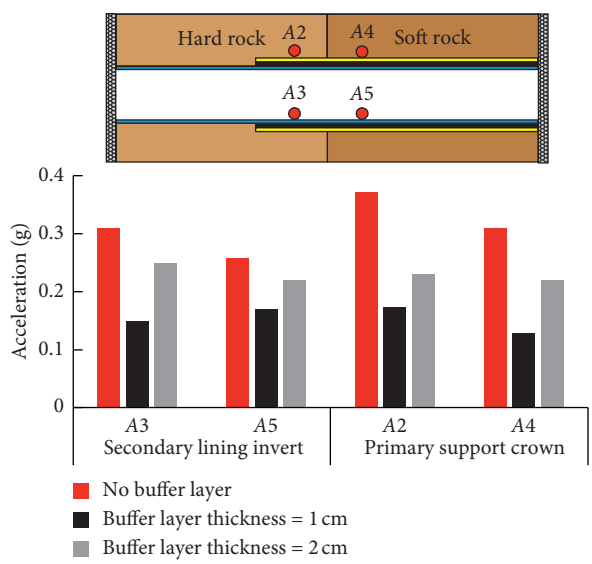

Figure 13: Contrast of peak acceleration.

that of the primary support in case of no buffer layer. Analysis of possible reasons was that "superposition effect" of incident wave and reflected wave existed on the inner surface of the secondary lining. After laying the buffer layer, on the one hand, due to the low Young's modulus and high damping ratio of the buffer layer, certain shear deformation was allowed between the primary support and the secondary lining; thus, partial energy of the seismic wave could be absorbed by the buffer layer during the strong earthquake. On the other hand, stiffness changes occurred between the primary support and the buffer layer, resulting in the "superposition effect" of the incident and reflected waves within the primary support. Therefore, the dynamic stress of the secondary lining decreased while that of the primary lining increased.

4.9. General Damage Observations. Figures 15–17 show the final cracks of composite lining after tests. In case of no buffer layer, longitudinal penetration cracks appeared in the crown, arch springing, and invert of secondary lining. Large area of falling blocks appeared in the arch springing of primary support (seen in Figure 15).

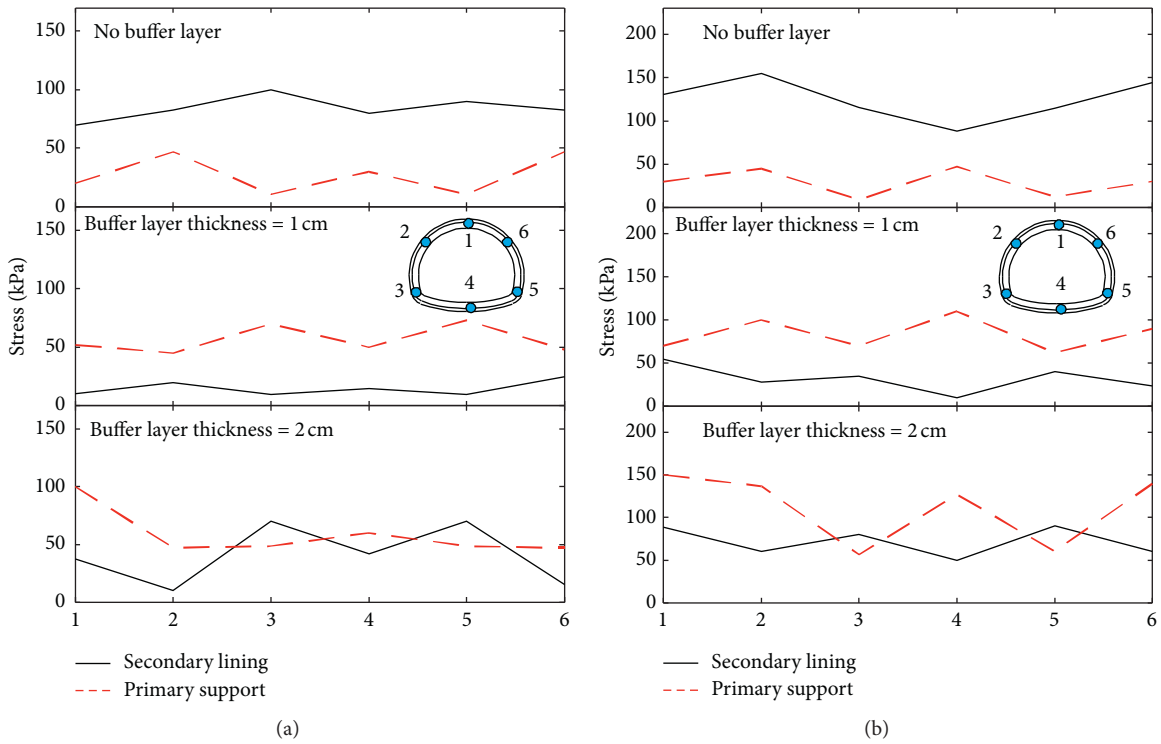

Figure 14: Dynamic stress amplitude. (a) Shaking table test. (b) Numerical simulation. 1: crown. 2: left spandrel. 3: left arch springing. 4: invert. 5: right arch springing. 6: right spandrel.

Figure 15: Damage of composite lining without buffer layer. (a) Transversal surface. (b) Longitudinal surface.

When the thickness of buffer layer was 1 cm, the right arch springing of the secondary lining was partially cracked, the invert of the secondary lining was partially uplifted, and there was no through crack (shown in Figure 16).

When the thickness of buffer layer was 2 cm, partial longitudinal cracks appeared at the invert and the right arch springing of secondary lining, while penetrating cracks appeared at the right arch springing of primary support (see Figure 17).

By comparing the cracks in the three cases, the crack numbers of the composite lining can be remarkably reduced with the buffer layer. When the thickness of buffer layer was 1 cm, the integrity of the composite lining was obviously better than that of 2 cm. This illustrated the fact that shock-absorbing performance was weakened when the thickness of buffer layer exceeded a certain range, and it was further verified that the optimal thickness of buffer layer in the analytical solution was correct and reliable. In addition, it can be deduced from the test that the crown, arch springing, and invert of composite lining were vulnerable to be damaged during the strong ground motion. The invert was more susceptible to be damaged after laying buffer layer; therefore, the seismic design of tunnel should be paid more attention to.

(a) (b)

Figure 16: Damage of composite lining with 1 cm buffer layer. (a) Transversal surface. (b) Longitudinal surface.

(a) (b)

Figure 17: Damage of composite lining with 2 cm buffer layer. (a) Transversal surface. (b) Longitudinal surface.

5. Conclusions

Based on the Fourier-Bessel series expansion, the dynamic stress concentration factor (DSCF) of composite lining tunnel with buffer layer subjected to plane SV waves at different angle of incidences was obtained. Then, the influence of geometric and mechanical parameters of the buffer layer on composite lining was systematically analyzed, which reveals the shock-absorbing mechanism of buffer layer. Afterward, a series shaking table tests and numerical simulations were conducted to validate the reliability and correctness of analytical solutions. Finally, damage patterns of composite lining with and without buffer layer were presented. The location and size of cracks were marked on the linings, and suggestions for seismic fortification were given. These comparisons attempted to demonstrate the advantages and disadvantages of buffer layer in composite lining tunnel. The following conclusions could be drawn from this study:

(1) Increasing the incident angle of plane SV waves at low frequency, the DSCF distribution of composite lining becomes more complex than the vertical incidence, while the amplitude of DSCF decreases gradually when the stiffness and thickness of buffer layer are constant.

(2) Changing the stiffness of buffer layer will play the role of "redistributing" the seismic load. Reducing the stiffness of buffer layer is beneficial to the secondary lining, but it will increase the dynamic stress of primary support. It is suggested that the stiffness ratio of buffer layer to surrounding rock is 1/10 ~ 1/50.

(3) Increasing the thickness of buffer layer, the dynamic stress of secondary lining decreases first and then increases, while the primary support gradually increases. Increasing the thickness of buffer layer does not necessarily achieve better shock-absorbing performance. We suggest that the ratio of buffer layer thickness to inner diameter of secondary lining is 1/40 ~ 1/20.

(4) General damage observations show that the crown, arch springing, and invert of composite lining without buffer layer are prone to cracking during the earthquake. The invert is more susceptible to be damaged after adopting the buffer layer, which should be paid more attention to in the seismic design of composite lining tunnels.

Data Availability

The data used to support the findings of this study are included within the article.

Conflicts of Interest

The authors declare that there are no conflicts of interest associated with this publication.

Acknowledgments

This work was supported by the National Natural Science Foundation of China (51778540, 51678501, and 51778539) and the National Key Research and Development Program of China (no.2019YFC0605104).

References

[1] Y. M. A. Hashash, J. J. Hook, B. Schmidt, and J. I-Chiang Yao, "Seismic design and analysis of underground structures," *Tunnelling and Underground Space Technology*, vol. 16, no. 4, pp. 247–293, 2001.

[2] T. Asakura, Y. Shiba, S. Matsuoka, T. Oya, and K. Yashiro, "Damage to mountain tunnels by earthquake and its mechanism," *Doboku Gakkai Ronbunshu*, vol. 659, pp. 27–38, 2000.

[3] Z. Z. Wang, Y. J. Jiang, C. A. Zhu, and T. C. Sun, "Shaking table tests of tunnel linings in progressive states of damage," *Tunnelling and Underground Space Technology incorporating Trenchless Technology Research*, vol. 50, pp. 109–117, 2015.

[4] H. Liu and E. Song, "Seismic response of large underground structures in liquefiable soils subjected to horizontal and vertical earthquake excitations," *Computers and Geotechnics*, vol. 32, no. 4, pp. 223–244, 2005.

[5] Seyyed, A. Hasheminejad, and Miri, "Seismic isolation effect of lined circular tunnels with damping treatments," *Earthquake Engineering & Engineering Vibration*, vol. 7, no. 3, pp. 305–319, 2008.

[6] S. Shimamura, H. Kasai, and M. Haruumi, "Seismic isolation effect for a tunnel with a soft isolation layer," *Structural Engineering Earthquake Engineering*, vol. 2, no. 16, pp. 143–154, 1999.

[7] H. B. Mohammad, R. M. Masoud, K. Dong-Soo, and W. C. Yun, "Effect of underground tunnel on the ground surface acceleration," *Tunnelling and Underground Space Technology*, vol. 44, pp. 10–22, 2014.

[8] D. S. Kim and K. Konagai, "Seismic isolation effect of a tunnel covered with coating material," *Tunnelling and Underground Space Technology*, vol. 15, no. 4, pp. 437–443, 2000.

[9] D.-S. Kim and K. Konagai, "Key parameters governing the performance of soft tunnel coating for seismic isolation," *Earthquake Engineering & Structural Dynamics*, vol. 30, no. 9, pp. 1333–1343, 2001.

[10] K. Konagai and D.-S. Kim, "Simple evaluation of the effect of seismic isolation by covering a tunnel with a thin flexible material," *Soil Dynamics and Earthquake Engineering*, vol. 21, no. 4, pp. 287–295, 2001.

[11] X. Ma, F. Wang, C. Guo, and B. Sun, "Seismic isolation effect of non-water reacted two-component polymeric material coating on tunnels," *Applied Sciences*, vol. 10, no. 7, p. 2606, 2020.

[12] Z. Y. Chen and H. Shen, "Dynamic centrifuge tests on isolation mechanism of tunnels subjected to seismic shaking," *Tunnelling and Underground Space Technology*, vol. 42, pp. 67–77, 2014.

[13] J. He, W. Chen, W. Zhao, S. Huang, and Y. Yao, "Numerical test on polystyrene tunnel seismic-isolation material," *Polish Journal of Chemical Technology*, vol. 18, no. 3, pp. 122–127, 2016.

[14] C. L. Xin, Z. Z. Wang, and J. Yu, "The evaluation on shock absorption performance of buffer layer around the cross section of tunnel lining," *Soil Dynamics and Earthquake Engineering*, vol. 131, p. 106032, 2020.

[15] S. Ma, W. Chen, and W. Zhao, "Mechanical properties and associated seismic isolation effects of foamed concrete layer in rock tunnel," *Journal of Rock Mechanics and Geotechnical Engineering*, vol. 11, no. 1, pp. 159–171, 2019.

[16] W. Zhao, W. Chen, and D. Yang, "Interaction between strengthening and isolation layers for tunnels in rock subjected to SH waves," *Tunnelling and Underground Space Technology*, vol. 79, pp. 121–133, 2018.

[17] T. Li, "Damage to mountain tunnels related to the Wenchuan earthquake and some suggestions for aseismic tunnel construction," *Bulletin of Engineering Geology and the Environment*, vol. 71, no. 2, pp. 297–308, 2012.

[18] Y. Shen, B. Gao, X. Yang, and S. Tao, "Seismic damage mechanism and dynamic deformation characteristic analysis of mountain tunnel after Wenchuan earthquake," *Engineering Geology*, vol. 180, pp. 85–98, 2014.

[19] H. Yu, J. Chen, A. Bobet, and Y. Yuan, "Damage observation and assessment of the Longxi tunnel during the Wenchuan earthquake," *Tunnelling and Underground Space Technology*, vol. 54, pp. 102–116, 2016.

[20] C. L. Xin, Z. Z. Wang, J. M. Zhou, and B. Gao, "Shaking table tests on seismic behavior of polypropylene fiber reinforced concrete tunnel lining," *Tunnelling and Underground Space Technology*, vol. 88, pp. 1–15, 2019.

[21] R. J. Bathurst, S. Zarnani, and A. Gaskin, "Shaking table testing of geofoam seismic buffers," *Soil Dynamics and Earthquake Engineering*, vol. 27, no. 4, pp. 324–332, 2007.

[22] S. Zarnani and R. J. Bathurst, "Experimental investigation of EPS geofoam seismic buffers using shaking table tests," *Geosynthetics International*, vol. 14, no. 3, pp. 165–177, 2007.

[23] H. Kim, D. Kim, Y. Lee, and H. Kim, "Effect of soil box boundary conditions on dynamic behavior of model soil in 1 g shaking table test," *Applied Sciences*, vol. 10, no. 13, p. 4642, 2020.

[24] H. Xu, T. Li, L. Xia, J. X. Zhao, and D. Wang, "Shaking table tests on seismic measures of a model mountain tunnel," *Tunnelling and Underground Space Technology*, vol. 60, pp. 197–209, 2016.

[25] M. Geniş, "Assessment of the dynamic stability of the portals of the Dorukhan tunnel using numerical analysis," *International Journal of Rock Mechanics and Mining Sciences*, vol. 47, no. 8, pp. 1231–1241, 2010.

[26] G. Gazetas, N. Gerolymos, and I. Anastasopoulos, "Response of three Athens metro underground structures in the 1999 Parnitha earthquake," *Soil Dynamics and Earthquake Engineering*, vol. 25, no. 7-10, pp. 617–633, 2005.

[27] J. Chen, L. Jiang, J. Li, and X. Shi, "Numerical simulation of shaking table test on utility tunnel under non-uniform earthquake excitation," *Tunnelling and Underground Space Technology*, vol. 30, pp. 205–216, 2012.

[28] H. Yu, Y. Yuan, Z. Qiao, Y. Gu, Z. Yang, and X. Li, "Seismic analysis of a long tunnel based on multi-scale method," *Engineering Structures*, vol. 49, pp. 572–587, 2013.

[29] G. Wang, M. Yuan, X. Ma, and J. Wu, "Numerical study on the seismic response of the underground subway station-surrounding soil mass-ground adjacent building system," *Frontiers of Structural and Civil Engineering*, vol. 11, no. 4, pp. 424–435, 2017.

[30] V. W. Lee and J. Karl, "Diffraction of SV waves by underground, circular, cylindrical cavities," *Soil Dynamics and Earthquake Engineering*, vol. 11, no. 8, pp. 445–456, 1992.

[31] C. L. Xin, Z. Z. Wang, and B. Gao, "Shaking table tests on seismic response and damage mode of tunnel linings in diverse tunnel-void interaction states," *Tunnelling and Underground Space Technology*, vol. 77, pp. 295–304, 2018.
[32] Y. H. Pao and C. C. Mow, *Diffraction of Elastic Waves and Dynamic Stress Concentrations*, Crane Russak & Company, New York, NY, USA, 1973.
[33] C. A. Davis, V. W. Lee, and J. P. Bardet, "Transverse response of underground cavities and pipes to incident SV waves," *Earthquake Engineering & Structural Dynamics*, vol. 30, no. 3, pp. 383–410, 2001.
[34] V. W. LEE and M. D. TRIFUNAC, "Response of tunnels to incident SH waves," *Journal of Engineering Mechanics*, vol. 105, no. 4, pp. 643–659, 1979.
[35] V. W. Lee and H. Cao, "Diffraction of SV waves by circular canyons of various depths," *Journal of Engineering Mechanics*, vol. 115, no. 9, pp. 2035–2056, 1989.
[36] V. W. Lee, "On deformation of near a circular underground cavity subjected to incident plane P waves," *European Journal of Earthquake Engineering*, vol. 7, no. 1, pp. 29–35, 1993.
[37] H. Xu, T. Li, J. Xu, and Y. Wang, "Dynamic response of underground circular lining tunnels subjected to incident P waves," *Mathematical Problems in Engineering*, vol. 2014, Article ID 297424, 11 pages, 2014.
[38] H. F. Kara, "A note on response of tunnels to incident SH-waves near hillsides," *Soil Dynamics and Earthquake Engineering*, vol. 90, pp. 138–146, 2016.
[39] C. H. Lin, V. W. Lee, M. I. Todorovska, and M. D. Trifunac, "Zero-stress, cylindrical wave functions around a circular underground tunnel in a flat, elastic half-space: incident P-waves," *Soil Dynamics and Earthquake Engineering*, vol. 30, no. 10, pp. 879–894, 2010.
[40] Z. Fan, J. Zhang, and H. Xu, "Theoretical study of the dynamic response of a circular lined tunnel with an imperfect interface subjected to incident SV-waves," *Computers and Geotechnics*, vol. 110, pp. 308–318, 2019.
[41] X. Ji, J. Liang, and J. Yang, "On dynamic stress concentration of an underground cylindrical lined cavity subjected to incident plane P and SV waves," *Journal of Tianjin University*, vol. 39, no. 5, pp. 511–517, 2006.
[42] V. W. Lee and H. CAO, "Diffraction of SV waves by circular canyons of various depths," *Journal of Engineering Mechanics*, vol. 115, no. 9, pp. 2035–2056, 1989.
[43] J. Liang, H. Zhang, and V. W. Lee, "A series solution for surface motion amplification due to underground twin tunnels: incident SV waves," *Earthquake Engineering and Engineering Vibration*, vol. 2, no. 2, pp. 289–298, 2003.
[44] G. Yan, B. Gao, Y. Shen, Q. Zheng, K. Fan, and H. Huang, "Shaking table test on seismic performances of newly designed joints for mountain tunnels crossing faults," *Advances in Structural Engineering*, vol. 23, no. 2, pp. 248–262, 2020.
[45] G. Yan, Y. Shen, B. Gao, Q. Zheng, K. Fan, and H. Huang, "Damage evolution of tunnel lining with steel reinforced rubber joints under normal faulting: an experimental and numerical investigation," *Tunnelling and Underground Space Technology*, vol. 97, p. 103223, 2020.
[46] Y. S. Shen, Z. Z. Wang, J. Yu, X. Zhang, and B. Gao, "Shaking table test on flexible joints of mountain tunnels passing through normal fault," *Tunnelling and Underground Space Technology*, vol. 98, p. 103299, 2020.